Order Number 9326343

Analysis of slow formation of plasmas in a coaxial double theta pinch

Berger, Russell George, Ph.D.

University of Washington, 1993

U·M·I
300 N. Zeeb Rd.
Ann Arbor, MI 48106

Analysis of Slow Formation of Plasmas in a Coaxial Double Theta Pinch

by

Russell Berger

A dissertation submitted in partial
fulfillment of the requirements for the degree of

Doctor of Philosophy

University of Washington

1993

Approved by Thomas R Jarboe
(Chairperson of Supervisory Committee)

Program Authorized
to Offer Degree Department of Physics

Date 3-19-93

In presenting this dissertation in partial fulfillment of the requirements for the Doctoral degree at the University of Washington, I agree that the Library shall make its copies freely available for inspection. I further agree that extensive copying of this dissertation is allowable only for scholarly purposes, consistent with "fair use" as prescribed in the U.S. Copyright Law. Requests for copying or reproduction of this dissertation may be referred to University Microfilms, 1490 Eisenhower Place, P.O. Box 975, Ann Arbor, MI 48106, to whom the author has granted "the right to reproduce and sell (a) copies of the manuscript in microform and/or (b) printed copies of the manuscript made from microform"

Signature Russell G. Bergen

Date 3-19-93

University of Washington

Abstract

Analysis of Slow Formation of Plasmas in a Coaxial Double Theta Pinch

by Russell Berger

Chairperson of Supervisory Committee: *Professor Thomas Jarboe*
Department of Aeronautics and Astronautics

Plasma formation in a coaxial double theta pinch device is analyzed. This device, called the Coaxial Slow Source (CSS), has demonstrated the formation of annular field reversed configurations on diffusive timescales. Three analytical models are developed and used to: characterize the coupling between the magnetic configuration and the driving circuit, predict a temperature limit due to impurity radiation, and reveal an instability due to localized radiation cooling. A comprehensive model incorporating the interactions of neutral and ionized particles is used to simulate the CSS experiment on a computer. This two-dimensional MHD two-fluid code called COAX is adapted from an earlier version used by Hahn [1]. Simulations are compared to experimental data from the CSS to test the models, and quantify the physical processes involved.

The slow forming plasma is strongly influenced by the surrounding neutral fill gas due to: the energy lost by ionization of these neutrals, and enhanced heat conduction from charge exchange collisions between neutrals and ions. The friction between the neutral and ionized fluids is important in modeling the formation dynamics. Impurities also play a role in the power balance of such plasmas by strongly emitting line radiation. Radiation from impurities appear unimportant unless the plasma contacts the vacuum chamber walls.

TABLE OF CONTENTS

LIST OF FIGURES

LIST OF TABLES

ACKNOWLEDGMENTS

I would like to thank those people who have helped in this work. First, my sincere appreciation to Professors Thomas Jarboe, Bob Brooks, and Ricardo Farengo for clarifying my thinking, motivating my progress, and for guidance throughout this project. Also, I thank Dr. Richard Milroy for volunteering to sit on my reading committee, and giving me advice on numerical techniques and philosophy. I also would like to thank the graduate students I have associated with, especially Bill Pierce and Ricky Maqueda for many interesting discussions and for their help in accessing and evaluating the CSS experimental data. Finally, I am most grateful to the people with the patience to stand by me throughout this long endeavor: my parents, Russell and Jeanette Berger, and my future wife, Dian. Without them, I would not have had the strength to finish.

Chapter 1

INTRODUCTION

Plasmas confined by magnetic fields in a field reversed configuration (FRC) have been extensively studied for their potential as fusion reactors [2]. FRCs are in the class of magnetic configurations called compact toroids, which have a toroidal topology, but no physical structure linking the torus. In an FRC, poloidal fields are generated by inducing currents in the confined plasma with a cylindrical coil (theta pinch coil). There are negligible toroidal fields in an FRC. Fusion reactors based on these configurations have useful features. They would be relatively easy to engineer due to the simple geometry of the electrical coils. The efficient use of the confining magnetic fields may allow for high power density output and use of advanced fuels.

The Coaxial Slow Source (CSS) at the University of Washington [3] was designed to demonstrate FRC production with lower voltages and longer time scales compared to the field reversed theta pinch method. Two coaxial theta pinch coils induce electrical currents in an annular region between them filled with plasma. This forms an annular FRC rather than a true FRC, as a coil structure protrudes into the central hole of the torus. Since this coil is cantilevered from one end, it is possible for the annular FRC to be translated off this structure to become a true FRC.

The purpose of this research is to analyze the novel formation technique demonstrated in the Coaxial Slow Source, with regard to its use as a method to generate FRC plasmas for magnetically confined fusion reactors. The issues addressing the practicality and usefulness of forming such plasmas for FRC fusion devices are: understanding and controlling the breakdown and formation phases, optimizing the transfer of energy and flux from the capacitor banks or the core region to the plasma region, and developing procedures to form a translatable plasma. Other pertinent issues are to explain certain experimentally observed behavior in terms of relevant theories and models developed or modified for this type of plasma. The plasma

formation considered here uses a somewhat different geometry and magnetic topology, slower timescale, and greater dependence on atomic processes, than other FRC formation schemes.

This dissertation uses various methods for analysis of the plasmas in the CSS device. The primary tool is a computer code called COAX, which models the plasma ions and neutrals as two separate fluids. These fluids are acted upon by the usual magnetohydrodynamic forces plus friction between species. This code produces a large amount of data about the dynamics of the plasma, but takes hours to run and analyze the results. A much simpler model regards the plasma as an electrical element in a circuit. This model shows the relation between circuit parameters and power input to the plasma and magnetic fields. An analytical model of the plasma as an Ohmically heated but radiating column shows the influence of radiation from impurities. This power balance model shows the origin and threshold for the low temperature/high density equilibrium state called radiative collapse. Another analytical model is used to investigate radiation induced instability. Throughout this analysis, simulations are compared to experimental data [4], first, to establish phenomena of interest, such as the observation of magnetic activity or radiation from impurities at certain times, and then to validate results of the analyses.

The remainder of this dissertation is organized as follows: as a starting point, section 1.1 of this chapter describes the formation of plasmas in the CSS and other FRC devices, giving the primary experimental results, and examining the physical issues thought to be important for the CSS plasma formation. Section 1.2 introduces atomic and collisional processes in a tutorial manner, describing the effects that these processes have on the plasma formation. The intent of this section is to prepare the way for discussions of the radiative collapse model, and to introduce the pertinent processes that are modelled using the COAX code. In chapter 2 some analytical models are developed, such as an electrical circuit model used to analyze energy and flux transfer to the plasma, and models to describe the phenomena of radiative collapse and local radiative instabilities. A version of the computer code COAX, which numerically solves the ion and neutral magnetohydrodynamic fluid equations, is described in chapter 3. This version of the code assumes that the neutrals are coupled to the ions with infinite friction. Results of simulations with this version are also presented in that chapter. Chapter 4 describes a modified and

improved version of COAX, which models the neutral and ion fluids with separate velocities coupled by finite friction. The results of simulations using the improved version of COAX are also presented in that chapter. Finally, chapter 5 summarizes this research.

1.1 Plasma Formation in the Coaxial Slow Source

In this section, a descriptive account of plasma formation in the CSS is given. The qualitative features of slow AFRC formation have elements in common with fast FRC formation and the much slower tokamak formation. This description follows from experimental data, from interpretations by computer simulations, and by examining the information in the literature on effects expected to be important. Some of the history of the CSS device is also given. From this perspective, some issues can be raised that will be addressed by the work described later.

1.1.1 Description of Field Reversed Configuration Plasmas

Plasma devices called magnetic pinches were first used in the 1950s to confine and heat plasmas in attempts to develop thermonuclear reactors. The dynamic theta pinch ionizes and implodes a cylindrical shell of plasma by inducing an azimuthal current in the plasma by means of fast rising currents in a surrounding coil, which produces an axial magnetic field that *pinches* the configuration. The field lines are *open* in that individual field lines cross the walls of the vacuum vessel beyond the coil ends, and particles drifting along these open field lines will rather quickly impact the wall, and long-time confinement of a hot, dense plasma is not achieved.

The field reversed configuration (FRC) is similar to the theta pinch configuration, in that azimuthal current is induced by an external coil, but the magnetic field at the geometrical axis is reversed in direction from the field at the coil. This configuration results in closed field lines in a toroidal topology confining a pinched plasma. The plasma β is defined as the ratio of plasma pressure to magnetic field pressure, that is, $\beta = 8\pi p/B^2$. β is nearly unity in such pinch configurations, meaning optimum usage of the available magnetic field for confining the plasma.

High beta fusion reactors have advantages over lower beta devices such as tokamaks. If the maximum magnetic fields in a fusion reactor are set by mechanical

stress or current limits, then high beta reactors could run with higher plasma pressure than lower beta configurations. A higher output fusion power density would result since fusion power increases as the square of the density ($P_{\text{fusion}} \propto n^2\langle\sigma v\rangle$). Also, since synchrotron radiation increases as the square of the magnetic field ($P_{\text{synch}} \propto B^2nT \propto (1/\beta)(nT)^2$), losses from synchrotron radiation must be overcome by fusion power output. Again, the high β plasma has an advantage, as the ratio of fusion power to synchrotron losses is $P_{\text{fusion}}/P_{\text{synch}} \propto \beta\langle\sigma v\rangle/T^2$. This advantage is particularly important if alternate fuels such at D-He^3 are used. The D-He^3 reaction produces far fewer neutrons than D-T reactions, but requires somewhat hotter and denser operating conditions [5] to achieve the same reactivity as D-T. Thus the higher β compensates for the higher operating temperature.

FRCs are usually produced with a field reversed theta pinch. That is, a plasma is preionized in the presence of a uniform magnetic field (bias field), and then the current in a single theta pinch coil surrounding the plasma is quickly reversed (see the review article in [2]). This fast reversal of current and field requires the application of a large voltage to the coil. By Lenz' Law, a current is induced in the plasma in the original direction of the coil current, trapping a portion of the initial magnetic flux within the preionized plasma. In this scheme, the reversal must occur quickly since the induced current in the plasma and the coil current are of the same sign during the first moments of formation before the field reverses. Hence the plasma is attracted to the coil and contact is made with the vacuum wall. Also, the preionized plasma is resistive, and tends to allow some leakage of the bias flux.

To use an FRC device to confine a plasma and produce fusion energy, instabilities and dissipation must be minimized or controlled. In laboratory plasma experiments to date, disruptive instabilities have been identified and found to be controllable. The electrical current decays at about the same rate as particle and energy loss in such high beta plasmas, but could conceivably be maintained by external drivers (beams, waves, or electrically charged fusion products). Looking ahead to larger, reactor sized devices, problems to overcome are: stabilizing the tilt mode, minimizing dissipative processes, and forming the configuration at technologically realizable voltages.

There are three problems that arise when extrapolating this technique to reactor sized plasmas. First, the final trapped magnetic flux is limited to the initial bias

magnetic flux: flux is dissipated during the formation phase, and no more can be added without some auxiliary current drive mechanism. Second, there is a period of time during which plasma is pushed outward against the vacuum chamber wall before the field reversal is completed, and so it is necessary to keep the timescale for field reversal short to prevent contaminants adsorbed on the wall to be introduced into the plasma, as well as to reduce the dissipation of initial bias magnetic flux. Third, reducing the timescale for reversal requires a higher coil voltage, and reactor sized plasmas would need much higher voltages than are technologically feasible at present.

To circumvent these problems, a slow formation technique has been developed at the University of Washington [3], using a device called the Coaxial Slow Source (referred to as the CSS hereafter). Two coaxial theta pinch coils surround a plasma in the annular region between them, and then by magnetic induction a current is produced in the plasma, similar to the theta pinch, but on a slower time scale. The plasma is formed in the shape of an elongated toroid between the two coils, resulting in an annular field reversed configuration (AFRC).

Because of the geometry, this device resembles a toroidal Z pinch, in which a current is also driven inside a toroidal plasma by induction from an azimuthal current in a toroidal shaped coil. This coil transfers magnetic flux from inside the toroidal core to the plasma region. A tokamak is basically a toroidal Z pinch with added toroidal and vertical fields to provide equilibrium and stability. The AFRCs produced in the CSS have closed poloidal field lines confining the plasma, with negligible toroidal field. Fluctuations, asymmetries in formation, or instabilities disturb the azimuthal symmetry and produce toroidal fields. The average toroidal field is still zero since there is no net axial current to produce it. In this sense, an AFRC can be viewed as a $q = 0$ tokamak.

Plasma is not confined indefinitely in this, or any magnetic confinement device. Collisions between unlike particles cause dissipation of the plasma current and confining fields, as well as diffusion of plasma across magnetic field lines. Also, the existence of lower energy states of the configuration can cause instabilities to develop, such as a tilt of the plasma, or field line reconnection.

The CSS device was proposed to test the formation of annular FRCs at low voltages. The plasma current is induced by opposing the change in currents in

inner and outer theta pinch coils surrounding it. By this method, flux is delivered as long as the currents in the coils rise (or fall), and the trapped flux is (ideally) proportional to the delivered flux. The CSS can be viewed as an elongated tokamak (without the strong toroidal magnetic field of a tokamak). Equilibrium is achieved by using flux shaping conducting walls (repulsive image currents) to center the plasma radially within the annulus. Experiments were performed in the 1970's on a similar device called a belt pinch which had a toroidal field and operated at high voltages with shock heating [6]. Kondoh et al. [7] also operated an annular theta pinch, but it too used high voltages and fast time scales.

The schematic circuit diagram for the CSS is shown in figure 1.1(a). This is the parallel configuration for programmed formation. Without the notch bank and the type D ignitron, this would be the tearing formation set-up. Independent configuration used separate main banks for each coil.

Also shown in figure 1.1 is typical inner coil flux data from the experiment. The outer coil flux almost matches the inner coil flux for parallel configuration shots. The frame labeled (b) is flux from a tearing formation shot. There is a transient ringing preionization before $t = 0$, and then the main bank is switched in. The loop voltage at the coils is highest at $t = 0$, and plasma current is induced starting at $t = 0$.

Frame (c) shows flux from programmed formation. The timing is different from tearing formation. Again the main bank is switched in at $t = 0$, and the loop voltage at the coils is highest then, but plasma is inhibited from forming. At about t =30 μsec, a ringing preionization voltage is applied to initiate ionization. Then at the quarter cycle time ($t = t_{1/4}$ =55 μsec), when the inner coil is filled with flux, a notch bank is switch in. This produces the steep slope in the plot. This voltage is needed to induce current in the plasma, as without the notch, the slope (loop voltage) at $t = t_{1/4}$ is zero.

The diagram in figure 1.2 shows the magnetic field line or flux surface topology at various times during the operation of the CSS device. If plasma is inhibited from forming during the initial application of voltage to the coils, then the inner core fills with flux for the first quarter cycle ($t < t_{1/4}$). By preionizing some plasma in the annulus at $t = t_{1/4}$, the flux can then be transferred to the annular region by inducing current in the ionizing plasma there. During this time, the flux lines

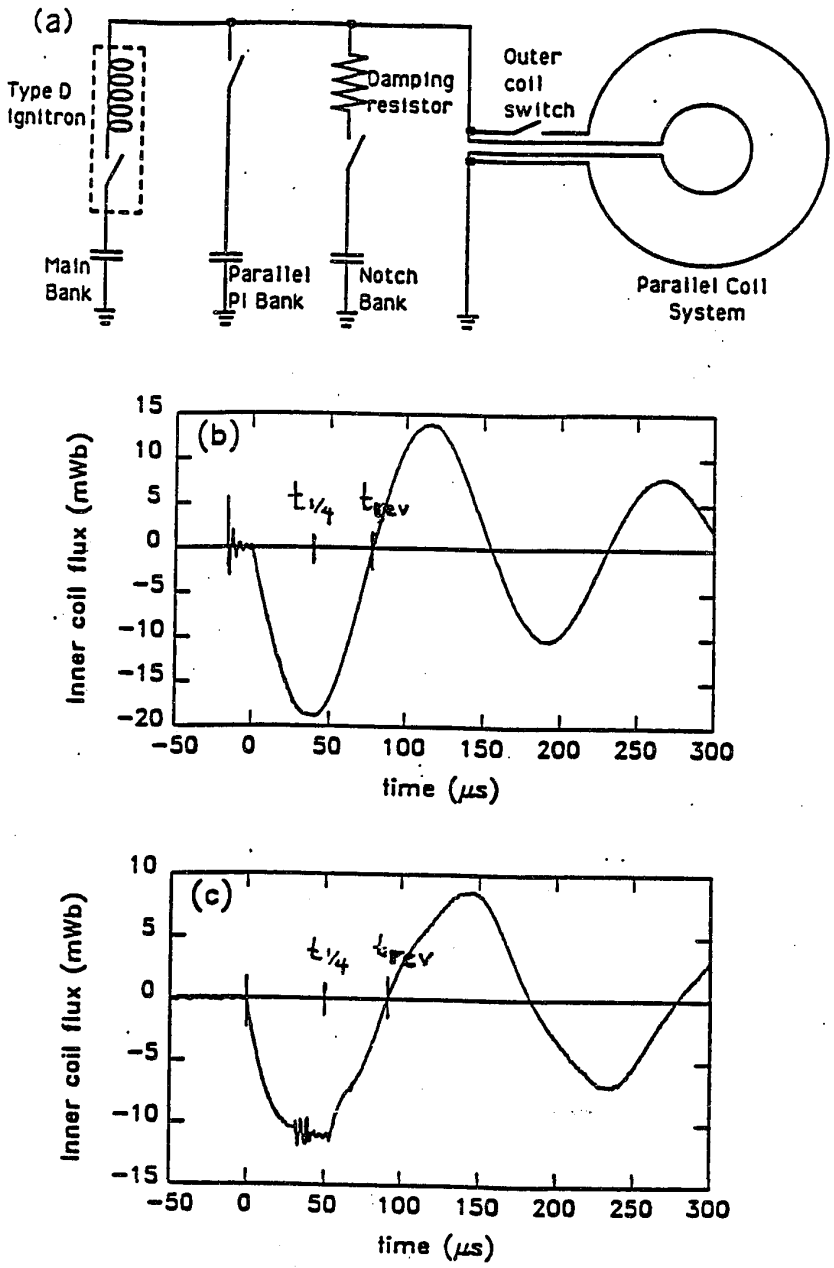

Figure 1.1: (a) Circuit schematic of CSS. Flux traces produced in experimental shots: (b) tearing formation, (c) programmed formation.

enclosing the plasma are all simple closed curves. The separatrix is defined as the last flux surface enclosing the plasma that does not also link a coil. The separatrix is on the coils in this case. When the separatrix is on a coil, the formation is called *programmed* because the flux value at the separatrix is then programmed to be the value at the coil (that is $\int V dt$).

At the time $t = t_{rev}$ the field in the inner core changes sign, the topology of the flux surfaces change, and the field lines became multiply connected. The separatrix is then not bounding either coil, but is located somewhere within the annulus determined by the rates of flux addition, flux dissipation, and field line tearing at the *x-points*, the saddle points of the flux function. This is called *tearing* formation phase. If the inner core had not been filled with flux before the plasma was formed, the initial formation sequence would have started with this topology, and this is called tearing formation. Since the magnetic field line topology is so different from the programmed formation phase, tearing formation leads to different results. A more detailed description of programmed and tearing formation can be found in the paper by Pierce et al. [4]

Field line tearing, or reconnection, occurs within the separatrix also. The plasma configuration split into large pieces, or small scale tearing can occur near the field null leading to enhanced dissipation of flux.

1.1.2 Atomic Physics Phenomena During Formation

The slow formation of plasmas in the CSS requires that a substantial density of neutral particles are present at the beginning of the discharge. There are many processes involving particle collisions between electrons, neutrals, ionized fill gas, and impurity atoms and ions, as well as radiation emitted by these particles. These atomic physics processes add important and often overlooked elements to the formation process beyond the formation of the desired magnetic configuration. The development of the physics of edge plasmas in tokamaks shows that atomic processes near the wall have a pronounced effect on the whole plasma. The formation of AFRCs entails many of the same processes.

First, ionization is of course necessary to generate the plasma. The gas often

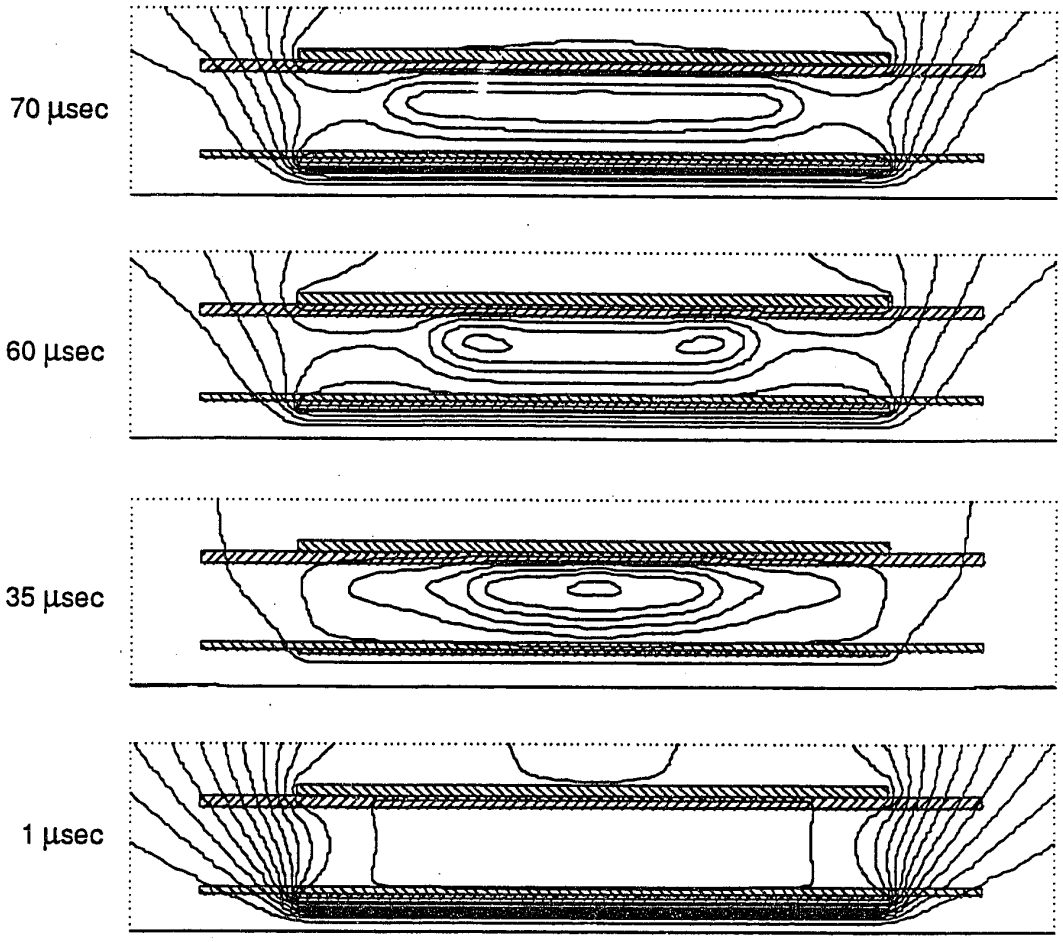

Figure 1.2: Magnetic field line topology during the formation of an annular FRC. the solid line at the bottom of each diagram is the azimuthal axis of symmetry. The shaded regions represent the inner and outer coils and vacuum vessel walls. The 1 μsec caption refers to a time just after $t = t_{1/4}$, and the 35 μsec caption refers to a time just before $t = t_{rev}$.

used in FRC experiments was deuterium (D).[1] Ionization occurs through inelastic electron collisions with either neutral H_2, its ion H_2^+, or atomic H. Excitation or dissociation can also occur. The energy needed to ionize, excite, or dissociate particles leads to a cooling effect on the electrons.

The presence of neutrals can effect plasma motion due to ion-neutral collisions. The result is an apparent drag between the ion and neutral fluids, since neutrals are not affected by the magnetic forces. Also, the collision between a neutral and ion of the same atomic structure can result in charge exchange, for instance $H + H^+ \rightarrow H^+ + H$. This means that a higher energy ion nominally tied to a field line can exchange an electron with a neutral to become a neutral itself, and thus be released from the confinement of the magnetic fields. Charge exchange can enhance cross-field ion heat conduction.

Radiation is emitted from spontaneous decay of collisionally excited molecules, atoms, or ions. This can also be a major energy loss, especially when higher Z particles (impurities) are present that are strongly radiative. Usually, plasma is optically thin to this radiation, i.e. the absorption length is longer than the thickness of the plasma, and so the radiation escapes. In the optically thin case, there may be $\sim$ 50 eV/particle required to produce each H ion, including the radiation emitted. In the optically thick case, when the density of neutrals is significant, the radiation is absorbed and re-radiated in a random walk fashion, the effect being an energy transport.

The collision of particles with the walls can release impurities adsorbed on the surface. These impurities can radiate strongly and affect the power balance with Ohmic heating. When the level of these impurities in the bulk of the plasma is above a limit, the radiation may be high enough to limit the temperature increase, and this leads to a high density, low temperature contraction of the plasma, called a radiative collapse.

---

[1] Deuterium acts almost identical to its isotopic equivalent protium (H) atomically and chemically, and so H will generally be substituted for D hereafter. There is, of course, the higher mass for D to consider when calculating particle kinetics.

1.1.3 Independent Coil Configuration

The CSS was first operated with independent driver circuits connected to each coil, called independent configuration. In this configuration of the circuit, flux addition rates (voltages) can not be made the same at the two coils at all times, and so the plasma radial position tends to shift from the inner vacuum wall, then to the outer wall, and back to the inner wall again. This motion of the plasma causes wall contact, and impurities such as carbon and oxygen are introduced to the plasma. These impurities radiate strongly when ionized to the lithium-like state. The radiation power peaks at temperatures of about 6 eV and 20 eV for carbon and oxygen, respectively. These peaks in radiation constitute the so-called "radiation barrier," which prevents the plasma from getting hotter.

As a result of the impurity radiation, the ohmic heating is balanced by radiative losses [8], and the plasma probably never exceeds the oxygen radiation barrier temperature of 20 eV. Annular FRCs are formed though, and these last as long as flux is supplied. Internal magnetic field mapping was performed by Smith [9] from which magnetic flux contours could be calculated, showing that the plasma shape and behavior in programmed formation phase is different than in tearing formation phase.

1.1.4 Parallel Coil Configuration

The CSS circuitry was later changed to allow parallel electrical connection of the coils to the driving circuit, called parallel configuration. This allowed the flux addition rate to be nearly equal from each coil, and plasmas are formed and maintained at a radius that bisects the annular area between the coils. Wall contact does not occur during initial formation as it does when using the independent configuration device, so radiation from impurities is not an issue at early times.

1.1.4.1 Tearing Formation

Tearing formation plasmas form easily at $t = 0$ when the applied voltage is at its peak. The plasmas do not show any tilting behavior, as they do in the topological distinct programmed formation plasmas. The plasma forms as a long, thin annulus, with x-points at the ends. The time behavior shows monotonic increases in

temperature, ionized particle inventory, and external field magnitude, with small radiation power losses up to a certain time. This time is consistent for many shots using the same operating conditions. Fluctuating magnetic fields in the toroidal direction appear, along with behavior in the poloidal magnetic fields that suggests azimuthally asymmetric field line tearing. Radiation also appears after this time from what seems to be plasma/wall contact. It is not known whether radiation from neutrals causes the tearing activity, if the converse is true, or if they are related at all. It is thought that neutrals enhance heat conduction because of the amount of neutrals present while the ionized inventory is slowly building.

The flux transfer from the external circuits to the plasma and fields is quite good. That is, flux produced in the inner coil links that in the annulus with small losses. Lack of flux linkage results from dissipation of trapped flux in the field reversed region. The plasma, while resistive, still acts as a relatively low impedance load to the circuit.

1.1.4.2 Programmed Formation

To form a plasma in programmed formation, ionization needs to be inhibited at $t = 0$, and then abruptly started at $t = t_{1/4}$. This is accomplished by making some changes to the external circuitry. At $t = 0$, the outer coil is not connected to the circuit. A fraction of magnetic flux in the core also links the annulus, and the resulting bias field in the annulus inhibits ionization. The outer coil is switched in at an appropriate time, so that external inductances from the cables connecting the coils then allows the field in the annulus to become nearly zero at $t = t_{1/4}$. At that time, a short duration, high voltage pulse is applied to start plasma breakdown (when otherwise the voltage is zero).

In programmed formation, the field lines confining the plasma are all closed, and the separatrix is on the coils, until around $t = t_{rev}$. After that time, the field within the inner coil changes sign, and a tearing phase starts, with x-points forming in the annulus at the ends of the coils. During the programmed formation phase, the plasma is short in axial extent, resembling a slightly elongated toroidal Z pinch. After the tearing phase starts, the plasma extends to approximately the length of the coils, as it does at the beginning of tearing formation.

When plasmas are formed by programmed formation, they tend to tilt, as pre-

dicted by linear stability theory[10]. Due to the similarity to a toroidal Z pinch, this instability is the analog of a kink instability, with a wavelength corresponding to one circumference around the device. While the image currents produced in the conducting inner wall would tend to prevent a kink from deforming radially, the plasma can translate axially in an asymmetric, tilting motion. The nonlinear or saturated state is unknown either theoretically or experimentally. Evidence of tilting has been observed using external magnetic probes [11,12]. The tilt appears to grow exponentially for a while and then saturate. The plasma is never totally disrupted by the tilting instability.

The energy transfer into the annular volume is small due to the short axial extent of the plasma and the small confining field. From the Poynting theorem, the power inflow is given by the surface integral around the annular volume of $P_{\text{Poynting}} = \oint ds \cdot (\mathbf{E} \times \mathbf{B})/\mu_0$. Since the electric field $\mathbf{E} = \hat{\mathbf{e}}_\theta V/2\pi r$ is determined by the voltage (V) on the coils, and the magnetic field B is limited to the value obtained if a perfect conductor were in the annulus, the short length of the plasma and resistive losses limit the value of P_{Poynting}. Magnetic energy within the inner coil before plasma formation is transferred to the annular region with an efficiency exceeding only a few percent. The bulk of this energy is coupled back into the capacitor bank instead.

1.2 Atomic and Collisional Phenomena

High temperature, fully ionized plasmas in magnetic fusion devices are typically considered collisionless. This means that during time scales of interest, MHD instabilities have much more significance than phenomena with origins from particle collisions, such as electrical resistivity, heat conduction, Ohmic heating, and radiation power loss. These phenomena can be treated as small perturbations in the collisionless case. For low temperature, partially ionized plasmas, such as the plasma near the vacuum wall in steady state devices, or during the formation of a plasma in the CSS, the behavior is dominated or greatly affected by these phenomena.

There are many significant processes resulting from collisions between particles in a plasma, especially during plasma formation. In two particle encounters, momentum and energy can be exchanged, the particles can be ionized or recombine through these collisions, or a particle may emit radiation either spontaneously fol-

lowing an exciting collision, or while recombining. By averaging these processes over a macroscopic region of plasma, the resulting effects are friction between differing fluid species, reactions transforming one fluid species to another, and heat conduction, radiation, or other energy loss. These effects can have a strong influence on the plasma behavior.

The physical processes described in this section are divided into five subsections: particle collisions, heat conduction, radiation, models of atomic/ionic state distributions, and ionization/recombination. Although these processes are all related, the separation into the following subsections is for clarity of presentation. For instance, an inelastic collision between an electron and positive ion can result in a recombination, while also producing an emitted photon, so that processes in three categories are present. The state distributions of ions/atoms can be calculated using either equilibrium or nonequilibrium models. These models can be used to calculate the radiative power emitted and the ionization levels of the constituents of a partially ionized plasma. The information presented in this section is preparatory for developing the radiative collapse model in chapter 2 and the COAX computer code described in chapter 3.

1.2.1 Particle Collisions

Since a plasma consists of particles on a microscopic scale, close encounters of one particle with other particles results in statistical fluctuations in the otherwise smooth electric and magnetic fields affecting the particle dynamics. These microfields can have either a cumulative effect, as in elastic scattering by many Debye shielded Coulomb fields, or a single event type of effect, as in an ionization of an atom. The result of particle interactions with microfields is the transport of particles, heat, and magnetic flux in the direction opposite to their concentration gradient, i.e. dissipation. Also, single collisions can transform particles into other species, transfer energy, and/or radiate photons.

1.2.1.1 Electron-Heavy Particle Collisions

Since electrons are the least massive and most mobile particles in a plasma, they tend to carry most of the electrical current. The mobility of electrons is limited by their collision frequency with ions and neutrals. Collisions between electrons

and heavier particles then allows the transfer of the directed kinetic energy in the electron current to be randomized amongst the electrons and the heavy particles. This is Ohmic heating.

Consider an electron fluid equation of motion, where the applied electric field E tends to accelerate the electrons, while collisions with a nearly motionless background of ions and neutrals tends to decelerate that directed motion by deflecting electrons via elastic collisions with frequency ν_e:

$$m_e \frac{du}{dt} = -eE - \nu_e m_e u \tag{1.1}$$

The steady state velocity is $u = -eE/\nu_e m_e$, and the electrical current for a electron density n_e is $J = -en_e u = e^2 n_e E/\nu_e m_e$. The resistivity η is then $E/J = \eta = \nu_e m_e/e^2 n_e$. This is the general formula for some unspecified collision frequency ν_e.

To determine ν_e, the formal method is to calculate the collision integral for the electron distribution function [13]

$$\nu_e n_e = \sum_\alpha \int C_{e\alpha} d\mathbf{v}_e = \sum_\alpha \int \left[f_e(\mathbf{v}'_e) f_\alpha(\mathbf{v}'_\alpha) - f_e(\mathbf{v}_e) f_\alpha(\mathbf{v}_\alpha) \right] |\mathbf{v}_e - \mathbf{v}_\alpha| \, d\sigma \, d\mathbf{v}_e \, \mathbf{v}_\alpha \tag{1.2}$$

where the sum is over the types of heavy particles with which the electrons can make collisions, the post-collision velocities $\mathbf{v}'_e$ and $\mathbf{v}'_\alpha$ are related to $\mathbf{v}_e$ and $\mathbf{v}_\alpha$ by the laws of elastic collisions (conservation of momentum and energy), and $d\sigma = \sigma(|\mathbf{v}_e - \mathbf{v}_\alpha|, \theta) d\Omega$ is the differential cross-section for scattering into solid angle $d\Omega = \sin\theta \, d\theta d\phi$. In general, the answer can be represented by $\nu_e n_e = \sum_\alpha n_e n_\alpha \langle \sigma_{e\alpha} v_{e\alpha} \rangle$, where $v_{e\alpha}$ is the velocity in the center of mass reference frame. The quantity in the angle brackets above is the ensemble average of an appropriate cross-section and velocity product, which has a general usage as a reaction rate coefficient for any type of collision.

Braginskii has calculated the above for elastic collisions with ions (of charge Z). The cross-section $\sigma_{ei} \approx (Ze^2/T_e)^2 \ln \lambda$, the square of the distance of closest approach times the Coulomb logarithm factor which represents the effect of the shielding of the infinite range Coulomb field by nearby plasma electrons ($\lambda \approx n_e \lambda_d^3$, i.e. the number of particles within a Debye sphere). The collision frequency for electrons elastically deflecting from ions is then $\nu_e = n_i \sigma v_e \propto Z n_e T_e^{-3/2}$, and the resistivity

from these collisions, called classical (or Spitzer, or Braginskii) resistivity is

$$\begin{aligned} \eta &= 1.15 \times 10^{-14} Z \ln \lambda T_e(\mathrm{eV})^{-3/2} \text{ sec [Gaussian units]} \\ &= 1.03 \times 10^{-4} Z \ln \lambda T_e(\mathrm{eV})^{-3/2} \text{ Ohm-m [SI units].} \end{aligned} \tag{1.3}$$

For a partially ionized plasma, the electron-neutral collisions enhance ν_e and hence also the resistivity and electron component of heat conduction. In this case, $\nu_e = n_i\langle\sigma_{ei}v_e\rangle + n_n\langle\sigma_{en}v_e\rangle$. Since the cross-section for electron-neutral collisions is of the order of a Bohr radius squared, and the number density of neutrals is high only for temperatures much lower than the ionization potential, the contribution of electron-neutral collisionality to the resistivity is substantial only for temperatures lower than about 1 eV (in steady state) [14]. The heat conductivity will be affected similarly, as the same enhancement of ν_e is used for the electron component of heat conductivity.

The value of $\langle\sigma_{e\alpha}v_{e\alpha}\rangle$ for nonpolar neutral particles tends to be nearly a constant for temperatures above a few eV. This is so because the cross-section can be shown to scale as $\sigma_{e\alpha} \propto v_{e\alpha}^{-4/p}$ for an electron in a scattering potential $V(r) \propto r^{-p}$ [15]. Since the electric field of the electron ($E \propto 1/r^2$) induces a dipole field in the neutral particle, $p = 4$, and $\langle\sigma_{e\alpha}v_{e\alpha}\rangle$ is constant. For H atoms, $\langle\sigma_{e\alpha}v_{e\alpha}\rangle = 1.67\times10^{-7}$ cm^{3}s^{-1} [16].

Electrons can also have inelastic collisions with heavy particles. Atoms or ions can be excited (or de-excited) to higher (or lower) energy states by collisions with electrons, that is, electrons within the bound system gain (or lose) some energy from the free electron. A special case is when one of the bound electrons is excited into the continuum, then the result is collisional ionization. The reverse can also occur, where the incident free electron is trapped into a bound state, with simultaneous emission of a photon, called radiative recombination.

Even in the simple hydrogenic atoms and molecules, there are many possible reactions between electrons and heavy particles. H_2 can be excited, dissociated into H + H, ionized to H_2^+, or dissociatively ionized to H + H^+. Likewise, atomic H can be excited or ionized, and the ionized molecule H_2^+ can be excited, dissociated, and further ionized. Since many of the excited states can spontaneously radiate, the energy to produce an electron-ion pair is greater than that needed to dissociate (4.4 eV) and ionize (13.6 eV/atom) the H_2 molecule. A simple one step ionization from

$H \rightarrow H^+$ is not realistic due to the many reactions possible, although ionization may be modeled as a one step process for simplicity. This is discussed in subsection 1.2.5.

Electrons can also cause excitation of impurity ions in the plasma. Excitation and de-excitation are related to radiation, since excited atoms tend to spontaneously decay by photon emission rather rapidly. Radiation will be discussed later, as well as the topics of equilibrium models for the collisional-radiative system. This is very significant since the power lost from impurity radiation can dominate the power balance of the plasma when the density of impurities is high enough. This topic will be discussed in chapter 2 when an analytical model of radiative collapse due to impurity radiation is developed.

1.2.1.2 Heavy Particle Collisions

Heavy particles can have collisions amongst themselves, although their slow velocities relative to electrons at the same temperature tend to make these collisions insignificant with respect to electron-heavy particle collisions. The exceptions to this are the physically relevant reactions of charge exchange and excitation transfer, and wall collisions.

Charge exchange reactions are those between two particles with similar electronic structure, but with differing ionization states. For example a neutral H atom and an H^+ ion can exchange the electron attached to the neutral, and continue on with nearly the same energies, but with a change in their respective charge states and with random trajectories. Since the electrically charged ion tends to be trapped by magnetic fields, while the neutral atom is not, hot ions can transfer their energy to colder neutrals which can more readily conduct the heat across field lines. The reaction rate for $H + H^+ \rightarrow H^+ + H$ increases from 10^{-8} to 10^{-7} cm^3s^{-1} for energies between 1 to 100 eV [17]. This is somewhat less than the elastic collision rate with electrons, but greater than the collisional ionization rate with electrons.

Heavy particles can collide with the vacuum chamber walls and cause emission of molecules bound to the wall surface. The surfaces of the vacuum chamber are typically covered with one to three layers of adsorbed molecules [18], made up of the working gas (usually D_2 for the FRC experiments), and compounds formed from the working gas and residual gases from room air, vacuum pump oil, cleaning

solvents, plastic, fingerprints, etc. These compounds can be bound to the surfaces by physisorption, due to van der Waals forces ($E_b \lesssim$ 0.5 eV binding energy) or chemisorption via chemical binding forces ($E_b \sim$ several eV), and so can be desorbed by collision with low energy particles as well as phonon interactions (heating the wall to elevated temperatures).

Physical sputtering is a higher energy phenomenon in which substrate atoms are knocked out of the wall material by fast heavy particles. This requires energies around 20 eV for carbon walls, and higher energies for higher atomic number materials, or more tightly bound substates. Chemical sputtering by chemically reactive low energy particles such as H or O involves the formation of molecular compounds of the impacting particles and the surface atoms, and the subsequent desorption of these loosely bound compounds. Volatile carbon compounds (like CH_4 and CO_2) can be formed this way from larger hydrocarbons adsorbed on the walls.

It should be noted that the amount of impurities introduced into a pure H or D plasma by the combined processes of desorption and sputtering can be quite significant. If the surface density of impurities were one atom per (10 Å)^2, a cylindrical vacuum vessel of 20 cm radius would produce an impurity ion density of 10^{13} cm^{-3} if the entire surface inventory were desorbed. Typical FRC experiments operate around 10^{15} cm^{-3} H^+ density, and 1% impurity fractions are in fact typically reported when no special cleaning of the walls has been performed. The radiation from partially ionized impurity ions can be a major power loss, as will be shown later. Glow discharge cleaning attempts to remove adsorbed impurities from the surfaces by flowing an appropriate partially ionized gas through the chamber (see [19] for instance). The desorbed wall contaminants are then continually pumped out.

1.2.2 Heat Conduction

Ohmic heating was described earlier in subsection (1.2.1.1) as an effect caused by electrons colliding with other particles, since it is primarily the electrons that carry the electrical current. Particle momentum deflecting collisions cause the dissipation of current, and diffusion of particles across field lines in a magnetically confined plasma.

Heat conduction is also caused by collisions. In a magnetized plasma, the col-

lisionality has a different effect on the heat conduction depending on the direction of the magnetic field to the temperature gradient. Without magnetic field, collisions impede the straight trajectories of particles with higher average kinetic energy from mixing with those of lower average energy, and heat conduction is reduced by collisions. With a magnetic field however, particle trajectories perpendicular to the field are in Larmor orbits around field lines. Collisions allow particles to be deflected onto another field line, and so collisions enhance heat conduction across field lines.

Braginskii [13] has calculated the heat conduction from charged particle collisions. The heat conduction vector $\mathbf{q}$ has units of energy density $\times$ velocity, and its components parallel and perpendicular to field lines is given by

$$\begin{aligned} \mathbf{q} &= -\kappa_{\|}\nabla_{\|}T - \kappa_{\perp}\nabla_{\perp}T \\ \kappa_{\|} &= f_{\|}\frac{nT\tau}{m} \\ \kappa_{\perp} &= f_{\perp}\frac{nT\tau}{m[(\Omega\tau)^2+1]} \end{aligned} \tag{1.4}$$

where the factors $f_{\|}$ and $f_{\perp}$ are numbers on the order of one that depend on the particle conducting the heat. The collision time τ is the average time for a momentum deflecting collision, and $\Omega = qB/mc$ is the Larmor frequency, dependent on the magnetic field strength.

From the form of these equations, it can be seen that the for highly magnetized plasmas $\Omega\tau \gg 1$, the perpendicular heat conduction is much lower than the parallel conduction, and so the temperature along field lines will tend to be uniform. Temperature gradients will tend to be in the direction perpendicular to nested flux surfaces in a well confined plasma. The ions and electrons have collision times in the ratio $\tau_i/\tau_e = \sqrt{2m_i/m_e}$ and Larmor frequencies in the ratio of m_e/m_i, so that the electron contribution dominates for parallel conduction, and the ions dominate perpendicular conduction.

Collisions with neutrals change this picture somewhat. The collision times are shorter from collisions with neutrals. This decreases the parallel conduction and increases the perpendicular conduction. For regions with significant neutral population, temperature gradients can develop along field lines, and large amounts of heat can flow across field lines by conduction. When the particles are mostly neu-

trals, heat can convect across field lines easily since the neutrals are not affected by the magnetic fields.

1.2.3 Radiation

Radiation processes in plasmas are enormously important. The emitted radiation can be used to monitor the conditions inside the plasma from afar, and so makes a useful noninvasive probe. Radiation is also an important energy loss mechanism in magnetically confined plasmas. In the CSS, Ohmic heating can be balanced by radiation from impurities, and this limits the temperature increase, resulting in a cold plasma. Some tokamaks have impurities introduced to the plasma from sputtering by fast plasma particles with the wall or limiter. These impurities can radiate significant amounts of power out of the plasma, and even cause disruptions.

1.2.3.1 Emission and Absorption of Line Radiation

Whenever an electronic transition is made in an atom, ion, or molecule[2] that decreases the potential energy of the system, but does not transfer that energy to another particle, then electromagnetic radiation is emitted to carry off the excess energy. Likewise, an upward electronic transition results when radiation is absorbed. If the electronic transition is between bound states, then line or bound-bound radiation is emitted. Continuum or free-bound radiation can also occur, such as during radiative recombination, when a free electron becomes bound to an atom, ion or molecule.

The photon has the energy of the difference between initial and final electronic levels, and so is determined by the quantum mechanics of that particular system. This photon energy E, or its corresponding frequency $\nu = E/h$, has a finite width in frequency due to various mechanisms. The natural width is the result of the finite lifetime of an excited atom, which is finite due to the possibility of spontaneous transitions to lower states. Just as an induced transition is caused by applying an electromagnetic field of the appropriate frequency, the virtual field of the vacuum also induces transitions, and this is what causes the spontaneous transitions. The

[2] The word atom may be substituted for any system of bound electrons and nuclei hereafter, instead of the specific terminology: atom, ion, or molecule.

rate of these transitions are proportional to the line strength, or square of the atomic dipole moment. Thus the natural line width depends on the particular atomic transition. For a spontaneous decay lifetime τ_{sp}, the spectral shape of the radiated line has a Lorentzian distribution:

$$I(\nu) = I(\nu_0)\frac{1}{1+[(\nu-\nu_0)2\pi\tau_{sp}]^2} \tag{1.5}$$

The FWHM of this distribution is given by $\Delta\nu_{1/2} = 1/\pi\tau_{sp}$.

Natural broadening is usually much less than the broadening caused by other mechanisms in a plasma. An emitted line may be Doppler shifted due to motion of the emitting atom. For an atom with velocity v in the line of sight of the observer, the frequency shift is $\Delta\nu = \nu_0 v/c$. A Maxwellian velocity distribution of atoms at temperature $T_a = m_a v_a^2$ then yields a Gaussian line shape profile:

$$I(\nu) = I(\nu_0)\exp\left[-(\nu-\nu_0)^2 m_a c^2/2T_a\nu_0^2\right] \tag{1.6}$$

with FWHM of this distribution given by $\Delta\nu_{1/2} = \nu_0(v_a/c)\sqrt{2\ln 2}$, where it was assumed that the FWHM from Doppler broadening was much greater than the FWHM of natural broadening.

Collisions of excited atoms with other particles can also cause broadening. If the time between collisions is τ_c and the natural decay time is $\tau_{sp} \gg \tau_c$, then classically, between collisions, a nearly continuous wavetrain is emitted, interrupted by random collisions with average time between occurrence of τ_c. This gives the Lorentzian distribution again, with FWHM of $\Delta\nu_{1/2} = 1/\pi\tau_c$. This collision time is given by the inverse of the collision frequency $\tau_c = 1/\sum_i n_i\langle\sigma_{ia}v_{ia}\rangle$. Thus the line width is proportional to the density, cross-sections, and velocities of colliding particles. Because of this dependence, collisional broadening is also called pressure broadening. It is typically dominated by electron collisions due to their higher velocity.

Another form of pressure broadening results from the Stark effect that electric fields exert on radiating atoms. The electric field here is produced by the charged particles in a plasma. For hydrogen atoms, the Stark effect is linear in E, and causes a symmetrical spread of degenerate lines, and no shift in the lines. Other atoms may have shifts, along with spreads that are quadratic in E. For the H_β line at

$\lambda = 486.1$ nm, i.e. the $n = 4 \rightarrow 2$ transition, the FWHM of the wavelength is [20] $\Delta\lambda_{1/2} = 0.040\ n_{14}^{2/3}$ nm, where n_{14} is the H^+ ion density in units of 10^{14} cm^{-3}.

Emitted photons can also be absorbed. The absorption length is an important quantity to know, so an estimate will be made here. In the following subsection on equilibrium models it will be seen that a plasma that absorbs and reradiates photons many times has a different equilibrium than a plasma with little absorption. The cross-section for optical absorption is given by the formula $\sigma_{abs} = 2\pi^2 r_e c f_{mn} L(\omega_0)$, where $r_e = e^2/mc^2$ is the classical electron radius, f_{mn} is the oscillator strength for transition $m \rightarrow n$, and $L(\omega_0)$ is the line shape function evaluated at the line center, normalized so $\int L(\omega)\, d\omega = 1$. The absorption length is then given by $\ell_{abs} = 1/n_m \sigma_{abs} \propto \Delta\nu_{1/2}/n_m$. For a high density of atoms in lower level m, or a narrow linewidth, then the absorption length will be short.

Estimates for the absorption length of the hydrogen L_α line (i.e. the $n = 2 \rightarrow 1$ transition) and an O^{+5} transition ($h\omega = 71.74$ eV) can be made as follows. For the L_α line ($\lambda = 0.12$ nm), the spontaneous decay lifetime is given by the inverse of the Einstein coefficient $A_{21} = 4.699 \times 10^8$ sec^{-1} [21]. The FWHM is then $\Delta\nu_{1/2} = 1.486 \times 10^8$ sec^{-1}. The FWHM for Doppler broadening is $6.8 \times 10^{10}\sqrt{T(\text{eV})}$ sec^{-1}, and is much larger than the natural width. Collisional broadening can be calculated by using the electron-neutral atom collisional rate coefficient $\langle \sigma v_e \rangle = 1.67 \times 10^{-7}$ cm^3 s^{-1}, and so $\Delta\nu_{1/2} = n_e \langle \sigma v_e \rangle / \pi = 5.316 \times 10^8 n_e (10^{14}\ \text{cm}^{-3})$ s^{-1}. The Doppler broadening dominates the others, and will be used to determine the absorption cross-section. The absorption length of the hydrogen L_α line is then $\ell_{abs} = 1/n_H \sigma_{abs}$ where $\sigma_{abs} = 2\pi^2 r_e c f_{12} L(\omega_0)$, $f_{12} = (g_2/g_1)(mc^3/8\pi^2 e^2 \nu^2) A_{21}$, and $L(\omega_0) = (1/2\pi\sqrt{\pi}\nu)\sqrt{mc^2/2T}$. Evaluating these formulas, using the degeneracy factors $g_1 = 2$ and $g_2 = 8$, $\ell_{abs} = 2.15 \times [\sqrt{T(\text{eV})}/n_H(10^{14}\ \text{cm}^{-3})]$ cm. For typical conditions with a mostly nonionized gas of about 10^{14} cm^{-3} density and atom temperature around 1 eV, the absorption length is about 2 cm. It can be concluded that when L_α radiation is important (during the ionization phase), the radiation is trapped in the surrounding neutral gas.

As another example, consider an important line from the OVI ion with $h\omega = 71.74$ eV. The oscillator strength is 0.661, and for a 10^{-15} cm^{-3} plasma density with 1% of the ions in the OVI state, the average ion is in this state at a temperature of about 20 eV [22]. At this temperature, the absorption length is about 6.0 cm [23].

The plasma may be close to optically thick for certain lines such as this.

1.2.4 Models of Atomic/Ionic State Distributions

From the previous descriptions of collision phenomena, it can be seen that there is a multitude of reactions amongst all the possible species present in a plasma, since each element present may be combined in several compounds, ionized to various states, and each of these states can have many excited levels. While rate equations between all possible reactants is possible in theory, the system is too complicated to solve without some simplifications. The following subsections describe some situations in which the proper assumptions can yield reasonably accurate and simple mathematical models for calculating the populations of the multitude of reactants. This is useful in determining the radiation emitted from a plasma for power loss considerations, as well as a tool in analyzing spectroscopic data to determine basic plasma parameters like temperature and density noninvasively.

1.2.4.1 Local Thermodynamic Equilibrium (LTE)

If all processes are in balance with their reverse process, total thermodynamic equilibrium is achieved. Then at temperature T, thermodynamic arguments show that the radiation energy spectrum is the blackbody spectrum, regardless of the plasma composition: $\rho(\nu) = 8\pi h\nu^3/[\exp(h\nu/T) - 1]c^3$ which has a peak at $h\nu \approx T$ (average photon has energy of average particle). The total radiated power per unit surface area is given by $W = 1.03 \times 10^5 T_{\mathrm{eV}}^4$ watts/cm^2 which only depends on the temperature also. The real radiation spectrum is always less than the black body spectrum because thermodynamic equilibrium for radiation assumes that photons are emitted, absorbed, and reradiated many times before leaving the plasma so that they are in equilibrium with the particles in the plasma. This condition is called optical thickness, which is quantified by the integral over the plasma thickness of the radiation absorption coefficient, $\int \kappa\, dl$. If this number is much greater than one, then only the plasma surface loses photons, else the plasma is optically thin, and photons leave from the interior of the plasma before achieving thermal equilibrium with the plasma. Optical thinness is the usual case, except for certain strongly absorbed lines, and so complete thermal equilibrium is not usually achieved.

If we allow the radiation to be decoupled from the plasma particles, then a relaxed version of total thermal equilibrium is possible, called local thermodynamic equilibrium (LTE), where the populations of the different excited states follows a Boltzmann distribution, and the distribution of ionization states is given by the Saha formula [20]:

$$\frac{n_e n_{i+1}}{n_i} = \frac{g_{i+1}}{g_i}\left[\frac{2m^3}{h^3}\left(\frac{2\pi T}{m}\right)^{3/2}\right] e^{-\chi_i/T}$$

where $\chi_i = E_{i+1} - E_i$ is the difference in energy between the ionization states. The quantity in brackets is approximately the inverse of an electron deBroglie wavelength cubed ($\lambda_{\text{deBroglie}} \sim 1$ Å), and so in hydrogen, for instance, significant ionization is possible even for $T < 13.6$ eV if n_e is high enough, e.g. if $n_e = 10^{15}$ cm^{-3}, $T = 1$ eV, n_1 = density of neutral H, n_2 = density of ionized H, $n_2/n_1 = 3.8$ or the plasma is almost fully ionized.

1.2.4.2 Corona Approximation

LTE may not be correct if the density is low enough, since then the collisional de-excitation rate needed to balance the collisional excitation will be low compared to radiative de-excitation (spontaneous emission and radiative recombination). The density needed for LTE to be valid for states separated by energy levels of ΔE is given by $n_e \gg 10^{13}(T_{\text{eV}})^{1/2}(\Delta E_{\text{eV}})^3$ cm^{-3} [24]. Even for a cold (~ 1 eV) plasma, with energy differences between transitions $\Delta E \approx 10$ eV, plasma densities of 10^{16} cm^{-3} or higher are needed for LTE to be true. On the other hand, excited levels near the $n \to \infty$ continuum may be in LTE amongst themselves, since $\Delta E \propto 1/n^3$ is small there.

The corona model was created so that the radiation power could be accurately calculated. The corona model assumes electron collisions cause upward transitions (excitation, ionization), and radiation is responsible for downward transitions (de-excitation, radiative recombination). If the plasma is optically thin, then radiation escapes before being absorbed, and does not participate in excitation. If the electron density is low, enough radiative decay occurs before collisions produce a de-excitation.

This can be quantified by writing a rate equation for each type of atom or ion, and calculating the radiation power emitted from each type of atom/ion in a similar

manner. Each ionization state can have many energy levels for each type of atom, so the density of each type is given by $n_{i,k}$, where i is the ionization state, and k is the excited level of that ionization state. Nomenclature: consider oxygen (O), with nuclear charge Z = 8. OI is neutral O, OII is one time ionized, or O^+, OVII is six times ionized (O^{+6}) or He-like oxygen (i.e. it has two electrons, and just the same structure as He but with Z = 6), OIX is a bare O nucleus, fully ionized. Each charge state has many energy levels (infinite in fact), but by approximating the distribution of levels within one charge state as being in equilibrium with the ground state of that charge state (collisional excitation balanced by radiative de-excitation), only equations for just the ground states of each charge state need be calculated. The rate equation for each ionization state i is then:

$$\frac{dn_i}{dt} = n_e \left[n_{i-1} S_{i-1} - n_i (S_i + \alpha_i) + n_{i+1} \alpha_{i+1} \right] \tag{1.7}$$

where S_i is the ionization rate from i to $i+1$ and α_i is the radiative recombination rate from i to $i-1$. Since in the corona model, radiation occurs immediately after collisional excitation, the power emitted from this plasma is $P = n_e \sum n_{i,k} Q_{i,k} \Delta E_{i,k}$ where $Q_{i,k}$ is the rate coefficient for excitation from ground state $(i,1)$ to state (i,k) with photon energy equal to the excitation energy $\Delta E_{i,k}$. Another rate equation for temperature might use this radiation power as a driving term.

Post et al. [25] have calculated the radiation power and charge state distributions by solving the steady state version of equation (1.7), i.e. balancing collisional ionization and radiative recombination: $n_{z-1} n_e S_{z-1} = n_z n_e \alpha_z$. The radiation power (in units of ergs-cm^3/sec) and average charge state $\langle Z \rangle$ for oxygen is shown in figure 1.3 from that reference. The actual power emitted is the number shown times the product of electron density, impurity ion density, and plasma volume. The sharp peak at about 20 eV is due to most oxygen ions being in a lithium-like charge state which has a loosely held outer electron, which is very optically active. At temperatures above 20 eV, the oxygen ions are almost all in the He-like charge state which is not as optically active, and so the radiated power drops to a much lower value. This peak is called the radiation barrier because the radiated power may prevent the temperature from rising further, and hence presents a barrier to achieving a hot plasma which does not radiate much power.

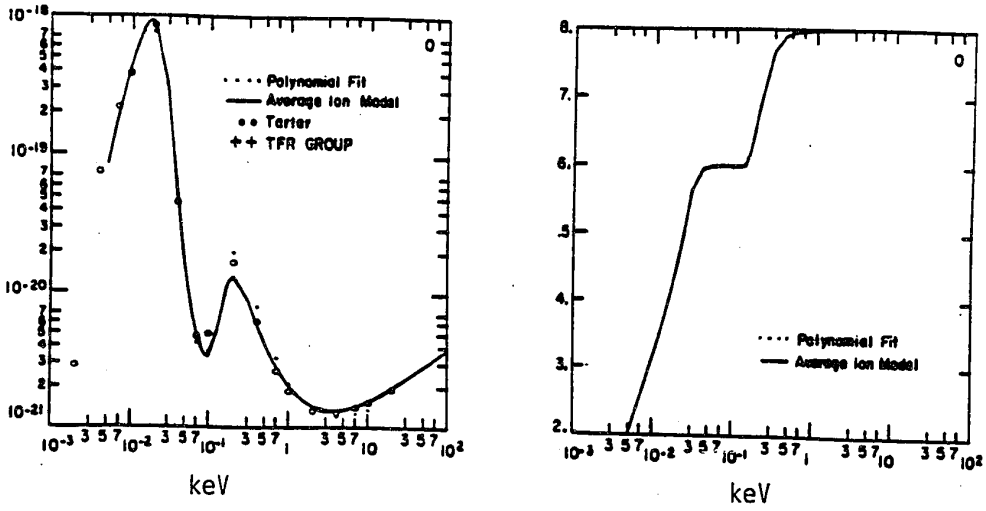

Figure 1.3: Radiated power and $\langle Z \rangle$ for oxygen, from Post et al. [25]. The left plot is cooling rate in ergs-cm^3/sec versus temperature in keV. The right plot is average ionization state versus temperature.

1.2.4.3 Nonequilibrium models

Equilibrium models are not appropriate when temperature and density vary faster than the characteristic time for level populations to be established. The slowest reaction creates a "bottleneck" that determines the time scale for the densities of the charge states to go to the steady state values. An estimate of this time [23,26] is given by $n\tau_{eq} \approx \langle \sigma_{n'n} v \rangle^{-1}$. For most impurities and temperatures, the product of this time scale and electron density is $n_e \tau_{eq} \approx 10^{10} - 10^{12}$ cm^{-3}sec [22]. For example, if $n_e = 10^{15}$ cm^{-3} then $\tau_{eq} \approx 10$ μsec $-$ 1 msec. If the temperature were suddenly raised from the radiation barrier value, to say 100 eV (for oxygen), the plasma would continue to radiate at the radiation barrier rate for a time $\tau \approx$ 10 μsec or more, and possibly cooling the plasma back to the radiation barrier temperature. Thus, overcoming the radiation barrier becomes even more difficult. Also, impurities typically are desorbed or sputtered from a wall facing the plasma, and these may radiate at the temperature barrier rate until they have equilibrated at the temperature of the plasma particles. The radiated power may be much more than that determined by the Post rates and the density of impurities.

In general, with a time varying electron temperature, the rate equations must be solved for non-steady state. To solve such a problem, equations (1.7) need to be solved given the appropriate rate coefficients S_i and α_i. These are typically only temperature dependent, although recombination at low densities can be primarily by dielectronic recombination, which gives a weak density dependence to α_i.

Numerically, these equations are *stiff*, meaning that they converge to a steady state answer, but at widely differing time scales. For numerical stability, a simple explicit time advance method would require a time step smaller than the inverse of the fastest convergence rate, which is impractical. Implicit methods must be used to get around this time step constraint.

A simple method of implicit solution is to assume n_e and T_e are constant during a time step. Then the finite differencing leads to the equation

$$n_i^{n+1} - \Delta t\, n_e \left[n_{i-1}^{n+1} S_{i-1} - n_i^{n+1}(S_i + \alpha_i) + n_{i+1}^{n+1} \alpha_{i+1} \right] = n_i^n \qquad (1.8)$$

which is a tridiagonal matrix equation for the densities n_i^{n+1} at the advanced time step t^{n+1} given rates S_i, α_i and densities n_i at the previous time t^n. Since the form of equations (1.8) is tridiagonal (only the higher and lower ionization states affect

any given state), this can be solved in approximately $6N^2$ steps for N ionization states n_i. The above equation can be solved locally in spatially dependent problems where the densities n_i are given at many mesh points. This can also be vectorized for use on Cray computers.

The above method gives stable numerical solutions for any size of time step, and conserves total particle number density. It is sufficiently accurate to model the slowest processes when the time step Δt is less than the timescales for the slowest ionization, or the inverse rates of change of T_e or n_e. The most difficult part of this problem is obtaining accurate rate coefficients α_i and S_i, as these are not always known with great precision.

1.2.5 Ionization and Dissociation

In this subsection, a model for ionization of hydrogen is developed. During the early ionization phase of the CSS plasmas, the processes of Ohmic heating and ionization are strongly connected, since they are both caused by electron collisions and are dependent on the electron temperature and density. The induced current in the plasma requires both some ionization and a high enough temperature to allow significant electrical conductivity. The structure of the magnetic fields induced in the plasma and the subsequent power flow from the external fields and capacitor banks into the plasma depend on this early phase in the plasma formation. Thus the simulation of the ionization phase is expected to need an accurate model of hydrogen ionization.

It will be shown in this subsection that the ionization fraction increases rapidly from nearly zero to nearly 100% as the electron temperature increases above a transition temperature of about 1 eV. Radiation from the H(2) to H(1) levels (Lyman alpha, or L_α) is trapped within the plasma. This means that the energy to ionize is just the 13.6 eV/ion plus about 4.4 eV/molecule of H_2 to dissociate. The energy to produce each ion/electron pair is thus about 16 eV, with an additional energy supplied equal to the thermal energy of the electron produced. It is assumed that the thermal energy of the initial H atoms is transferred to the thermal energy of the final H^+ ions.

Since ionization requires energy, it acts as a cooling mechanism in the same manner as the deposition into latent heat during a phase transition from liquid

to vapor, for instance. The electron temperature is increased by Ohmic heating, decreased by heat conduction and ionization, and all of these processes depend on the number density of both electrons and neutrals.

Ionization of atomic hydrogen in general proceeds through a ladder-like process of electron collisions with ground and lower level excited states resulting in either ionization ($n \rightarrow \infty$) or excitation ($n \rightarrow m > n$) to higher levels. Spontaneous emission of radiation ($n \rightarrow m < n$) is the usual route for de-excitation to lower levels. This is because the radiative de-excitation rate is much greater than the electron-atom collisional de-excitation rate for levels below some level m^* [26]. For the levels $m > m^*$ the collisional de-excitation rate is higher, so these levels are in LTE amongst themselves. This is the corona model (see subsection 1.2.4.2). The rate equations for the levels $m < m^*$ can be solved assuming a quasiequilibrium condition exists, which is typical for most plasmas of interest.

For low density plasmas, and untrapped radiation, the rate coefficients are calculated by the corona model. The ionization rate coefficient $S_{\rm cor}$ is given [27] as

$$S_{\rm cor} = \frac{10^{-5}(T_e/E_\infty)^{1/2}}{E_\infty^{3/2}(6 + T_e/E_\infty)} \exp(-E_\infty/T_e) \text{ cm}^3/\text{sec} \qquad (1.9)$$

where the ionization energy E_∞ and temperature T_e are given in eV. The radiative recombination rate coefficient for untrapped radiation $\alpha_{\rm cor}$ is given [27] as

$$\alpha_{\rm cor} = 5.2 \times 10^{-14}[0.43 + (1/2)\ln(E_\infty/T_e) + 0.469(E_\infty/T_e)^{-1/3}] \text{ cm}^3/\text{sec} \qquad (1.10)$$

There are two situations when the corona model does not apply: high electron density, and plasma optically thick to L_α radiation. For high electron density plasmas ($n_e > 10^{13}$ cm^{-3}), the corona model may not be valid due to higher collisional de-excitation rates [28]. That is, the higher electron density increases the collision rates while the radiative rates remain unchanged. A more complicated set of reaction rate equations for a collisional-radiative model must be solved. The result is that the ionization rate can be increased by an order of magnitude over that for low density plasmas. This situation is typical for fusion experiments with high density/warm temperature plasma near a limiter or divertor wall where ionization of recirculating neutrals occurs.

For situations with high neutral gas density ($n_n > 10^{14}$ cm^{-3}), typical of the conditions in the CSS experiment as well as similar experiments in FRCs during

the ionization phase, the Lyman alpha radiation ($n = 2 \rightarrow 1$) is trapped in the un-ionized gas as shown in subsection 1.2.3.1. In the case where radiation is considered trapped in the plasma, the radiation emitted during de-excitation of any atom will immediately excite a neighboring atom in the lower energy state, and thus atoms in adjacent energy levels are connected by radiative excitation and de-excitation processes. The corona model must then also be generalized to a collisional-radiative model. In this case also, the ionization rate can be increased by an order of magnitude over that for low density plasmas [29].

Bates, Kingston, and McWhirter [30] show that the ionization of hydrogen can be represented by rate equations for densities of the ionized state (n_i, assumed equal to electron density n_e), the ground state (n_1), and the first excited state (n_2). The levels $n \geq 3$ are in LTE, and are treated as ionized (continuum states) [29]. Actually, the $n = 2$ level is degenerate, with the 2s state metastable to radiative transition to ground state. Due to electron collisions, this state is tied to the 2p state which does radiatively decay to ground state [29], so that the 2s and 2p states are indistinguishable.

The three rate equations derived for the situation with trapped Lyman alpha radiation are

$$\begin{aligned} \dot{n}_1 &= n_e\left(a_1 n_e + P_{21} n_2 - R_1 n_1\right) \\ \dot{n}_2 &= n_e\left(a_2 n_e + P_{12} n_1 - R_2 n_2\right) \\ \dot{n}_e &= -\left(\dot{n}_1 + \dot{n}_2\right) \end{aligned} \tag{1.11}$$

The coefficients for combined collisional and radiative recombination are a_1 and a_2, P_{12} and P_{21} are coefficients for transitions between the ground (n =1) and first excited state ($n = 2$), and R_1, R_2 are coefficients for ionization or for transition into the other hydrogen states. These coefficients are tabulated [30] and are dependent only on electron temperature and density. It would be simpler if these equations could be reduced to the one-step ionization equation

$$\dot{n}_1 = n_e\left(\alpha n_e - S n_1\right) \tag{1.12}$$

as then only the values for neutral and ionized hydrogen densities are needed. This is the situation for plasmas without trapped radiation and with low electron density.

To reduce the two-step ionization equations represented in equation 1.11 to the one-step equation 1.12, the density of atoms in the $n = 2$ state can be approximated

to be in quasiequilibrium with those in the $n = 1$ state. The quasiequilibrium density can be calculated as

$$n_2^Q = \frac{A_2 n_e + P_{12} n_1}{R_2} \tag{1.13}$$

Then equations 1.11 can be recast in the form of equation 1.12 with the ionization and recombination coefficients for the case of trapped radiation expressed in terms of the coefficients from equation 1.11, which are

$$\begin{aligned} S_{\rm tr} &= R_1 - P_{21} P_{12}/R_2 \\ \alpha_{\rm tr} &= a_1 + P_{21} a_2/R_2 \end{aligned} \tag{1.14}$$

This quasiequilibrium is valid when perturbations equilibrate in a time that is short compared to the time for ionization to balance with recombination. These times can be calculated by determining the eigenvalues of the linearized equations of 1.11. The equilibrium values of the densities are

$$\begin{aligned} \bar{n}_1 &= \frac{a_1 R_2 + a_2 P_{21}}{R_1 R_2 - P_{12} P_{21}} n_0 \\ \bar{n}_2 &= \frac{a_2 R_1 + a_1 P_{12}}{R_1 R_2 - P_{12} P_{21}} n_0 \\ \bar{n}_e &= n_0 - \bar{n}_1 - \bar{n}_2 \end{aligned} \tag{1.15}$$

where $n_0 = \bar{n}_e + \bar{n}_1 + \bar{n}_2$ is the total conserved ion/neutral particle density.

Linearizing the two-step equations 1.11 about the equilibrium values gives a linear system for the perturbed densities $\Delta n_1 = n_1 - \bar{n}_1$, $\Delta n_2 = n_2 - \bar{n}_2$, $\Delta n_e = n_1 - \bar{n}_e$,

$$\frac{d}{dt}\begin{pmatrix} \Delta n_1 \\ \Delta n_2 \\ \Delta n_e \end{pmatrix} = n_e \begin{pmatrix} -R_1 & P_{21} & a_1 \\ P_{12} & -R_2 & a_2 \\ (R_1 - P_{12}) & (R_2 - P_{21}) & -(a_1 + a_2) \end{pmatrix} \begin{pmatrix} \Delta n_1 \\ \Delta n_2 \\ \Delta n_e \end{pmatrix} \tag{1.16}$$

The eigenvalues of this matrix are the rates for the corresponding eigenvectors to exponentially damp to zero. One of these eigenvalues is zero since the sum of the ion/neutral hydrogen densities is conserved. The other two eigenvalues correspond to rates for the H(2) density to relax to the quasiequilibrium value n_2^Q and the rate for the H(1) density to relax to $\bar{n}_1$. This can be demonstrated by solving

for the eigenvectors of these nonzero eigenvalues at $T_e = 6000°\text{K} = 0.69$ eV, and $n_0 = 10^{15}$ cm^{-3}. The eigenvalues are -5.7×10^5 sec^{-1} and -10.4 sec^{-1}, and the corresponding normalized eigenvectors are

$$\begin{pmatrix} -0.15 \\ 0.77 \\ -0.62 \end{pmatrix} \text{ and } \begin{pmatrix} -0.71 \\ 0.00 \\ 0.71 \end{pmatrix} \tag{1.17}$$

This shows that the faster relaxation rate (the first eigenvalue) corresponds to the relaxation of the H(2) density to quasiequilibrium and the slower relaxation rate (the second eigenvalue) corresponds to the relaxation of the H(1) and H^+ densities to equilibrium.

In simulations done by Duchs and Griem [29] to explore the dynamic phase of a theta-pinch, they found that the two-step model did not produce significantly different results from the simpler one-step model. The following reasoning shows why this is so.

The quasiequilibrium approximation for n_2 used to reduce equations 1.11 to the one-step equation 1.12 is valid when the ratio of the relaxation rates is high. Figure 1.4 shows the relaxation times for these two eigenvectors for $n_e = 10^{14}$ cm^{-3}. The curve labeled τ_2 is the relaxation time for quasiequilibrium being established for the n_2 density, and τ_1 is the time for relaxation to true equilibrium for the n_1 and n_e densities. It can be seen that $\tau_2 \ll \tau_1$, so that the quasiequilibrium assumption is valid.

The equilibrium ionization fraction (n_e/n_0) is plotted in figure 1.5 for both the trapped L_α radiation and corona models. The ionization fraction increases rapidly to nearly 100% at a temperature around 1 eV for the trapped radiation model. It can be seen in figure 1.4 that the time for steady state (ionization rate equals recombination rate) to be established is many microseconds at low temperatures. At temperatures above 1 eV, the relaxation time is short enough for the equilibrium to be established much faster than any other significant processes, such as change in temperature or density.

At temperatures above about 1 eV the plasma would be fully ionized if in equilibrium. If not in equilibrium, the characteristic ionization time is given by $\tau_{\text{ioniz}} = 1/Sn_e$. For $n_e = 10^{14}$ cm^{-3}, $T_e = 1$ eV, and L_α radiation trapped, this

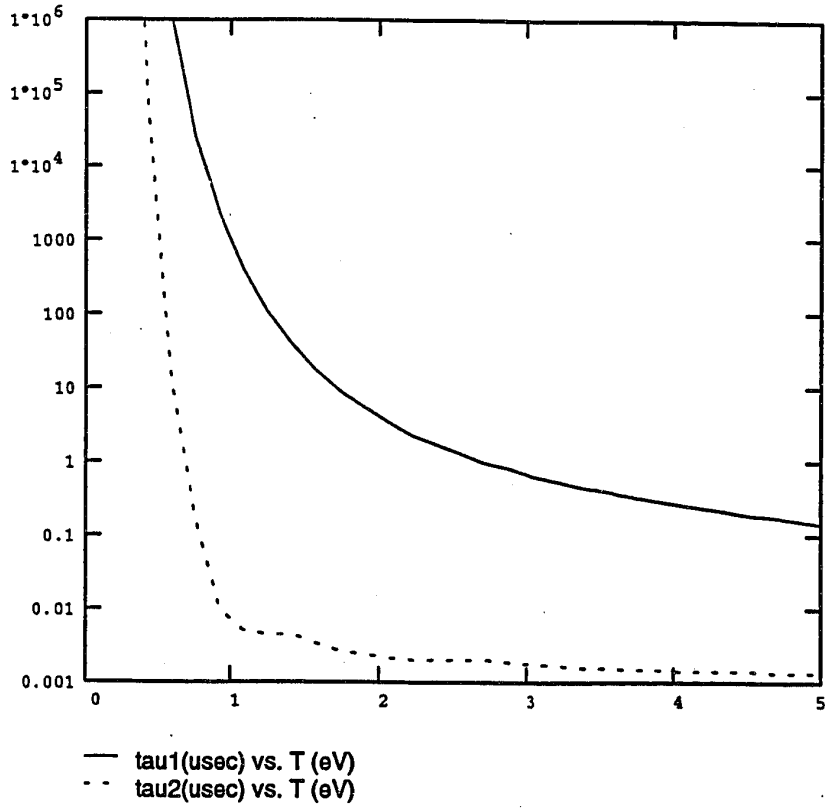

Figure 1.4: Relaxation times for $n_1 \rightarrow \bar{n}_1$ (τ_1) and $n_2 \rightarrow \bar{n}_2$ (τ_2).

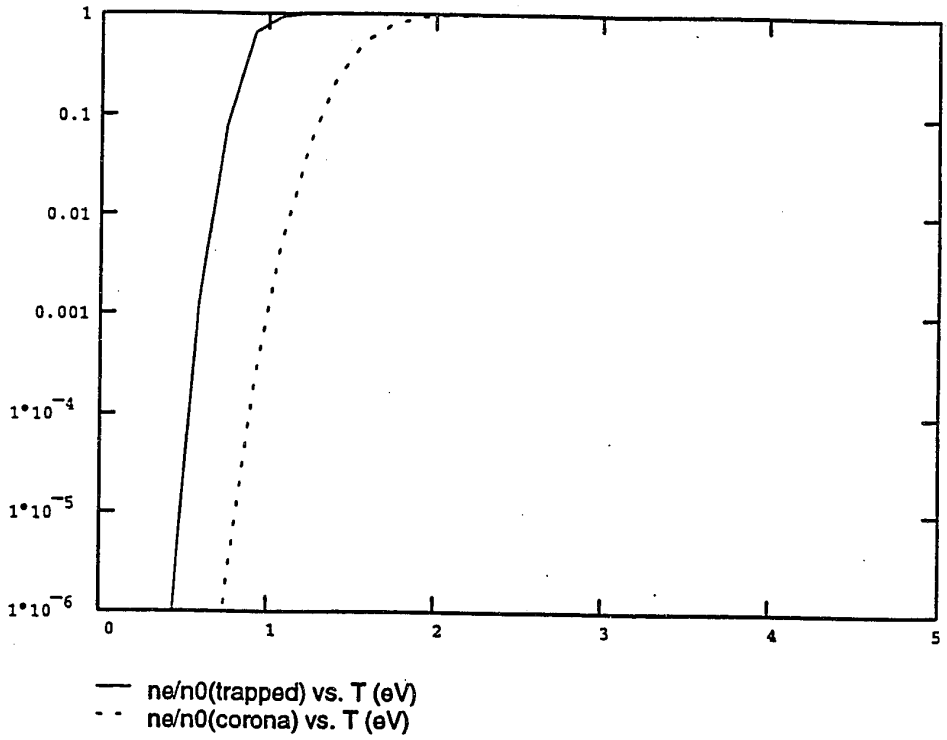

Figure 1.5: Ionization fraction in equilibrium for trapped radiation model and corona model.

ionization time is about 10,000 μsec, but decreases to about 6.7 μsec at $T_e = 3$ eV. Thus atoms accreted into hotter, ionizing regions of plasma will ionize in these characteristic times.

When L_α radiation is trapped within the plasma, the ionization rate can increase by an order of magnitude over that of the corona model. Figure 1.6 compares the ionization and recombination rates for the trapped L_α radiation and corona models. The ionization/recombination equilibration time is $1/Sn_e$, is over an order of magnitude shorter for the trapped radiation model due to the higher ionization rate coefficient $S_{\rm tr}$ and the resulting higher electron density n_e.

The result of this analysis is the establishment of effective ionization and recombination rate coefficients. The COAX code originally used the corona model rate coefficients $S_{\rm cor}$ and $\alpha_{\rm cor}$. One way to incorporate the rate coefficients for trapped radiation is to use factors to multiply the corona model rate functions. This is expedient and simple to implement, and so this is what was done. The ionization rate using the corona model is less than that using the trapped radiation model, so the ionization rate multiplier needs to be about 10–100 to compensate for this difference.

1.2.6 Summary of Atomic and Collisional Phenomena

- Particle collisions between electrons, ions, and neutrals need to be considered to properly model ionization, neutral-ion fluid friction, heat conduction, and electrical resistance.

- Heat conduction by neutrals is caused by charge exchange collisions of neutrals with ions and subsequent neutral-neutral collisions that enhance transport of thermal energy across magnetic field lines.

- L_α radiation is generally trapped in the neutral gas surrounding the ionizing regions that emit L_α radiation.

- Impurity radiation is generally untrapped and can be a significant energy loss mechanism.

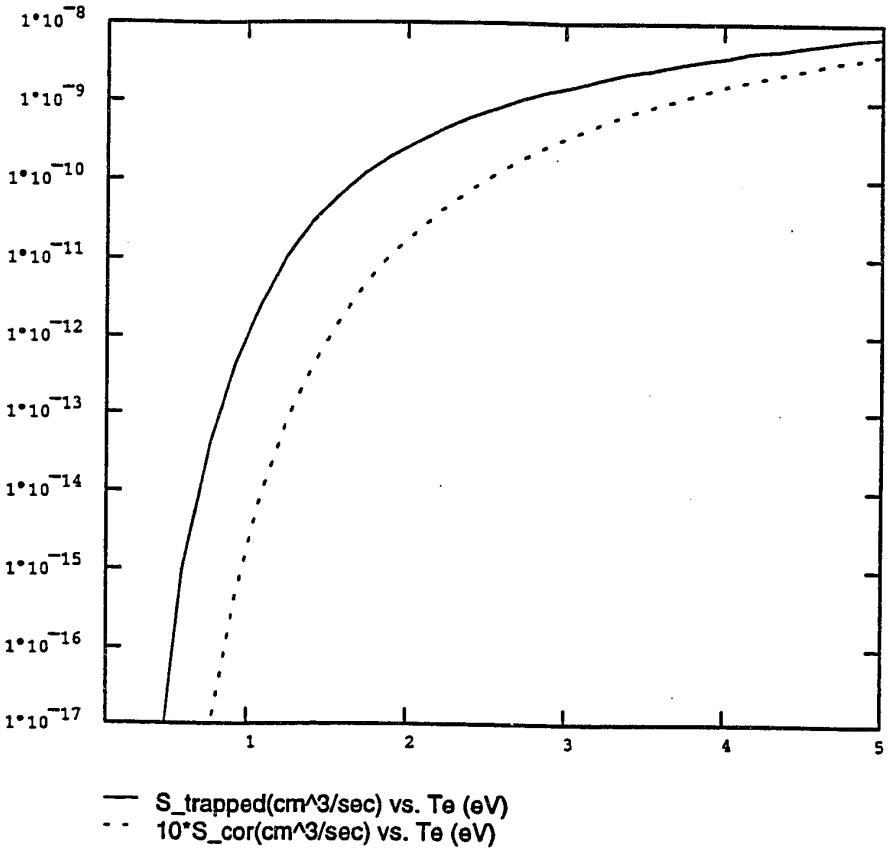

Figure 1.6: Ionization rate coefficients for trapped radiation and corona models. The rate coefficient for the corona model is shown multiplied by 10.

- Ionization of hydrogen can be reduced to a simple one-step model with a higher ionization rate for trapped L_α radiation than for untrapped radiation (the corona model).

Chapter 2

ANALYTICAL MODELS OF THE CSS

Analytical models of AFRC plasmas are presented in this chapter. While the models are developed from assumptions that are only approximately true, they can still show how various phenomena scale with parameters that are controllable by the experimenter. First, an electrical circuit model is presented, which can be used to determine energy and flux transfer properties of the CSS device. In the second section, a model of an elongated, radiating plasma column demonstrates the phenomena of radiative collapse, and determines the threshold conditions for this to occur. Radiation can also cause local density perturbations to grow and this instability is treated in the third section.

2.1 Electrical Circuit Model of CSS

The CSS coils, plasma, and external circuitry can be modeled as discrete circuit elements. Then a set of first order differential equations for currents and voltages can be derived to model this idealized circuit. These equations can be solved numerically, as for instance with the electrical circuit modeling program SPICE. The solutions of these equations can be used to examine the dependence of such parameters as the coil sizes (inductances) and the capacitor bank size (capacitance) to determine how the transfer of energy and flux to the plasma region can be optimized.

2.1.1 Derivation of Circuit Equations

Some simplifying assumptions have been used so that only the geometric sizes of the coils and the resistance of the plasma determine the circuit characteristics. Assuming that the aspect ratios of the coils are large (coils much longer than their width), we can reduce the problem to one dimension. There are no end effects, that is nonuniform fields or curvature, and no field on the outside of the outer coil. All field lines are thus parallel and reversed in sign on either side of the plasma

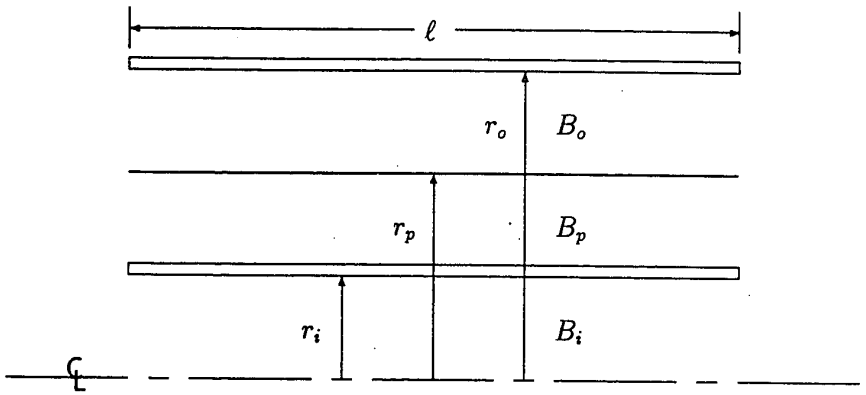

Figure 2.1: Geometry of Coils and Plasma for Circuit Model.

layer (assuming the plasma is not wall supported—that case is not included here), and due to pressure balance, the fields are equal in magnitude in the annulus. The plasma itself is assumed to be infinitesimally thin in radius, massless, but with finite resistance. Axial dynamics are not included due to the one-dimensional assumption, but can be incorporated by using an assumed plasma length which determines the effective length of the coils. The plasma resistance and length have been considered constant in time, but there is no reason they cannot be allowed to vary, dependent on some function of circuit quantities or externally imposed function of time.

The one-dimensional aspect of the model splits the radial space into four regions (see figure 2.1.1): inside the inner coil ($r < r_i$), the region between the inner coil and the plasma ($r_i < r < r_p$), between the plasma and the outer coil ($r_p < r < r_o$), and the region outside the outer coil ($r_o < r$), which has no plasma and no fields by assumption, and so is ignored. Normalizing the radii by the inner coil radius r_i, yields a fundamental quantity $\alpha = r_o^2/r_i^2$ which is the ratio of outer to inner coil cross-sectional areas.

Using Ampere's Law, we can write the magnetic field in each region as a function of the current in each coil (I_i or I_o for inner or outer current, and considering the

plasma ring as a coil also, with current I_p):

$$\begin{aligned} B_i &= \frac{\mu_0(N_i I_i + I_p + N_o I_o)}{\ell} \\ B_p &= \frac{\mu_0(I_p + N_o I_o)}{\ell} \\ B_o &= \frac{\mu_0 N_o I_o}{\ell}. \end{aligned} \tag{2.1}$$

where N_i and N_o are the number of turns for the inner and outer coils, and ℓ is the axial length of the coils and plasma.

Then we can define the magnetic flux enclosed within the maximum radius of each region as

$$\begin{aligned} \Phi_i &= B_i \pi {r_i}^2 \\ &= \frac{\mu_0 \pi}{\ell}[I_i(N_i {r_i}^2) + I_p {r_i}^2 + I_o(N_o {r_i}^2)] \\ &= \frac{1}{N_i}[L_i I_i + M_{ip} I_p + M_{io} I_o] \end{aligned} \tag{2.2}$$

$$\begin{aligned} \Phi_p &= \Phi_i + B_p \pi({r_p}^2 - {r_i}^2) \\ &= \frac{\mu_0 \pi}{\ell}[I_i(N_i {r_i}^2) + I_p {r_p}^2 + I_o(N_o {r_p}^2)] \\ &= [M_{ip} I_i + L_p I_p + M_{op} I_o] \end{aligned} \tag{2.3}$$

$$\begin{aligned} \Phi_o &= \Phi_p + B_o \pi({r_o}^2 - {r_p}^2) \\ &= \frac{\mu_0 \pi}{\ell}[I_i(N_i {r_i}^2) + I_p {r_p}^2 + I_o(N_o {r_o}^2)] \\ &= \frac{1}{N_o}[M_{io} I_i + M_{op} I_p + L_o I_o] \end{aligned} \tag{2.4}$$

where the self and mutual inductances are used in the last forms of equations (2.2–2.4). These inductances are defined as that part of the flux enclosed within a coil produced by the current in one of the other coils (mutual inductance) or by the same coil (self inductance) divided by that current, and thus are determined totally by the cross-sectional areas of the coils and their numbers of turns in this simplified

geometry, so

$$\begin{aligned} L_i &= \frac{\mu_0 N_i^2 \pi r_i^2}{\ell} & M_{ip} &= \frac{\mu_0 N_i \pi r_i^2}{\ell} \\ L_p &= \frac{\mu_0 \pi r_p^2}{\ell} & M_{io} &= \frac{\mu_0 N_i N_o \pi r_i^2}{\ell} \\ L_o &= \frac{\mu_0 N_o^2 \pi r_o^2}{\ell} & M_{op} &= \frac{\mu_0 N_o \pi r_p^2}{\ell}. \end{aligned} \tag{2.5}$$

Using the equations for the fluxes (eqns. 2.2-2.4) in terms of the currents I_i, I_p, I_o, we can write the loop voltages for each of the coils as the time derivative of flux times the number of turns for the corresponding coil, e.g.

$$V_i = N_i \dot{\Phi}_i = L_i \dot{I}_i + M_{ip} \dot{I}_p + M_{io} \dot{I}_o.$$

Using the three voltages V_i, V_p, V_o and currents I_i, I_p, I_o as the independent variables, with external circuits providing the relations between the voltages and currents, e.g. $\dot{V}_i = -I_i/C_i$, where C_i is the inner coil capacitance, a set of two first order differential equations can be derived for each coil. This does not work when the plasma radius r_p is also time dependent, as L_p and M_{op} are thus also time dependent. An additional relation is needed to eliminate one other variable. Using magnetic field pressure balance: $B_o = -B_p$ and equation (2.1), we find that $I_p = -2N_o I_o$, and so we can eliminate I_p as a variable.

We can also eliminate V_p using the voltage loop equation for the plasma ring: $V_p + I_p R_p = 0$, so $V_p = 2R_p N_o I_o$. Write the flux at the outer coil in terms of Φ_p

$$\Phi_o = \frac{\pi \mu_0}{\ell} \left(N_o I_o r_o^2 - N_i I_i r_i^2 \right) + 2\Phi_p \tag{2.6}$$

Now the voltages across the inner and outer coils can be expressed in terms of the coil currents and time derivatives with no other independent variables.

$$\begin{aligned} V_i &= L_i \dot{I}_i - M_{io} \dot{I}_o \\ V_o &= L_o \dot{I}_o - M_{io} \dot{I}_i + 2N_o V_p \\ &= L_o \dot{I}_o - M_{io} \dot{I}_i + 4N_o^2 R_p I_o. \end{aligned} \tag{2.7}$$

The only inductances needed now are L_i, $L_o = \alpha (N_o/N_i)^2 L_i$, and $M_{io} = M \equiv (N_o/N_i) L_i$.

When there is no plasma (or the plasma resistance $R_p \to \infty$), equation 2.7 is changed to what one would expect for two coupled inductors (i.e. no plasma):

$$\begin{aligned} V_i &= L_i\dot{I}_i + M_{io}\dot{I}_o \\ V_o &= L_o\dot{I}_o + M_{io}\dot{I}_i \end{aligned} \tag{2.8}$$

These voltages can then be used for any circuit (either parallel or independent mode) one can devise for the CSS. For instance, in independent mode, with two independent capacitor banks (C_i and C_o) connected to inner and outer coils respectively through external inductors (L_{ix} and L_{ox}) and resistors (R_{ix} and R_{ox}) we get the set of equations:

$$\begin{aligned} \dot{V}_{C_i} &= -\frac{I_i}{C_i} \\ \dot{V}_{C_o} &= -\frac{I_o}{C_o} \\ V_{C_i} &= L_{ix}\dot{I}_i + I_iR_{ix} + V_i \\ V_{C_o} &= L_{ox}\dot{I}_o + I_oR_{ox} + V_o \end{aligned} \tag{2.9}$$

where V_{C_i} and V_{C_o} are the voltages on the capacitors, V_i and V_o are given above in equation (2.7). For the parallel mode, we have only one capacitor, so the set of equations changes to

$$\begin{aligned} \dot{V}_C &= -\frac{(I_i + I_o)}{C} \\ V_C &= L_{ix}\dot{I}_i + I_iR_{ix} + V_i \\ &= L_{ox}\dot{I}_o + I_oR_{ox} + V_o. \end{aligned} \tag{2.10}$$

2.1.2 Solution of Circuit Equations for the Plasma Radius

In parallel configuration, the coils are electrically connected in parallel, so that the voltage on each is identical. Assuming that the flux at each coil was initially zero, and that they have the same number of turns, then they will always have the same value of flux thereafter in parallel mode: $\Phi_i = \Phi_o = \int N_oV_o\,dt$. Since the plasma (infinitesimally thin in this model) must have equal and opposite magnetic field on the inside and outside of its radial position r_p, the plasma position is such that it splits the annulus between the coils into equal areas, and so $\bar{r}_p^2 = (r_i^2 + r_o^2)/2$. In

the general case of independent configuration, the coils may have different voltages and flux values, and the plasma radius is given by

$$r_p^2(t) = \frac{(r_i^2 + r_o^2)}{2} - \frac{\ell(\Phi_o - \Phi_i)}{2\pi\mu_0 N_o I_o} \tag{2.11}$$

From equation 2.11 we can see how the plasma could have significant radial motion if the external circuit did not provide voltage waveforms to keep the inner/outer coil flux difference $\Delta\Phi = \Phi_o - \Phi_i$ small. This was the case for the experimental runs with the independent configuration, where initially some field lines in the inner core returned through the annulus before plasma was formed, making $\Delta\Phi$ positive. Plasma then initially formed on the inner coil. The voltages and timing of the circuit switches were picked to get the best waveform to center the plasma, but without fixing $\Delta\Phi = 0$ this is impossible to do exactly. The plasma radius was observed to expand outward from the inner coil after formation, to beyond the radius in parallel configuration $\bar{r}_p$, and then it contracted again to slightly less than $\bar{r}_p$ at the time of crowbar, when the coil voltages are clamped to nearly zero by shorting the connections to the coils. After the crowbar time, the radius quickly decreased and the plasma was quenched by contact with the wall at the inner coil.

The circuit equations show that the rapid motion of the plasma radius after crowbar is due to resistive dissipation of the flux in the annulus. To show this, first define the trapped flux, i.e. that flux between the plasma and the closest coil:

$$\Phi_{tr} = \Phi_i - \Phi_p = \frac{\mu_0\pi}{\ell} N_o I_o (r_p^2 - r_i^2) \tag{2.12}$$

where the inner coil is assumed to be closer to the plasma radius. Second, define the flux decay time τ_ϕ by $\dot{\Phi}_{tr} = \dot{\Phi}_i - \Phi_{tr}/\tau_\phi$, then we find

$$\tau_\phi = \frac{\mu_0\pi}{2R_p\ell}(r_p^2 - r_i^2) \tag{2.13}$$

For a given plasma resistance R_p, this decay time is longest when the plasma is "centered", as in parallel configuration. Then $r_p = \bar{r}_p$, and the flux decay time is given by

$$\bar{\tau}_\phi = \frac{\mu_0\pi}{4R_p\ell}(r_o^2 - r_i^2) \tag{2.14}$$

After the time of crowbar, neglecting external resistances, $\dot{\Phi}_i = 0 = \dot{\Phi}_o$, the plasma radius can be calculated using equation 2.11 to be

$$r_p^2(t) = \bar{r}_p^2 + [r_p(t_{cr})^2 - \bar{r}_p^2] \exp[(t - t_{cr})/\bar{\tau}_\phi] \tag{2.15}$$

This states that in the independent mode, if the fluxes are not balanced at the time of crowbar (i.e. the plasma radius is not centered at $\bar{r}_p$), then the plasma radius is exponentially unstable with an e-folding time of $\bar{\tau}_\phi$.

2.1.3 Coil Geometry for Translation Capability

To make a practical fusion power device, it is expected that FRC plasmas will be formed in one section of a machine, and burned in another, which conveniently separates the formation technology from the nuclear power technology. A CSS type of formation device must then allow the annular FRC to be axially translated off the cantilevered inner coil, transforming it into a true FRC. Then the FRC plasma can be further compressed and heated, to produce a thermonuclear burning plasma in a region removed from the formation device. For translation we need zero flux in the core, so that there are no field lines that the plasma has to "break through" to be translated.

In one scheme, the capacitor bank is crowbarred at the peak magnetic field to maintain the compression of the plasma. This requires that there be a small amount of energy left in the capacitors at that time, as this energy would be quickly dumped when the capacitor bank is crowbarred (shorted). If we stipulate that there be zero energy in the capacitor bank at the crowbar time (same time that $\Phi_i = 0$), and assume that there is no external resistance or inductance, and zero plasma resistance (no dissipation of energy or flux), then a simple calculation shows that the ratio of outer to inner coil cross sectional areas (defined as $\alpha = r_o^2/r_i^2$) must be five.

To show this, initially at $t = 0$, all energy was stored in the capacitors. At $t = t_{1/4}$ all the energy is in field in the core (no plasma formed), and all of this is transferred to field in the annulus at the crowbar/translation time $t = t_{cr}$

$$W = \frac{B_i^2(t = t_{1/4})}{2\mu_0} \pi r_i^2 \ell \tag{2.16}$$

$$= \frac{B_o^2(t = t_{cr})}{2\mu_0} \pi (r_o^2 - r_i^2) \ell \tag{2.17}$$

$$= \frac{B_o^2(t=t_{cr})}{2\mu_0}\pi r_i^2(\alpha-1)\ell \tag{2.18}$$

Also all of the initial flux is transferred to the annulus

$$\Phi = B_i(t=t_{1/4})\pi r_i^2 \tag{2.19}$$
$$= B_o(t=t_{cr})\pi(r_p^2-r_i^2) \tag{2.20}$$
$$= B_o(t=t_{cr})\pi r_i^2(\alpha-1)/2 \tag{2.21}$$

Solving these equations simultaneously gives the optimum area ratio $\alpha = 5$. For $\alpha > 5$, there is still a voltage applied to the coils at $t = t_{cr}$, so there is energy in the capacitor banks which must be discharged at the time of crowbar.

2.1.4 Flux Transfer Efficiency

The flux trapped between the plasma null and the inner or outer coils can be defined as

$$\Phi_{tr} = B_o\pi(r_o^2-r_p^2) = B_o\pi(r_o^2-r_i^2)/2 \tag{2.22}$$

where $\Delta\Phi$ is assumed to be zero, so that the plasma radius is centered. The flux decay time can be defined in terms of the difference in the decay rates of the trapped flux and the inner or outer coil flux addition rate

$$\dot{\Phi}_{tr} - \dot{\Phi}_i = -\frac{\Phi_{tr}}{\tau_\phi}. \tag{2.23}$$

Using equation 2.7 with the parallel coil condition $V_i = V_o$, and the definition $\alpha = r_o^2/r_i^2$, gives the flux decay time in terms of the plasma resistance and inner coil inductance

$$\tau_\phi = \frac{(\alpha-1)L_i}{4N^2R_p} \tag{2.24}$$

We can solve this equation easily for two cases of source voltage, with the trapped flux initially at zero. Tearing formation can be approximated by setting $\dot{\Phi}_i = V_0\cos(\omega t)/N$, and programmed formation by $\dot{\Phi}_i = V_0\sin(\omega t)/N$. The solutions are

$$\begin{aligned}\Phi_{tr} &= \frac{V_0}{\omega}\frac{\omega\tau_\phi}{1+(\omega\tau_\phi)^2}\left[(\cos(\omega t)-e^{-t/\tau_\phi})+\omega\tau_\phi\sin(\omega t)\right] \quad \text{tearing} \\ &= \frac{V_0}{\omega}\frac{\omega\tau_\phi}{1+(\omega\tau_\phi)^2}\left[\sin(\omega t)-\omega\tau_\phi(\cos(\omega t)-e^{-t/\tau_\phi})\right] \quad \text{programmed}\end{aligned} \tag{2.25}$$

The flux transferred to the annular region is maximized when $\tau_\phi = \infty$ i.e. $R_p = 0$. Figure 2.2 shows the normalized trapped flux for $\omega\tau_\phi = 0.5$, 1.0, 2.0, and ∞. Note that as $\omega\tau_\phi$ increases, the flux transfer increases, until it is 100% of the available flux when $\omega\tau_\phi = \infty$.

2.1.5 Power Transfer Efficiency

We can also consider maximizing the power into a device like the CSS. In this case, assume that there is a steady sinusoidal voltage source driving the device. The Poynting flux into the annulus is given by

$$\begin{aligned} P_{in} &= \frac{1}{\mu}\int_{\text{coils}} \mathbf{E}\times\mathbf{B}\cdot\hat{n}\,dS = 2V(t)I_o(t) \\ &= \frac{2\eta}{(1+\eta^2)(\alpha-1)}\frac{V_0^2}{\omega L}\left[\sin^2(\omega t) - \eta\sin(\omega t)\cos(\omega t)\right] \end{aligned} \tag{2.26}$$

where $\eta = \omega\tau_\phi$ is the normalized flux decay time.

During part of any half-cycle the Poynting flux will be directed out from the annulus, but the rest of the time power is input into the plasma and magnetic field energy. Figure 2.3 shows the Poynting power into the annular region over one half-cycle. To optimize the inflow of power over a period, the normalized flux decay time must be $\eta = 1$. This is the same as matching the impedance to the external circuit.

If we suppose that the frequency of the voltage source is variable, then it could be arranged to adjust $\omega = 1/\tau_\phi = 4N^2R_p/(\alpha-1)L_i$. A device such as this could serve as a plasma source for various purposes, such as a source for injecting preionized plasma into annular FRCs, a radiation source for lighting or possibly lasers, plasma propulsion, or for processes such as plasma enhanced deposition or etching. The plasma need not be fully ionized, nor be constituted of hydrogen, but could be formed from any gas.

2.2 Radiative Collapse Model

The introduction of impurity species into a magnetically confined hydrogen plasma changes its behavior quite dramatically. This is because even small amounts of incompletely ionized particles can radiate away a significant portion of the plasma energy. In tokamak plasma discharges, major disruptions can be triggered by line

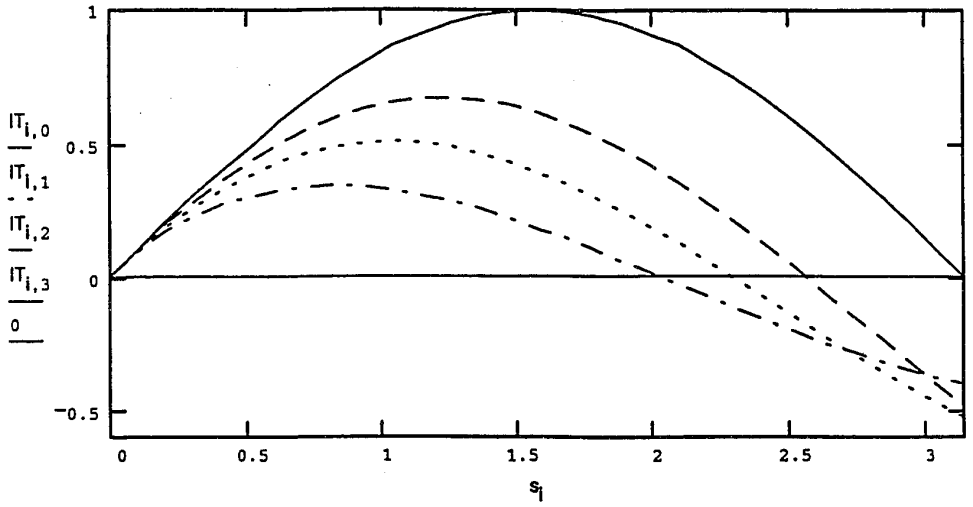

a. Tearing formation

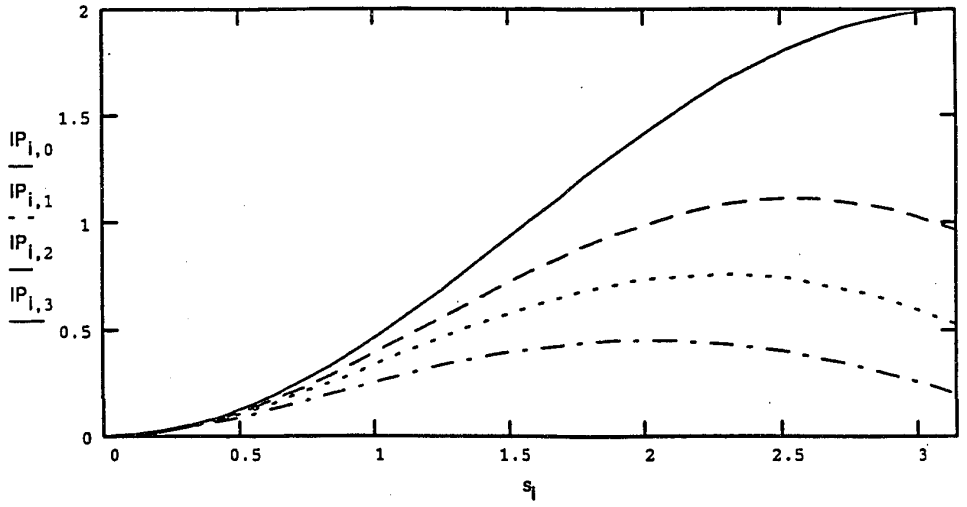

b. Programmed formation

Figure 2.2: Normalized trapped flux vs. normalized time ($\omega\tau$) for $\omega\tau_\phi = 0.5$ (dash-dot curves), 1.0 (dots), 2.0 (dashes), and ∞ (solid).

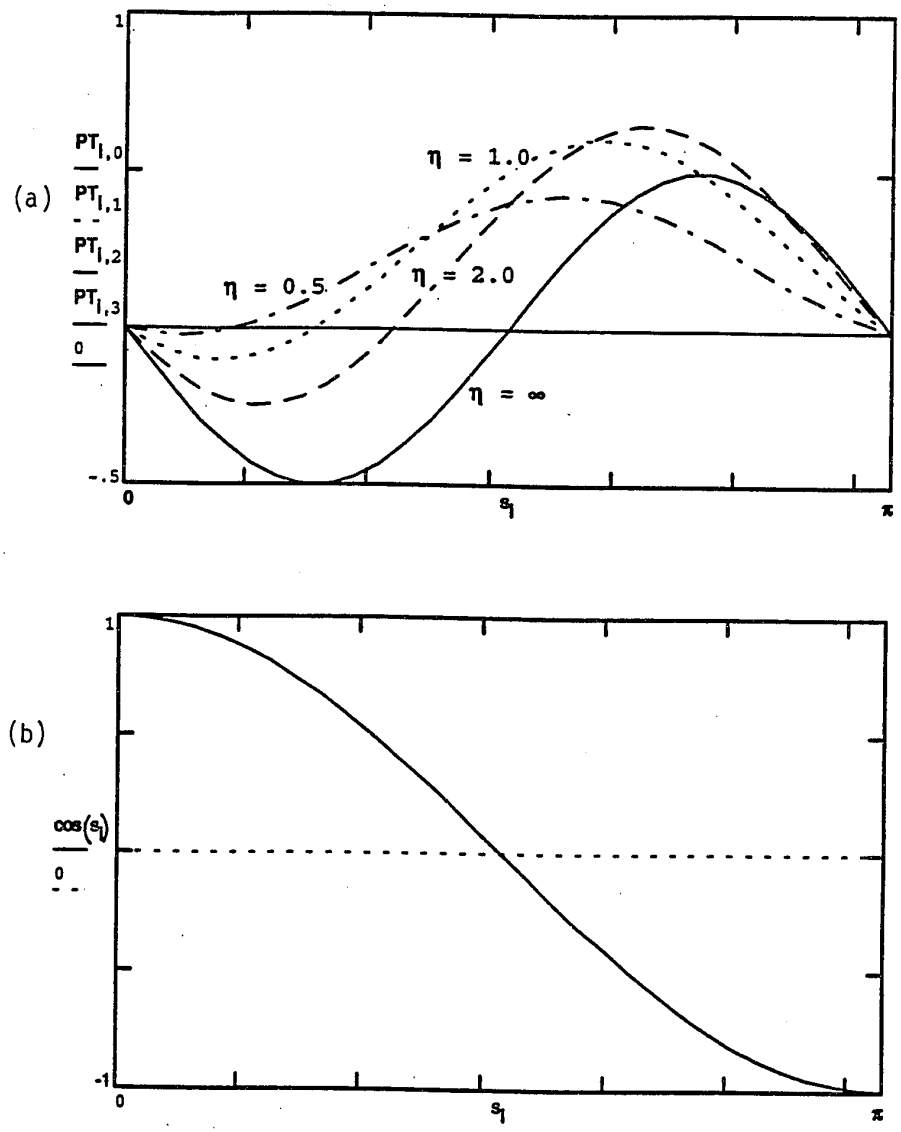

Figure 2.3: (a) Normalized Poynting power into the annular region over one half-cycle vs. normalized time ($\omega\tau$), for normalized decay times of $\eta = 0.5, 1.0, 2.0, \infty$. (b) Normalized voltage at the coils.

radiation from impurities entering the edge plasma (due to the inevitable wall contact there). A limit on plasma density in tokamaks to avoid this disruption is called the Murakami density limit [31]. Reversed field pinches suffer a similar radiative limit, called the I/N limit [32]. Simply stated, when the Ohmic heating power is equaled or exceeded by the radiation from impurity ions in a reversed field pinch, a thermal condensation or radiative collapse occurs [33]. Just before such a limit is reached in tokamaks, bands of very high density, low temperature, poloidally asymmetric plasma occur at the outer edge. These localized structures are called MARFEs, and may be the result of localized instabilities caused by the increase of radiation power compared to Ohmic heating at the edge.

This section describes the theory of radiative collapse in field-reversed configurations, where the balance between plasma pressure and magnetic pressure is an important consideration. After the radiative collapse, there is power balance between heating and cooling processes, the temperature is limited from increasing, and the resulting plasma is left in a relatively cold, dense state. A model is presented to demonstrate the phenomenon of radiative collapse, and the conditions for its occurrence are determined. This model is similar to that of Farengo and Brooks [34]. It is an attempt to discover a simple relation between impurity inventory and limits to temperature in Ohmically heated plasma columns. In chapter 3.3 on results from the COAX simulations, the radiative collapse model presented here will be tested, and shown to agree qualitatively with CSS simulations and experimental results.

The phenomenon of radiative collapse can be demonstrated with a model of a cylindrical plasma column. This model represents the plasma in only an approximate way, but does possess the important qualities of an annular FRC. Instead of an elongated plasma ring, as in an AFRC, the model uses a linear column of plasma, with elliptical cross section. By imagining the ends of the column to be topologically joined to each other, the geometry is that of an AFRC with infinite aspect ratio (major to minor radius). The CSS experiment has coaxial coils with inner and outer boundaries on the plasma of about $r_i = 6$ cm and $r_o = 21$ cm, respectively. Thus the actual aspect ratio is $r_p/(r_o - r_p) \gtrsim 3$ where the plasma radius is given by $r_p = \sqrt{(r_i^2 + r_o^2)/2}$. Thus the linear pinch model is expected to be a reasonable representation of the annular plasma.

Consider first a circular cross-section column. In equilibrium, the external pres-

sure of the magnetic field balances the plasma kinetic pressure. This is expressed in the Bennett relation [35]

$$\mu_0 I^2/8\pi = (1+Z)NT = P \tag{2.27}$$

where I is the total current in the plasma column, Z is the average number of electrons per ion, N is the number of ions per unit length in the column (line density), T is the temperature, assumed equal for electrons and ions, and P is the total plasma pressure integrated over the cross-sectional area. Note that this relationship does not depend on the plasma radius.

Assume that the particle inventory within the plasma column is constant (no creation or loss of particles). The differential equation for temperature evolution is dependent on the balance of heating, cooling, and compressive work:

$$\frac{d}{dt}\left[\frac{3}{2}(1+Z)NT\right] = P_\Omega - P_{rad} - \int p(\nabla\cdot\mathbf{u})2\pi r\,dr \tag{2.28}$$

Assume that the compression $\nabla\cdot\mathbf{u}$ = constant, or $u_r = \dot{a}r/a$, where a is the plasma radial extent, and so the last term is $-2(\dot{a}/a)P$. The heating term $P_\Omega = f_\Omega \int \eta(T)J^2 2\pi r\,dr$ is from Ohmic dissipation. An anomaly factor f_Ω has been added to accommodate additional heating from anomalous mechanisms. When $f_\Omega = 1$, this represents classical plasma resistivity from electron-ion Coulomb scattering as given by Braginskii [13]. For the classical resistivity, $\eta = 1.03\times 10^{-4} Z \ln\Lambda\, T(\mathrm{eV})^{-3/2}\,\Omega$-m, and is dependent only on temperature, except for the slow dependence of the Coulomb logarithm Λ on density ($\propto \ln(T^{3/2}n^{-1/2})$).

The cooling is from radiation emitted from impurity ions and atoms in the plasma whose radiated power is dependent on the rate of exciting collisions with electrons. Assuming the impurity density is in a fixed proportion to the ion density $n_{imp} = f_{imp} n_i$, then $P_{rad} = \int f_{imp} Z n_i^2 L(T, \{f_k(t)\})$. In this equation, L is a linear combination of rate coefficients dependent on the distribution of the impurities in each charge state $\{f_k(t)\}$. In coronal equilibrium, this distribution of states is determined by the temperature only, and has been tabulated by Post *et al.* [25]. In general, if the temperature is changing faster than the distribution can adjust to it, the radiated power is dependent on $\{f_k(t)\}$, and a time dependent model must keep track of each impurity charge state (as described in the previous chapter).

Assume quasi-equilibrium exists, that is, the heating from compression is negligible, and the impurities are in the temperature dependent equilibrium distribution. Then power balance $\dot{T} = 0$ would give $P_\Omega = P_{rad}$ or $\int f_\Omega \eta(T) J^2 2\pi r\, dr = \int f_{imp} Z n_i^2 L(T) 2\pi r\, dr$. If we assume a uniform temperature and current density profile, the density profile is parabolic, $n_i = (2N/\pi a^2)[1 - (r/a)^2]$, where a is the radius of the plasma. Carrying out the integrations over the plasma area, factors containing the plasma radius cancel, and the power balance gives $f_\Omega \eta(T) \bar{I}^2 = 4 f_{imp} Z N^2 L(T)/3$, where $\bar{I}$ is the current at which $P_\Omega = P_{rad}$. Since quasi-equilibrium is assumed, we can use the Bennett relation (equation 2.27) to express the line density in terms of the temperature and current. Then we get

$$\bar{I}^2 = 48\pi^2 (1+Z)^2 f_\Omega \eta(T) T^2 / \mu_0^2 f_{imp} Z L(T) \tag{2.29}$$

In the case where the radiation is from Bremsstrahlung instead of line radiation, $L(T)$ has a $T^{1/2}$ dependence, and since $\eta \propto T^{-3/2}$, the equilibrium current is independent of temperature, and is called the Pease-Braginskii current. For $\ln \Lambda = 10$, $Z = 1$, the Pease-Braginskii current for this density profile is 1.44 MA.

In the case where the radiation is from impurities, we can use the cooling rate coefficient due to Post [25] for the $L(T)$ function. This assumes coronal equilibrium for each of the impurity charge states. By plotting the quasi-equilibrium phase space in I^2 and T coordinates, stable and unstable points are found. In figure 2.4 a family of curves for the Bennett condition is plotted for various values of impurity line density $N_{imp} = \int n_{imp} 2\pi r\, dr = f_{imp} N$. These curves are the straight lines in the log-log graph, and are plotted in terms of $f_{imp} I^2$ versus T. Also $f_{imp} \bar{I}^2$ (where $\bar{I}$ is the current when $P_\Omega = P_{rad}$) is plotted against T for an oxygen impurity. The quasi-equilibrium condition means that as temperature varies, the Bennett relation restricts the plasma current to an $I(T)$ characteristic curve. When $I > \bar{I}$, then $P_\Omega < P_{rad}$, and the plasma will cool: $\dot{T} < 0$. Conversely, when $I < \bar{I}$, $\dot{T} > 0$, and the temperature will rise. The fixed points where $\dot{T} = 0$ are marked on the plot, and arrows represent the direction in which the quasi-equilibrium will evolve, corresponding to the sign of $\dot{T}$. Thus it can be seen that some of the $\dot{T} = 0$ points are stable points (or attractors, arrows point toward points), while the others are unstable points (repellers, arrows point away). The quasi-equilibrium will tend toward the stable points (true equilibrium).

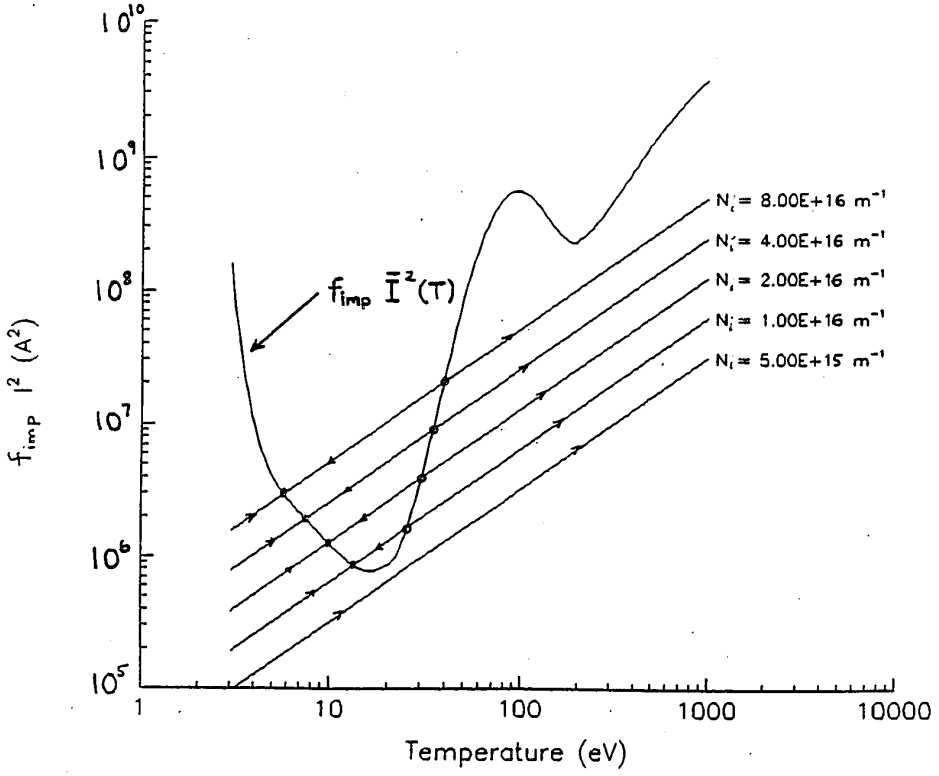

Figure 2.4: Family of $f_{imp}I^2(T)$ lines for various values of impurity line density N_{imp} representing the Bennett condition. $f_{imp}\bar{I}^2(T)$ curve represents the balance between Ohmic and radiative powers for a fractional oxygen impurity of f_{imp}. Quasi-equilibrium points lie along any $f_{imp}I^2(T)$ lines, with fixed points at the filled circles (stable) or open circles (unstable).

Imagine, for instance, a plasma that has been suddenly heated so that its temperature has risen to 30 eV, but it is dynamically in equilibrium. The plasma may not be in full equilibrium, but it is in quasi-equilibrium so that the plasma current is determined by the Bennett relation. If the total particle inventory is 8×10^{18} m^{-1} and 1% of this is oxygen impurity, then the quasi-equilibrium current is $I^2 = 1.3 \times 10^9$ A$^2 > \bar{I}^2(T = 30$ eV). This would be unstable as the cooling power is greater than the heating power, and the quasi-equilibrium would move down the $I(T)$ curve to the lower temperature point $T = 6$ eV, $I^2 = 3 \times 10^8$ A^2. This point is stable, as the cooling power equals the heating power there. The temperature has dropped precipitously, and it can be shown that the plasma radius decreases also. This is an example of radiative collapse: a transient instability ending in a new equilibrium point, where the plasma temperature and radius collapse.

The existence of stable points for the $f_{imp}I(T)$ curves with $N_{imp} > 5 \times 10^{15}$ m^{-1} means that the plasma will eventually reach the temperature and current of the closest stable point to the starting configuration. If the $I(T)$ operating point is not at an equilibrium point but is somewhere on one of the quasi-equilibrium Bennett curves, the operating point will tend toward a stable point as indicated by the filled-in dots.

The peak in the radiation curve in figure 1.3 is referred to as the radiation barrier, and the meaning is evident from the above discussion. When $N_{imp} > 5 \times 10^{15}$ m^{-1}, there exist stable and unstable pairs of points on the $I(T)$ curves, and it is not possible to increase the temperature from below the stable point to above the stable value. On the other hand, if the configuration were to be put at an $I(T)$ point with a higher temperature than the unstable point, the temperature will tend to increase. Likewise, if impurities enter the plasma slowly enough that the temperature can rise above the corresponding unstable point, the plasma temperature will continue to rise. Thus it may be possible for FRCs produced by fast shock heating methods to overcome the radiation barrier and attain higher temperatures, limited by cooling processes other than radiation.

We can generalize the above model to elongated plasmas by assuming that the temperature and current density are uniform, as before, but that the particle density

has the form of an elongated paraboloid:

$$n = n_0 \left[1 - \left(\frac{x}{\epsilon b}\right)^2 - \left(\frac{y}{b}\right)^2 \right] \tag{2.30}$$

where the cross-section is elliptical, with major and minor axes of a and b, respectively, with $\epsilon = a/b$ being the ellipticity factor. Combining the force equilibrium relation $\mathbf{J} \times \mathbf{B} = \nabla p$, with Ampere's Law $\nabla \times \mathbf{B} = \mu_0 \mathbf{J}$, we get the generalized Bennett relation for the elongated plasma

$$\frac{\epsilon^2 + 1}{2\epsilon} NT = \frac{\mu_0 I^2}{8\pi} \tag{2.31}$$

When the ellipticity factor $\epsilon = 1$ this gives the usual Bennett relation, as expected.

The previous analysis can then be modified for the case of the elongated plasma by using the factor $f_\epsilon = (\epsilon^2+1)/2\epsilon$ to increase the limit on the impurity line density $N_{imp} = f_{imp} N$. Including the elongation factor and the anomalous resistivity factor f_Ω, the limit on impurity line density to avoid radiative collapse is

$$N_{imp} < \begin{cases} 1 \times 10^{16} f_\epsilon f_\Omega \text{ m}^{-1}, & \text{carbon} \\ 5 \times 10^{15} f_\epsilon f_\Omega \text{ m}^{-1}, & \text{oxygen} \end{cases} \tag{2.32}$$

The radiation power coefficient has peaks of approximately 10^{-31} Watt-m^3 at the "radiation barrier" temperatures of about 6 eV for carbon and 20 eV for oxygen. For values of N_{imp} above a critical level depending on the ellipticity and composition of impurities, the simultaneous solution of equation (2.29) with the generalized Bennett relation (equation 2.31) is a temperature below the radiation barrier that is not very sensitive to N_{imp} or ϵ. This is the condition for radiative collapse: a plasma with an impurity content exceeding the critical level will tend to evolve to this state with the temperature given by the solution to (2.31).

The critical impurity line densities are given by equation 2.32. For the CSS, the circumference at the magnetic null is approximately 1 meter, and the annular volume is about 10^{-1} m^3, so that these critical line densities can be related to critical impurity densities of $N_{imp} = 5 \times 10^{16} f_\epsilon f_\Omega$ m^{-3} for oxygen and $N_{imp} = 1 \times 10^{17} f_\epsilon f_\Omega$ m^{-3} for carbon. For fill pressures of 5 mtorr, $f_\epsilon = 1$ and $f_\Omega = 1$, these limits correspond to impurity fractions of 0.014% for oxygen and 0.03% for carbon, which are very small limits. In reality, the plasma in the CSS will form in

a somewhat elongated shape, so that the ellipticity factor increases these limits by perhaps a factor of 10. Also, a more peaked current profile than the uniform profile assumed here can raise these limits, as can higher resistivity due to anomalous effects.

2.3 Radiation Induced Instability

Tokamaks have a phenomena called a MARFE which is an abbreviation for Multi-faceted Asymmetric Radiation From the Edge. It is thought to be the result of a radiation induced instability. This instability is similar in physics to the radiative collapse described in the previous section, in that radiation power is proportional to the product of electron and impurity density, and so an increase in density increases the radiation power. When a radiative collapse occurs, the whole plasma is reorganized to be in a new equilibrium with heating and cooling powers balanced. In the case of a MARFE or other radiation induced instability, fluctuations in density become unstable due to the enhanced radiation cooling in the higher density regions. These instabilities do not cause a collapse of the whole plasma, but can cause fluctuations to grow to a large level in a local region. In tokamaks, these MARFEs produce toroidal bands of radiating plasma near the inner radius side of the machine. In the case considered here, there is no toroidal field, so these instabilities are not the same as MARFE's. Assume a uniform plasma (or wavelengths of fluctuations much less than the characteristic gradient length of the magnetic field or pressure). Also assume that fluctuations take the form of acoustic wave modes. The linearized fluid equations including Ohmic heating, radiative cooling of the form $L(T)n^2$, and heat conduction (using heat diffusivity coefficient χ) are

$$\partial_t n_1 = -n_0 \nabla \cdot \mathbf{u}_1 \tag{2.33}$$

$$\rho_0 \partial_t \mathbf{u}_1 = -\nabla p_1 \tag{2.34}$$

$$3n_0 \partial_t T_1 = -2n_0 T_0 \nabla \cdot \mathbf{u}_1 + \eta_1 J_0^2 - [L(T)n^2]_1 + n_0 \chi \nabla^2 T_1 \tag{2.35}$$

Write the linearized quantities for pressure, radiation cooling power density, and electrical resistivity as

$$p_1 = 2(n_1 T_0 + n_0 T_1) \tag{2.36}$$

$$(Ln^2)_1 = 2L_0 n_0 n_1 + L' n_0^2 T_1, \text{ where } L' = \left.\frac{dL}{dT}\right|_{T_0} \tag{2.37}$$

$$\eta_1 = -\frac{3T_1}{2T_0}\eta_0 \tag{2.38}$$

Let the linearized quantities have the form $\exp[i(kx - \omega t)]$. Equations (2.33)-(2.35) can then be rewritten with $\partial_t \to -i\omega$ and $\nabla \to i\mathbf{k}$. Defining $\tilde{n} = n_1/n_0$, $\tilde{T} = T_1/T_0$, and taking the dot product of $\mathbf{k}$ with equation (2.34), we get the transformed equations

$$\omega\tilde{n} = \mathbf{k}\cdot\mathbf{u}_1 \tag{2.39}$$

$$\mathbf{k}\cdot\mathbf{u}_1 = 2k^2 T_0/m_i(\tilde{n} + \tilde{T}) \tag{2.40}$$

$$\begin{aligned} -3i\omega n_0 T_0 \tilde{T} = {} & -2n_0 T_0 i\mathbf{k}\cdot\mathbf{u}_1 - \frac{3}{2}\eta_0 J_0^2 \tilde{T} \\ & - 2L_0 n_0^2 \tilde{n} - L' T_0 n_0^2 \tilde{T} - k^2 \chi n_0 T_0 \tilde{T} \end{aligned} \tag{2.41}$$

We desire a dispersion relation for $\omega(k)$ to see if instability is possible. Substituting equation (2.39) in equation (2.40) to eliminate $\mathbf{k}\cdot\mathbf{u}_1$, and then combining the resulting equation gives the dispersion relation

$$\begin{aligned} D(\omega,k) = {} & (\omega^2 - 2v_i^2 k^2)\left[-3n_0 T_0(i\omega) + L' T_0 n_0^2 + n_0 T_0 \chi k^2 + \tfrac{3}{2}\eta_0 J_0^2\right] \\ & [2n_0 T_0(i\omega) + 2L_0 n_0^2]\, 2v_i^2 k^2 = 0 \end{aligned} \tag{2.42}$$

where $v_i^2 = T_0/m_i$.

For the case $L = 0 = L' = \chi = \eta_0$, i.e. no heating or cooling taking place, the three roots of (2.42) are $\omega = \pm\frac{10}{3}k^2 v_i^2 = k^2 c_s^2$ and $\omega = 0$. Two of the roots represent acoustic waves with phase velocity $c_s^2 = \gamma(T_e + T_i)/m_i$, where $\gamma = 5/3$ is the ratio of specific heats for an ideal gas. The third root is the mode of concern for radiative instability. Looking for solution to equation (2.42) near $\omega = 0$, we can estimate ω by Taylor expansion near zero: $\omega \simeq -D(0,k)/\partial_\omega\, D(\omega,k)|_{\omega=0}$, or

$$\omega \simeq i\left(\frac{2L_0 n_0^2 - L' T_0 n_0^2 - n_0 T_0 \chi k^2 - \frac{3}{2}\eta_0 J_0^2}{5n_0 T_0}\right) \tag{2.43}$$

Since this frequency is purely imaginary, this mode is either purely growing or damped, and the imaginary part of ω is the growth rate. Thus when the numerator

is positive, there is instability. Define $\tau_\Omega = 3n_0T_0/\eta_0J_0^2$ as the Ohmic heating time, and $\tau_{rad} = 3n_0T_0/L_0n_0^2$ as the radiative cooling time, and $Q = T_0L'/2L_0$ is a dimensionless measure of the slope of the radiation cooling rate with temperature. The growth rate $\gamma = \omega/i$ can then be written

$$\gamma = \frac{1}{5}\left[6(1-Q)\tau_{rad}^{-1} - \frac{9}{2}\tau_\Omega^{-1} - \chi k^2\right] \tag{2.44}$$

It can be observed that heat conduction is stabilizing, that shorter wavelengths are stabilized the most, and that Ohmic heating also stabilizes. The radiative cooling is destabilizing if Q is negative enough.

Consider the case where Ohmic heating balances the sum of radiative cooling and heat conduction: $\eta_0J_0^2 = n_0^2L_0 + \chi k_0^2 n_0T_0$, where k_0 is the shortest wavenumber of the system, representative of the inverse characteristic length of the plasma. Then the growth rate is

$$\gamma = \frac{1}{5}\left[\left(\frac{3}{2} - 6Q\right)\tau_{rad}^{-1} - \chi\left(\frac{3}{2}k_0^2 + k^2\right)\right] \tag{2.45}$$

The most unstable mode is when $k = k_0$ (the longest wavelength allowed), and $\gamma = \frac{1}{5}\left[(\frac{3}{2} - 6Q)\tau_{rad}^{-1} - \chi(\frac{5}{2}k_0^2)\right]$.

If Q has a large enough negative value, γ will surely be positive, and instability is assured. Of course, the previous analysis of radiative collapse assumed the power balance as above, and so a radiative collapse would leave the plasma at a temperature where the radiation cooling rate $L(T)$ increases with T, and Q would be positive. The radiative instability would be stable after a radiative collapse.

Now consider a plasma with temperature increasing past the radiation barrier, and thus the power balance above does not apply. The extra Ohmic heating is stabilizing. On the other hand, the radiation cooling rate $L(T)$ decreases with T above the radiation barrier when the coronal equilibrium model applies, so Q is negative, and destabilizing. The coronal equilibrium model does not apply when temperature is changing on a shorter timescale than the equilibration time $\tau_{eq} \sim 10^{12}/n$ sec-cm^{-3} which is longest just at and above the radiation temperature barrier [22]. For temperature growing on timescales shorter than τ_{eq}, $L(T)$ is approximately constant, and $Q \approx 0$. Thus the radiative instability is stable for Ohmic heating high enough to increase the temperature on a faster timescale than both τ_{eq} and τ_{rad}.

2.4 *Summary*

- A set of equations is derived using a simplified model of plasma and magnetic fields so that the plasma/coil physical system could be treated as electrical circuit elements (inductors and resistors).

- Solving this set of equations for the case of crowbarred (shorted) coils, the plasma radius deviates exponentially in time from the radial position at which there is equal flux between plasma and each coil.

- Flux transfer efficiency is defined in terms of the frequency of the applied voltage times the flux decay time, i.e. $\omega\tau_\phi$.

- Power transfer efficiency is optimized when $\omega\tau_\phi = 1$.

- Radiative collapse of a plasma column was described as the evolution of quasi-equilibria to a fixed point (stable equilibrium) where Ohmic heating is equal to radiative loss.

- There is a barrier to temperature increase caused by radiative collapse when the line density of impurities is above a limit.

- A radiative instability is shown to exist theoretically, but is stabilized under typical operating conditions.

Chapter 3

COAX COMPUTER CODE: INFINITE FRICTION MODEL

In this chapter, the COAX computer code will be described. A discussion of the utility of computer codes for understanding complex physical systems such as the CSS will precede actual descriptions of the code and results from its use. Then the code will be described, entailing its physical models, numerical algorithms, and use in practice. Finally the results of simulations with the code will be discussed. This chapter represents a learning situation in that the limits and accuracy of the physical model are uncovered.

The next chapter describes an improved version of the code that generates simulations which compare better to experimental data.

3.1 The Relevance of Computer Simulations

In principle, a complete physical description of a plasma requires only an application of the mechanics of electromagnetically interacting particles, and possibly a phenomenological application of quantum mechanics for atomic radiative processes or nuclear reactions. While the basic physics in these areas is well known and tested, the application to a system of particles such as a plasma leads to many complex, interacting phenomena. This is due to the huge number of degrees of freedom present in a plasma, that is, three degrees of freedom for each of the positive and negative particles. Typically these phenomena are categorized as either waves or instabilities, and studied separately from the others by proper design of experiment or formulation of the equations of description. In practice, this situation is difficult to achieve, since most naturally occurring or laboratory plasmas are very nonlinear systems, coupling many of these phenomena together.

For example, a uniform plasma in a magnetic field supports many different wave modes. Some of these waves have analogs to commonplace phenomena such as sound waves, electromagnetic waves, and vibrations of plucked strings. Other waves exist

only because of the charged particles in the plasma (such as electron plasma waves).

In a nonuniform plasma, such as a magnetically confined plasma, the simple wave modes do not exist. More complicated modes do exist, such as combinations of the basic modes, or completely new phenomena such as drift waves. Free energy from the nonuniformity of the confined plasma can produce so-called microinstabilities that feed energy into the most unstable modes. Nonlinearity redistributes the energy into the other modes. Meanwhile, fluid instabilities may develop, driven by unfavorable curvature of magnetic field lines, current distributions, plasma pressure or some combination of these. Electrical resistivity of the plasma can cause other fluid instabilities to become unstable. Radiation from partly ionized ions, or Bremsstrahlung from electron-ion encounters can cause energy loss from localized regions of the plasma. Because of the interactions between all of these processes, energy is redistributed, fluid motion and microturbulence develop, and all phenomena are coupled in a complicated way.

A plasma can be described as several interpenetrating fluids, and treated by classical fluid mechanics including interactions with classical electromagnetic fields. Particle interactions can be incorporated into the fluid description by modeling the collision processes phenomenologically or by kinetic theory. The fluid description is simple for comprehension, for analytical calculations, and for computer calculations. Alternatively, a method employing Boltzmann equations for each species of particles would describe the plasma more completely, but is much more difficult to implement. This model uses the velocity distribution in space and time, and requires a collision operator for both elastic and inelastic binary particle collisions between all species. Also, computational methods such Particle-in-Cell (PIC) combined with Monte Carlo Collision (MCC) techniques can simulate the particle dynamics as well as collision processes by calculating interactions and trajectories of many individual particles.

Solving the same problem using each of these descriptions in the above order becomes progressively more difficult to implement computationally as well as requiring longer computer run time. The fluid description was chosen for CSS plasma calculations due to its relatively simpler methodology. Also, as long as the number of particles is large, and collision lengths and times are shorter than characteristic lengths and times in the problem considered, the fluid description is adequately

accurate, and much easier to use.

The equations describing a plasma can be written to include as much detail as desired. The Boltzmann equation describes the full kinetics of each particle species by giving a partial differential equation for the phase-space distribution statistics. A simplification is usually made to describe fluid motions. The moments of the Boltzmann equation yield differential equations for fluid quantities such mass, momentum, and energy density. These moments are derived in Appendix A where collision processes between species are included.

More simplifications are usually made to get a tractable set of equations. The magnetohydrodynamic (MHD) equations are one such set that in some simple geometries can predict instabilities and their growth rates fairly accurately for plasmas with appropriate characteristics. Various versions of these equations can be developed for describing specific phenomena qualitatively and quantitatively with reasonable accuracy.

In situations where simple analytical models are not appropriate or accurate, more complicated models requiring numerical solution may be desired. This is the situation in modeling the CSS plasmas: magnetic fields are three dimensional and nonuniform entities and cannot be represented simply as straight field lines; neutrals ionize into ions and electrons; Ohmic heating is dependent on plasma temperature and in turn the heating affects the local temperature; etc. The appropriate model to describe even the most important aspects of this physics is beyond any simple analytic expression. The equations representing these phenomena have to be solved numerically on a computer, typically a supercomputer or fast workstation.

Numerical simulations can be useful in studying the behavior of complex systems. It is important that the model used in the simulation accurately describes the physical system. Once the model has been developed and tested, it can be used to interpret experimental measurements and observations, evaluate new ideas, extend theoretical models into new parameter regimes, and quantitatively test existing theories.

Simulations can be used to make predictions about other experimental geometries without actually building them. Other timescales or length scales can thus be investigated without the expense of re-engineering the physical system.

Features can be examined that are not detectable by experimental means, such as

neutral particle density. This is an important result of this work, since neutrals have a great influence on the formation and dynamics of plasmas in the CSS. Without the simulations, these effects could not be quantifiable.

In some studies, numerical computations are designed to converge to a steady state solution. Others are formulated to advance a linearized set of equations to determine unstable modes and their growth rates. COAX is designed to simulate time dependent, two dimensional, resistive magnetohydrodynamic fluid models. As much physics as is known or practically implemented is used in the models.

To validate the physical models used, the results of simulations are compared to experimental data. That is, direct comparison of data from simulations and experiment can be compared by overlaying plots of certain quantities. Many simulation studies do not attempt to do this either because experimental data is not available, or the simulations represent a simplified system that is not expected to accurately model the experimental situation. The simulations here are intended to be an accurate portrayal of the experimental device.

Since time dependent, two dimensional fluid codes generate huge amounts of data, data visualization techniques are necessary to interpret the results of any simulations. Modern workstations are often used along with powerful data management and graphics software to render the data in forms useful for human interaction and understanding. For example, animations are used to see time dependent behavior. Interactive techniques are used to view quantities of interest in specific spatial or temporal regions.

Unfortunately, this research effort was not afforded the opportunity to utilize the powerful equipment and software to perform such data visualization. Cray mainframe supercomputers at the National Energy Research Supercomputer Center (NERSC) were used to run the COAX code and generate data. Post-processing on this data was done with separate codes that generated black and white line plots, such as magnetic field versus time or radial position, or contours of particular two dimensional quantities at a point in time. Animations could be produced by selecting a series of time values to generate such plots. Then these plots could be viewed a frame at a time on the mainframe computer, or the graphics information could be transferred to a microcomputer and the time sequence of plots viewed as an animation. The process of generating and viewing such graphics is rather

time consuming (more so than the interactive methods mentioned above), but can reveal information otherwise not apparent in plots of less detail (such as maximum temperature versus time, etc.).

The COAX code and accompanying post-processor were originally developed by Barnes and Schnack [36]. It was adopted for use in the dissertation work of K.D. Hahn at the University of Washington in studying transport in an early version of the CSS experiment [1]. Various changes to these codes have been made during this research effort to add additional physical models or improved numerical techniques and graphics. These changes are listed in subsection 3.2.4.

3.2 Description of the COAX *Computer Code*

This section describes the COAX computer code as used until the last year of this research effort. The version described here uses an infinite friction model, i.e. the neutrals have the same velocity as the ions due to this interspecies friction. This particular model was found unsatisfactory as the simulations resulting from it did not adequately model the experimental data. This will be discussed in the last subsection. In chapter 4, a version of this code will be described that allows for the neutral fluid to have a separate velocity from the ion fluid (finite friction model). This modification to the code made a large improvement in agreement with the experimental data.

3.2.1 Physical Phenomena Modeled

The computer code COAX solves the fluid equations for the electrons, ions, and neutrals, in two dimensions, i.e. radial and axial coordinates. Strict azimuthal symmetry is assumed, which prevents behavior such as tilting or azimuthally asymmetric tearing from occurring in the code results. While these phenomena may in fact occur in the experiment, numerical simulations can still give insight into formation issues, and accurately model the real plasma in situations where the three dimensional effects are not present. It would be safe to say that when there are no toroidal field (B_θ) perturbations observed in the experiment, then there are no three dimensional effects, and the code should model those situations adequately.

In the version of COAX described in this chapter, infinite friction between the ion

and neutral fluids was assumed. This was justified by estimating the equilibration time for the two fluids to reach steady state under a constant force (on the ions). This is given by the characteristic time $\tau_{\text{equil}} = [(n_n + n_i)\langle\sigma v\rangle]^{-1}$, which is less than 0.1 μsec under typical conditions assumed ($n_n + n_i \approx 10^{15}$ cm^{-3}, $T > 1$ eV). The simplifying approximation was then made to set the fluid velocities for both ions and neutrals to be equal. This infinite friction model then simplifies the solution algorithm of the fluid code so that only one velocity field needs to be advanced in time. The mass density involved in this velocity equation is thus the sum of ion and neutral fluid mass densities. When the plasma is only partially ionized, the $\mathbf{J} \times \mathbf{B}$ force acts on the total mass density.

While setting the ion and neutral velocities equal is a convenient simplifying assumption, it means that there is no slippage between the two fluids under the $\mathbf{J} \times \mathbf{B}$ force that acts only on the ions. This was not thought to be significant at first. In the next chapter, the improved version of COAX uses a finite friction between ions and neutrals after problems with the infinite friction assumption were found.

Electrical resistivity results from the collision of the current carrying electrons with the background particles, either the ions or neutrals. The collision frequency is determined by the sum of: the classical value as calculated by Braginskii [13] which is proportional to $n/T^{3/2}$ due to the accumulation of many small angle encounters with charged particles; an anomalous collision frequency due to Bohm, $\nu_{\text{Bohm}} = \omega_e/16$; an anomalous collision frequency due to Chodura [37], $\nu_{\text{chor}} = \omega_{pi}[1 - \exp(-v_d/v_i f_{\text{chor}})]$, i.e. the frequency approaches the ion plasma frequency as the drift parameter (ratio of electron current speed to ion thermal speed ratio) becomes much greater than some number f_{chor} (called `fudge` in the code); and the electron collision frequency with neutrals which for hydrogen as the dominant neutral particle, is proportional to neutral density only. Parameters can be input to multiply any of these collision frequencies by a factor (`anomr, chor, fbohm`) to either turn on or off the related physical resistivity, or to enhance or diminish them as a test of their effect.

Ionization and recombination of deuterium is determined by a rate equation approach. This must be done using an implicit algorithm for the time advance due to the possible stiffness of the equations, i.e. the time scale for relaxation towards a steady state value may be much less than a time step. The hydrogen is consid-

ered to be in either the atomic form or ionized, so only two species are considered, and the rates for ionization and radiative recombination used are those given in Book's Plasma Formulary [38]. Radiation is emitted at the same rate as excitation of $H(1s) \rightarrow H(2s)$, which follows the assumption that radiative decay is essentially immediate. The energy (`eexcite`) of these radiative de-excitation photons is variable to simulate optical thinness or thickness of the gas to the radiation. For transparency of the neutral gas to radiation, `eexcite` is set to that of the L_α photon energy, 10.4 eV. For optical thickness (the radiation being fully trapped), `eexcite` is set to zero.

The radiation power dissipated by impurities is given by the steady state coronal equilibrium tables of Post et al. [25]. The nonequilibrium dynamics of the impurity charge state evolution can be ignored if $\langle n_e \tau \rangle \gg 10^{10}$ cm^{-3}sec, where τ is a characteristic time scale of the temperature or density. This is the case when a radiative collapse occurs giving $n_{max} \geq 10^{16}$ cm^{-3} so that the characteristic time $\tau \gg 1$ μsec is longer than the equilibration time for impurity charge states.

The radiation is dependent on the number density of each element (other than hydrogen), and a temperature dependent function for each element. This is implemented by assuming that each impurity is always present at a fixed ratio of the number density of the sum of neutrals and ions. The three elements considered are carbon, nitrogen, and oxygen, which are input by the variables `facimp(1)`, `facimp(2)`, `facimp(3)`, respectively.

The geometry of the coils is determined by input of the coil lengths (`zc1`, `zc2`) and widths (`rc1`, `rc2`), as well as the dimensions of the vacuum vessel (`znt1`, `znt2`, `rnt1`, `rnt2`), which fits within the coils. Boundary conditions are enforced at these surfaces. The flux function is a fixed value at each individual coil (coils are flux shaping surfaces). The value of temperature is uniform at the start, but is fixed at each vacuum wall. The velocity is also fixed at zero at each wall (no slip conditions), and the density has zero gradient at each vacuum wall.

The flux value at the coils is determined in one of two methods in the code. The first method (with input parameter `icirp = 0` for independent coils, or `icirp = 1` for parallel connected coils) employs a circuit solver routine with inputs for initial voltages (`vct`), capacitances (`xct`), inductances (`xlt`), and resistances (`xrt`) of external elements to determine the flux values consistent with this external circuit.

This consistency is important to have, since the plasma dynamics can affect the currents and voltages in the external circuit, and so a given waveform (such as a sine wave) cannot be imposed arbitrarily to simulate a real shot with real linear circuit elements. The second method (with input parameter `icirp = 2`) is used if the value of the flux has been measured experimentally for the conditions of the simulation. These numbers are supplied directly by reading a data file (`pscfile`) of digitized (and smoothed) data from the experiment. This is useful when trying to simulate a given experimental situation, as it minimizes the matching of external circuit parameters needed to give the correct waveform at the coils. This method is not consistent with any simply realizable external circuit though.

3.2.2 Model Equations

Given the assumptions of equal temperatures for the three species: electrons, ions, and neutrals, and the infinite frictional coupling between the ions and neutrals. The fluid equations for fluids can be combined to yield a consistent set:

$$\partial_t n_i + \nabla \cdot n_i \mathbf{u} = S = -(\partial_t n_n + \nabla \cdot n_n \mathbf{u}) \tag{3.1}$$

$$\partial_t (\rho \mathbf{u}_i) + \nabla \cdot \rho \mathbf{u}_i \mathbf{u}_i = -\nabla p + \frac{1}{c} \mathbf{J} \times \mathbf{B} \tag{3.2}$$

$$\partial_t \varepsilon + \nabla \cdot \varepsilon \mathbf{u} = (\gamma - 1)(n_e + n_i + n_n)^{1-\gamma}(Q - \nabla \cdot \mathbf{q} - ST) \tag{3.3}$$

$$\varepsilon = T(n_e + n_i + n_n)^{2-\gamma} \tag{3.4}$$

$$(\partial_t + \mathbf{u}_i \cdot \nabla)\psi = \frac{\eta c^2}{4\pi} \Delta^* \psi \tag{3.5}$$

where $p = (n_e + n_i + n_n)T$, $\rho = m_i(n_i + n_n)$, and S is the ionization rate. Δ^* is called the Grad-Shafranov operator, and in cylindrical coordinates is given by $\Delta^* = \nabla^2 - (2/r)\partial/\partial r$.

The temperature of electrons and ions are approximately equal if the time scale for plasma dynamics is much longer than the equilibration time for electrons and ions. This equilibration time is proportional to $T^{3/2}/n$ and is less than 4 μsec for plasma density greater than 10^{15} cm^{-3} and temperatures less than 10 eV. Neutrals

are typically coupled to the ions strongly, the neutral-ion temperature equilibration time is even shorter, so the single temperature approximation is adequate for present CSS operating conditions.

The derivation of these equations from the Boltzmann equations is presented in Appendix A.

3.2.3 Numerical Techniques

The numerical techniques used in COAX are for the most part those also used in a family of two- and three-dimensional codes called FLX. These codes are extended versions of COAX developed by D. Barnes, the original author of COAX. The paper describing these codes [39] gives more complete information on the numerical techniques sketched below.

Most of the calculations are vectorized, to take advantage of the Cray computer's ability to operate on 64 elements of a vector simultaneously. Thus the COAX code discretizes the spatial dimensions into a 128 x 61 (axial-radial) grid, giving axial and radial step sizes of about 1.2 cm and 0.5 cm respectively.

Spatial differencing is accomplished by using a staggered grid structure. Quantities such as density (n), temperature (T), and magnetic flux (ψ) are defined on the grid vertices. Magnetic field is defined by the numerical differencing of the equation $\mathbf{B} = \nabla\psi \times \nabla\theta$, where θ is the azimuthal coordinate. This leads to the components of $\mathbf{B}$ defined between grid vertices.

The components of velocity $\mathbf{v}$ are also defined between grid vertices in a natural way so that finite differencing of quantities such as $\nabla \cdot \mathbf{v}$ would be defined on the grid vertices.

The timestep is determined dynamically so that it is small enough to give reasonable accuracy and numerical stability. The equations for density, velocity, and temperature are advanced using the explicit method of upwind differencing, which is numerically stable as long as the time step is less than the minimum of all ratios of grid increment to velocity: $\Delta t < \min(\Delta z/v_z, \Delta r/v_r)$, the Courant restriction. For numerical accuracy, the timestep is set to at most 10% of this limit.

Since the velocity of Alfvén waves in low density regions of the plasma becomes very high ($v_A = B/\sqrt{4\pi\rho}$), the explicit time advance would require exceedingly small time steps due to the Courant condition. The Alfvén waves in low density

regions have no important effect on the plasma dynamics, and so this time step restriction is artificial. The semi-implicit method [40,41,42] for velocity advance eliminates the Courant restriction by using a modification to the explicit method, essentially adding a diffusive term $\Delta t^2 c_A^2 \nabla^2 d\mathbf{u}/dt$ to the velocity equation, and solving this term implicitly. The coefficient c_A^2 is proportional to the largest value of $(p + B^2/4\pi)/\rho$ on the grid, which gives just enough artificial viscosity to stabilize the numerical instability. This term can be seen to give numerical consistency, since it tends to zero as the square of the timestep.

The diffusion of temperature and magnetic flux are also advanced with an implicit method for numerical stability. The implicit solution of the velocity, temperature, and flux equations uses the method of relaxation. These equations have terms like $\nabla^2 T$, which couple nearest neighbor grid points in a five point stencil, when finite differenced. This problem is similar to that of finding the solution to the Poisson equation $\nabla^2 T = S$, for some source $S_{i,j}$ given on each grid point (i, j). The method of successive over relaxation (SOR) is used to iterate to a solution for such problems. The number of iterations needed is of the order of the grid number in the largest direction. The vectorization capability of the Cray supercomputer is used to advantage by solving a single row of points simultaneously using the tridiagonal algorithm, and using SOR on the line solutions.

Any numerical solution of partial differential equations must include boundary conditions to allow determination of values along the periphery of the computational domain, and at interfaces between different materials. The geometry including number, size, and position of coils is dependent on input values. In cases reported here, there are inner and outer coils, with a thin insulating wall between the vacuum region and the coils. The computational domain extends radially from the azimuthal axis of symmetry to a radius beyond the outer most coil input as `rwall`, with an axial extent (`zl, zr`) longer than the coils. Boundaries exist at the coil surfaces, the inner surface of the vacuum wall, and the bounds of the computational domain. In COAX, the plasma is restricted to the volume between the axial ends of the computational domain and the inner and outer vacuum walls. The temperature is fixed at the initial value `tmp0` on these surfaces, and the velocity is fixed at zero there. The ion and neutral densities have zero gradient on these surfaces.

The magnetic flux is calculated throughout the computational domain. It is

specified at each of the coils, either by values read from a file (`pscfile`), or calculated by solving the electrical circuit equations, as described in subsection 3.2.1. The flux value at $r = 0$ is always zero. At the radial and axial extent of the computational domain, the flux is determined by a boundary integral method as described in reference [39]. This allows the radial extent of the domain to be relatively near to the coils. The alternative to this method is to set the flux to zero at a perfectly conducting boundary far from the coils. This method would require a significant amount of grid points in the region outside of the plasma domain if the grid were of nearly uniform spacing, and thus would be computationally inefficient.

The numerical data generated by COAX is output to binary files at certain intervals in time for later post-processing. The post-processor then reads these files and plots actual data or calculates related quantities to be plotted. Time histories of the dynamics can then be visualized by a time series of snapshots: contours of temperature, flux, densities, velocity vectors, and sections through the midplane, like $T(r, z = z_{mid})$. Also, certain values are plotted by their time history, like maximum temperature, density, field at the midplane of the coils, heating power, radiation power, etc. This is used to compare to experimental data for both qualitative and quantitative differences.

3.2.4 History of COAX *Development*

The COAX code has gone through many revisions. At the beginning of this project, the changes to the source code were recorded by hand. When a UNIX-like system was added to the CTSS operating system at NERSC, the Source Code Control System (SCCS) set of tools was adopted for this purpose. These routines allow the source code for COAX to be modified, with all of the various versions kept within a master file. This file actually is a record of only the differences from one version to the next. Thus the results of changes can be automatically tabulated by the computer instead of by writing in longhand. This provides a much more accurate documentation system also.

Tables 3.1(a)-(c) list in brief form the modifications made to COAX over the period of time of this research project, up to the point when the operating system was changed. The code was used under the CTSS operating system until February, 1992. Then the code was modified for compatibility with the UNICOS operating

system. The changes for updating to the UNICOS operating system are listed in chapter 4.

3.2.5 Summary of COAX *Description*

This section has discussed the use of computer simulations for understanding physical phenomena like the CSS experiment. In particular, the computer code COAX has been described. The physical models used and equations solved in the code were presented. The numerical methods used to solve these equations were outlined, along with the input parameters and methods of operation. The history of the many versions of the code were listed. In the next section, the results of simulations will be presented that used versions of COAX with neutrals advecting at the same velocity as ions, as well as a modification whereby the neutrals were stationary.

Chapter 4 describes changes made to the COAX code starting with version 54.0, when the neutral fluid was allowed to have a separate velocity and friction with the ion fluid.

Table 3.1a: COAX changes: CTSS operating system

DATE	VERSION	CHANGES
5/88	36	Version of COAX inherited from K.D. Hahn
5/89	37	Added stationary neutral fluid; added ionization/recombination rate equations; power losses from ionization; electrical resistivity from electron-neutral collisions; frictional drag from neutrals
6/89	38	Added radiation from excited state of hydrogen; speed-up by using look-up tables for radiation rates
7/89	39	Corrections in temperature advance algorithms because of neutral fluid
7/89	40	Heat conduction coefficient includes electron collision frequency as in electrical resistivity (including anomalous contributions); entropy advance includes particle creation contribution; lower limits on densities, temperature
10/89	41	Changed mesh to allow finer mesh within plasma region
11/89	42	Timestep restriction due to ionization; vectorized look-up function
2/90	43	Output global powers and energies to data file
4/90	44	Correction to electron-neutral collision frequency; correction to thermal conduction power to walls; restrict temperature to nonzero values

3.3 Results of Simulations With Infinite Friction Model

The computer code COAX explained in the last section has been used to simulate laboratory plasmas. These simulations should be considered to be numerical experiments which ideally give results exactly the same as the actual physical experiment. The information obtained by the computer simulation is much more extensive than that from the actual laboratory experiment. Thus, insight into the processes of for-

Table 3.1b: (continued)

DATE	VERSION	CHANGES
5/90	45.0	Electrical conductivity limited by drift parameter factor
5/90	45.1	Added Poynting and compressional powers to output file
5/90	45.2	Minor changes to mesh routine, power calculations
5/90	45.3	Added relaxation parameters as inputs in namelist
5/90	46.0	Electron-neutral collision rate coefficient set to a constant value; fixed errors in a common block giving zeroes for some powers
6/90	46.1	Corrections to Poynting power calculation
6/90	47.0	Added multipliers for parallel and perpendicular heat conduction and Lα photon energy to input list; modifications and corrections to heat conduction calculation
6/90	47.1	Added calculation for total number of ions and neutrals, and output this to file; minor correction regarding mesh spacing in calculations
6/90	48.0	Set densities to have zero gradient boundary condition; ionization advance is made implicit; time step restricted by rate of ionization
8/90	49.1	Piecewise constant mesh routine
9/90	49.2	Spline fit grid
9/90	49.3	Grad-Shafranov operator changed
9/90	49.4	Density minimum in KAPP
10/90	50.0	Correct Braginskii coefficients in KAPP
10/90	50.1	Timestep reduced from 0.2 to 0.1 of Courant limit
10/90	50.2	Viscosity maximum for low density regions
10/90	50.3	Viscosity maximum removed
10/90	50.4	Timestep increased from 0.1 to 0.2 of Courant limit

Table 3.1c: (continued)

DATE	VERSION	CHANGES
10/90	51.0	Set positive definite ion density
10/90	51.1	Correction to positive definite ion density
10/90	52.0	Added flux input option for circuit solver
11/90	53.0	Line SOR solver alternates rows, then columns
11/90	53.1	Set positive definite neutral density
11/90	53.2	Correction to lookup routine for input flux
5/91	53.3	Mesh can be finer in plasma region than in vacuum regions
5/91	53.4	More accurate boundary conditions for densities
5/91	53.5	Modification of row/column SOR solver
5/91	53.6	Deleting three-body recombination
5/91	53.7	Turn off temperature correction for heat conduction truncation errors
6/91	53.8	Neutral advection removed; added heat conduction by neutral-ion and neutral-neutral collisions
6/91	53.9	Correction to neutral-neutral collision rate
6/91	53.10	Neutrals tied to ions with infinite friction
8/91	54.0	Neutrals with separate velocity, finite friction with ions
8/91	54.1	Timestep reduced to avoid stiffness from ion-neutral friction; corrections to finite friction algorithm
8/91	54.2	Implicit velocity advance for frictional terms
8/91	54.3	Modifications for positive definite neutral density

mation that are otherwise unobservable experimentally may be obtained by using simulations.

The numerical experiments must be properly calibrated against the available experimental data to be useful as simulations of the actual experiment. In practice, it is generally not possible to simulate the actual experiment exactly. Discrepancies between simulation and experiment may indicate that the physical models used in the simulation use incorrect input parameters or are lacking in some important feature, or else that there are errors in the numerical methods or programming, or possibly errors in the experimental data. A numerical experiment can be compared to a physical experiment where there is clearly different behavior. An interpretation based on physical intuition may indicate what phenomena are important or have been left out of the numerical experiment. Examples of such comparisons are: cases where impurities are present in the plasma, leading to radiative collapse, compared to simulations with no impurities or radiation; plasmas simulated from 100% ionized conditions when ionization actually proceeds throughout the discharge; or experimentally observed tilting configurations, while the simulations require azimuthal symmetry. Numerical experiments neglecting these effects give dramatically different behavior, indicating where the important physics issues lie.

The simulations presented in this chapter used the version of COAX which kept the neutrals and ions flowing together with one velocity (infinite friction). This tended to result in near vacuum regions near the walls as the plasma was swept away by the pinching action of the induced magnetic fields. These regions tended to show a higher temperature than the center of the plasma due to finite Ohmic heating in these regions where there was little heat capacity. This hot spot behavior has been troublesome for other computer modelers too. Lindemuth [43] describes setting a minimum ion density to alleviate this problem. While this was implemented in the COAX code, the constant inward pinching effect causes the non-physical minimum density plasma to be continually accreted into the main plasma body. New particles are artificially produced to maintain the minimum density condition, which violates total particle conservation. This prevents the minimum density from being set too high. The hot spot behavior tended to persist in these simulations until a modification was made to keep the neutrals stationary and thus populating the regions near the walls.

The COAX code requires various input parameters for each computer run, which correspond to the different physical effects that are modeled and the magnitude of these effects. These physical effects are not well diagnosed experimentally. For instance, impurities such as carbon and oxygen are expected to be present in CSS discharges because their line radiation has been observed. The amount of these elements and their origins have never been precisely determined, so the introduction of impurities into the plasma in the simulations is done by prescribing the density of each impurity element to be a small fraction of the density of hydrogen particles. More complicated models can be implemented, but the simple fractional density model indicates the importance of the radiated power from these impurities.

The following subsections describe the results of comparing hundreds of simulations to their physical equivalent on the CSS device using several different electrical configurations or formation modes. Many of these computer experiments revealed flaws in the computer code (i.e. numerical instabilities or nonphysical features), and were the equivalent of the "shake down" phase of operating a new experimental device. Also, the numerical experiments used many input parameters that were "free" in the sense that the physics they represented was of unknown magnitude (for example, anomalous resistivity, or impurity atom content). Many simulations were required to determine the interdependencies of these parameters and their effects on the results as compared to the experimental data.

Comparison to the independent coil configuration experimental results shows the large effect that radiation from the impurities have on the plasma. The physical model in the code seems to be realistic in describing a radiative collapse of the plasma. Ionization occurs throughout the experimental shot and the effects of ionization were found to strongly impact the simulation results also.

Other numerical experiments of the tearing and programmed formation modes of operation show similar behavior when impurities are present in sufficient quantities. When the coils were electrically connected in the parallel configuration, there appears to be less plasma contact with the walls in both experiment and simulation, so that the impurity content was assumed to be less than in the independent configuration. Simulations of programmed formation leading to radiative collapse did not accurately reproduce the experimental data, but gave more valid results than simulations without radiative collapse. The cooling effect from the impurity

radiation seems to be as important as the energy losses during ionization. This indicates that the neutral particle effects needed to be modeled better than they were with this version of COAX.

The last part of this section discusses simulations of the tearing mode of formation with no impurity radiation, but with power loss associated with ionization of neutrals. It was found that by modifying the model of infinite friction between ion and neutral fluids to that of stationary neutrals, there was much better agreement with the experimental data. This shows the importance that ionization and ion/neutral interactions have during formation. The next chapter reports on the modifications to COAX to better incorporate these interactions as suggested by the results of simulations with this intermediate model.

3.3.1 Radiative Collapse Simulations

3.3.1.1 Radiative Collapse in Independent Configuration

Early in the experimental work on the CSS, it was discovered that there was significant radiation emitted from impurities in the plasma. Line radiation of oxygen and carbon was observed in particular. An analysis of the experimental data by Raman [8] showed that this radiation was the dominant power loss mechanism. Thus it was expected that including line radiation losses in the simulations would result in radiative collapse as theorized in chapter 2. Simulations of the independent configuration did result in radiative collapse, and generally agreed with data from the experiment.

Various different input parameters were used to find those which gave reasonable agreement with experimental results. The most crucial parameter was the impurity density (actually input as a fraction of plasma plus neutral density). These impurities (carbon and oxygen) are expected to come from plasma/wall contact. Traces of substances such as grease (from finger prints, vacuum pump oil, cleaning solvents and residues) and water adsorbed on the vacuum chamber walls (quartz or Pyrex tubes) are difficult to remove except by high temperature or plasma contact. Experimental data, as well as simulations and circuit modeling show that the plasma radius starts at the inner wall, later moves to the outer wall, then back to the inner wall again at the end (see figure 3.1). The times when plasma contacts the walls is

when the impurities are assumed to be introduced into the plasma.

Using a resistivity model which included both classical and anomalous (Bohm) contributions, radiative collapse occurred whenever the impurity line density was above a limit of about 5×10^{17} m^{-1} for each species, carbon and oxygen. This agrees with the theory of radiative collapse presented in section 2.2 and diagrammed in figure 2.4. In cases of such radiative collapse, the plasma collapsed to a high density, narrow ring at the midplane. The low temperature from radiation losses resulted in higher density by pressure balance, and the higher density caused a higher radiation rate. Below the impurity inventory limit, the behavior was quite different. Then, the temperature was higher as there were fewer cooling mechanisms.

Run #172 was an attempt to simulate experimental shots with charging voltages of 5 kV (inner coil) and 2.1 kV (outer coil), at fill D_2 densities of 14 mTorr. Table 3.2 lists the relevant COAX input parameters. Figure 3.2 shows the contours of flux, density, and temperature during the radiative collapse. The azimuthal axis of symmetry is indicated in these plots by the short/long dashed lines. The coils are represented by the filled rectangular areas surrounding the vacuum walls (which are represented by the longer and thinner rectangles).

The flux contours show a single closed flux surface that is near the separatrix. The cusps at the ends are near the x-points. Inside the region enclosed by the separatrix is the highest concentration of ionized plasma. The temperature contours indicate a local minimum at the position of the density maximum, with hotter regions near the inner wall and axially past the x-points. These results are typical of radiative collapse simulations.

The experimental data from external and internal magnetic probes agreed fairly well with simulations. Figure 3.3 shows the magnetic field radial profile at the midplane from both simulation and experiment. Also shown are the radial profiles of temperature and density with the range of temperatures found experimentally using Thomson scattering. Note the high temperature near the inner wall (vacuum vessel wall is at 6.75 cm). This hot spot in the low density region is typical of these simulations.

The simulations used an electrical resistivity model that was based on classical resistivity (collision frequency $\nu_{cl} \propto n_e/T^{3/2}$) with enhancement by an anomalous collisional rate. The anomalous rate (ν_{anom}) in this case was chosen to be a multiple

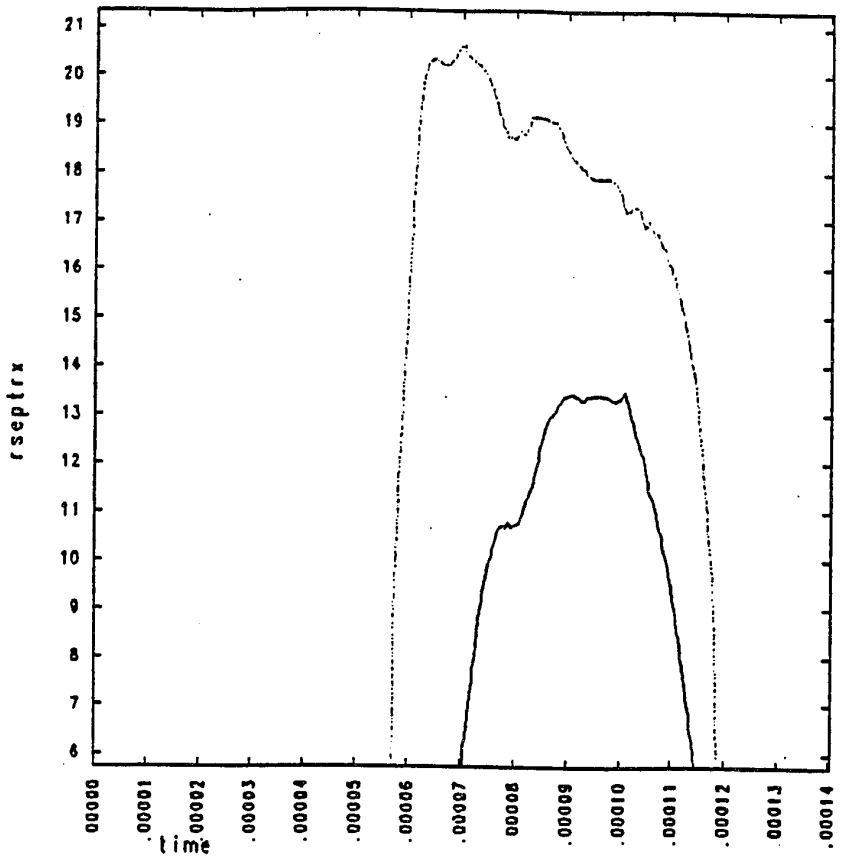

Figure 3.1: Outer and inner separatrix radius from a simulation of independent configuration.

Table 3.2: COAX input parameters for independent configuration radiative collapse run.

parameter	run #172	units
en0	1.e15	cm^{-3}
vct(1,1)	5.e3	volts
tswt(2,1)	8.e-6*	sec
vct(2,2)	-2.1e3	volts
tmp0	0.1	eV
eion	13.6	eV
preion	0.001	fraction
anomr	1.0	multiplier
fbohm	1.0	multiplier
facimp(1)	0.01	O fraction
facimp(3)	0.015	C fraction
version #	40	

*Switching time for the outer coil voltage to turn-on after the inner coil voltage swings through zero.

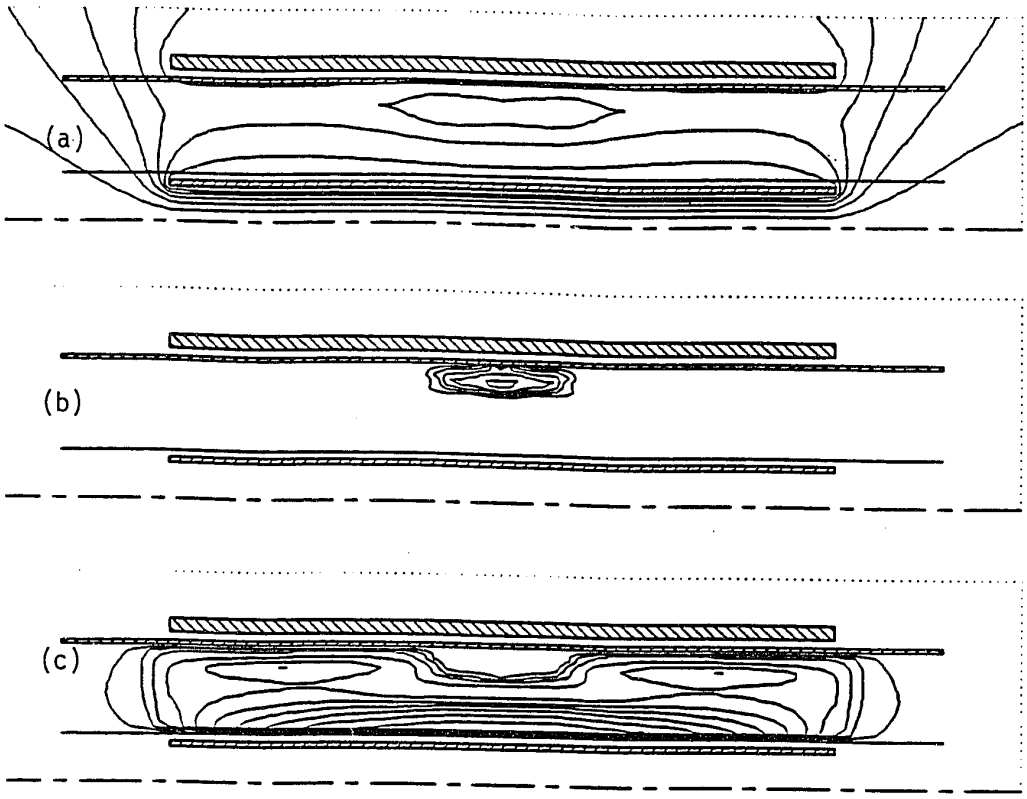

Figure 3.2: Contours of (a) magnetic flux, (b) density, and (c) temperature from simulation of the radiative collapse of a CSS plasma in the independent configuration at 90 μsec from the start of the simulation.

of the Bohm rate $\nu_{anom} = f_{anom} eB/16 m_e c$. Since this anomalous rate is proportional to the field strength, and conductivity $\eta \propto n_e/(\nu_{cl} + \nu_{anom})$, the highest conductivity region is restricted to a narrow band near the magnetic null. Figure 3.4 shows the resistivity from both classical and anomalous models. Since the temperature was fairly high on the small radius side of the magnetic null, the reduction of conductivity was from the anomalous collision rate $\nu_{anom} \propto B$. The temperature on the large radius side was reduced in balancing with the high density caused by the radiative collapse. The conductivity there was reduced by the classical collision frequency $\nu_{cl} \propto n_e/T^{3/2}$. The electron drift parameter $J/en_e v_i$ is also plotted, demonstrating that because this parameter is of order 1 in the electric current region, drift instabilities may reasonably be assumed to be present, justifying the use of the anomalous collision frequency.

The time history of the magnetic field were also compared to experimental values, and are plotted in figure 3.5. The general features agreed fairly well. The field started at a nearly uniform bias value due to some flux lines linking the annular space with the inner coil. In the experiment the plasma was preionized nonuniformly and to an unknown extent before the main discharge started at $t = 0$[1] In the simulation, a uniform preionization of 0.1% was initiated at $t = -42$ μsec. Due to the differences in simulated versus actual plasma conditions at the start of the main discharge at $t = 0$, the plasma current started immediately in the experiment, but was delayed by about 15 μsec in the simulation as the plasma density slowly increased. After the plasma ionized in the simulation, the magnetic fields showed quick field reversal as in the experiment. Oscillations of the plasma radius were duplicated by similar oscillations of B_z at the inner coil.

The magnitude of the fields were similar at their peaks and in the middle plateau region for both experimental and simulation data. The decay rate was a bit slower for the simulation, but the plasma configuration disintegrated at about the same time when the field reversal ended around 75 μsec. Comparing to figure 3.1, it can be seen that the flux imbalance due to the independent mode of operation drove the null radius into the inner wall at about 114 μsec (72 μsec on the experiment

[1] In the simulation, the starting time is defined as $t = 0$, and the main discharge (inner coil voltage reversal) started at $t = 42$ μsec. In the experiment, the main discharge is defined as $t = 0$, so a time shift of 42μsec was made for simulation time scales.

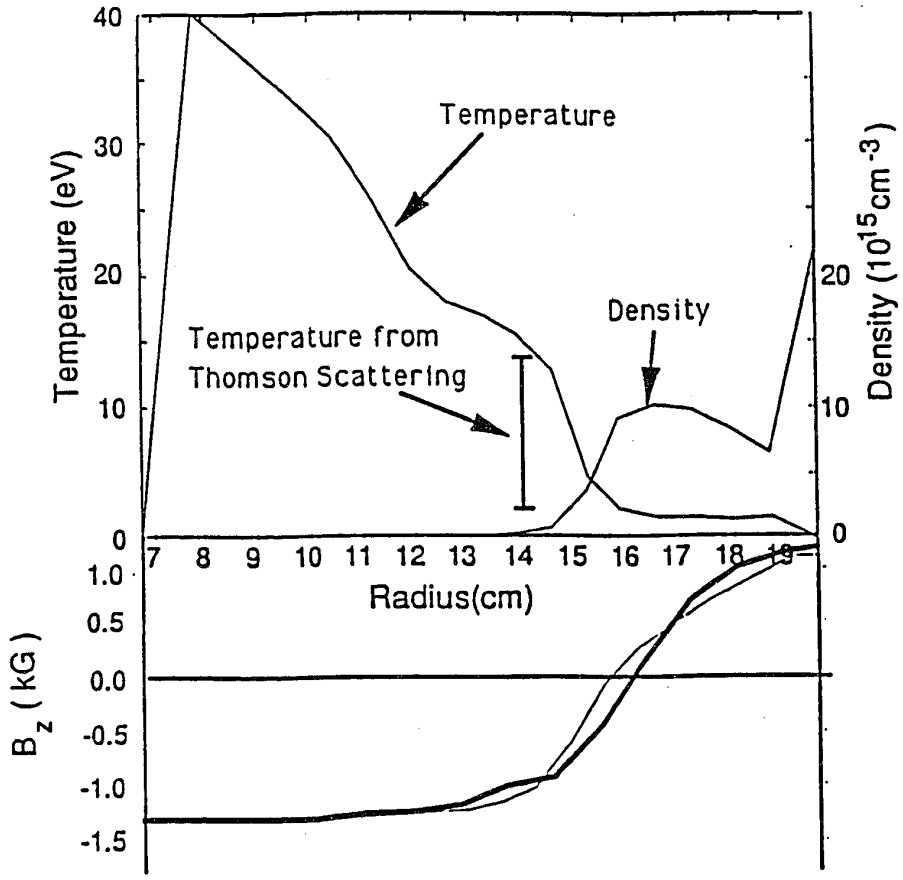

Figure 3.3: Radial profile of B_z at the midplane at $t = 90$ μsec from simulation #172 of independent configuration (thin line) and experimental data (thick line). Also shown are the temperature and ion density, with an indicator of the location and range of values found for temperature experimentally.

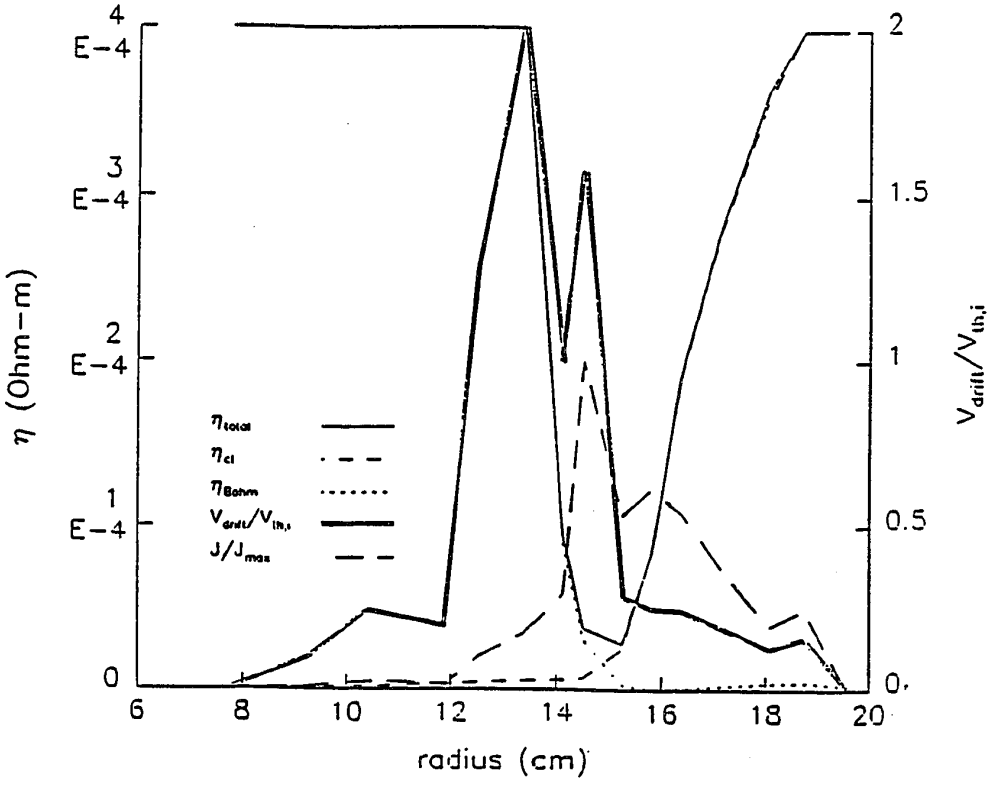

Figure 3.4: Radial profile of total, classical, and anomalous (Bohm) resistivity at the midplane at $t = 90\mu$sec from simulation of independent configuration. Also shown are the normalized electrical current density, and the electron drift parameter.

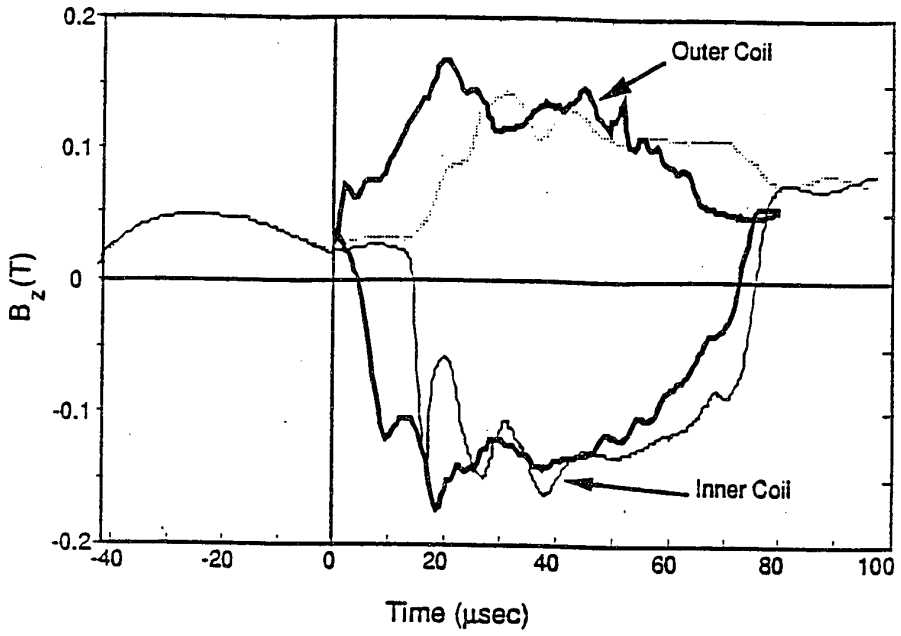

Figure 3.5: Magnetic field at inner and outer coils at the midplane. Simulation results are plotted in thin lines, experimental data in thick lines. The simulation starting time is referenced to -42 μsec in this plot.

time scale). This was the cause of the rapid destruction of the configuration.

3.3.1.2 Radiative Collapse in Parallel Configuration

Simulations were also made for the CSS operating with the coils electrically connected in parallel. The expectation was that radiative collapse would explain the axial contraction and low fields observed experimentally. The experimental results also indicated that the plasma tilted in most cases—this could not be simulated, as COAX simulates only azimuthally symmetric plasmas. It was hoped that the radiation power loss might approximate the anomalous energy losses associated with tilt instability saturation mechanisms.

The runs described here of programmed formation used either 0% or 0.5% of both oxygen and carbon impurities. These simulations were directly compared to experimental data for equivalent shots using the 10 mTorr fill pressure of D_2 and 8 kV charging voltage. The flux values as measured experimentally were used as input to the code since the waveform included a "notch" in voltage that was difficult to model properly. The preionization was fixed at 100% even though that was not the case experimentally, but was used here for simplicity in demonstrating the effect that impurity radiation has on the plasma dynamics. The relevant COAX input parameters are listed in table 3.3.

It is clear that the behavior of the experimental device did not follow that of the simulation #268 with 0% impurities and 100% ionization. The coupling of energy from stored field in the inner core to the plasma was much better in the simulation than seen experimentally. Figure 3.6 compares the magnetic field at the inner and outer coils in the simulation with those from the actual experiment. The magnetic field continued to rise as long as the coil voltage is positive (it changed sign at 90 μsec). Since the plasma current was proportional to the field, the approximate relation $\dot{I}_p \propto V$ holds. This is expected for inductively coupled systems with small plasma resistance, as in this case.

Figure 3.7 shows the time histories of the maximum and null point density and temperature from the simulation. The plasma temperature reached 50 eV, and the density rose due to the pinching of the plasma column which had a length about half that of the coils after formation. In the experiment, T_e was never more than about 10 eV [4] in programmed formation. The high density that appeared after

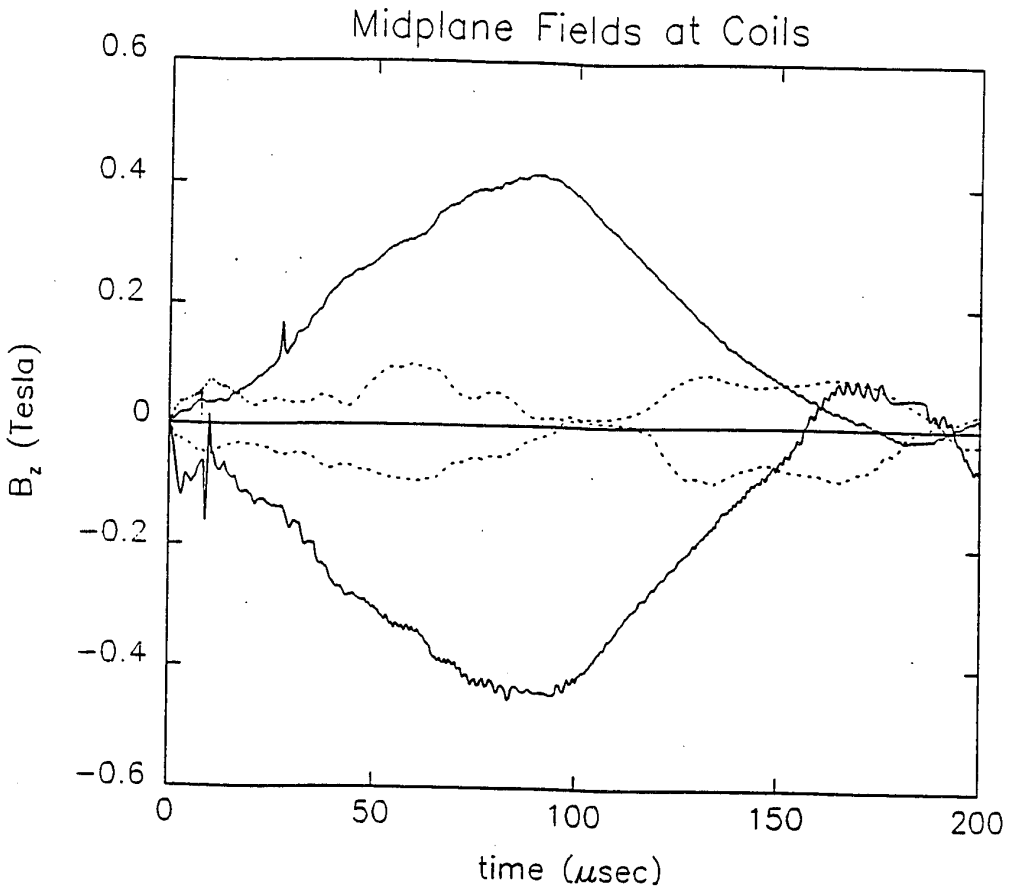

Figure 3.6: Magnetic fields at midplane for inner coil (lower curves) and outer coil (upper curves). The solid lines show the results from the simulation #268 with 0% impurities and the dashed lines show the experimental data.

Table 3.3: COAX input parameters for 0% or 0.5% impurity fraction comparison runs.

parameter	run #268	run #274	units
`en0`	7.1e14	7.1e14	cm^{-3}
`tmp0`	1.	1.	eV
`facimp(1)`	0.005	0.005	O fraction
`facimp(3)`	0.005	0.005	C fraction
`preion`	1.	1.	fraction
`anomr`	1.	1.	multiplier
`fbohm`	0.	0.	multiplier
`chor`	0.	0.	multiplier
version #	52.0	52.0	

120 μsec was due to plasma pile-up at the outer wall after plasma expansion when the coil voltage changed sign.

The flux, density, and temperature that resulted from this simulation are shown in two sets of snapshots in time in figures 3.8 and 3.9. Contours of these three quantities are plotted at 25 μsec into the discharge in figure 3.8 when the field lines around the plasma were all closed (programmed phase), and after the field in the core had reversed sign to produce open field lines around the plasma (tearing phase) in figure 3.9. At both times the temperature and density were peaked close to the magnetic null point. This should be compared to the radiative collapse example from the independent configuration (figure 3.2). Again note the hot spot—the relatively high temperature at the inner wall radius.

The behavior in the simulation when there are impurities present was markedly different. Run #274 used a 0.5% impurity fraction, and again 100% ionization. There was a temperature inversion at the midplane in the same region where the density was concentrated. That is, the temperature near the peak density point was a local minimum. This is another example of a radiative collapse. The null point temperature never exceeded 6 eV and the density peaked at over 15 times the fill

(a)

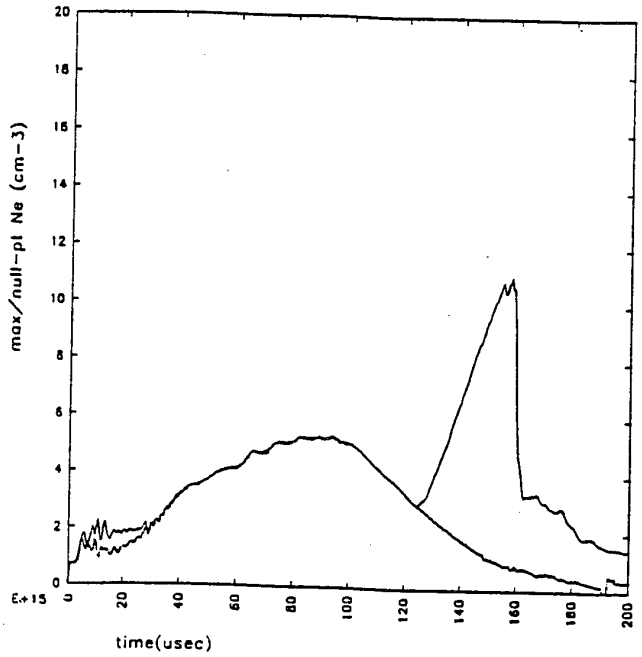

(b)

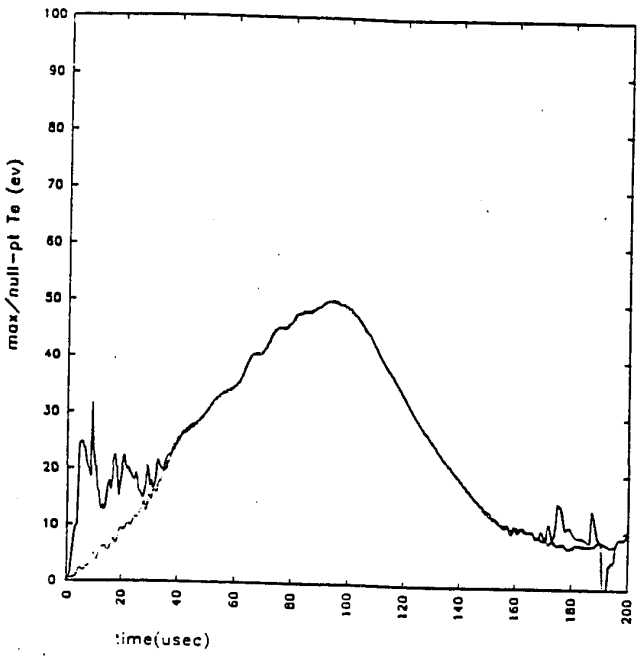

Figure 3.7: Time history of maximum and null point values for (a) density and (b) temperature for 0% impurities.

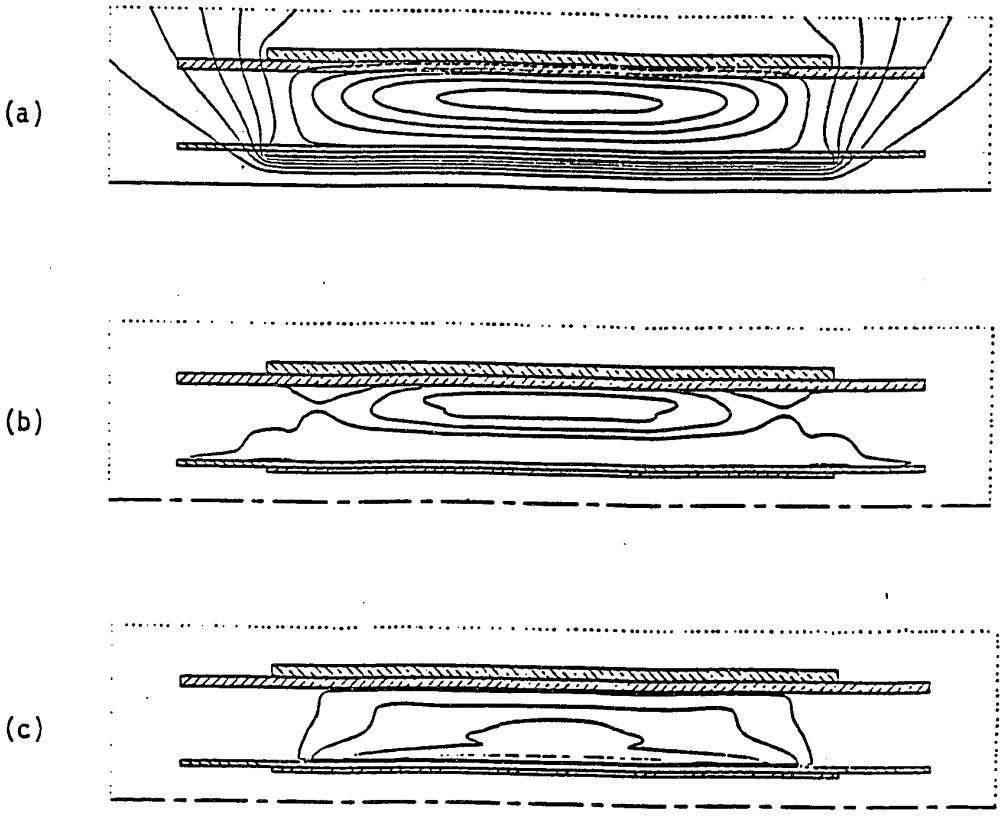

Figure 3.8: Contours for 0% impurities case at t = 25 μsec. (a) Flux with 1 mWb increments; (b) density with 0.5×10^{15} cm^{-3} increments; (c) temperature with 4 eV increments.

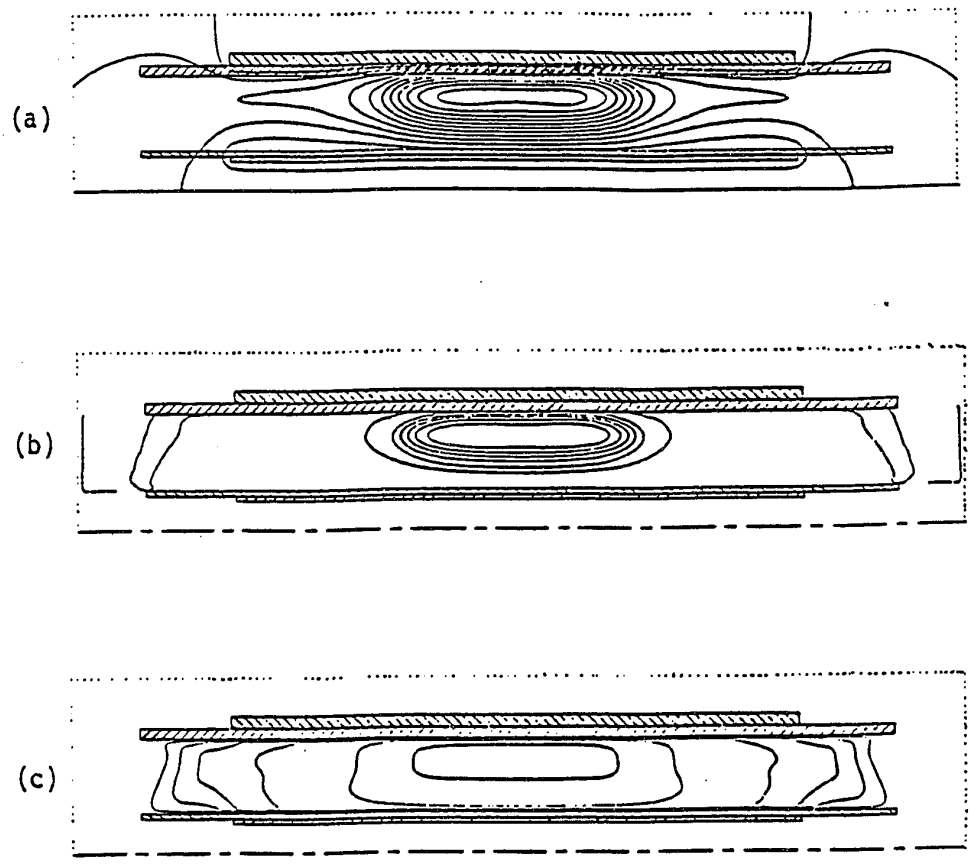

Figure 3.9: Contours for 0% impurities case at t = 45 μsec. (a) Flux with 1 mWb increments; (b) density with 0.5×10^{15} cm^{-3} increments; (c) temperature with 4 eV increments.

density (see figure 3.10). The flux, density, and temperature at the same times as in figures 3.8 and 3.9 are shown in figures 3.11 and 3.12 (note that the increments between contours of density and temperature have been changed).

The configuration just started to collapse at 25 μsec. The temperature near the inner coil was higher than that at the null point because of the hot spot problem mentioned earlier. The electric field ($\propto 1/r$) was higher there which causes higher heating power ($\propto \sigma E^2$) into the low particle density. By 45 μsec, the radiative collapse was established. The temperature had a minimum at the magnetic null, while the density was peaked there.

The experimental time history of the magnetic fields at the coils did not exactly match that in the simulation, but the magnitudes of the fields were in closer agreement. The field is roughly constant until the voltage changed sign at 90 μsec. In this case, the plasma current was approximately proportional to the applied voltage, $I_p \propto V$. This is the situation for resistively coupled systems, that is, the plasma resistance in this case was much higher than the inductive impedance due to the lower temperature.

The power dissipated by the impurities lowered the temperature and hence raised the resistance of the plasma so that there was less coupling of energy to the plasma than in the 0% case. Hence the better agreement for the magnetic field data. The heating power and radiated power were approximately balanced (see figure 3.14), as they should be for a radiative collapse, which explains why the temperature remained low for the 0.5% impurities case.

The radiation power measured experimentally was smaller than that produced in the simulation. It is expected that the amount of impurities should be smaller than that in the independent coil configuration experiment because the plasma is never pushed against a vacuum vessel wall. It will be shown later that power is lost in ionizing the plasma. By including the correct ionization model and allowing neutrals and ions to have separate fluid velocities, the plasma dynamics should be in reasonable agreement with experiment without using any impurities in the simulations. (Although tilting cannot be simulated with COAX.)

An interesting case was run using no impurities, but the ionizing hydrogen was allowed to radiate energy from an excited level (Lyman α) and this was enough to cause a radiative collapse also. It is expected that in reality the neutral gas sur-

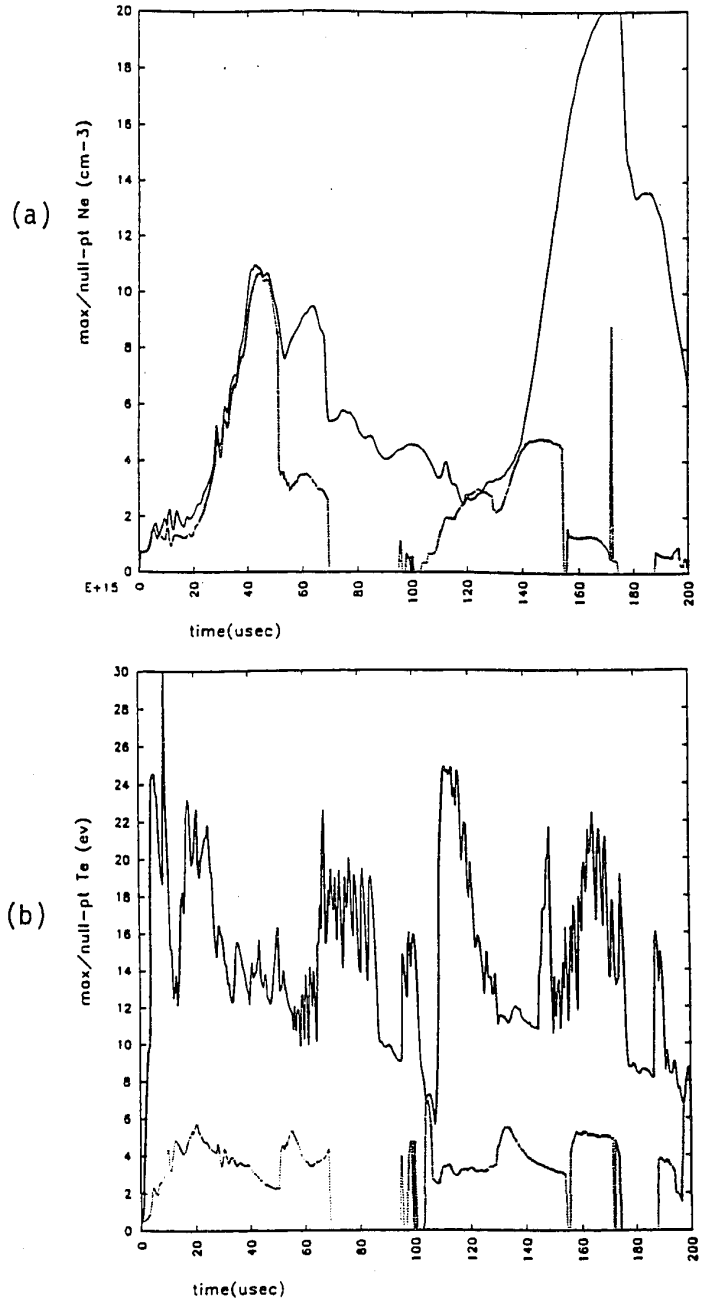

Figure 3.10: Time history of maximum and null point values for (a) density and (b) temperature for run #274 with 0.5% impurities.

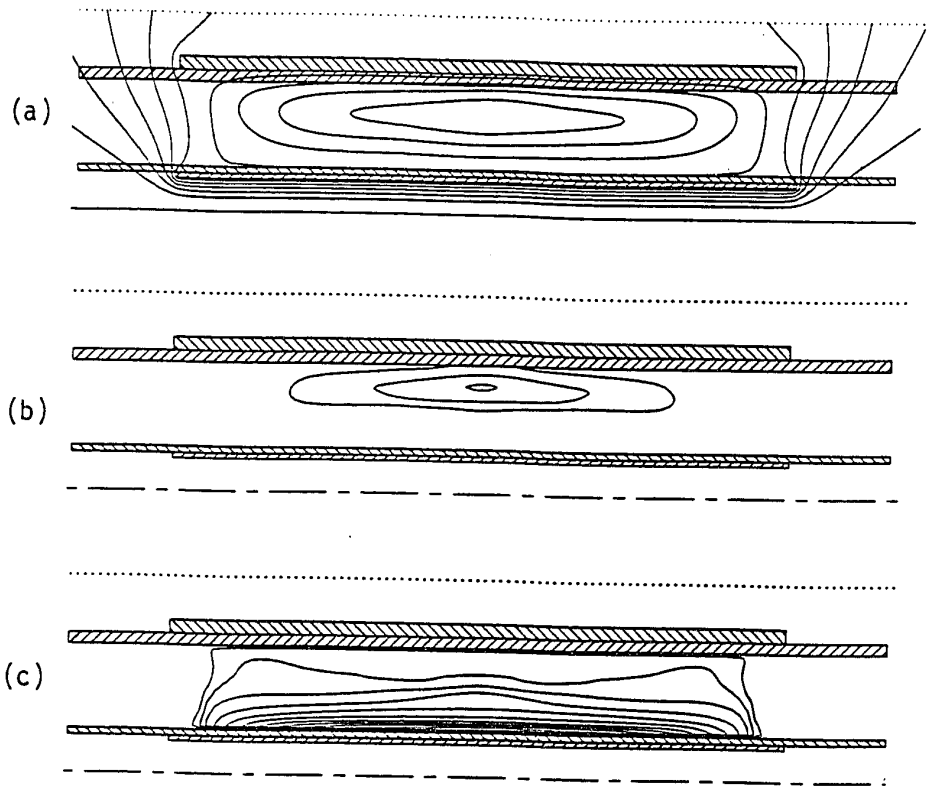

Figure 3.11: Contours for 0.5% impurities case at t = 25 μsec. (a) Flux with 1 mWb increments; (b) density with 1.0×10^{15} cm^{-3} increments; (c) temperature with 2 eV increments.

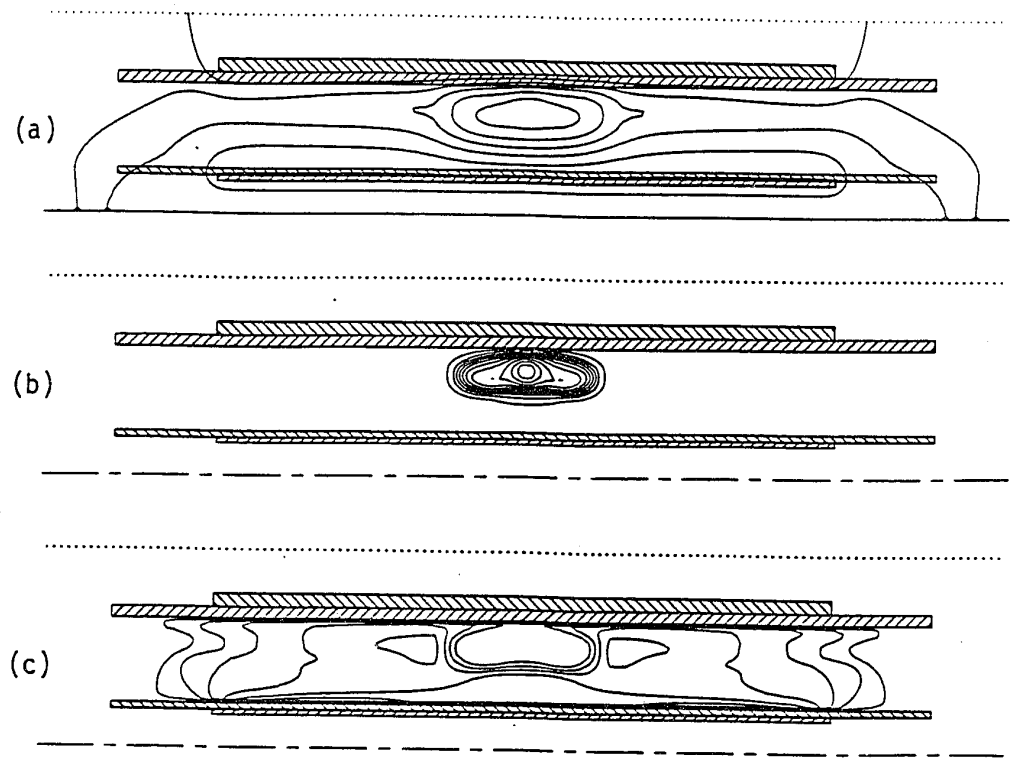

Figure 3.12: Contours for 0.5% impurities case at t = 45 μsec. (a) Flux with 1 mWb increments; (b) density with 1.0×10^{15} cm^{-3} increments; (c) temperature with 2 eV increments.

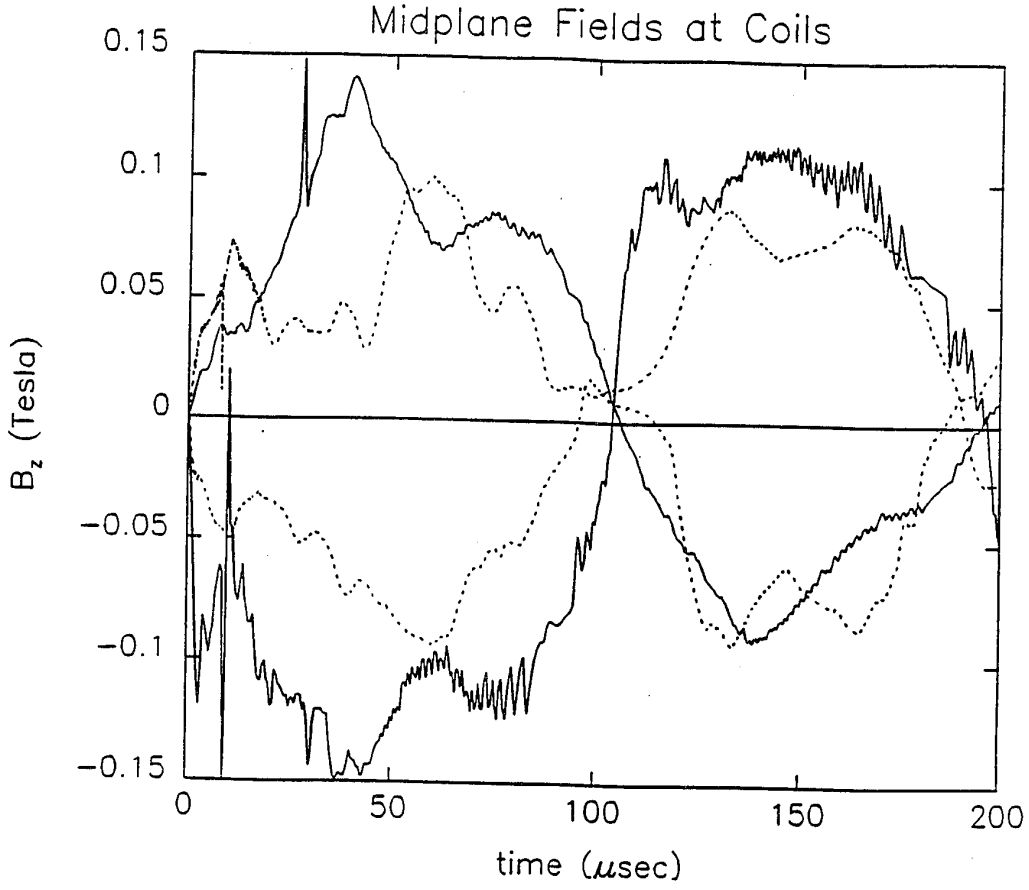

Figure 3.13: Magnetic fields at midplane for inner and outer coils. The solid lines show the results from the simulation with 0.5% impurities and the dashed lines show the experimental data.

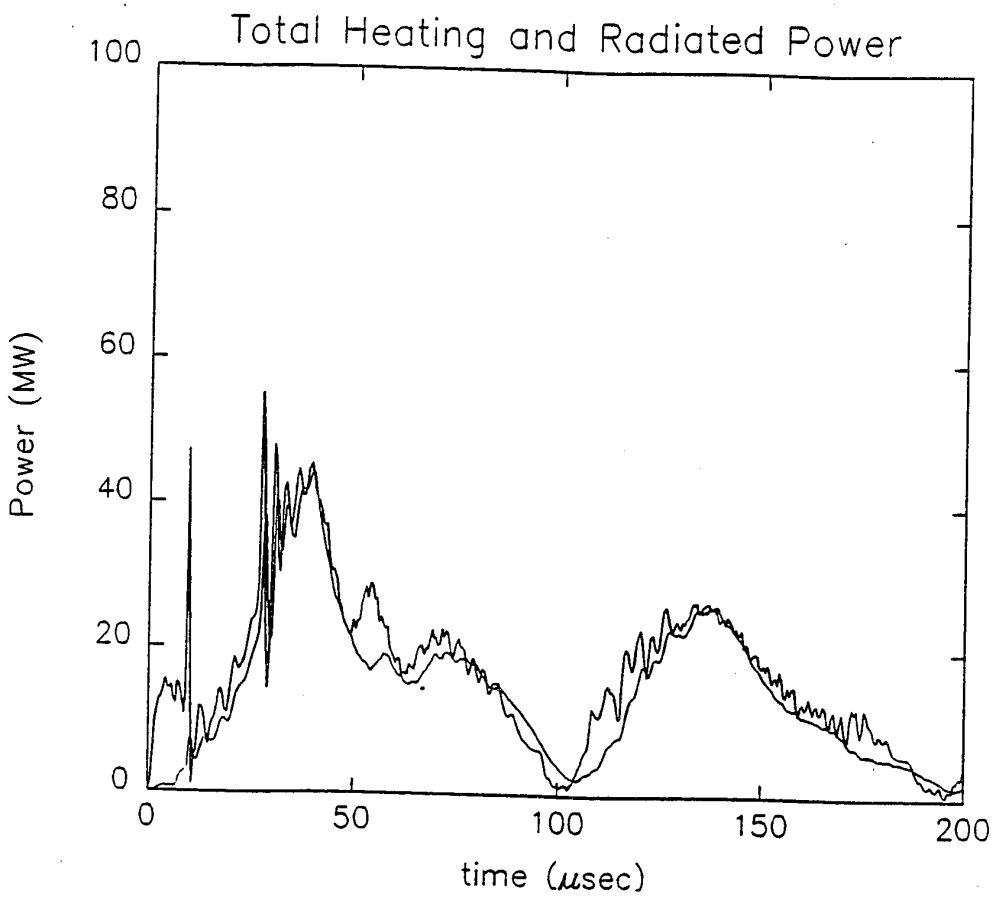

Figure 3.14: Total heating power (Ohmic + compression + viscous) and radiative power (smoother curve).

rounds the ionizing plasma and absorbs the Lyman α radiation strongly. Nonetheless, this example shows that a slow forming plasma is strongly influenced by the surrounding neutral fill gas. Proper modeling of the dynamics of the neutral gas, its ionization, and radiation are necessary to understand the coupling of power to the plasma and power losses from the plasma.

The ionization and radiation power losses in COAX simulations may approximate the hypothesized anomalous power loss from the experimentally observed tilting, although the physical mechanism is not correct. The simulations do not allow tilt due to the limitation of the two dimensional model used. The experimental plasmas generated by programmed formation tended to tilt under the same conditions as the simulations used in this section. The analytical model of Pierce [12] shows that the tilting mode may be unstable, but that it saturates in amplitude. Anomalous power loss may result by the transfer of energy from the symmetric mode (i.e. the only mode that COAX would generate) to the tilt mode, with dissipation of this energy from the tilt mode.

When operated at higher fill pressure and lower voltage, the plasmas do not tilt [12]. Simulations under these non-tilt conditions need not emulate the anomalous power losses. The next chapter includes results of simulations using non-tilt conditions, and shows the importance of the improved modeling of neutral/ion interactions, including finite interspecies friction.

3.3.2 Comparison of Infinite and Zero Friction Models

Previous simulations using the infinite friction model typically resulted in temperatures with local maxima near the inner coil. This region had low density of both ions and neutrals as they were pushed away from the walls due to the pinching action of the induced plasma currents and the infinite friction between ion and neutral fluids. Thus any Ohmic heating in this low density region raised the temperature significantly due to the low heat capacity there. Figures 3.2, 3.3, 3.8, 3.11, and 3.12 show this hot spot phenomenon for independent coil configuration and programmed formation runs.

This hot spot phenomenon may be expected to vanish if there were neutral gas in the region near the inner wall. To test this hypothesis, a modification to the code was made by decoupling the neutral fluid from the ion fluid by artificially setting

the neutral fluid velocity to zero at all times. This version of COAX (version 53.9) is called the zero friction model, as it simulates the effects of zero interspecies friction (although ignoring the dynamics of the neutrals that would result from pressure gradients).

The best mode of formation to test this code modification is tearing formation. Tearing formation resulted in plasmas with length about the same as the coils, and a thin radial extent. There was no evidence of tilting. The experimental data was reproducible shot-to-shot, until magnetic activity started when the confining magnetic fields reached their peak magnitudes. This activity seemed to be associated with tearing activity due the formation of secondary magnetic field peaks. Due to its asymmetric structure (in the toroidal direction), this instability could not be simulated with the COAX code. It fact no symmetric tearing was observed in simulations. Simulations could be directly compared to the experimental data for times up to the experimentally observed magnetic activity.

Two simulations are compared here. The intent was to expeditiously change the COAX code so that the effect of the zero friction model could be determined in direct comparison to the infinite friction model. The result was as expected: the hot spot was eliminated in the new model.

Similar input parameters were used in both simulations. These runs could be compared to experimental shots for tearing formation, with 3 kV charging voltage and 15 mTorr D_2 fill pressure. Input parameters that were identical in both simulations were: classical resistivity with Bohm added, ionization potential of 16 eV, 0% impurities, and initial temperature of 1 eV. Run #291 used the version of COAX with infinite friction and run #300 used the zero friction model. There were some differences, such as run #291 (infinite friction model) included losses due to L_α radiation, had some anomalous Chodura resistivity, and started with a 1% preionization fraction, while run #300 had none of these extra features, and started with a 10% preionization fraction. The important input parameters are listed in table 3.4.

The electrical circuit parameters of main bank capacitance, external resistances and inductances, and were set to agree with the assumed values of the actual experimental configuration. This included external inductance (due to the electrical cables and ignitrons) which prevented the coils from being connected at the same

Table 3.4: COAX input parameters for infinite and zero friction model comparison runs.

parameter	run #291	run #300	units
en0	1.06e15	1.06e15	cm^{-3}
tmp0	1.	1.	eV
eion	16.	16.	eV
eexcite	10.2	0.	eV
preion	0.01	0.10	fraction
anomr	1.	1.	multiplier
fbohm	0.1	0.1	multiplier
chor	0.5	0.	multiplier
fudge	1.	0.	multiplier
version #	53.7	53.9	

exact voltage. This caused some flux difference between the coils, and a resulting drift in the plasma null radius.

Simulation run #291 with the infinite friction model resulted in a persistent hot spot near the inner wall, while the ion density peaked midway between the coils, as can be seen in figure 3.15. Since the neutrals were dragged with the ions during the plasma compression, the ion density as well as the neutral density was low adjacent to the walls. This region had a finite Ohmic heating power density, and thus the relatively high temperature there.

In run #300, using the zero friction model, there were no hot spots near the walls as in run #291. Instead the temperature and density both peaked at the same radius, about midway between the coils (see figure 3.16). After about 25 μsec into the discharge, an axial contraction left vacuum regions at the ends of the coils, which did form hot spots. These results were as expected, since neutrals were left near the walls as the ions were bunched and heated Ohmically in the region near the magnetic null radius. The axial contraction occurred after significant ionization of the neutrals in the end regions, so that there were low neutral density spots left

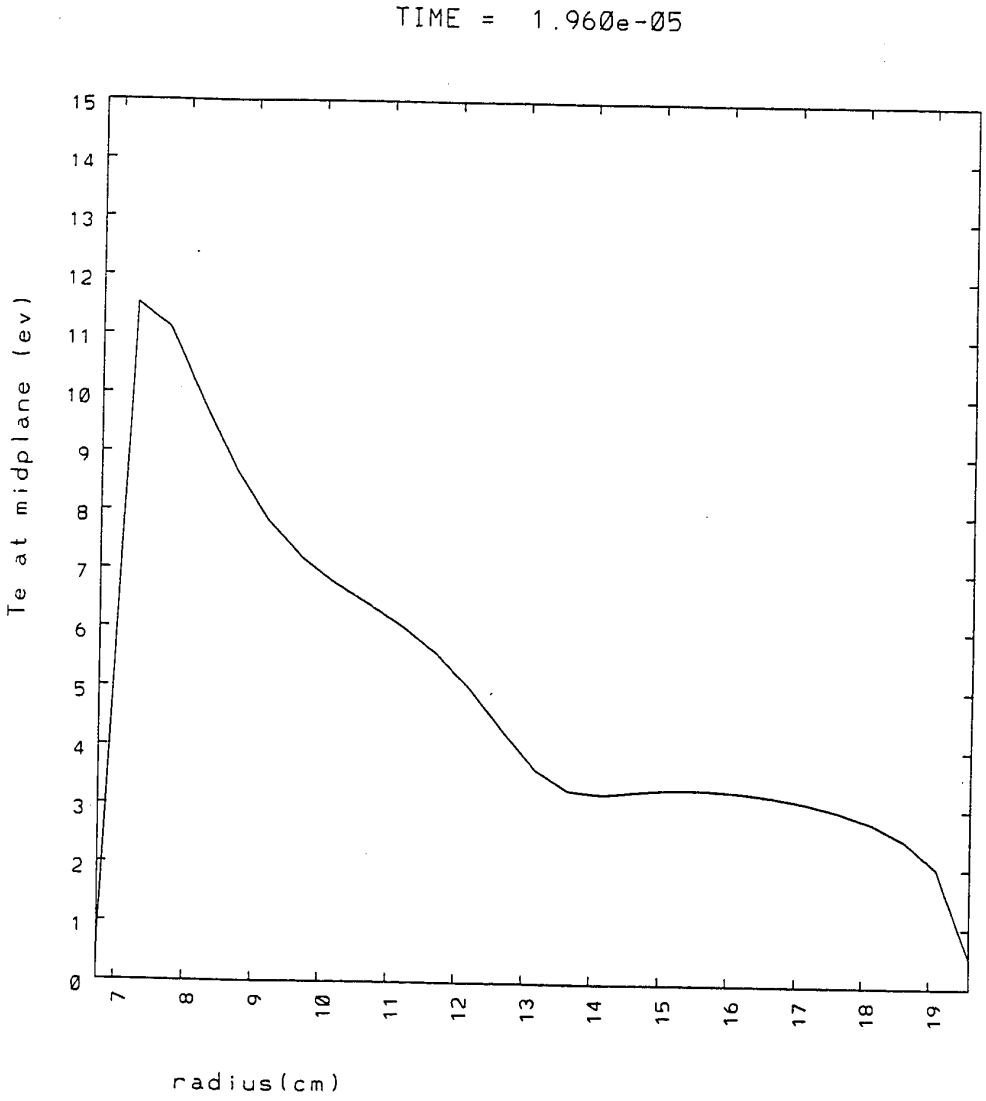

Figure 3.15: (a) Radial profile of temperature for run #291 at 20 μsec.

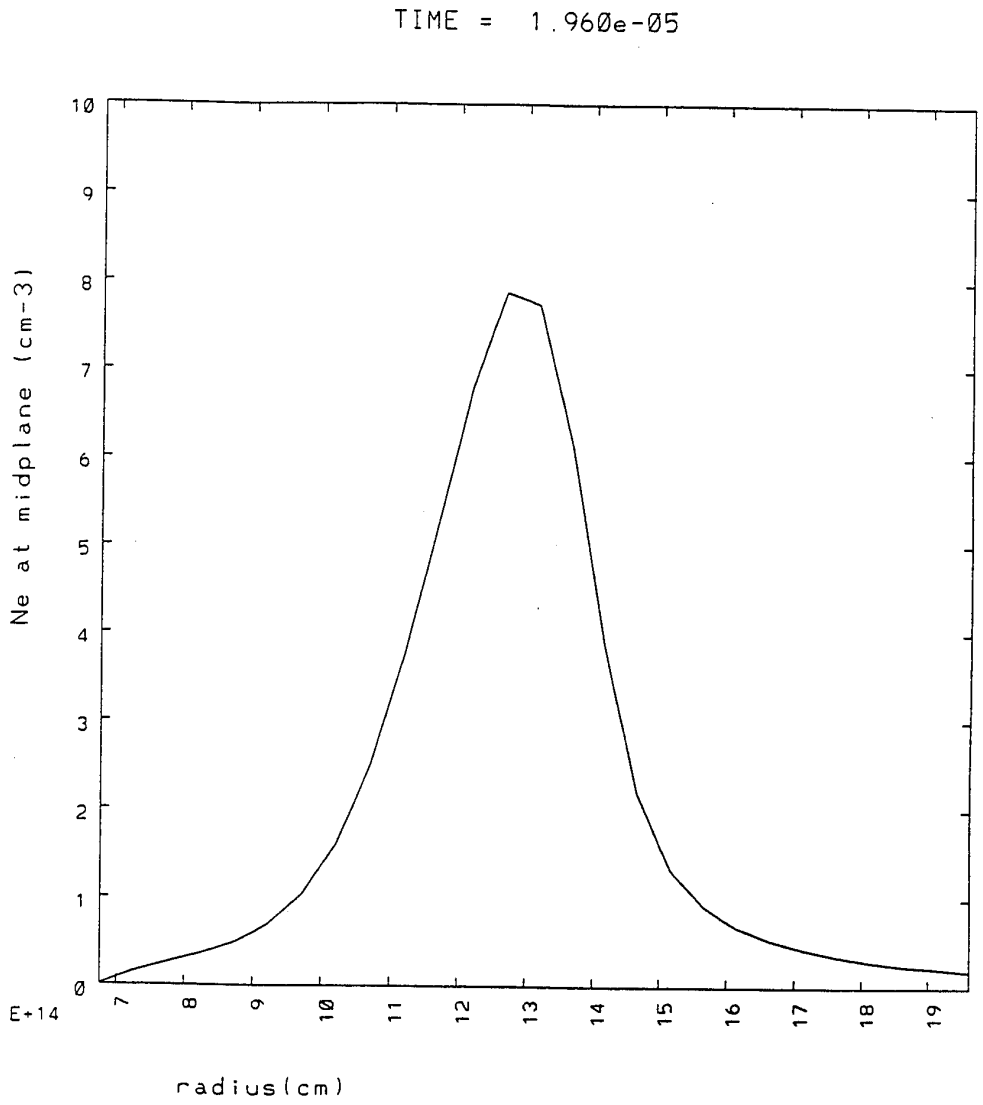

Figure 3.15: (b) Radial profile of ion density for run #291 at 20 μsec.

behind when the plasma contracts. These spots were then subject to finite Ohmic heating and formed hot spots for the same reason as those formed near the walls in simulation #291.

Simulation #300 generated magnetic fields that almost matched the experimental data. Figure 3.17 shows this. The magnetic field rose while the applied voltage was nearly constant (up until about 30 μsec). The field peaked after this time due to the axial contraction. This result must be contrasted to that of simulation #291 using the infinite friction model. It that case, the magnetic field was much lower than in the experiment ($|B_{sim}| < 0.06$ T, peaking at about 30 μsec). Low temperature in the vicinity of the null radius led to a high resistance in the plasma, and thus more flux losses and lower fields resulted.

In comparing the two versions of COAX with and without neutral motion, it is apparent that the influence of the neutrals on the formation is an important feature of the simulations. The stationary neutrals gave a more realistic portrayal of experimental results because they remained near the walls as the ionized plasma was pinched inward. This provided the motivation to change the code to allow neutrals to flow with a separate velocity, rather than use the unrealistic stationary model. The neutrals should be dragged with the ions by a finite interspecies friction as well as have dynamical forces from their own pressure gradients. The next chapter describes the changes made to accomplish this goal, and the results of simulations with the finite friction model. These modifications to the code were expected to combine the best features of the previous two models, and this indeed is what happened. The neutrals will be shown to flow with the ions as in the infinite drag version, but in the new version, the drag is finite, and is proportional to the density of the ions. In regions of low ion density, the neutrals will remain stationary, unless there exists a pressure gradient. The neutral pressure gradient causes slow inward diffusion of neutrals into the ionized plasma in a natural way, so that neutral density can remain significant near the walls as the ions and some of the neutral gas is swept into the center of the annulus. The wall-blanketing neutrals will then be accreted into the plasma by diffusion caused by the neutral pressure gradient and countered by the friction against the ionized plasma.

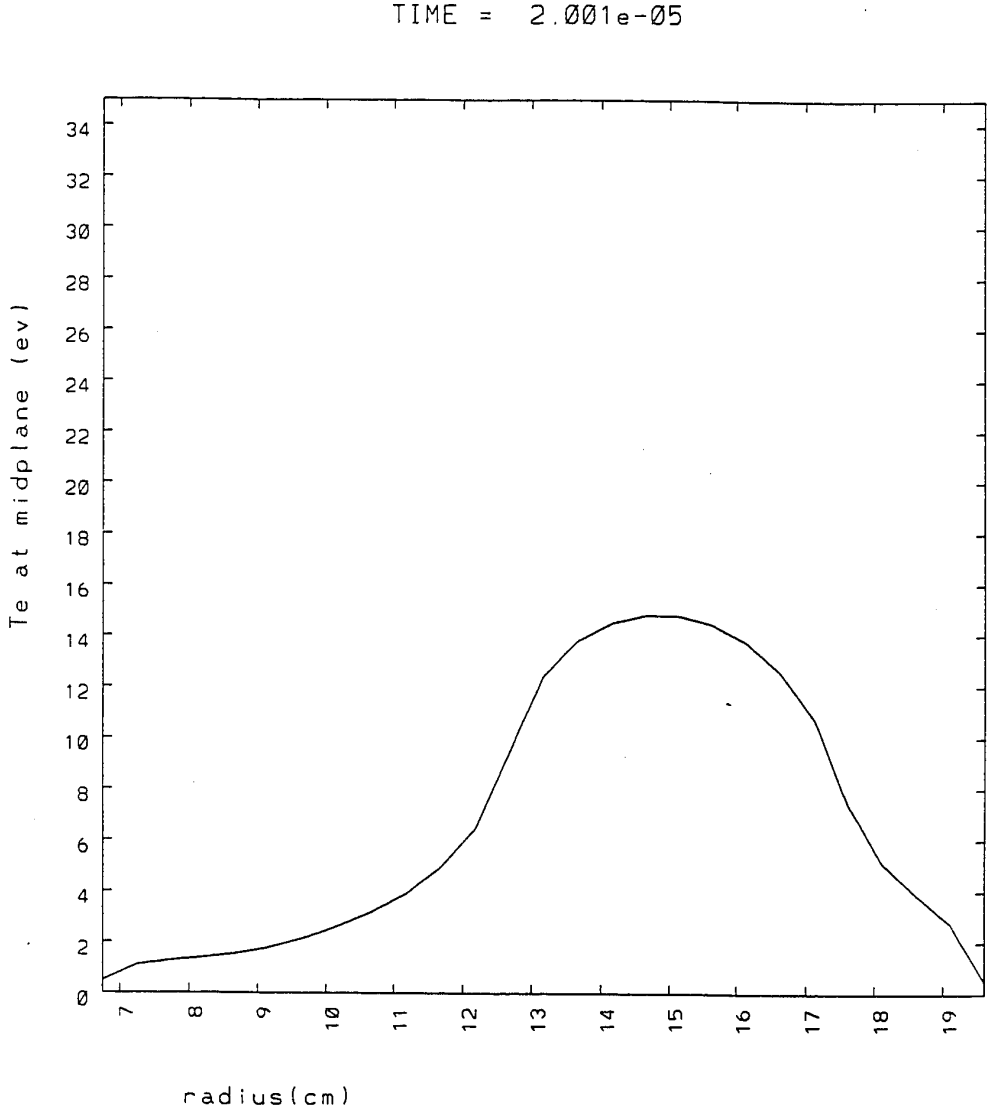

Figure 3.16: (a) Radial profile of temperature for run #300 at 20 μsec.

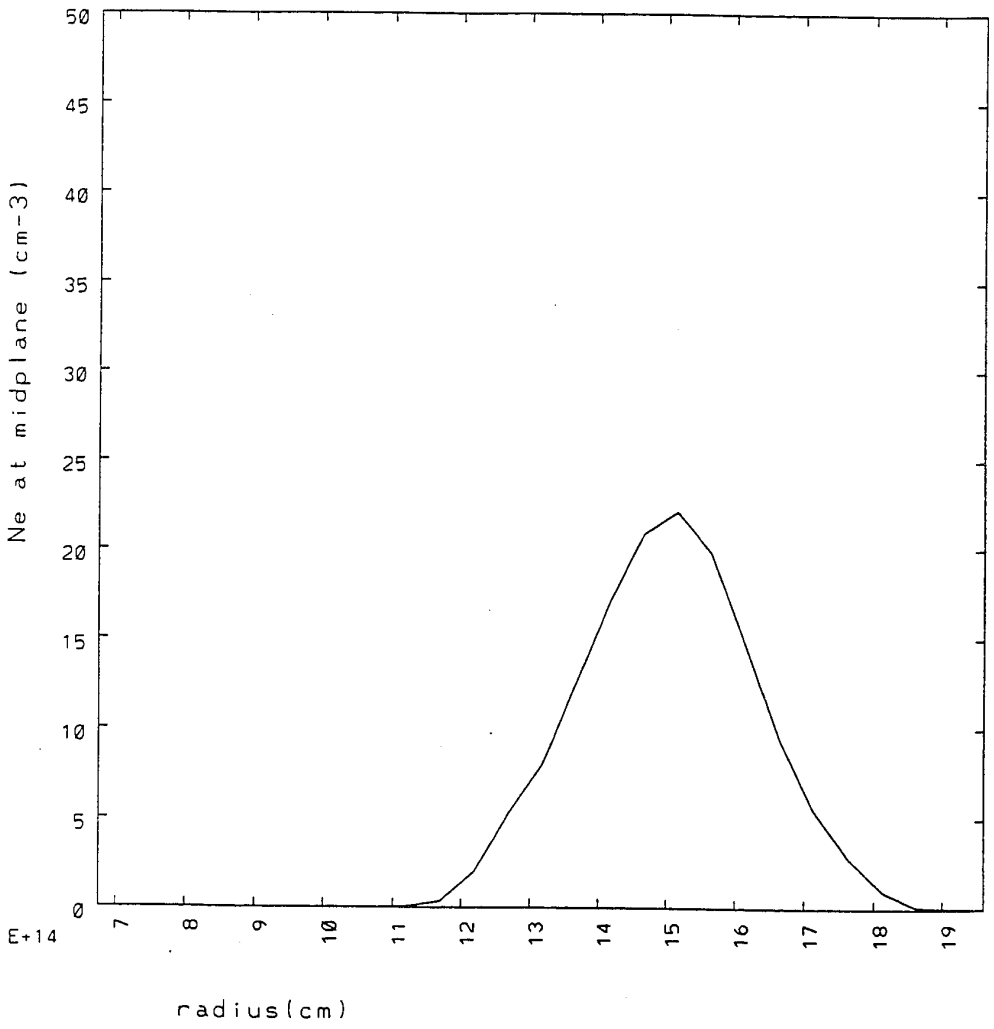

Figure 3.16: (b) Radial profile of ion density for run #300 at 20 μsec.

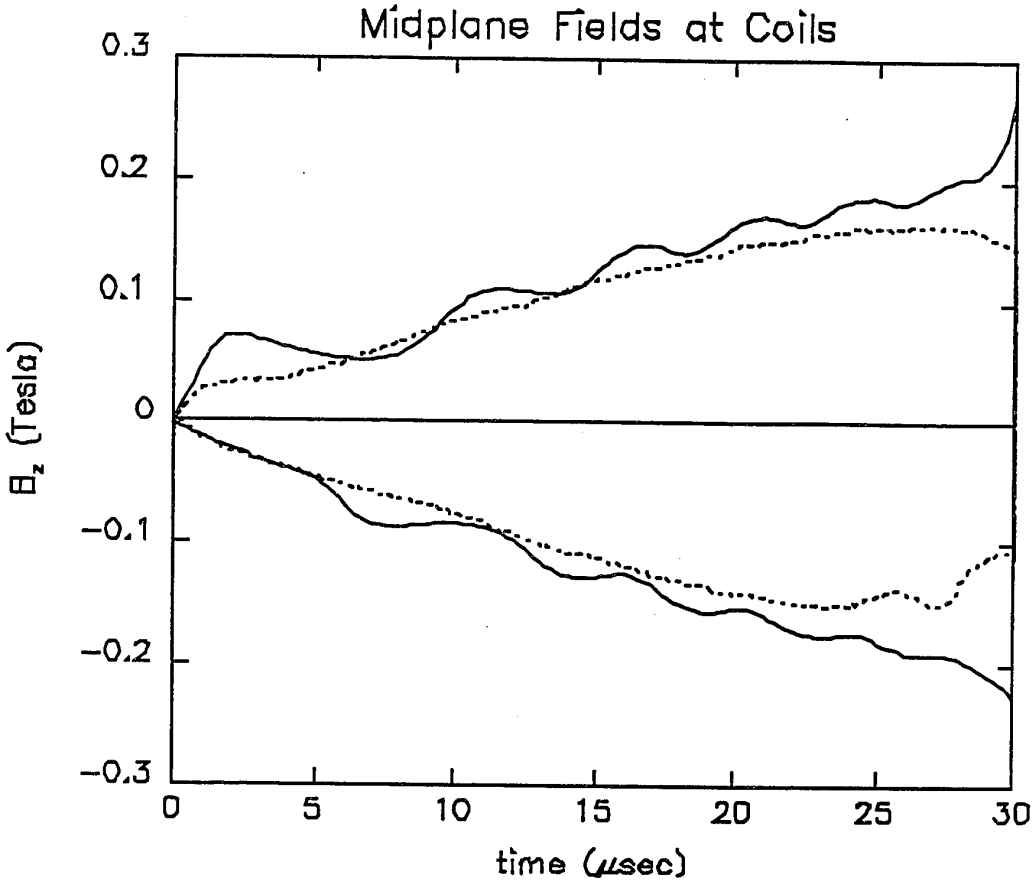

Figure 3.17: Midplane fields at inner coil (upper traces) and outer coil (lower traces) for run #300 (zero friction model). Simulation data is plotted as solid lines, experimental data as dashed lines.

3.4 Summary

- Radiative collapse results in plasmas with an impurity inventory above the limits theorized in chapter 2.

- Independent configuration was dominated by radiation from impurities and resulted in radiative collapse; the impurities came from plasma contact with the walls at various times in its formation.

- Hot spot formation disappeared after modifying COAX to have stationary neutrals remain near the inner wall; this modification was expanded to include finite friction—the subject of the next chapter.

Chapter 4

IMPROVED COAX COMPUTER CODE

4.1 Description of Improved COAX Computer Code

This chapter describes the version of COAX which has separate ion and neutral fluid velocities, with frictional coupling between them. This version is "improved" because the results obtained with it are quite different from those described in the previous chapter. The simulations with this version of COAX give much better agreement with the experimental data from the CSS experiment. The resulting physical behavior of the simulated plasma is clearly more realistic than that from the previous version of the code.

Section 3.2 in the previous chapter lists the changes made to various versions of the COAX code while it was used under the CTSS operating system. Starting with version 54.0, the neutral fluid has a separate velocity from the ion fluid. Several months after these changes were made, some of the NERSC computers were changed to the UNICOS operating system (a Cray Computer variant of the UNIX operating system). The code was then modified to operate under the UNICOS system.

Several types of changes were required to get the code running under UNICOS. The source files needed to be transferred and translated to the new UNICOS machine. In CTSS, macros were used with a precompiler to input repeated common block and type statements at the beginning of program modules. In UNICOS, the compiler allowed `include` files. The macros were rewritten to generate about 25 separate `include` files. Also, the whole program was separated into files for each program module (main, subroutines, function subroutines). There were then about 75 files making up the source code for COAX.

Other details of conversion involved changing CTSS `CALL LINK` statements to the conventional `OPEN` file statements. The `NAMELIST` format was found to be slightly different. Also, string variables are handled more conventionally in UNICOS, so a new subroutine was created to deal with naming families of filenames (i.e. output data files).

Since the graphics utilities were changed under the new operating system, a decision was made to change the graphics routines to the NCAR set of routines. This involved at least a couple months of programming and troubleshooting. The result was higher quality graphical presentation, as well as much more versatile capabilities in post-processing and visualization.

There were significant changes made to COAX to implement new physics. In comparing the two versions of COAX described in the previous chapter (the versions with and without neutral motion), the influence of the neutrals is an important feature of the simulations. The stationary neutrals give a more realistic portrayal of experimental results because they remain near the walls as the ionized plasma contracts radially from the walls. In response to this observation, the code was changed so neutrals flow with a separate velocity from that of the ions, rather than use the unrealistic stationary model. The neutrals are then dragged with the ions by a finite interspecies friction.

The frictional force is implemented in COAX by using a coefficient of friction, $\langle \sigma_{in} v_{in} \rangle \approx 2 \times 10^{-8}$ cm^{3}sec^{-1}, the reaction rate coefficient for ion-neutral collisions. Elastic charge exchange collisions dominate the ion-neutral collision rate, so the charge exchange cross-section (σ_{cx}) is used in $\langle \sigma_{in} v_{in} \rangle$. This cross-section is determined by the formula [44,45]

$$\sigma_{cx} = 0.6937 \times 10^{-14} [1 - 0.155 \log(E)]^2 \text{ cm}^2 \tag{4.1}$$

where E is the center of mass energy in eV. The formula for the reaction rate coefficient is $\langle \sigma_{in} v_{in} \rangle$ = `faccx` $\times \sigma_{cx} \sqrt{16 T^*/\pi m_i}$. In this formula, $T^* = T + (\pi m_i/16)|v_i - v_n|^2$. T^* is the effective temperature—it includes a term for relative drift between ions and neutrals. The effective temperature is used in the cross-section formula by: $E = \frac{4}{\pi} T^*$. The factor `faccx` is a multiplier used to adjust the frictional coupling. It is normally set to `faccx = 1`.

It is necessary to make the algorithm for the velocity advance implicit in the part that couples the ion and neutral velocities by friction:

$$d\mathbf{v}_i/dt|_{\text{friction}} = -n_n \langle \sigma_{in} v_{in} \rangle (\mathbf{v}_i - \mathbf{v}_n) \tag{4.2}$$

$$d\mathbf{v}_n/dt|_{\text{friction}} = -n_i \langle \sigma_{in} v_{in} \rangle (\mathbf{v}_n - \mathbf{v}_i) \tag{4.3}$$

The implicitness is necessary to avoid numerical instability when the time step is

Table 4.1: Heat conduction coefficients

species	$\kappa_{\|\|}$	$\kappa_\perp$		x
e	$3.16\frac{n_e T \tau_e}{m_e}$	$\frac{4.664x^2+11.92}{x^4+14.79x^2+3.7703}$	$\frac{n_e T \tau_e}{m_e}$	$\frac{eB\tau_e}{m_e c}$
i	$3.91\frac{n_e T \tau_i}{m_i}$	$\frac{2x^2+2.645}{x^4+2.70x^2+0.667}$	$\frac{n_e T \tau_i}{m_i}$	$\frac{eB\tau_i}{m_i c}$
n	$3.91\frac{n_n T \tau_n}{m_i}$	$3.91\frac{n_n T \tau_n}{m_i}$		

larger than the frictional damping time $[(n_i+n_n)\langle\sigma_{in}v_{in}\rangle]^{-1}$. This time is much less than a microsecond in regions of large ion or neutral density.

The heat conduction includes terms from each species. The electron and ion heat conduction terms are split into the cross-field and parallel-field components: $\kappa_\perp$ and $\kappa_{||}$. For high collisionality ($\Omega_c\tau \ll 1$), these components are equal. At low collisionality, the charged particles are tied to flux surfaces, and only conduct heat parallel to field lines. The neutrals are not affected by magnetic field, and have $\kappa_\perp = \kappa_{||}$. Table 4.1 lists the heat conduction coefficients. These formulas are adapted from Braginskii [13], where only a pure ion-electron plasma is considered. The formulas still hold when neutrals are present, but the calculations for the collision times (τ_e, τ_i, τ_n) must include collisions with neutrals also. The reciprocal of the collision time is the collision rate, the sum of all interspecies and intraspecies rates. Thus, $\tau_\alpha^{-1} = \nu_{\alpha i} + \nu_{\alpha n}$, for any species α = electrons, ions, or neutrals. The rates $\nu_{\alpha e}$ are ignored, since they are negligible compared to the others. Table 4.2 lists these collision rate formulas.

Input parameters are used to provide adjustability to the cross-sections for electron-neutral (`facen`), charge exchange (`faccx`), and neutral-neutral collisions (`facnn`). The use of the factor `faccx` was already shown in the formula for $\langle\sigma_{in}v_{in}\rangle$.

Friction between the ions and neutrals causes frictional heating. This heating power is written

$$P_{\text{fric}} = m_i n_i n_n \sigma_{cx} \sqrt{16T^*/\pi m_i} |\mathbf{v}_n - \mathbf{v}_i|^2 \tag{4.4}$$

The factors `fioniz` and `frecom` are used to adjust the ionization and recombi-

Table 4.2: Collision rate formulas

α	$\nu_{\alpha i}$	$\nu_{\alpha n}$
e	$2.91 \times 10^{-6} n_e \ln\Lambda T_e^{-3/2}$	$n_n \sigma_{en} \sqrt{8T^*/\pi m_e}$
i	$4.78 \times 10^{-8} n_e \ln\Lambda T_e^{-3/2}$	$n_n \sigma_{cx} \sqrt{16T^*/\pi m_i}$
n	$(n_i/n_n)\nu_{in}$	$n_n \sigma_{nn} \sqrt{16T/\pi m_i}$

where $T^* = T + (\pi m_i/16)|v_i - v_n|^2$, or $T^* = T + (\pi m_e/8)|v_e - v_n|^2$,
$\ln\Lambda$ = Coulomb logarithm (see Braginskii [13]),
$\sigma_{en} = [2.14 + 47.4/(E_{\rm eV} + 1.3)] \times 10^{-16}$ cm^2, $\sigma_{nn} = 3.52 \times 10^{-16}$ cm^2, $E = 4T^*/\pi$.

nation rates. When `fioniz = 1` and `frecom = 1`, the ionization and recombination rates are those of the corona model (see Book [38]). Increasing these factors simulates trapped radiation effects (see section 1.2.5).

The functional forms for the ionization and recombination rates, as taken from Book, are modified by using an effective electron temperature. This effective temperature includes the drift velocities of electrons (see the second form of T^* in table 4.2). When the drift velocity ($v_e = |J/en_e|$) is large, as it can be when n_e is small, the effective temperature can be much larger than the thermal temperature. This can increase the ionization rate substantially.

The following table lists the changes for the successive versions of COAX used under the UNICOS operating system. The changes made under the CTSS system were listed in chapter 4.1.

4.2 Results of Simulations With Improved COAX Computer Code

4.2.1 Introduction

In this section the results of computer simulations using the improved version of the COAX code are presented. By comparing the simulation data directly to experimental data (averaged over many shots), the validity of the improved code is evident. These direct comparisons of simulations to experiment will be used often in subsequent presentations of results. Cases of similarity and dissimilarity indicate

Table 4.3a: COAX changes: UNICOS operating system

DATE	VERSION	CHANGES
2/92	1.0	Modifications required for change to UNICOS operating system; stop statements replaced by message/stop subroutine
2/92	1.1	Change to data file size
2/92	2.0	Output heat flux vectors to data files; Courant limit on timestep from neutral advection; correction to heat flux
4/92	3.0	Added ionization/recombination rate multipliers; Ohmic heating array is output to data files; density advance algorithm modified
5/92	3.1	Temperature changed from $T_e + T_i$ to $T = T_e = T_i = T_n$; modifications to energy advance; entropy of mixing ions and neutrals added; compressional power from ions+electrons and neutrals; heat conduction collision frequency same as in electrical resistivity
5/92	3.2	Correction to mesh routine due to failure on new machine
5/92	3.3	More corrections
6/92	3.4	Modifications to velocity advance
6/92	3.5	Timestep restricted due to neutral/ion friction
6/92	3.6	Removed friction force from semi-implicit solver; friction solved implicitly in separate step; timestep restriction due to friction removed
6/92	3.7	Changed iteration error limits

Table 4.3b: (continued)

DATE	VERSION	CHANGES
7/92	3.8	Allowance for end mirror coils when flux input is supplied
7/92	3.9	Deleted automatic circuit crowbar
8/92	3.10	Heat conduction includes neutral contribution, electron contribution dependent on collisionality in resistivity calculation
8/92	3.11	Correction to neutral contribution to heat conduction
9/92	3.12	Changed cross section formulas for electron-neutral, ion-neutral, and neutral-neutral collisions, with input parameters to control these effects; collision frequencies used in resistivity, heat conduction, and ion-neutral friction; ionization rates include effective temperature from drift velocities of electrons
9/92	3.13	Corrected error in effective temperature from drift velocities of electrons
11/92	3.14	Boundary condition changed from normal derivative of density = 0 to normal derivative of pressure = 0
12/92	3.15	Boundary conditions changed back to normal derivative of density = 0

respectively, either appropriate or inappropriate physical or numerical modeling.

In the first subsection, the physical models incorporated in the computer code are tested by comparing the simulation results against the experimental data. By doing so, the necessary features of the model are determined. It is assumed that by adjusting the input parameters, better agreement can be achieved. Some phenomena, like ionization, are not sensitive to these parameter variations. The ionization is not dependent on the rates involved, but on the rate of influx of neutrals into regions of ionizing plasma.

In the testing phase of code development, comparison of computer runs with a variation in only one parameter are used to test the sensitivity of the model to these variations. Sometimes, rather than vary an input parameter, a slightly new version of the code is compared with results from the previous version, to determine the effectiveness of such changes to the code.

The second subsection will evaluate simulations of tearing and programmed formation using the validated model. The results of the simulations of tearing formation look quite similar to the experimental data, and show a correlation between the onset of the experimentally observed magnetic activity with the axial contraction observed in the simulations. The energy input through Poynting flux, and its subsequent redistribution into magnetic energy, plasma thermal energy, and losses, are similar in both the calculations from experimental data and simulation data.

The simulations of programmed formation show the large effect that neutrals have on the formation dynamics and energy redistribution. More energy is dissipated by ionization of neutrals and heat conduction to the walls than energy which is distributed as magnetic or plasma energy. As a result, the temperature remains cool, the plasma is very resistive, and the magnetic flux retained in the plasma region is not very high.

4.2.2 Tests of Physical Modeling

In this subsection the results of various simulations are evaluated to test the validity of the physical models used. This is done by testing the effects of varying a single input parameter to the code, such as the initial temperature (`tmp0`), or the particular version of the code. Comparison to the experimental data (when the corresponding experimental shots are well behaved) determines which simulations

are accurate. Deviations of simulations from the experimental data are assumed to indicate failures in the models used. Sometimes these deviations indicate phenomena that COAX is incapable of simulating. For instance, azimuthal asymmetries require a three dimensional model, and COAX is a two dimensional code.

The experimental data used in these comparisons are: the magnetic field at the midplane of both the inner and outer coils ($B_i(t)$ and $B_o(t)$), the flux values at these coils ($\psi_i(t)$ and $\psi_i(t)$), the integrated electron density across the plasma along a cord near the inner coil ($\int n\, d\ell(t)$), and the temperature determined on a single shot basis by Thomson scattering ($T(t)$).

Because shot-to-shot variations and noise are present in the data, the significance of the experimental data is determined by calculating the statistical average and standard deviation from several shots with identical operating conditions. That is, for each time series of data $X_i(t)$ from shot i (where t is actually a discrete time determined by the digitizer sampling rate), the average is $\langle X(t)\rangle = \frac{1}{N}\sum_{i=1}^{N} X_i(t)$, and the standard deviation is $\sigma(t) = \sqrt{\frac{1}{N-1}\sum_{i=1}^{N}[X_i(t) - \langle X(t)\rangle]^2}$. In plots, the experimental data is represented with a short-dashed line for $\langle X(t)\rangle$ and long dashed lines for $\langle X(t)\rangle \pm \sigma(t)$. The temperature data is not averaged, but plotted as "+" signs, one for each T datum taken for each shot.

The ability of the code to calculate the currents and voltages in the coils self-consistently is tested against the actual measured values. It is difficult to get good agreement with experiment due to the existence of external inductances of unknown size, so the experimentally measured flux values at the coils are typically used as input to the code. Comparisons are made of simulations using the circuit solver, simulations using input flux values, and actual experimental data.

Ionization is difficult to model properly, since L_α radiation is trapped in dense neutral regions, but not trapped in regions of low neutral density. Also, the hydrogen ionization is simplified in the modeling to be a single step process, neglecting molecular ionization and dissociation and various excited states of atomic and molecular hydrogen. The ionization enhancement factor (`fioniz`) does not significantly change the results in typical cases. A modification to the ionization rate by using an effective electron temperature incorporating drift velocity of electrons does change the ionization early in the discharge.

In the experiment, a ringing waveform causes preionization before the main

voltage is applied. Simulations of this technique did indeed cause the intended preionization in the simulations. The simulation of ringing preionization also causes heating of the neutral gas, and dynamics before the main part of the discharge.

Other one-parameter variations used in testing COAX sensitivities are the initial starting conditions of: `preion` (preionized fraction) and `tmp0` (temperature). The one-step ionization process modelled in COAX is a simplification, so there are arbitrary multipliers `fioniz` and `frecom` for the ionization and the recombination rates, respectively. Also tested is the use of a multiplier for the cross-section of charge exchange collisions (`faccx`) which affects the friction between ions and neutrals, as well as cross-field heat conduction by ions due to collisions with neutrals.

4.2.2.1 Circuit Solver vs. Input Flux Values

Runs using the circuit solving routine calculate self-consistently the currents and voltages at the coils. The input of appropriate values of external inductances and resistances is necessary to do this accurately, but these values are not accurately known. There is probably some resistance and inductance in the ignitrons used as switches in the experiment, as well as external inductance in the cables connecting the capacitors and the coils.

The inductances of the coils themselves are determined self-consistently in COAX, but are estimated to be 115 nH and 2387 nH by measurement [46]. Simulation run #377 uses values of 72 nH and 14 nH for the inner and outer coil external inductances, respectively. No external resistances are used. This run is a simulation of tearing formation for fill pressure of 15 mTorr and main voltage of 3 kV. Figure 4.1 shows the flux values at the coils from the simulation of run #377 and the corresponding averaged experimental flux data from 17 shots. In the graph, the slope of the coil flux (that is, the loop voltage) from the simulation using the circuit solver is larger than that measured experimentally. To agree with the experimental data, there should be more voltage drop across the external inductances, i.e. the values input to the computer are not large enough. The result of this run is that the circuit solving routine generates voltages at the coils that are too large.

The resulting magnetic fields are also too high as compared to experiment, since the loop voltage is too high. Higher ionization also results from these higher effective voltages. In figure 4.2 the results of runs #377 and #389 are shown compared

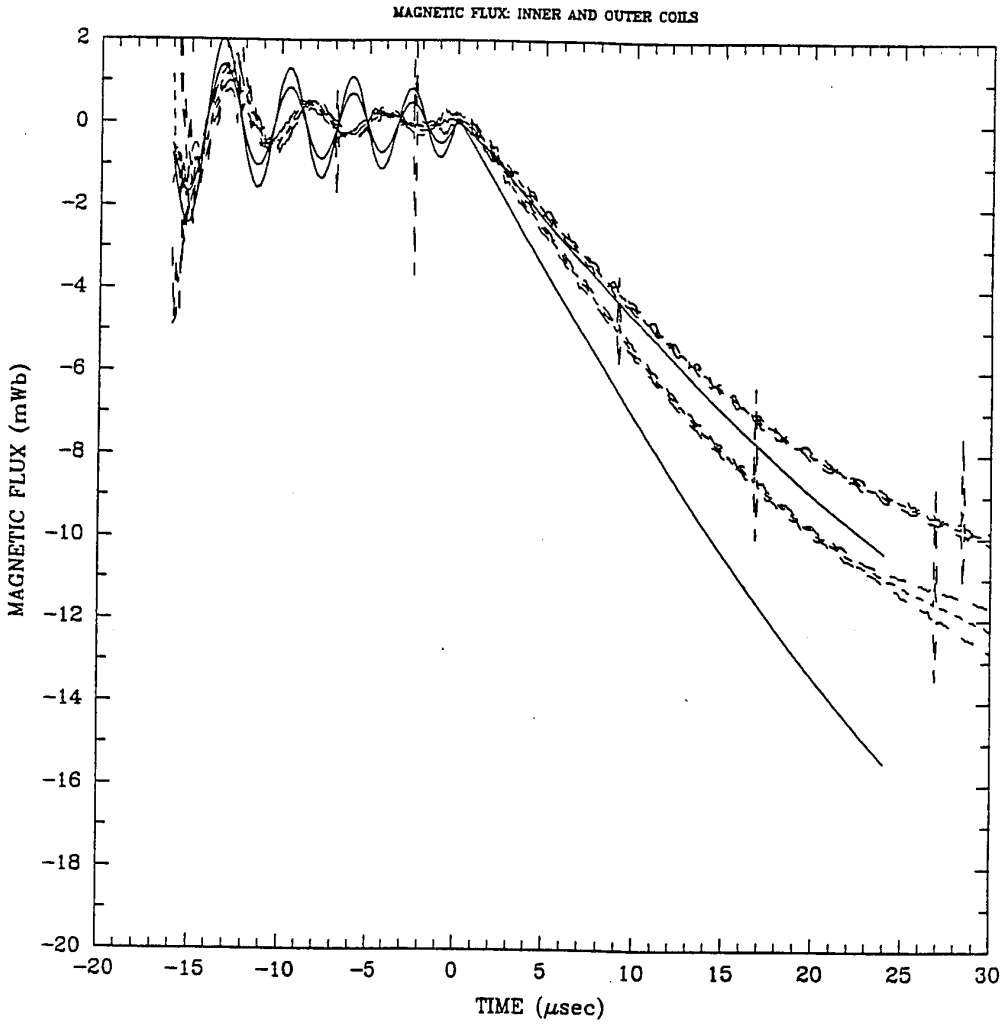

Figure 4.1: Magnetic flux at inner and outer coils. Solid lines represent simulation data from run #377 using circuit solver, dashed lines are experimental data $\langle\psi\rangle$ and $\langle\psi\rangle \pm \sigma$, from 17 experimental shots. The lower set of curves are the outer coil values, and the upper set of curves are the inner coil values.

against the experimental data for the magnetic fields at the midplane of each coil, and the cross tube interferometry measurement ($\int n\, d\ell$) for the two runs is shown in figure 4.3. Both runs are simulations of tearing formation for the fill pressure of 15 mTorr and main voltage of 3 kV, but #377 used the circuit routine for calculating flux values at the coils, and #389 used the experimental flux values at each coil as input directly.

The experimental flux data is equal to the measured loop voltage integrated over time: $\int V\, dt$. The coils have a common electrical connection (except for some inductance in the connecting cables), and so the loop voltages are approximately the same at each coil. The flux values are thus also approximately the same at each coil. This tends to center the plasma radially as flux is injected at the same rate from each coil. The resulting magnetic fields are determined by the flux transferred to the annulus (that trapped between the magnetic null and the coils), the dissipation of the flux due to resistivity, and the dynamics of the plasma. The agreement between the magnetic fields from the simulation and the experimental data is excellent. This agreement is not forced by using the experimental flux data for the simulation.

The point of this test is to show that the voltage applied must be accurate. When the averaged experimental flux values are used, the results compare well with the experimental data. The resulting magnetic fields and cross-tube $\int n\, d\ell$ are sensitive to the voltage applied.

The circuit used in the programmed formation situation is more complicated than the tearing formation case due to the extra capacitor bank used to produce the "notch" in the voltage waveform (refer to figure 1.1). This notch can be seen in figure 4.4, where the steep slope in the flux values starting at 57 μsec is from the 9.5 kV voltage across the notch bank, which is connected to the coils at this time. This circuit is difficult to model, and as seen before in the tearing formation results, the external inductance must be input accurately to get accurate voltages. The slight difference in the inner and outer flux values shown in the figure is the result of external inductances. Without any external inductances the flux values at each coil must be identical due to the parallel electrical connection.

Using the flux values from experimental measurements, the resulting magnetic field at early times (before the notch) was found to be the wrong sign when compared to the measured experimental values. This observation lead to the determination

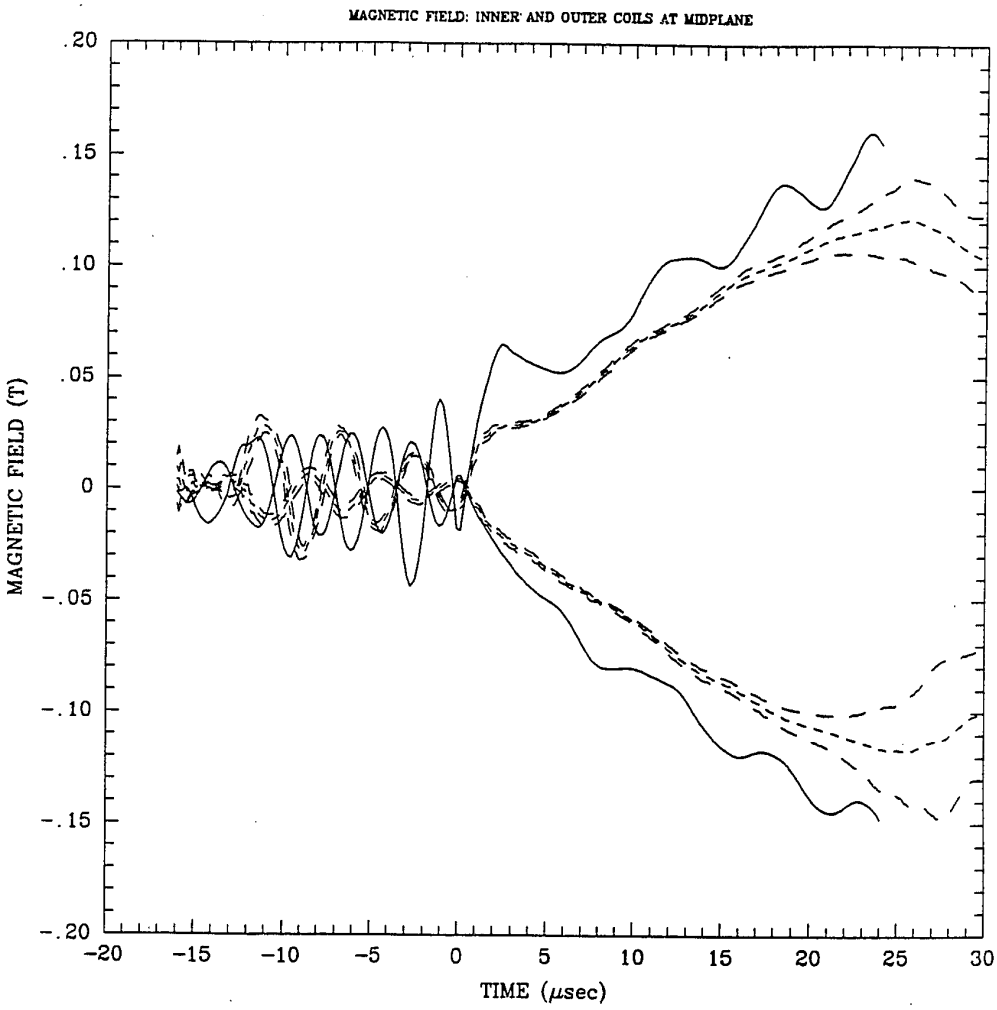

Figure 4.2a: Magnetic fields at inner and outer coils for run #377 (circuit solver used). Solid lines represent simulation data, dashed lines are experimental data $\langle B \rangle$ and $\langle B \rangle \pm \sigma$. The experimental data is from 14 shots. The lower set of curves are the outer coil values, and the upper set of curves are the inner coil values.

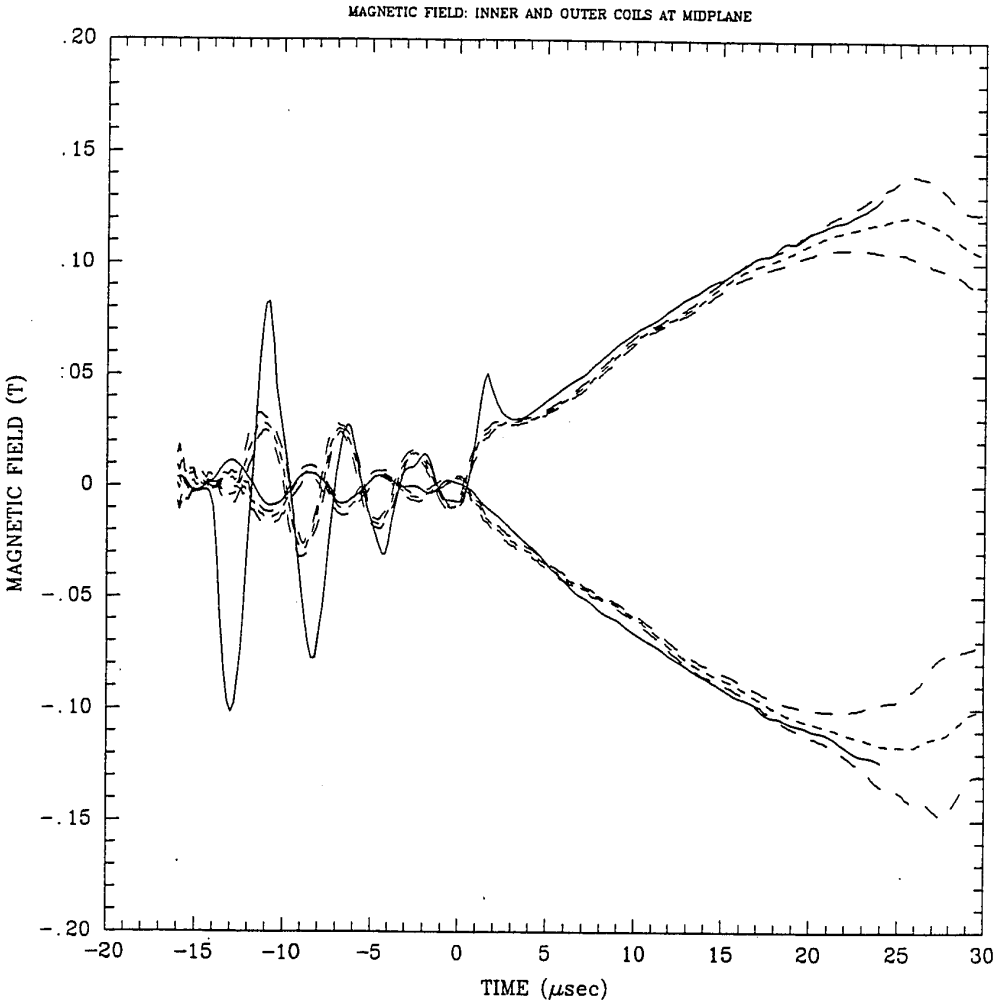

Figure 4.2b: Magnetic fields at inner and outer coils for run #389 (flux from averaged experimental data used). Same experimental data as in (a).

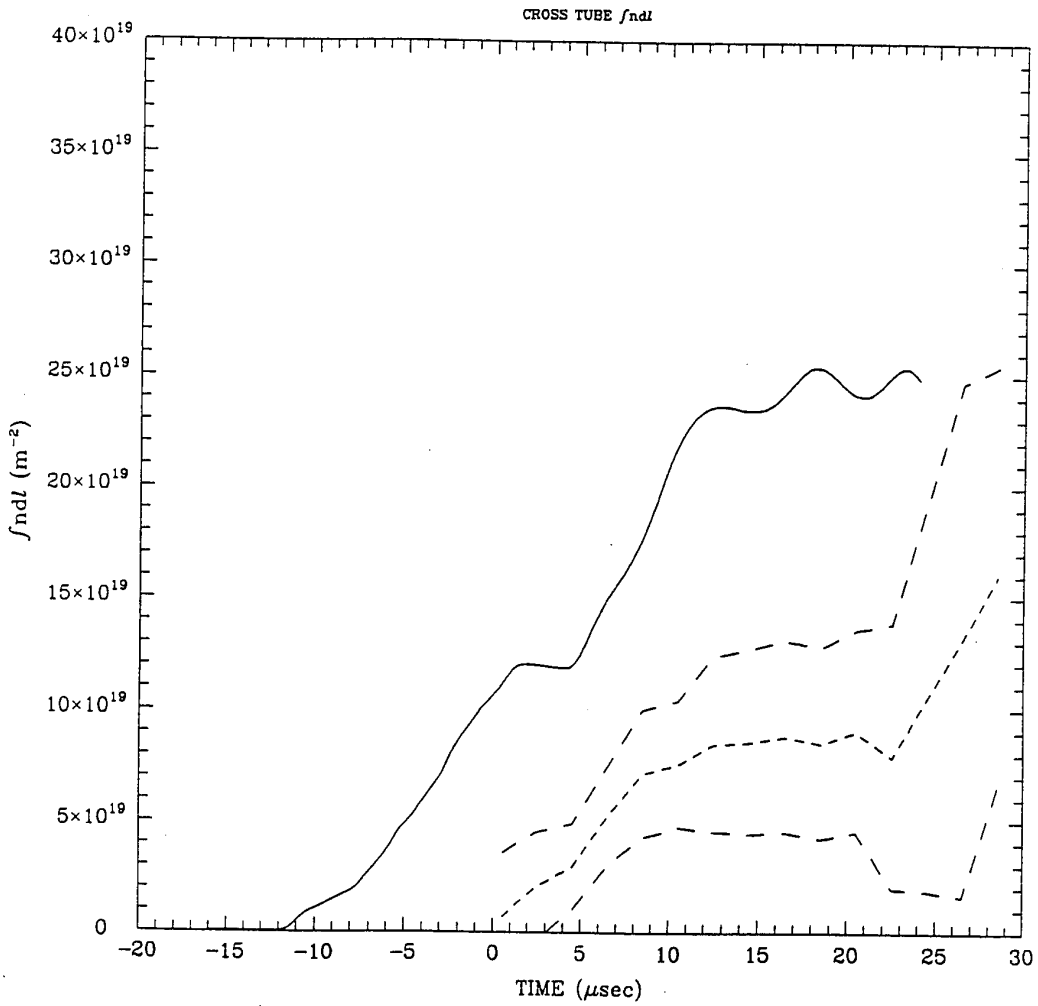

Figure 4.3a: Cross tube interferometer data $\int n\, d\ell$ for run #377 (circuit solver used). Solid lines represent simulation data, dashed lines are experimental data $\langle \int n\, d\ell \rangle$ and $\langle \int n\, d\ell \rangle \pm \sigma$. Experimental data from 14 shots.

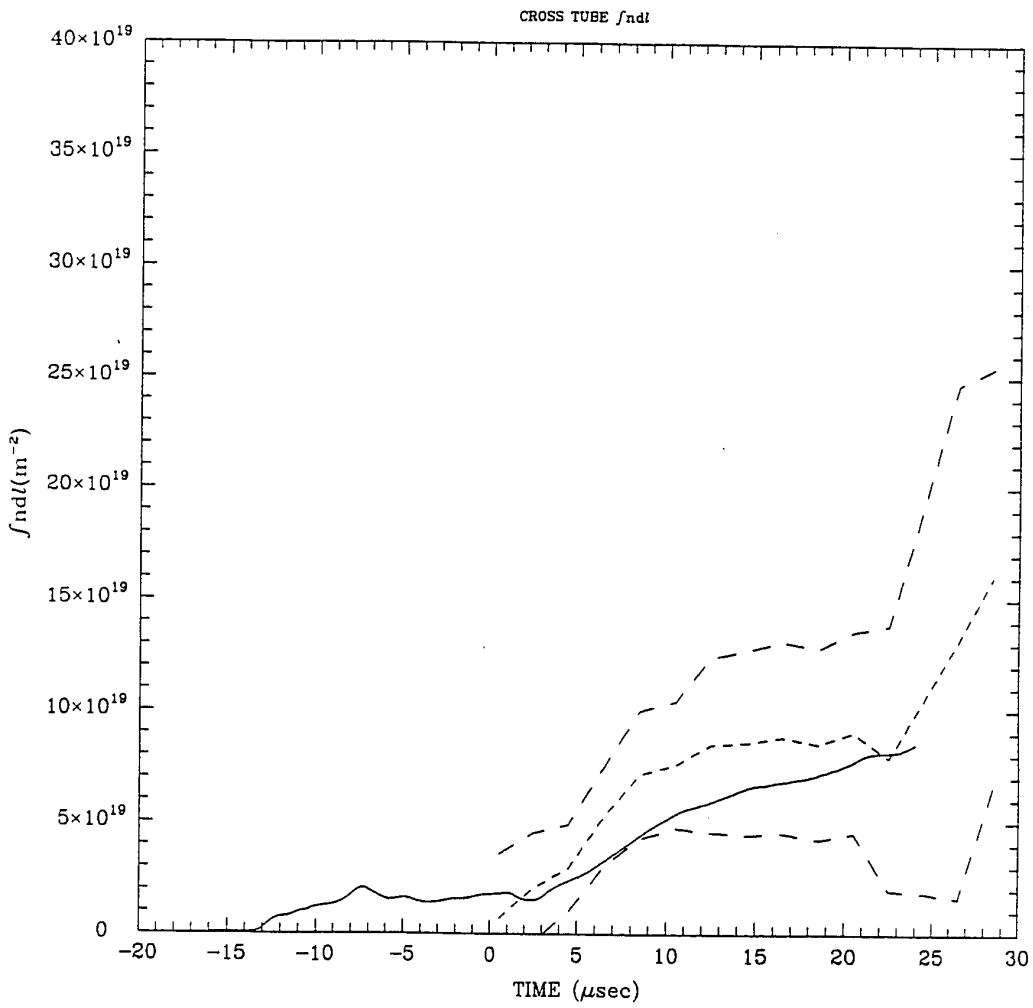

Figure 4.3b: Cross tube interferometer data $\int n\, d\ell$ for run #389 (flux from averaged experimental data used). Same experimental data as in (a).

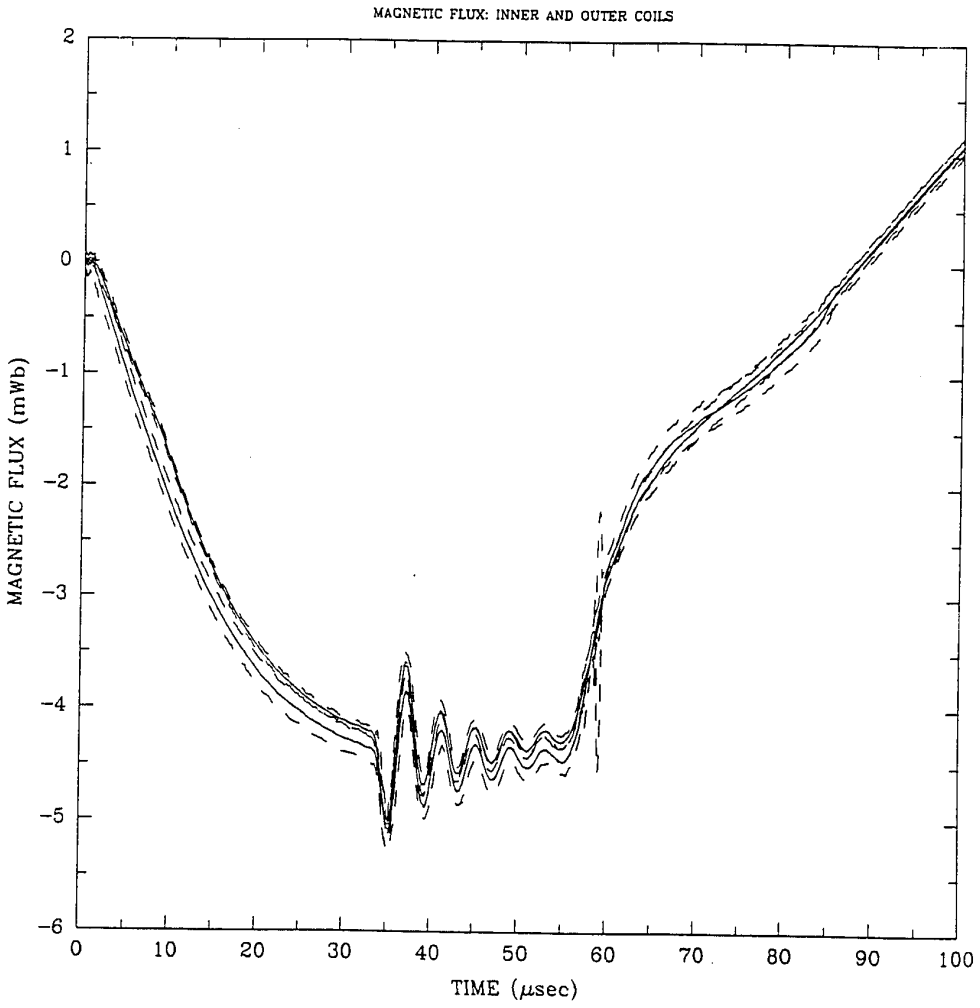

Figure 4.4: Flux at inner and outer coils in programmed formation, run #395. Averaged experimental flux data used in the simulation. Dashed lines indicate statistical variation in the data.

that the magnetic flux data had been mislabeled in the data acquisition system. After correcting this error in the experimental data, the resulting simulations show the same fundamental results.

4.2.2.2 Ionization

Ionization is difficult to model accurately. The reasons for this are many. First, the only ionization reaction considered here is that of a one step ionization of atomic, ground state H to H^+. Molecular reactions and excited atomic reactions are not considered. Even considering just the one step reaction, the rate depends nonlinearly on temperature and possibly on non-Maxwellian electron energy distributions. Thus a marginal condition exists if the plasma is just hot enough to start ionization. Current can start to flow, resulting in Ohmic heating, and the temperature can increase further above the threshold. Once initiated by an increase in temperature, ionization increases exponentially if far from equilibrium. The early ionization stage is difficult to model or simulate due to this nonlinearity. Ionization instability may also exist. Once ionization is well underway, the neutrals diffuse into the ionized region and are in turn ionized, and this is the determining limit on the ionization rate then.

4.2.2.2.1 Ringing Preionization for Tearing Formation In the experiment, the method of generating some initial ionization before applying the main voltage is called ringing preionization. A sinusoidal waveform is applied by letting a relatively small capacitor bank ring after it is switched on. This provides a seed plasma of typically small ionization level.

Simulations generally start with a low level of uniform preionization. By simulating this ringing preionization, a locally preionized plasma forms prior to the main discharge triggering time. Also, the temperature is non-uniform and thus more realistic. Without this ringing preionization, the starting conditions for the main discharge would be unrealistically uniform.

Computer run #394 is a good example of ringing preionization for tearing formation. Starting with uniform temperature (`temp0` = 0.01 eV) and density, with ionization fraction `preion` = 0.001, and fill pressure of 15 mTorr (neutral plus ion density of `en0` = 1.06×10^{15} cm^{-3}), the flux waveform averaged from experimental

shots at 3 kV charging voltage is input (i.e. the same waveform as the experimental data plotted in figure 4.1). The result is that after the preionization phase, the ion density is fairly uniform in the annular region between the coils with about 1-2% ionization fraction. The temperature peaks near the inner coil due to the higher electric field there, with $T = 1.1$ eV at its peak.

Figure 4.5[1] shows the contours of ion density and temperature just before the main voltage is applied (at $t = 0$). Note that if the ringing preionization is not simulated, then a uniform density and temperature would exist at the time $t = 0$. More interestingly, the ringing preionization causes heating in the neutral gas, expansion in the warm regions, and thus lower density in the warm region and higher density at the walls. Figure 4.6 shows the density contours for the neutrals at $t = 0$. The neutral layer along the walls will be shown later to diffuse into the ionized region, and to act as a cross-field heat conduction medium. Also, the lower neutral density in the region where plasma forms results in higher temperatures due to the lowered heat capacity of the gas there.

When simulations are run without the ringing preionization, i.e. starting with 1% uniform ionization at the time of the main discharge ($t = 0$), the results are different than those when simulating the ringing preionization. Table 4.4 shows the parameters used in runs #379 (no ringing preionization) and #389 (ringing preionization simulated). Figure 4.7 shows the temperature at the Thomson scattering location from the simulations compared with the experimentally measured temperature for the cases of ringing preionization (run #389) and no ringing preionization (run #379). In run #379, the neutrals do not form a high density layer along the walls, and the density is not diminished in the middle of the annulus by the preionization heating as it is in run #389. The temperature is thus lower in simulations without ringing preionization due to the higher central density and heat capacity.

Both runs #379 and #389 give reasonable agreement with experiment when comparing the magnetic field at the coils. Figure 4.8 shows experimental data and

[1] Note that in contour plots such as these, the left edge of the figure is the midplane, so that only half of the axial extent is shown due to the narrow aspect ratio of the geometry. The vacuum chamber walls are represented by the pairs of parallel lines adjacent to the plasma region. The coils are the thin rectangular regions outside the vacuum chamber walls.

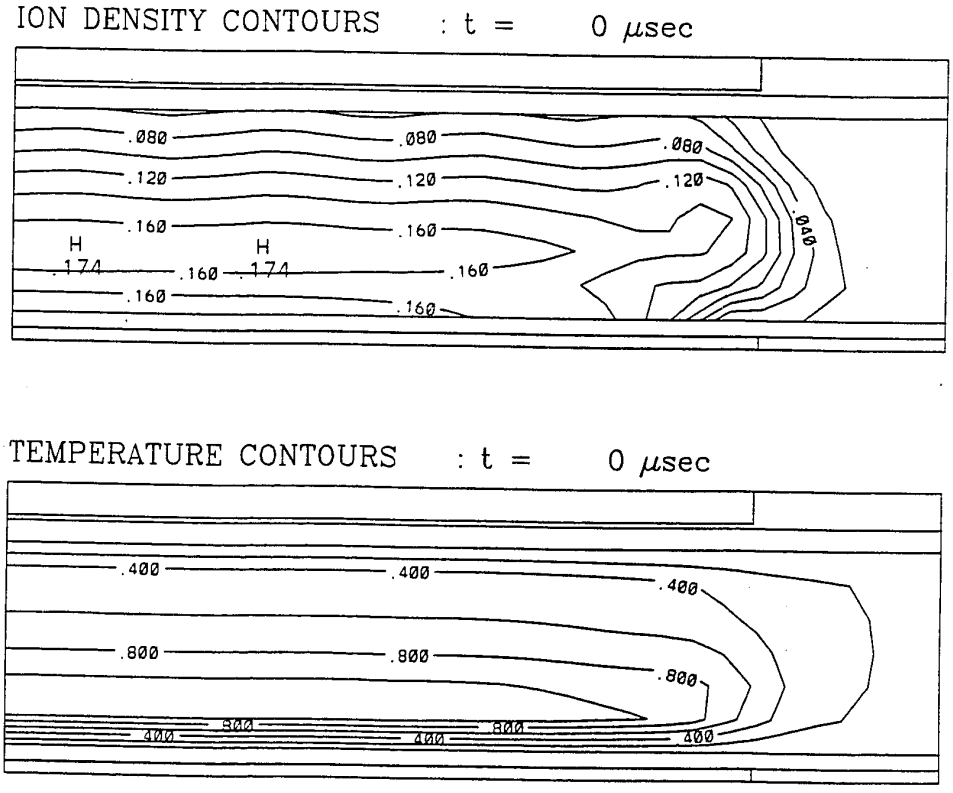

Figure 4.5: Contours of ion density and temperature from run #394 at $t = 0$. The contours are in units of 10^{14} cm^{-3} and eV, with contour increments of 2×10^{12} cm^{-3} and 0.2 eV.

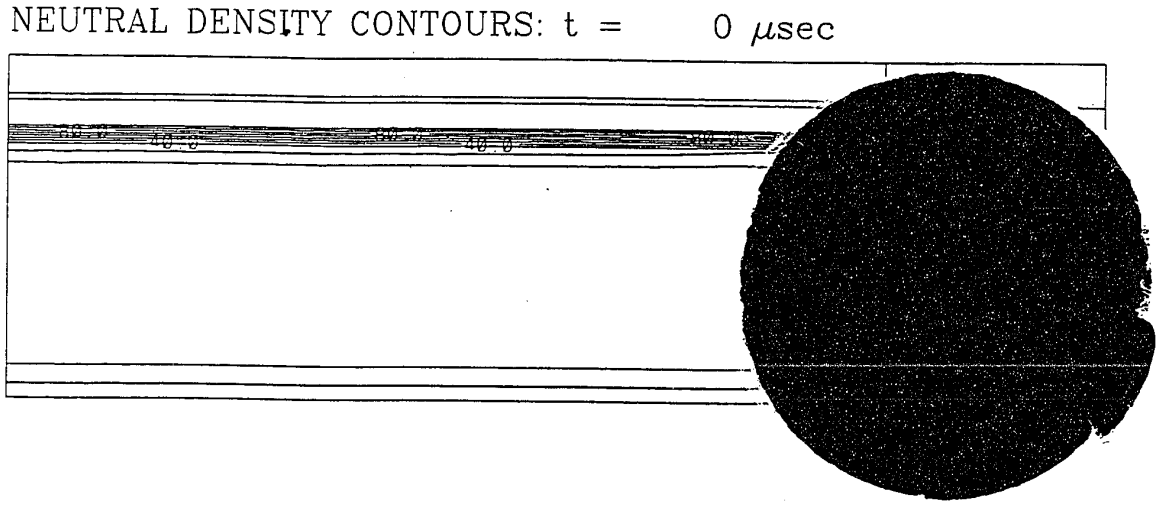

Figure 4.6: Neutral density contours from run #394 at $t = 0$. The contours are in units of 10^{14} cm^{-3}, with increments of 10^{15} cm^{-3}.

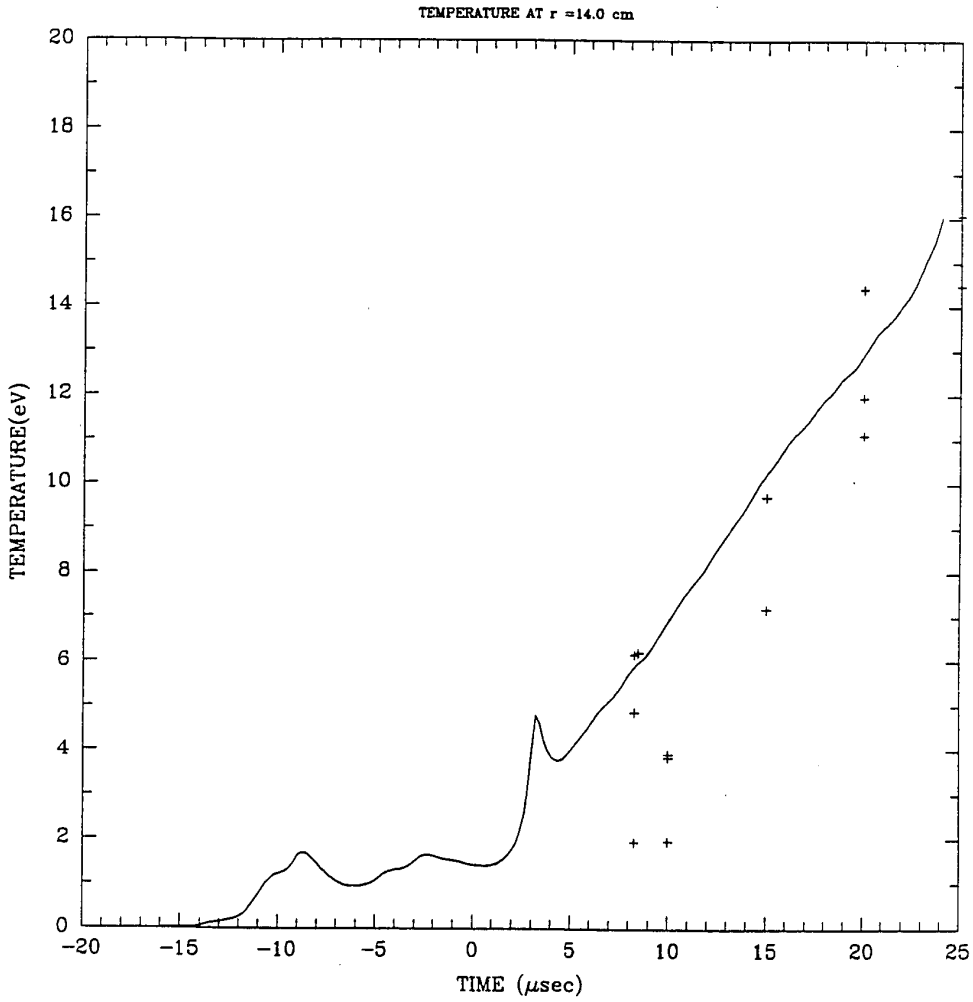

Figure 4.7a: Temperature at $r = 14$ cm from simulation #389 (using ringing preionization) and experimental data.

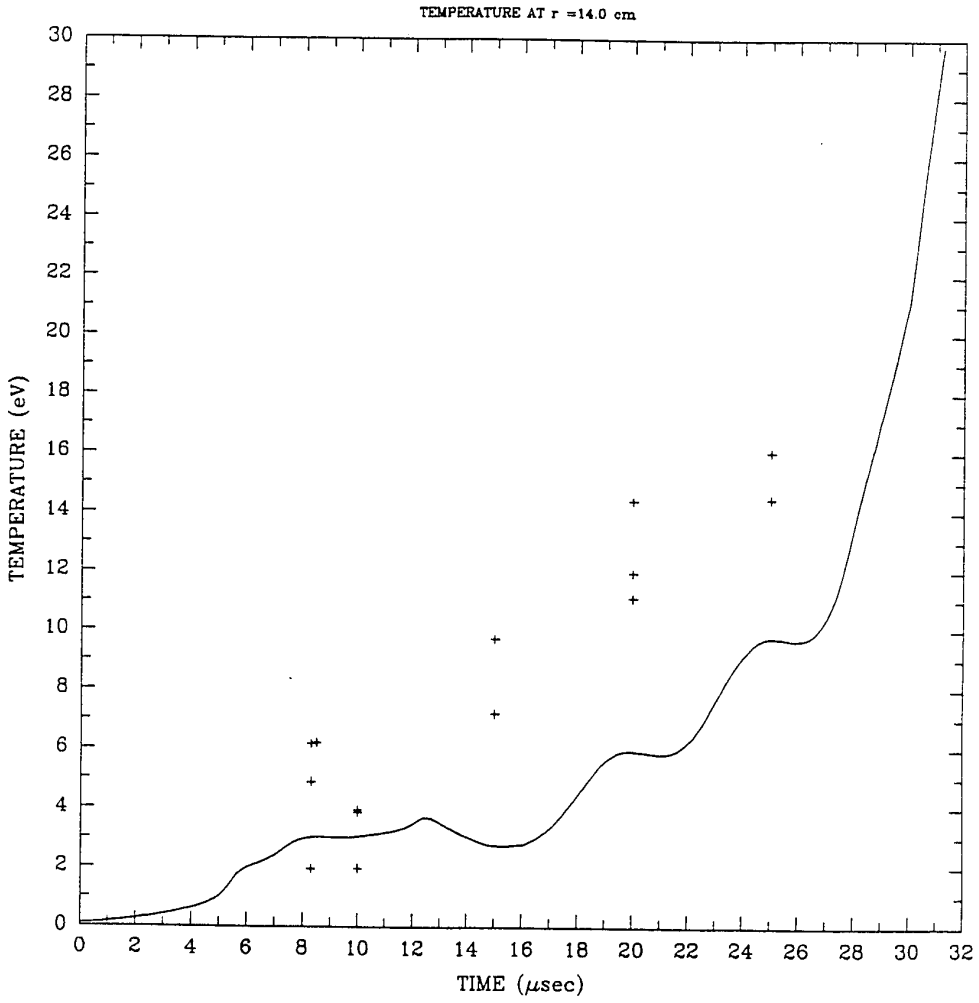

Figure 4.7b: Temperature at $r = 14$ cm from simulation #379 (without ringing preionization) and experimental data.

Table 4.4: Parameters used in runs #379 and #389

parameter	run #379	run #389	units
ringing PI?	no	yes	
`en0`	1.06e15	1.06e15	cm^{-3}
`tmp0`	0.1	0.01	eV
`vct(1,1)`	3.e3		volts
flux input?	no	yes	
`eion`	17	17	eV
`preion`	0.01	0.001	fraction
`anomr`	1.0	1.0	multiplier

simulation results for run #379 (without ringing preionization) and figure 4.2b shows experimental data and simulation results for run #389 (with ringing preionization). There is a transient peak in the B field in run #389. This is because there is warm ($T \approx 1$ eV), conducting plasma near the inner wall after the ringing preionization. The flux addition near the time $t = 0$ causes a transient bunching of field lines. Since the conducting plasma is tied to the field lines (neglecting slippage due to resistive effects), the plasma inertia delays radial movement in reaction to the magnetic pressure of the bunched field lines. In run #379 on the other hand, there is cold and resistive plasma near the inner wall ($T \approx 0.1$ eV at $t = 0$) and field lines can slip through the plasma without much bunching. The experimental data shows a small transient bump in the inner coil magnetic field.

While the magnetic fields from the simulations compares well with the experimental data in either of these cases, it should be remembered that run #379 used the circuit solver routine, while run #389 used the experimental flux data as input. As discussed earlier, the voltage should be less at the coils than at the capacitor bank due to external inductances. Since the external inductance values are not input correctly in run #379, the loop voltage at the coils is higher compared to #389. If this is taken into account, the magnetic field for run #379 should be higher than that

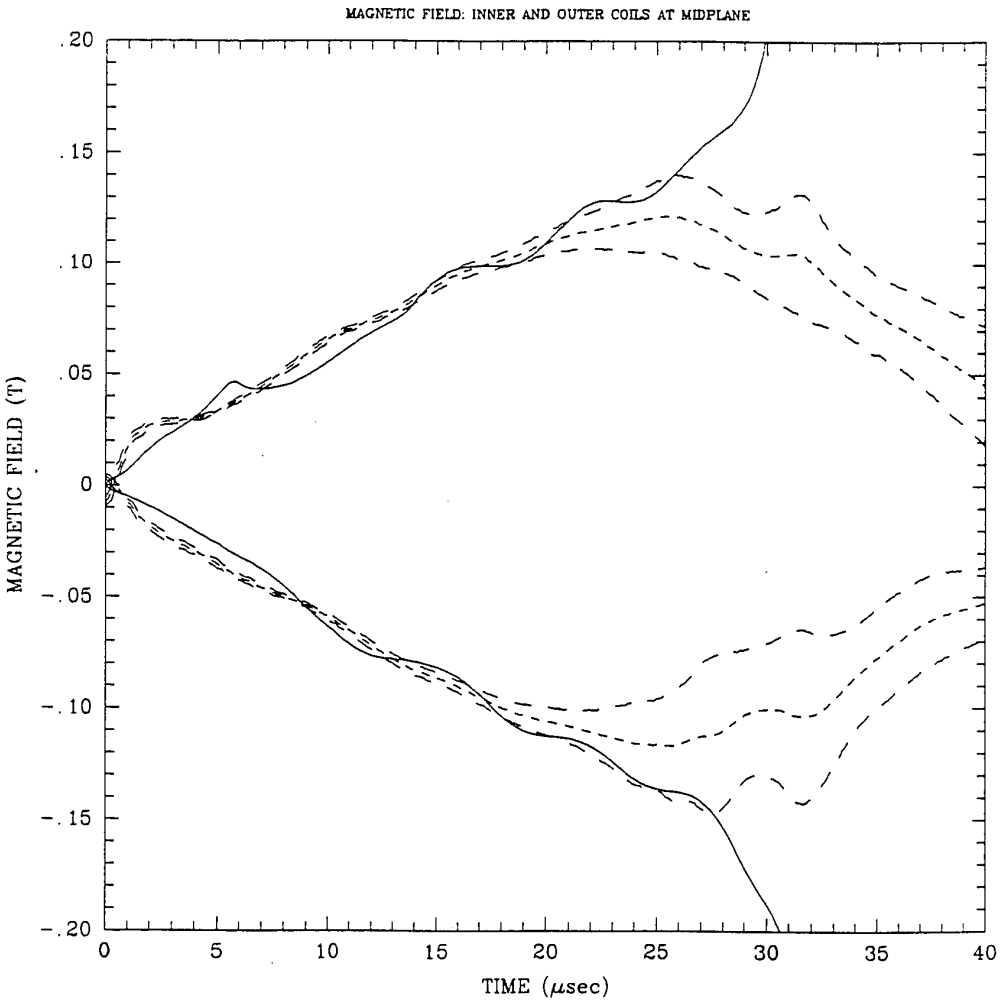

Figure 4.8: Magnetic field for run with no ringing preionization (run #379).

in #389, all else being the same. The conclusion is that the ringing preionization gives reasonable initial plasma conditions for tearing formation.

4.2.2.2.2 Ringing Preionization for Programmed Formation For programmed formation, the ringing preionization is also important. Without the ringing preionization, simulations show that the initial neutral density is higher than with the preionization. The same situation holds as in the tearing formation: the neutral density decreases in the central region as the ringing discharge heats the gas, and the temperature increases. A temperature of at least 0.1 eV is necessary to get field reversal at the start of the main discharge (when the "notch" voltage is applied). The field reversal is needed to center the plasma and induce currents for further heating and ionization.

4.2.2.2.3 Initial Temperature Sensitivity The initial temperature (`tmp0`) is varied to test the sensitivity of this input parameter. In tearing formation runs, the peak temperature quickly reaches about 1 eV during the ringing preionization regardless of whether the value of `tmp0` = 0.1 or 0.01 eV. There is a threshold value for `tmp0` which depends on the voltage of the preionization waveform. When the ionization rate is changed to use an effective temperature that includes a drift velocity, that is, $T_{\text{eff}} = T + \pi m_e |\mathbf{v}_e - \mathbf{v}_n|^2/8$, this threshold is essentially removed. The drift velocity of the initial seed electrons can be large, and thus $T_{\text{eff}} \gg T$ in that situation. The sensitivity of simulations to `tmp0` is not very significant, as similar temperatures and densities result after a few cycles of the ringing preionization whatever the value of `tmp0`.

4.2.2.2.4 Initial Preionization Sensitivity Sensitivity to the initial uniform ionization fraction `preion` is similar to the initial temperature `tmp0`. That is, there is a minimum needed to allow any significant ionization to proceed, but above this threshold, after a few ringing cycles the same final density results.

4.2.2.2.5 Ionization Rate Sensitivity The ionization rate can be much higher in the situation where the L_α radiation is trapped in the plasma. This is discussed in section 1.2.5. In this subsection, the sensitivity to changes in the ionization rate multiplier (`fioniz`) are discussed. The functional form of the ionization rate used

is that for the optically thin case. Although the rate for trapped radiation has a somewhat different functional form, its main difference is the increase in magnitude. To simulate this effect in a simple way, the rate for the optically thin case is increased by the factor `fioniz`. Since the L_α radiation is not seen experimentally, and the estimate in section 1.2 shows that trapped radiation is expected, the ionization rate should be increased due to the trapped radiation effect [29].

Simulations using `fioniz` from 1 to 100 are made. The surprising result of this test is that raising the rate multiplier did not change the final number or density of ionized particles, but merely shifted the timescale for the ramp-up of these quantities at early times. After significant ionization had occurred, the density and its rate of increase are not much affected by the value of `fioniz`.

Figure 4.9 shows several plots of ion and neutral radial density profiles at the midplane. The first plot is at 6 μsec after the main voltage is applied for tearing formation simulation #394. The second and third are at 10 and 14 μsec, respectively. As the configuration forms, the ionized particles are swept towards the magnetic null at $r = 14.5$ cm. Any neutrals dragged along are ionized quickly—the time for this ionization to occur depends on the ionization rate, and hence `fioniz`. By $t = 14$ μsec, the neutrals have almost totally ionized where the neutral density overlaps the ion density. The limiting process to the increase of ion inventory is the rate that the neutrals are accreted into the ionized region, which does not depend on the ionization rate at all. This process is dependent on diffusion of neutrals through the ion fluid, and so is a function of the collision rate between ions and neutrals, and the neutral pressure gradient.

4.2.2.2.6 Summary of Ionization Tests The results of testing COAX for ionization input parameters are that the initial temperature and ion density must be large enough to cause significant ionization to initiate. The thresholds for these values are dependent on the voltage that is applied to the coils. Using a drift velocity dependence in the ionization rate lowered these thresholds. Simulations show that the ringing preionization causes heating of the neutral gas as well as ionization before the main discharge starts. This localized heating causes the decreased density of the neutrals. This helps to raise the plasma temperature when the main discharge commences due to the lower heat capacity of the expanded gas. The conditions un-

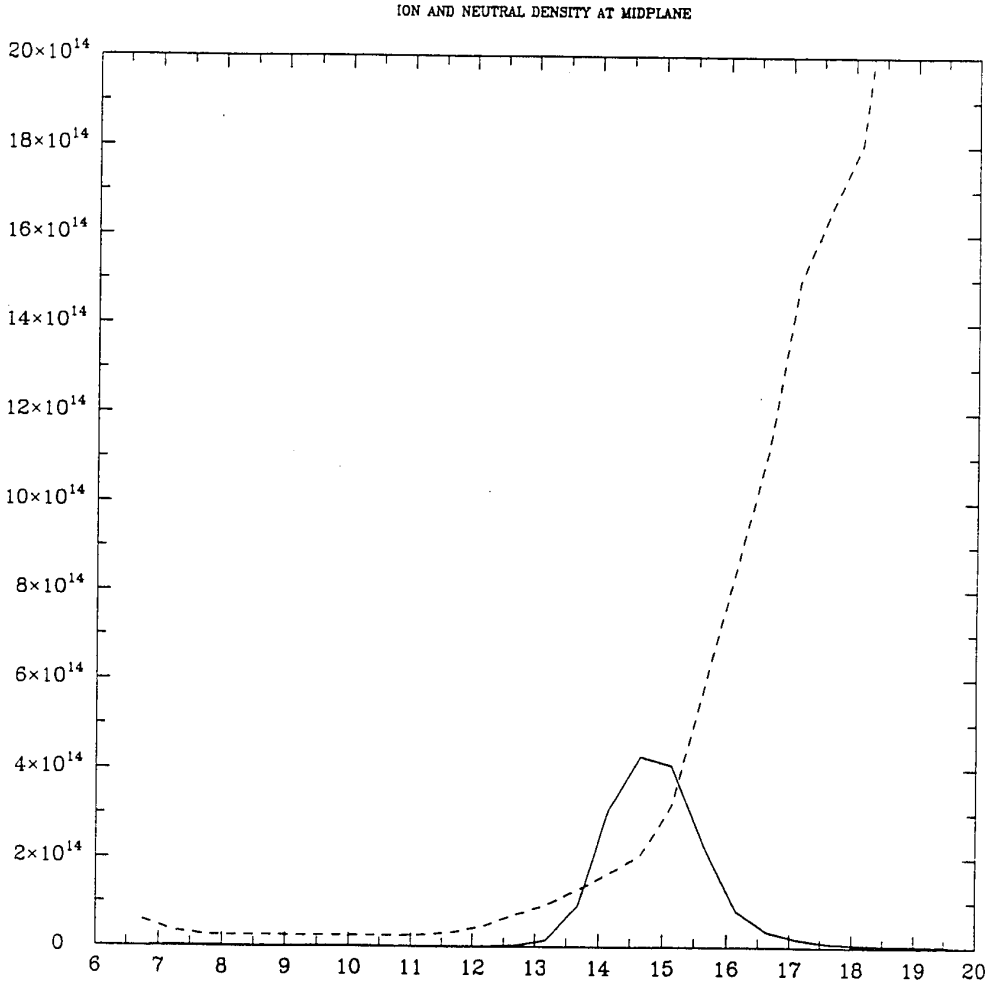

Figure 4.9a: Sequence of ion (solid lines) and neutral (dashed lines) density profiles across the midplane from simulation #394. $t = 6$ μsec.

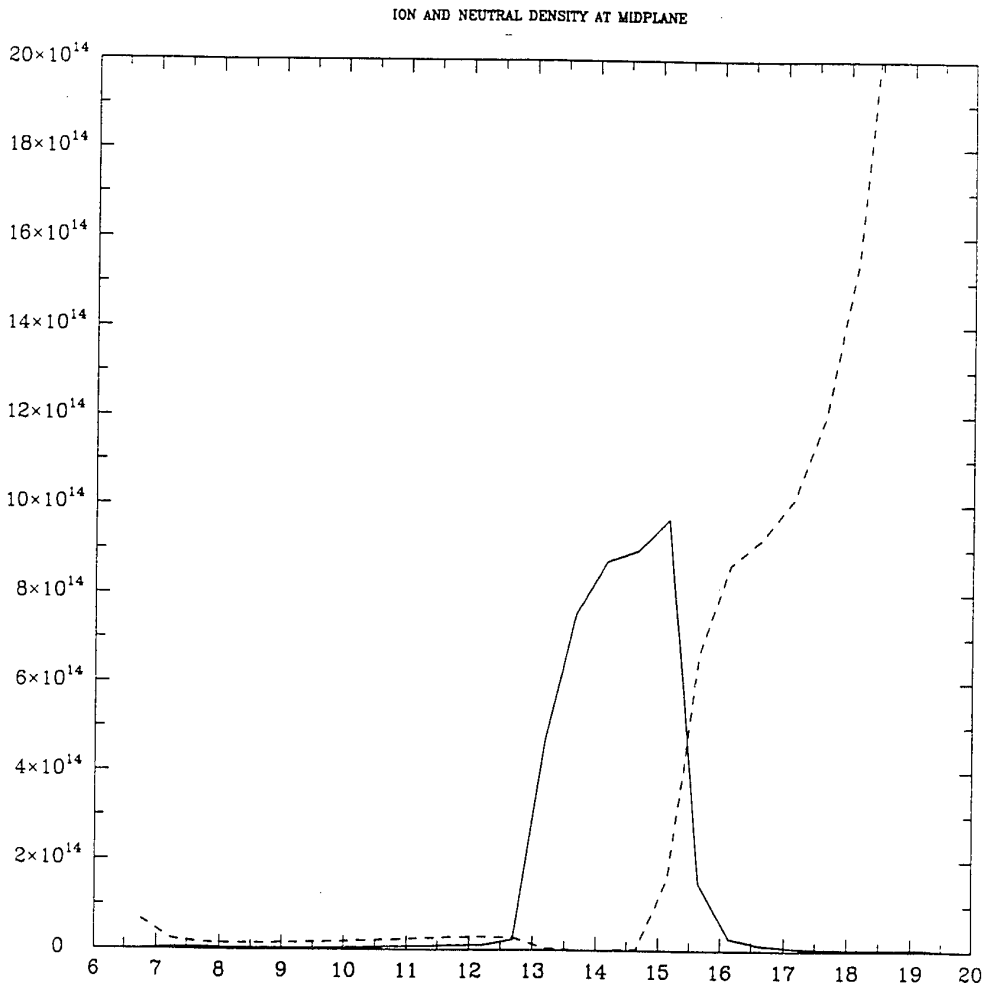

Figure 4.9b: $t = 10$ μsec.

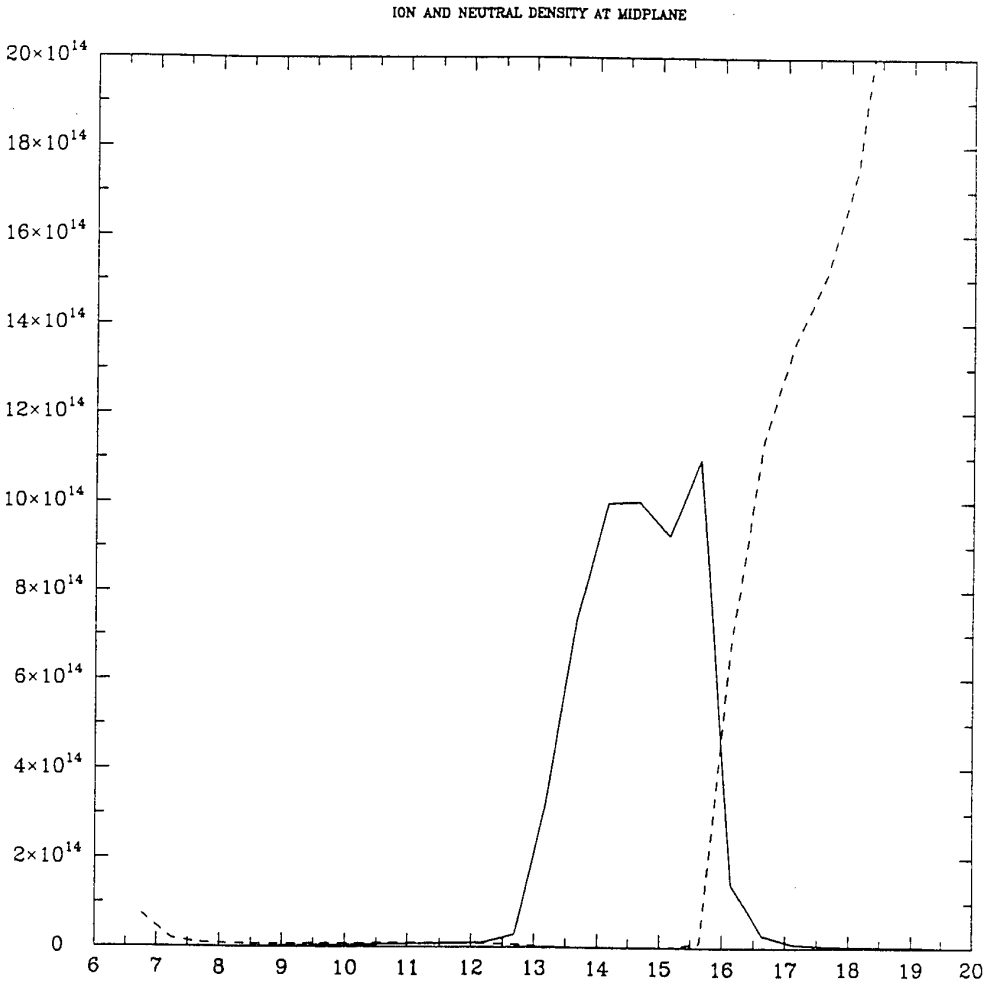

Figure 4.9c: $t = 14$ μsec.

der which the CSS is operated are sometimes marginal, in that without a sufficient ionization level and temperature, there is not enough electrical conductivity to get field reversal. This field reversal is necessary to confine the plasma, induce plasma currents which heat the plasma and neutral gas, which further ionizes the plasma. There is a feedback mechanism at work here, so that ionization does not proceed below a threshold in voltage. This seems to be true in the experiment also.

In the simulations, once the ionization starts in earnest, the increase in ion inventory is not determined by the ionization rate. The increase in ion inventory is determined by the rate of accretion of the neutrals as they diffuse into the ionized region and themselves ionize. The initialization values for temperature and ionization level are not significant, which indicates that the code is robust in these aspects.

4.2.2.3 Collision Model Test

The ion-neutral collision model is tested by varying the multiplier `faccx`. This multiplier adjusts the cross-section for charge exchange. Run #396 is run exactly as #395 (programmed formation, 22 mTorr, 3 kV), but the frictional coupling is lowered by setting `faccx = 1.e-3` from `faccx = 1`. The result is that in #396, ions are pushed through the neutrals by the magnetic pressure of the small bias field before the notch. Since there is little friction with the neutrals, these ions are pushed through the gas and are piled against the outer wall. They stay pushed against the outer wall, even though a reversed field configuration forms. There is very little ionization, as ions are pushed to the outer wall after they are created.

This result is much different from the situation in #395 with `faccx = 1`. It this case, the plasma has more ionization, the fields are higher and in closer agreement with experiment. Obviously, the lack of friction in run #396 prevented the simulation from forming a confined plasma.

4.2.2.4 Trapped vs. Untrapped L_α Radiation

From section 1.2, the theoretical estimate of the absorption length of L_α radiation is about 2 cm. Since the L_α radiation is not seen experimentally, it must be trapped in the neutral gas. To test this, a simulation of programmed formation is made with the plasma optically thin to L_α radiation (run #266). The input parameter `eexcite`

was set to 10.2 eV in run #266, that is, each time an H(1) atom is excited to the H(2) state, it emits a photon of 10.2 eV which escapes. The result is very similar to radiative collapse from impurity radiation. The radiation power losses from neutrals balances the Ohmic heating, the temperature remains cold, and the plasma contracts axially into a ring-like structure of high density and low temperature.

4.2.2.5 Summary of Tests of Physical Modeling

- Need to supply the flux data for the code runs to accurately simulate the experimental coil voltages. This is due to:
  - External inductances.
  - Difficulty with notch circuit modeling.
- Ionization is limited by neutral diffusion into ionized plasma.
- Ionization rates are not that important.
- Initial temperature and ion density must be above a threshold that is voltage dependent. Above the threshold value, there is little sensitivity to these parameters.
  - Must have a high enough temperature to allow initial electrical conduction; ohmic heating will increase it further.
  - Power lost in ionizing must be overcome by this early Ohmic heating.
  - An effective temperature in the ionization rate reduces this threshold (early time drift velocity can be high).
- Ringing preionization gives reasonable starting conditions for density and temperature compared to uniform preionization.
- Neutrals are pushed to walls and out ends. This lowers the gas density and heat capacity in the central region, and accelerates the temperature rise from Ohmic heating.
- The neutral-ion and neutral-neutral collision model is reasonable:

  - Allows ions to be pushed up against neutrals without flowing through (to wall).
  - Gives reasonable heat flux through neutrals.

- L_α radiation is trapped by neutrals at walls and around plasma. This radiation is not observed at magnitudes to indicate that it is untrapped in the experiment either.

4.2.3 Examination of Simulations with Validated Model

This subsection describes the results of using the COAX code with the set of various input parameters and physical models that are tested and shown to best replicate the experimental data. The simulations used here are thus expected to be representative of the physical reality of the CSS experiment. Observations using the detailed information obtained by these simulations give insight into the phenomena observed as well as phenomena otherwise hidden from the experimentalists.

4.2.3.1 Tearing Formation

In this subsection, the data from two computer runs are compared to the data from experimental shots of the same operating conditions to show their agreement. Runs #393 and #394 used the same input parameters but different supplied flux (voltage) data. This data represents the averaged flux data from experimental shots at 5 kV and 3 kV respectively, all at 15 mTorr fill pressure of D_2. The 3 kV data is averaged from 17 experimental shots, and the 5 kV data is averaged from 36 experimental shots. The simulation input parameters for these runs are listed in table 4.5.

Figures 4.10, 4.11, 4.12, show the simulation results with the experimental data overplotted. There is very good agreement between the simulation and experiment, particularly the magnetic field data. It should be noted that the deviation between the experimental and simulation magnetic field data occurs when magnetic activity appears. This is indicated in the figure by the increase in the statistical deviation in the experimental data denoted by the long-dashed lines. After the time when this magnetic activity starts, azimuthal magnetic field fluctuations are detected experimentally—an indication of three dimensional physical phenomena. The COAX code is only two dimensional, so it cannot simulate this activity accurately.

Table 4.5: Parameters used in runs #393 and #394

parameter	run #393	run #394	units
ringing PI?	yes	yes	
flux input?	yes	yes	
exp. voltage	5	3	kV
`en0`	1.06e15	1.06e15	cm^{-3}
`tmp0`	0.01	0.01	eV
`eion`	17	17	eV
`preion`	1.e-6	1.e-6	fraction
`eexcite`	0	0	eV
`fioniz`	10	10	multiplier
`faccx`	1	1	multiplier
`facimp(3)`	0.002	0.002	O fraction
`anomr`	1.0	1.0	fraction

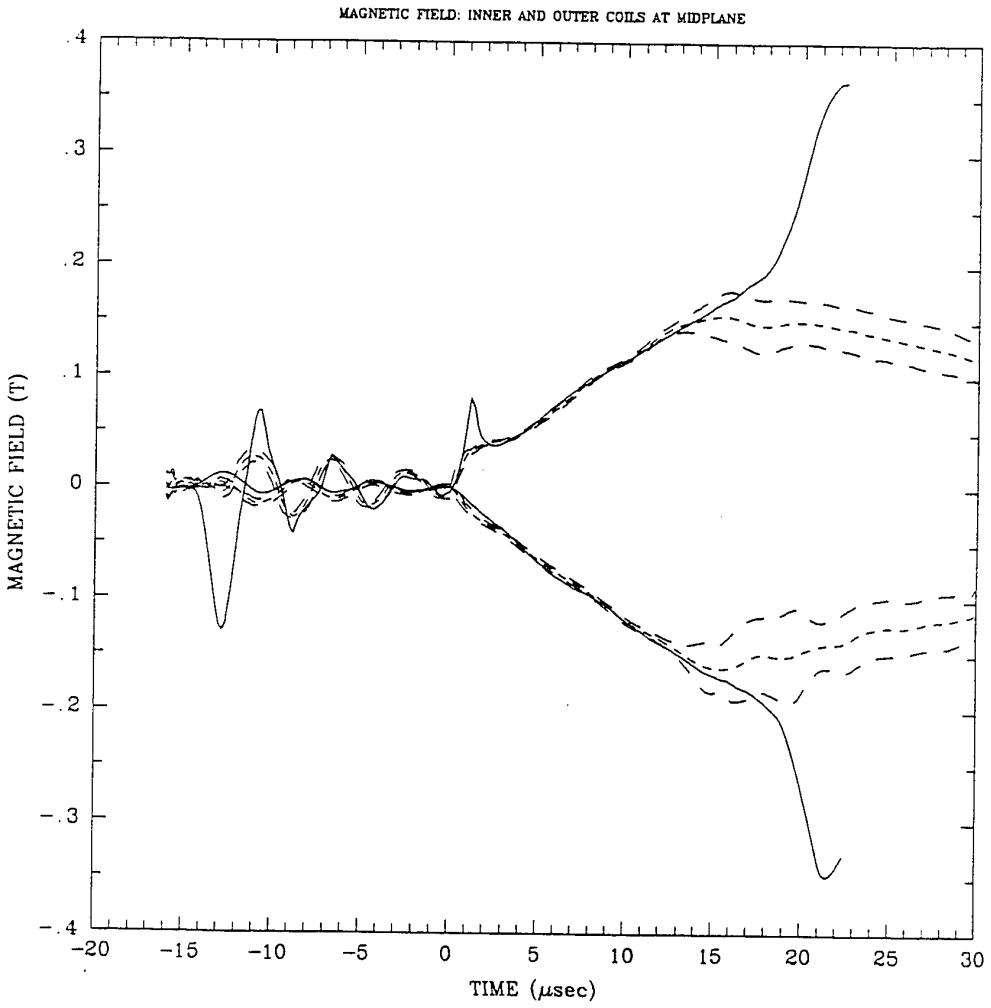

Figure 4.10a: Magnetic field data from simulations and averaged experimental data. Run #393 (5 kV).

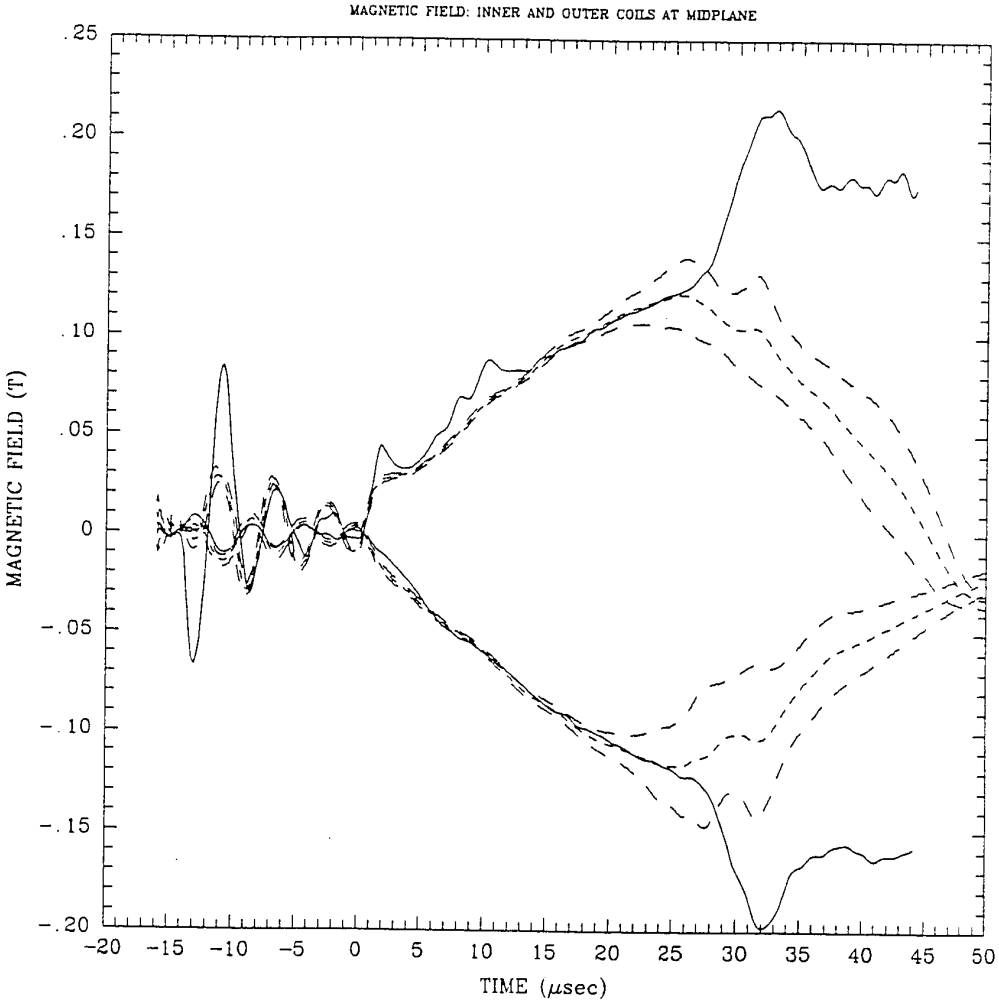

Figure 4.10b: Run #394 (3 kV).

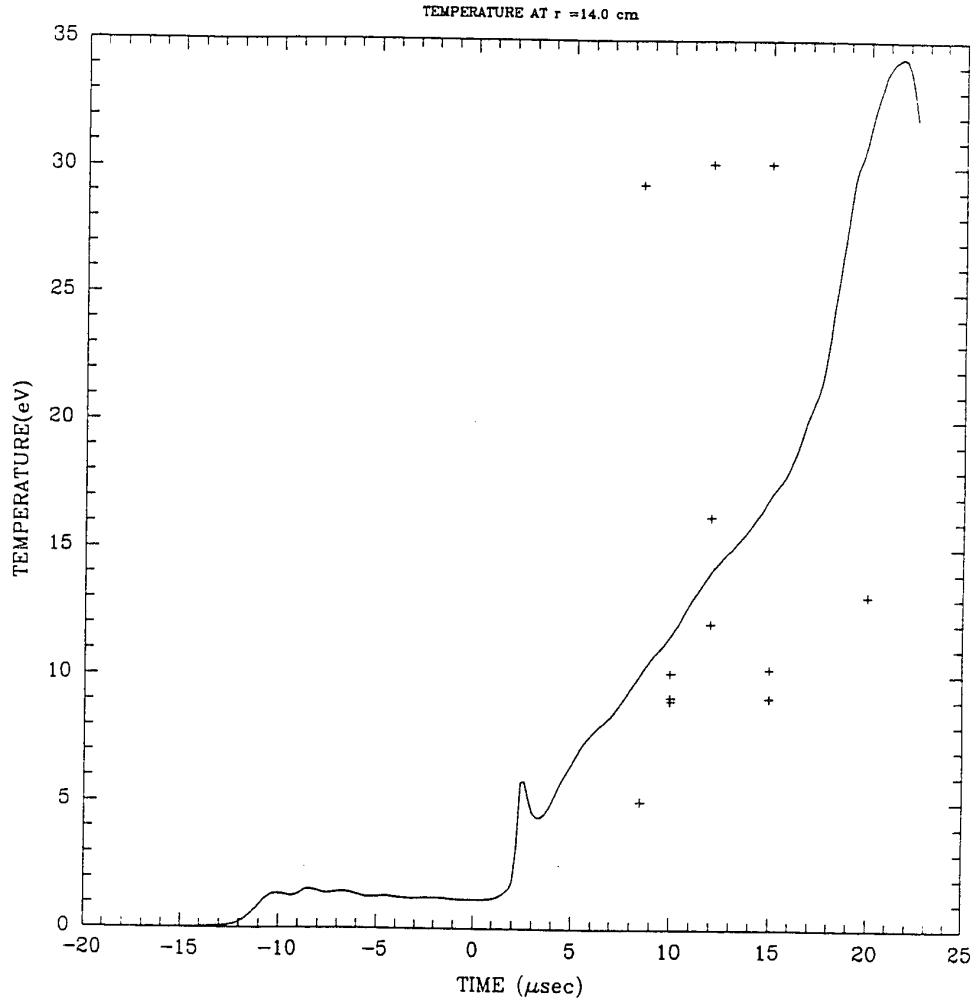

Figure 4.11a: Temperature data from simulations and experimental data. Run #393 (5 kV).

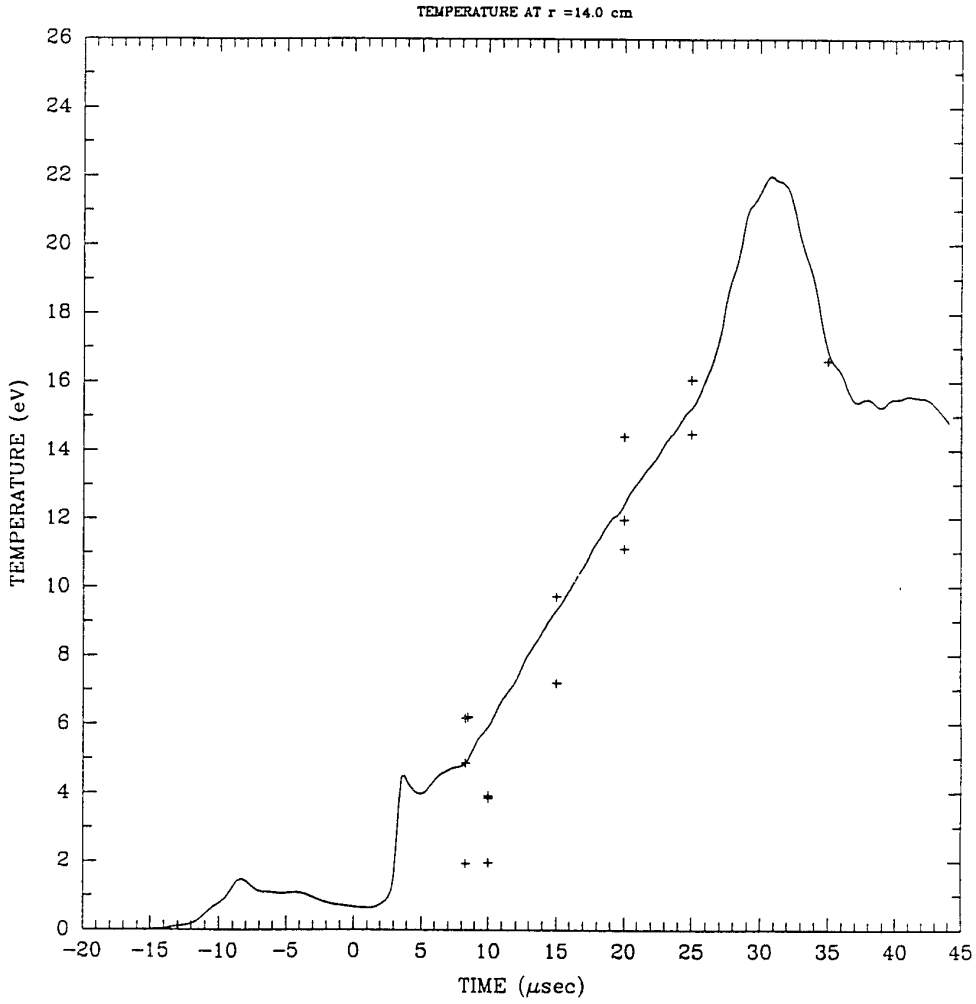

Figure 4.11b: Run #394 (3 kV).

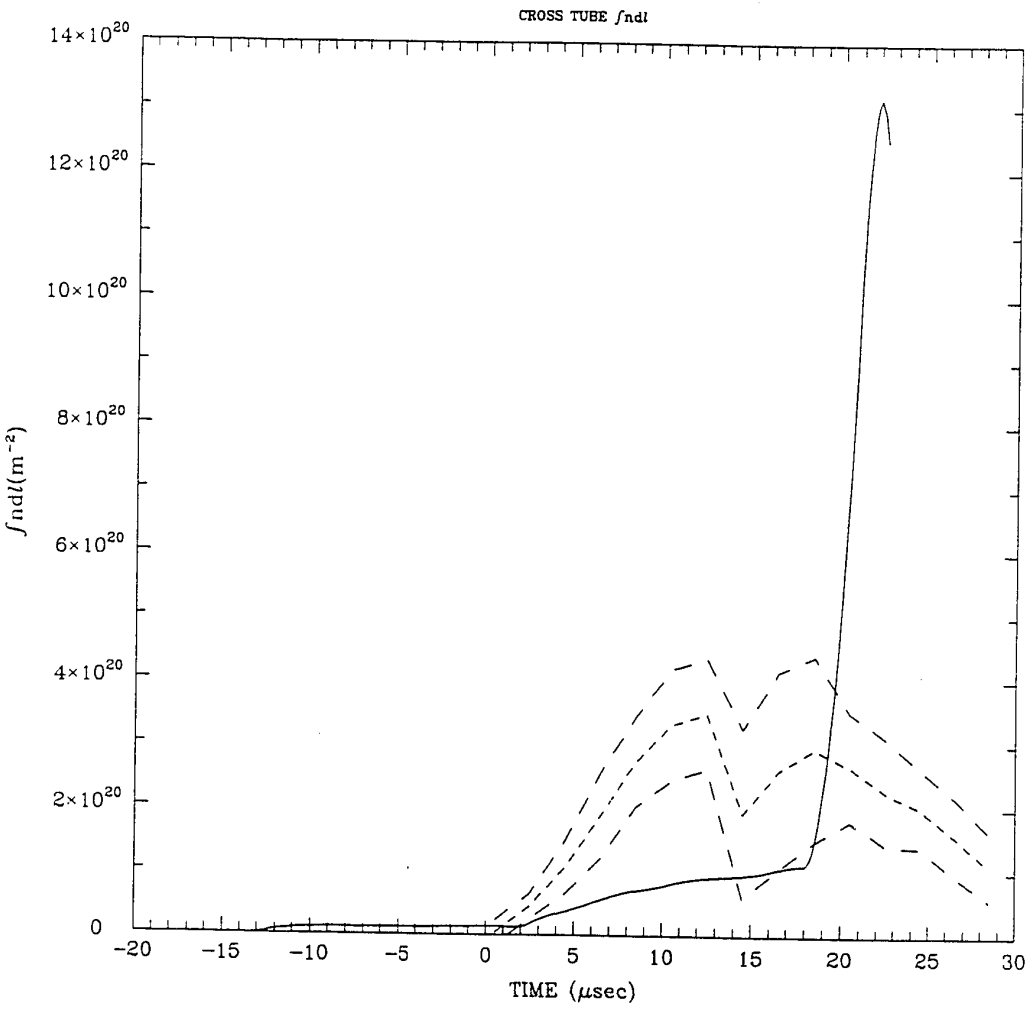

Figure 4.12a: Calculated interferometer data from simulations and actual experimental data. Run #393 (5 kV).

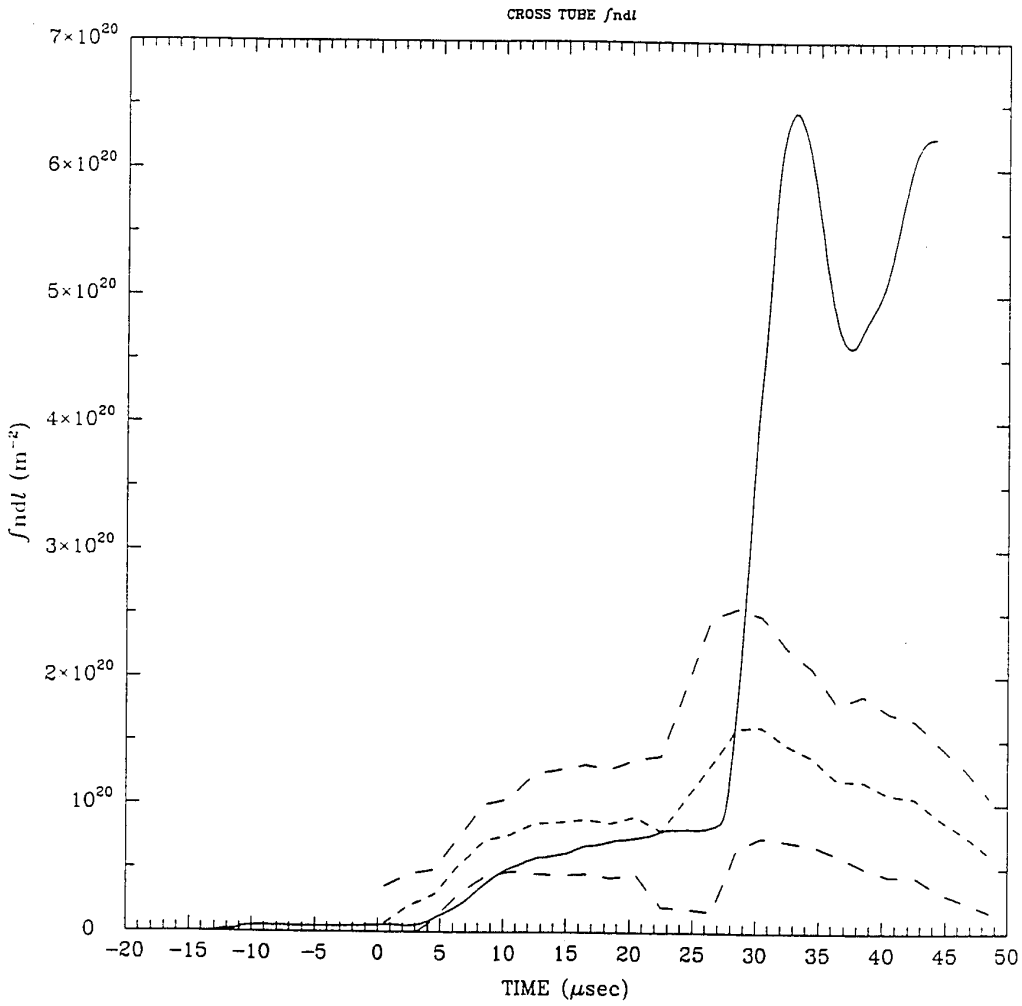

Figure 4.12b: Run #394 (3 kV).

The simulations show an axial contraction that coincides with the magnetic activity. The peaks in magnetic field, $\int n\, d\ell$, and temperature are the result of this axial contraction in the simulations. This contraction is indicated in figure 4.13, where the effective length defined by $L_{\rm eff} = \int B_z^2(z)\, dz / B_z^2(0)$ is plotted as a function of time.[2] This effective length can be shown to be equal to the full width at half maximum (FWHM) for magnetic field axial profiles of functional form $B_z^2(z) = B_z^2(0)(1 - |z|/z_{max})$. For functional forms $B_z^2(z) = B_z^2(0)(1 - |z|^n/z_{max}^n)$, $L_{\rm eff}$ ≈FWHM to within 6% for $0.8 < n < \infty$. Thus $L_{\rm eff}$ can be considered the FWHM in general.

In the simulations, because they are only two dimensional, the axial contractions are azimuthally symmetric. They are also symmetric axially because there are no symmetry breaking effects like nonuniform preionization or stray magnetic fields from coil asymmetries. The experimental data suggests that azimuthally and axially asymmetric tearing may be occurring. Azimuthal field fluctuations are observed as well as sometimes doubly peaked $B_z(z)$ profiles (as reflected in the dips in the $\int n\, d\ell$ experimental data at the time of the start of the magnetic activity). A three dimensional model would be required to simulate such effects.

The axial contractions in the simulations are consistent temporally with the time of magnetic activity observed in the experiment. Note that the start of axial contraction as determined by the knee in the $L_{\rm eff}(t)$ curves is approximately the same time as the peak in the experimental magnetic fields. This time is 22 μsec for the 3 kV run, and 15 μsec for the 5 kV run.

The resistivity model used in this and all simulations presented in this subsection uses only the classical electrical resistivity, with no anomalous effects (except the collisions of electrons with neutrals, which is a small effect). While the temperature is cool in these simulations ($T_e = T_i = T_n \approx$ 1–20 eV) relative to other FRC or fusion experiments (i.e. hundreds of eV, or even tens of keV), the electrical resistivity is low enough in these tearing formation runs to give a flux decay time that is relatively long. In subsection 2.1 of chapter 2, the normalized plasma resistance is defined as $\omega\tau_\phi$, where τ_ϕ is the flux decay time defined by the driven/dissipative linear differential equation $\dot{\Phi}_{tr} - \dot{\Phi}_i = -\Phi_{tr}/\tau_\phi$. The frequency of the approximately sinusoidal applied flux waveform is $\omega = 1.6 \times 10^5$ sec^{-1}.

---

[2] The dips in $L_{\rm eff}$ at times $t < 0$ are due to the oscillating field during the ringing preionization.

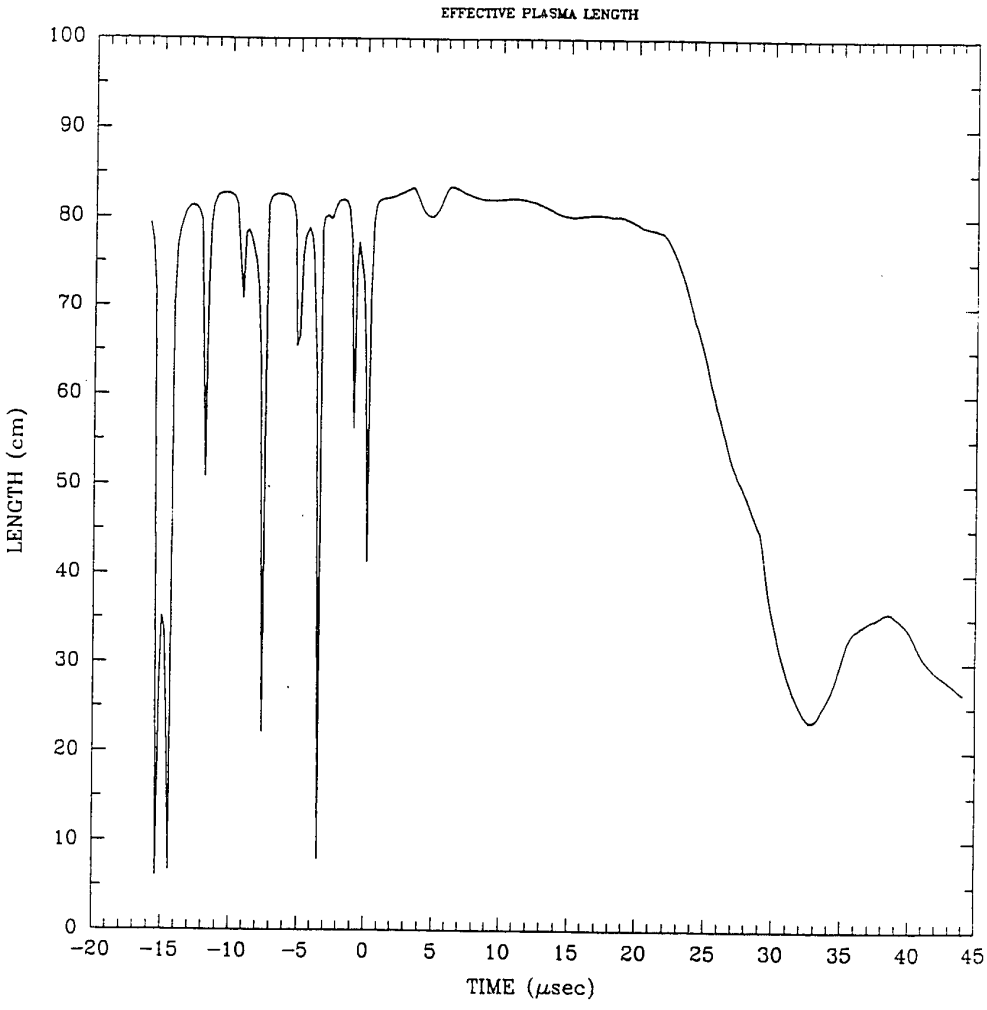

Figure 4.13: Effective length for run #394.

The flux decay time for run #394 is plotted in figure 4.14. The product $\omega\tau_\phi$ is about 10 at $t = 22$ μsec (start of the axial contraction) and as discussed in subsection 2.1, the circuit modeling predicts 100% retention of transferred flux for $\omega\tau_\phi \gg 1$. The equivalent magnetic field produced by 100% flux linkage is defined by $B_{eq}(t) = \Phi_i(t)/[\pi(r_o^2 - r_i^2)/2]$, that is, the magnetic field that results when all the flux lines within the inner coil return through the annulus between the plasma and the coil. This calculation ignores the finite thickness of the plasma. Figure 4.15 shows the efficiency of the flux transfer by comparing the actual field from run #394 and this equivalent magnetic field (B_{eq}). Flux annihilation at the magnetic null decreases the actual field in comparison to B_{eq}. The finite width of the plasma tends to increase the magnetic field strength by excluding flux from the plasma cross-sectional area. After the axial contraction, the plasma bulges radially and causes a large excluded flux and increase of actual magnetic field beyond that of the 100% flux transfer effective field. Before the contraction, the plasma area is only about 25% of the full annular area, so excluded flux effects are small.

The flux decay time is even longer for run #393, which is the simulation of a shot at 5 kV, instead of 3 kV. The larger voltage applied resulted in a larger magnetic field and temperature also. The higher voltage caused more energy to be input, and thus more plasma heating. The plasma resistance is thus less, and the magnetic field tracks the equivalent magnetic field produced by 100% flux linkage until the time of axial contraction. Again, the contraction causes radial plasma expansion and corresponding flux exclusion and a peaking of magnetic field at the coils.

The energy that heats the plasma comes primarily from Ohmic heating, i.e. flux dissipation, which ironically, is necessary to produce a hot enough plasma to allow significant conductivity, and thus flux transfer without too much dissipation. As discussed in section 2.1 on circuit modeling, the optimum energy transfer is achieved when $\omega\tau_\phi = 1$, the situation when there is a balance between energy flowing into Ohmic heating and magnetic energy increase.

There are of course other energy dissipation mechanisms besides Ohmic heating, such as ionization losses and heat conduction. Also the simple circuit model does not include the thermal and kinetic energy in the plasma.

To make an energy accounting from the experimental data, R. Maqueda of the CSS group calculated an energy balance for the conditions of run #394 [4]. The

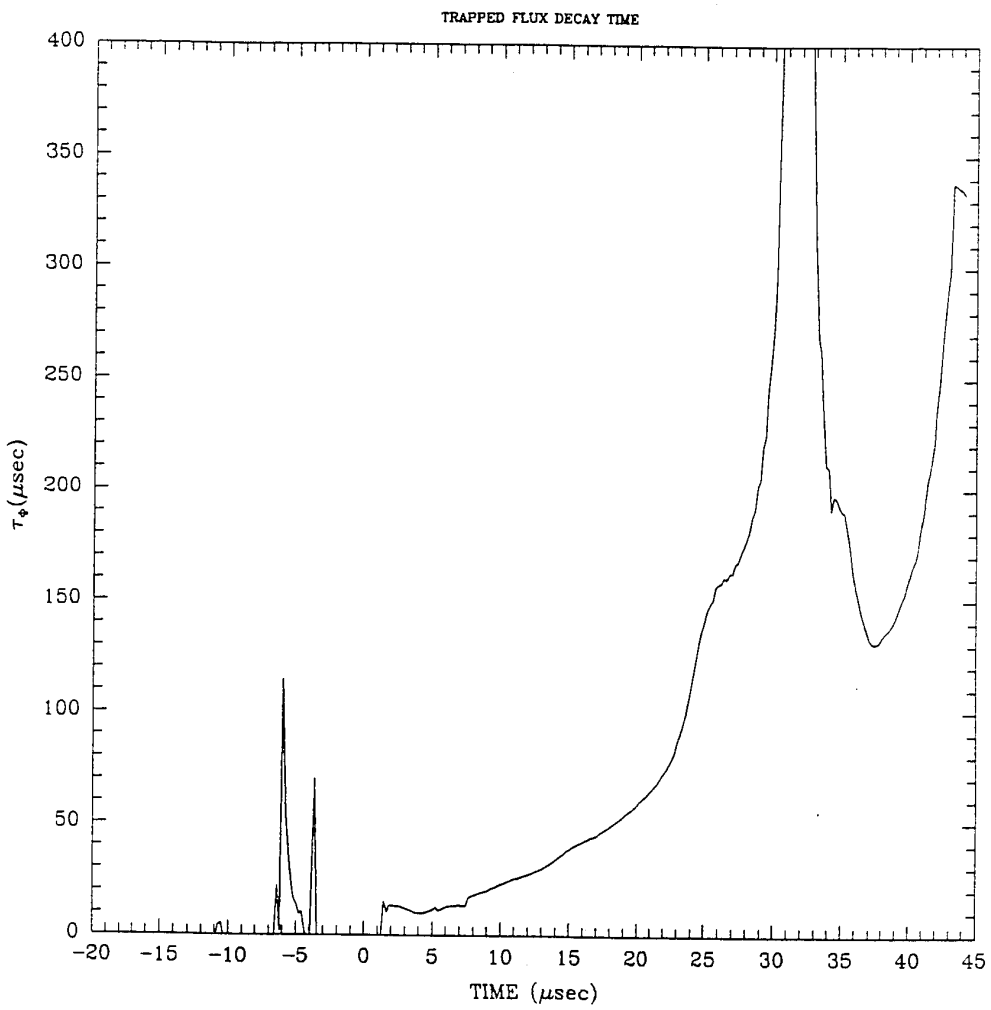

Figure 4.14: Flux decay time for run #394.

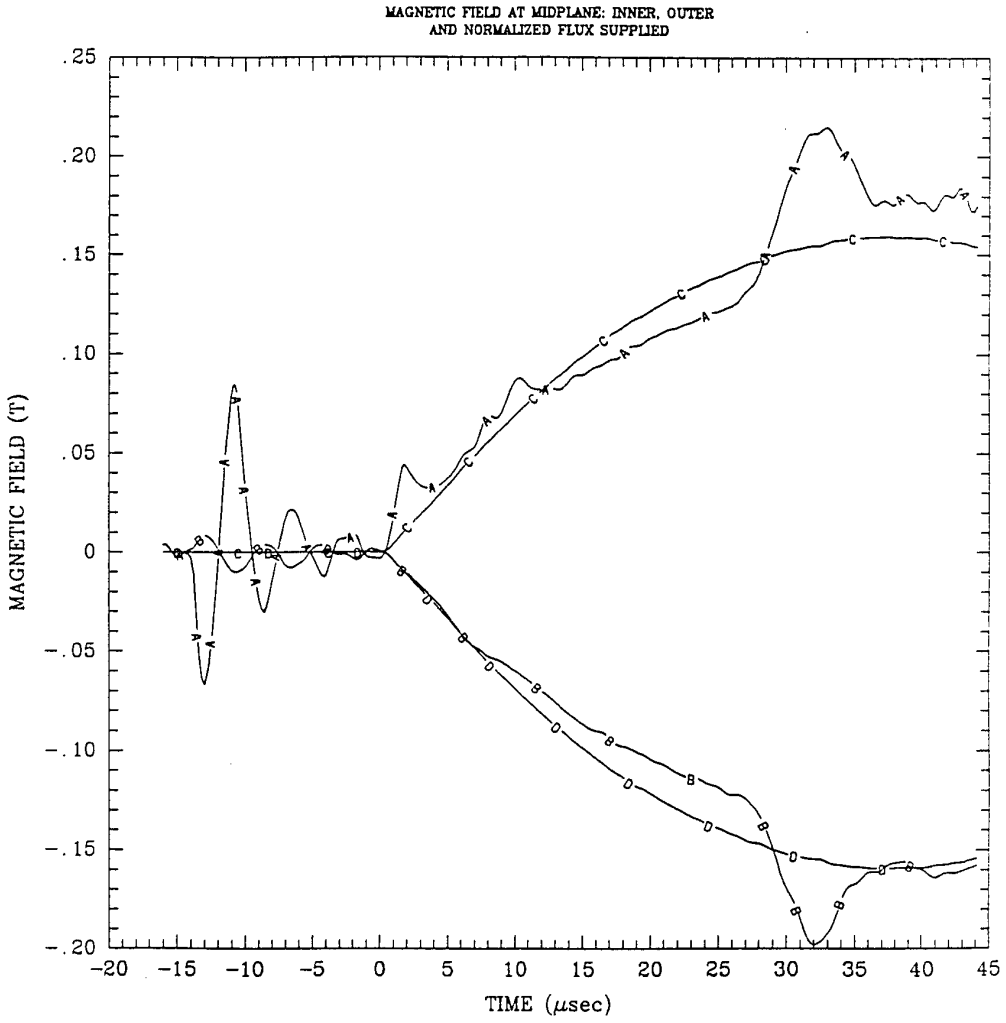

Figure 4.15: Magnetic field (A,B) from simulation #394, and the equivalent field (B_{eq}) produced by 100% flux linkage (C,D). A and C label the inner coil, B and D label the outer coil.

plasma thermal energy (E_{plasma}) is estimated by assuming a uniform temperature throughout the plasma, as determined by the Thomson scattering diagnostic. The plasma electron (or ion) inventory (N_{total}) is estimated from the $\int n\, d\ell$ measurement, and the effective length (L_{eff}) determined in the method described above. The magnetic energy (E_{mag}) depends on the radial and axial profile of both radial and axial field components. To simplify, the radial component is ignored, and the radial field dependence is removed by calculating a quantity called E_{ub} which is the magnetic energy if the magnetic field is assumed uniform across the radial region between the coils. Assuming pressure balance: $B_0^2 = B^2(r) + 8\pi p(r)$, the energy $E_{ub} = \int B_0(z)^2/8\pi\, dV = E_{\text{mag}} + \frac{2}{3}E_{\text{plasma}}$.

This relation is tested by calculating both the quantity E_{ub} as done by Maqueda using only the external field variation at the coils ($B_0(z)$) and the magnetic and plasma energy using the full radial and axial variation and both components of field. Comparing E_{ub} with $E_{\text{mag}} + \frac{2}{3}E_{\text{plasma}}$ in figure 4.16 shows that the equality assumed is reasonable, in general. Two curves are compared to that of $E_{ub}(t)$, those of $E_{\text{mag}} + \frac{2}{3}E_{\text{plasma}}$, and $E_{\text{mag}} + \frac{2}{3}(E_{\text{plasma}} + E_{\text{neut}})$, that is, the thermal energy excluding and including the neutral thermal energy. The extra thermal energy of the neutrals is small compared to electron plus ion thermal energy.

Also calculated in the energy balance from experimental data is the Poynting energy into the annular region between the coils (E_{in}). This is made by calculating $c/4\pi \int \mathbf{E} \times \mathbf{B} \cdot \hat{r}\, dS$, that is assuming the all the Poynting flux enters from the coils, with negligible flux from the axial end regions. This assumption is found to be quite accurate. The Poynting power from the coils and ends is calculated from simulation results, and the power from the end regions accounts for less than 1% of the total in general. To complete the energy balance from experimental data, the energy lost to the ionization of particles and radiation is accounted for. The effective ionization potential of 17 eV is chosen to agree with the value used in the energy balance by Maqueda, so that the energy lost to ionization is $E_{\text{ionize}} = 17\ \text{eV} \times N_{\text{total}}$. The energy lost by radiation is due to impurities in the plasma. No significant L_α radiation is observed experimentally. This is reflected in the simulation input parameters by setting the photon energy to zero for this process, as this radiation is assumed to be trapped in the neutral gas surrounding the ionized regions.

After subtracting from the Poynting energy the energies in the magnetic field,

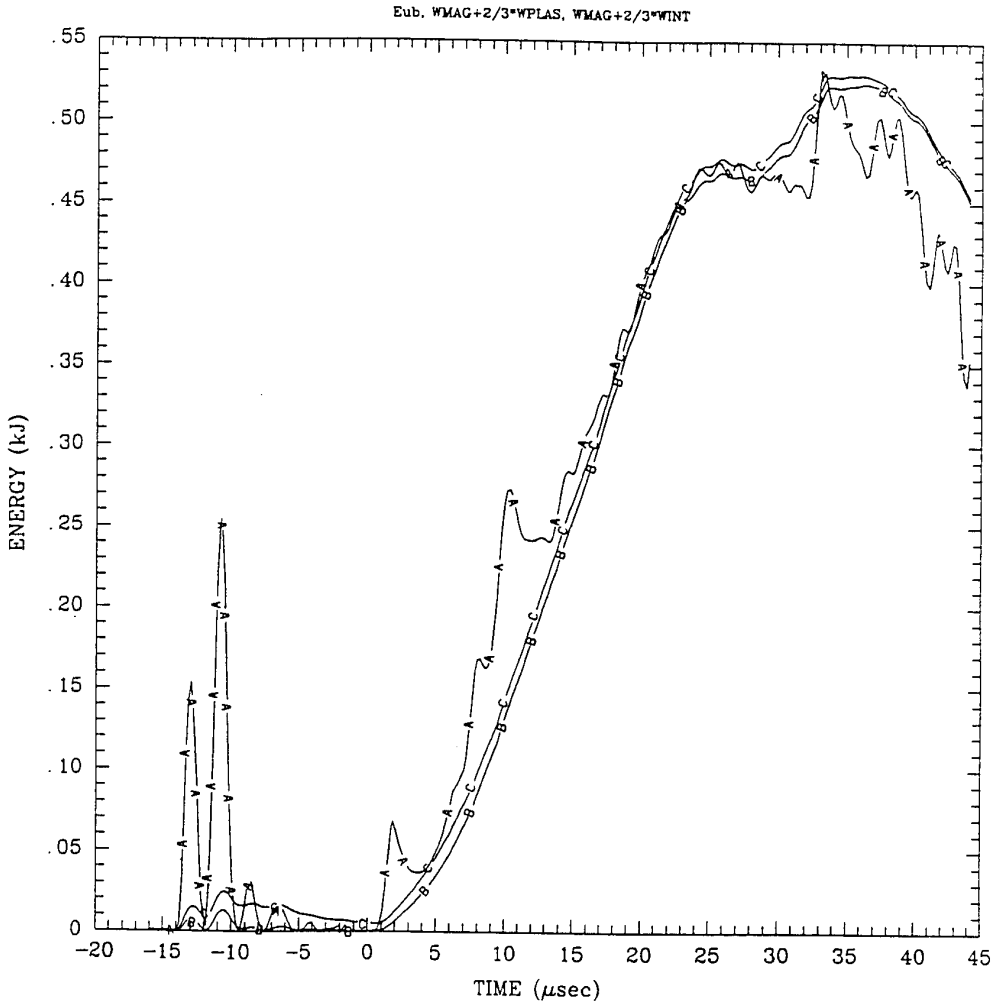

Figure 4.16: (A) E_{ub}, (B) $E_{\mathrm{mag}} + \frac{2}{3}E_{\mathrm{plasma}}$, and (C) $E_{\mathrm{mag}} + \frac{2}{3}(E_{\mathrm{plasma}} + E_{\mathrm{neut}})$ for run #394.

plasma, and losses from ionization and radiation, the remainder is the energy into neutrals, kinetic energy of ions and neutrals, heat conduction, and energy convected out of the control volume used in this calculation. This energy is called E_{other} in Maqueda's work. The itemization of each of these energies from experimental data [4] and simulation results are plotted in figures 4.17 and 4.18, respectively. The experimentally calculated energies are reinitialized to zero at $t = 0$ in figure 4.17, while the energies from the simulation start from zero at the time of ringing preionization in figure 4.18. The control volumes used in the calculations extend from inner to outer vacuum chamber wall. The full length of the coils is used for the control volume of the experimentally determined energies. The length of the control volume used for the energies determined from simulations is shorter than that used with the experimental data. This is because the magnetic fields at the coils ends have some large and spurious peaks due to numerical differencing effects. About 5 cm from the ends, the fields do not have these spurious peaks, and so the control volume does not include the last 5 cm from either end.

Looking at figure 4.18, it can be seen that during the ringing PI time period the Poynting energy is small but significant, and goes into E_{other}, that is, the Ohmic heating of the slightly ionized gas is converted into thermal neutral particle energy, and most of this heat is conducted to the walls. After the main voltage is applied at $t = 0$, the Poynting energy increases with a corresponding increase in the magnetic energy, but only about half the Poynting energy manifests itself as magnetic or plasma energy. The remaining half of the energy balance is distributed into ionization of the plasma and heat conduction to the walls.

In the simulation with the higher applied voltage of 5 kV, the energy is distributed more into magnetic, then plasma, with about the same absolute magnitude into ionization and heat conduction. The point is that ionization and heat conduction are necessary losses during the formation of plasmas in the CSS. The energy per ionized particle that is lost due to ionization and heating neutrals is about 25 eV over various operating conditions. The 17 eV per ion is of course necessary for ionization, and the other 8 eV are losses due to heating neutrals which conduct the heat to the walls before they are themselves ionized.

In the experiment, there seems to be wall contact after the magnetic activity starts. Impurity radiation then becomes stronger. The simulations assume a con-

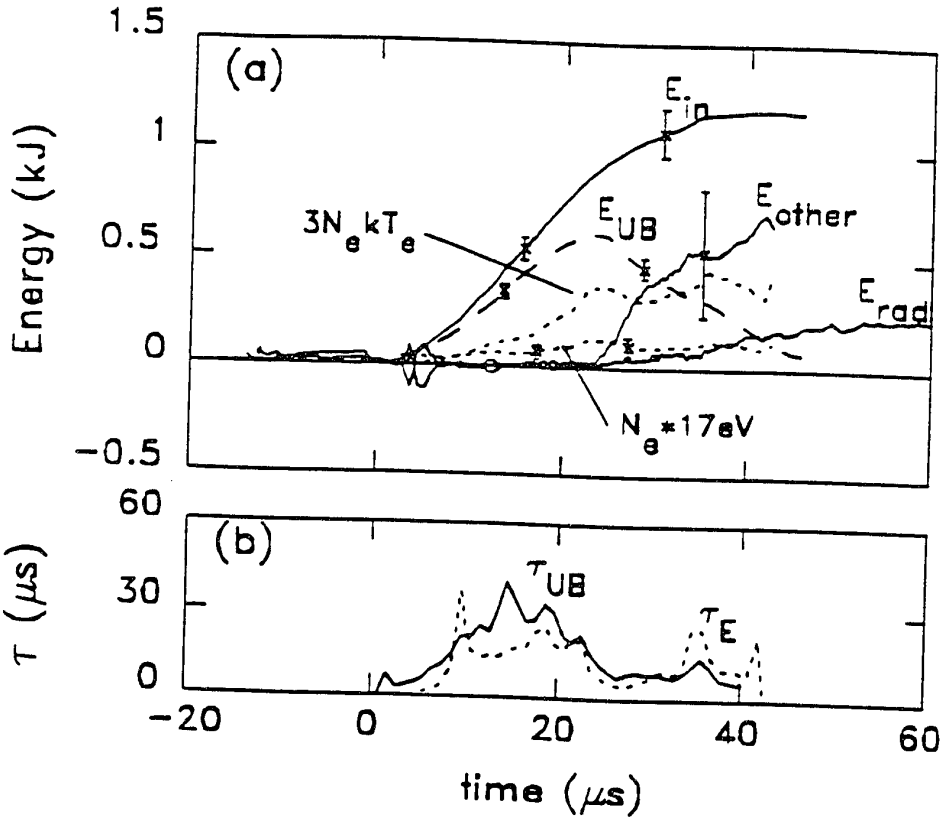

Figure 4.17: Energy inventory from experimental data with decay times for E_{ub} and total energy, from [4].

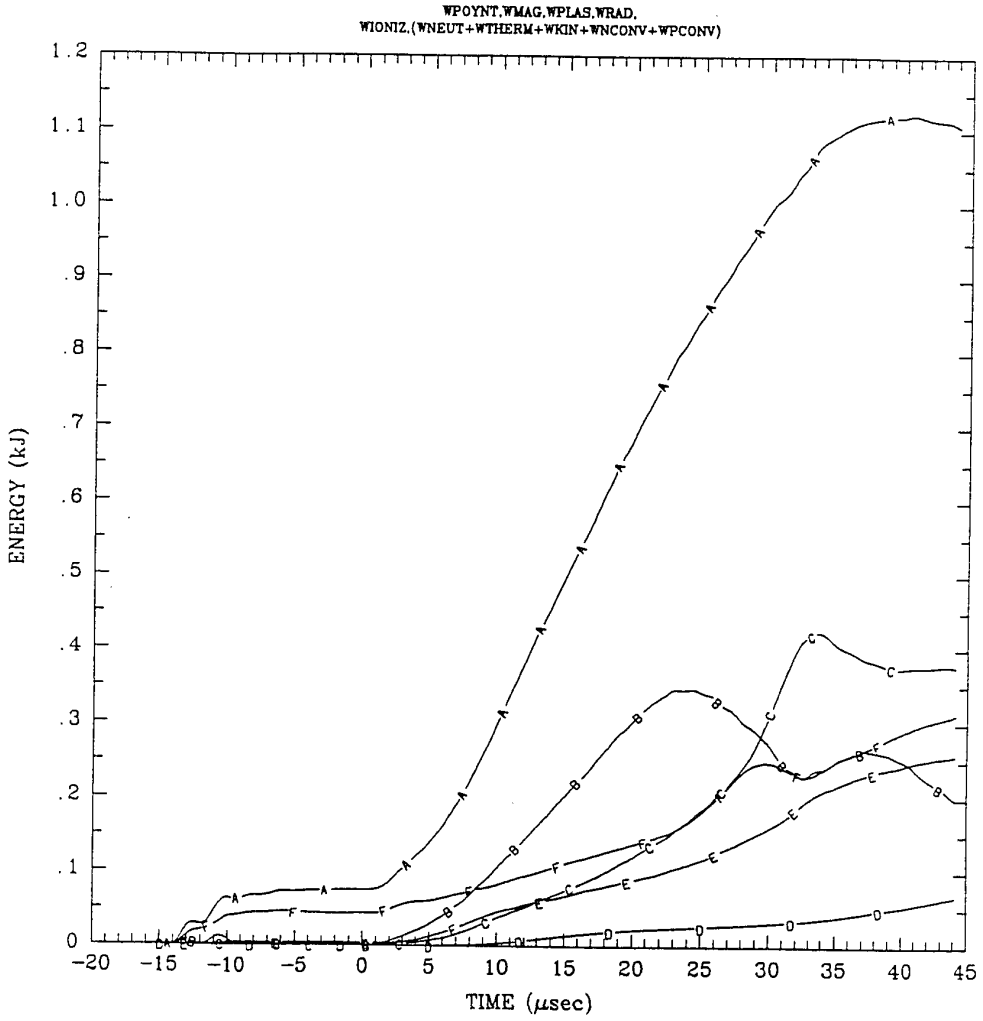

Figure 4.18: Energy inventory simulation for run #394. (A) E_{in}, (B) E_{mag}, (C) E_{plas}, (D) E_{rad}, (E) E_{ioniz}, (F) $E_{\text{other}} = E_{\text{neut}} + E_{\text{kin}} + E_{\text{conv}} + E_{\text{cond}}$

stant fraction (0.2%) of oxygen ions to neutral and ionized hydrogen. The impurity radiation in the simulations does not increase as much after the magnetic activity as in the experiment because of this.

There are energies that can be quantified from simulations that are hidden from the experimental measurement techniques. These are heat conduction, neutral thermal energy, kinetic energy of ions and neutrals, and energy convected out of the control volume. Even during axial contractions, the kinetic component is a relatively small fraction. The heat conduction is the largest of these energies, and most of this is conduction into the vacuum walls, with typically less than 30% of the conduction out of the ends of the control volume. Figure 4.19 shows the heat conduction (E_{cond}) and neutral thermal (E_{neut}) energies, as well as the plasma (ion and electron) thermal energy (E_{plas}), the time integrated Ohmic heating (E_{Ohm}) and ionization (E_{ioniz}) powers. The thermal energy in neutrals is low in comparison to the other energies. This is so even though the neutral particle inventory is high because the neutrals are in contact with the walls, and thus have a low temperature. The thermal conduction energy is approximately the same magnitude as the ionization energy, and the sum of these energies is approximately the magnitude of the Ohmic energy. This shows that most of the Ohmic heating is used to ionize the neutrals, and then much of the thermal energy of the ionized plasma is lost to heat conduction through the cold neutral regions at the walls.

4.2.3.2 Programmed Formation

Two simulations of programmed formation are analyzed in this subsection. The first (run #404) uses the operating conditions: external applied voltage of 3 kV, fill pressure of 22 mTorr. This set of conditions does not exhibit the tilting behavior of higher voltage and lower fill pressure shots in the experiment. It is actually a very marginal situation in that for slightly lower voltage or higher pressure, much less ionization and lower magnetic fields result. These conditions are chosen for simulation because of the lack of tilting observed [12] in the experiment. Thus it is hoped that the two dimensional limitation of the COAX code could give accurate rendering of the experimental situation. The other run (#405) used a second set of conditions (5 kV and 14 mTorr) that are in the middle of the range of applied voltages and fill pressures that show tilting behavior in the experimental plasmas.

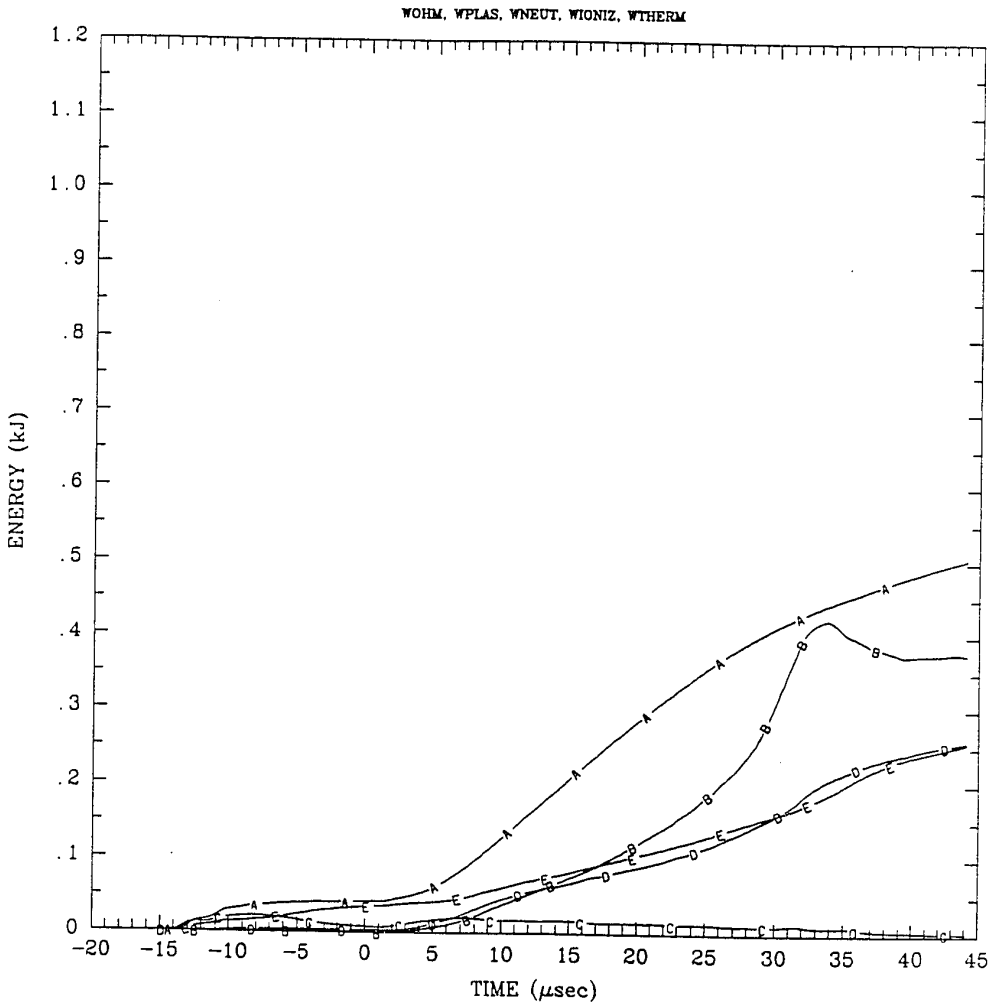

Figure 4.19: Other energies from simulation #394. (A) E_{Ohm}, (B) E_{plas}, (C) E_{neut}, (D) E_{ioniz}, (E) E_{cond}.

Table 4.6: Parameters used in runs #404 and #405

parameter	run #404	run #405	units
ringing PI?	yes	yes	
flux input?	yes	yes	
exp. voltage	3	5	kV
`en0`	1.56e15	1.e15	cm^{-3}
`tmp0`	0.01	0.01	eV
`eion`	17	17	eV
`preion`	0.001	0.001	fraction
`eexcite`	0	0	eV
`fioniz`	100	10	multiplier
`faccx`	1	1	multiplier
`facimp(3)`	0.002	0.002	O fraction
`anomr`	1.0	1.0	multiplier

Nonetheless, the operating conditions of 5 kV and 14 mTorr are used to see what would result, realizing that the tilting behavior could not be imitated by COAX.

Before detailing results from these two runs, a point can be made about the Barnes relation. The Barnes relation [2] can be derived from theoretical principles for the case of the CSS geometry to give $\langle\beta\rangle = 1 - A_s/2A_{an}$ [1]. In this formula, A_s is the area between the inner and outer separatrices of the configuration, and A_{an} is the total cross-sectional area of the annular region. The derivation of this relation requires straight magnetic field lines at the midplane (where the average beta condition is to be determined) as well as straight field lines and uniform field at the ends of the coils where there is no plasma pressure.

The conditions for the validity of the Barnes relation are only approximately satisfied in programmed formation when there are non-negligible radial fields at the ends of the coils. These radial fields are typically negligible in comparison to the axial field strength at the midplane. These conditions are not well met for tearing

formation, where there are nonuniform axial and radial fields at the coil ends. The average beta is calculated by the relation above as well as by the definition of average beta: $\langle\beta\rangle = \int_a^b p(r) r\, dr/[B_0^2(b^2 - a^2)/4\pi]$ for each run. Here, a and b are the inner and outer separatrices determined by a routine in the post-processor that finds the separatrix location. There is only approximate agreement for programmed formation runs. The average beta for tearing formation runs agrees even less well. The magnetic field line curvature after axial contraction invalidates the Barnes relation. Also, the axial and radial fields at the coil ends invalidates the Barnes relation for tearing formation.

4.2.3.2.1 Run #404 Magnetic field and interferometer data is available for comparison with simulation results for run #404, but not the Thomson scattering diagnostic. The experimental and simulation data are compared in figure 4.20. The data for the magnetic field at the outer coil (upper traces) is almost identical for both experiment and simulation. There is a significant difference between experiment and simulation at the inner coil (the lower traces). The simulation shows a large amplitude transient, similar to that seen in the tearing formation shots, but it is larger in magnitude for programmed formation shots. The field at the inner coil is also larger in magnitude than the field at the outer coil. This is also true for the experimental data, but to a lesser extent. This apparent magnetic pressure imbalance can be explained by the neutral particle pressure at the outer wall.

Figure 4.21 shows a sequence of pressure profiles for this run. Defining magnetic pressure by $p_{\rm mag} = B^2/8\pi$, plasma pressure by $p_{\rm plas} = (n_e + n_i)T$, and neutral gas pressure by $p_{\rm neut} = n_n T$, these plots show $p_{\rm mag}$, $p_{\rm mag} + p_{\rm plas}$, and $p_{\rm mag} + p_{\rm plas} + p_{\rm neut}$, by solid lines, short dashes, and long dashes, respectively.[3] Pressure balance is indicated when the long-dashed lines (total of all three pressures) are strictly horizontal. At the time of the first plot (55 μsec), the ringing preionization has been on for about 20 μsec and the notch bank voltage is just about to be switched on. There is negligible magnetic or plasma pressure, but significant neutral pressure at the outer wall. It is nonuniform due to dynamics during the ringing preionization. At 60 μsec, the notch bank has just fired (at 57 μsec). The flux addition from 57

[3] The boundary conditions in COAX fix the temperature at the wall to that of the initial temperature. This results in very mall pressures at the walls.

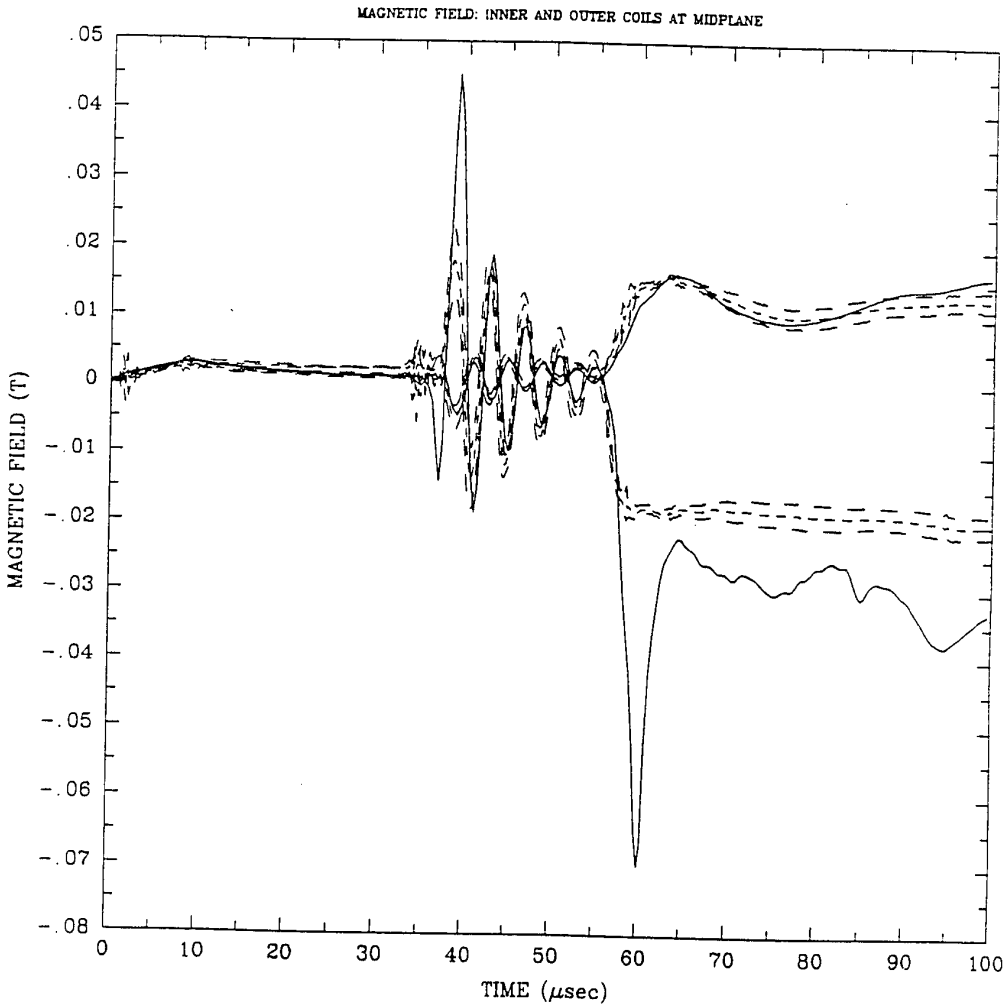

Figure 4.20a: Magnetic field from simulation of run #404 and experiment.

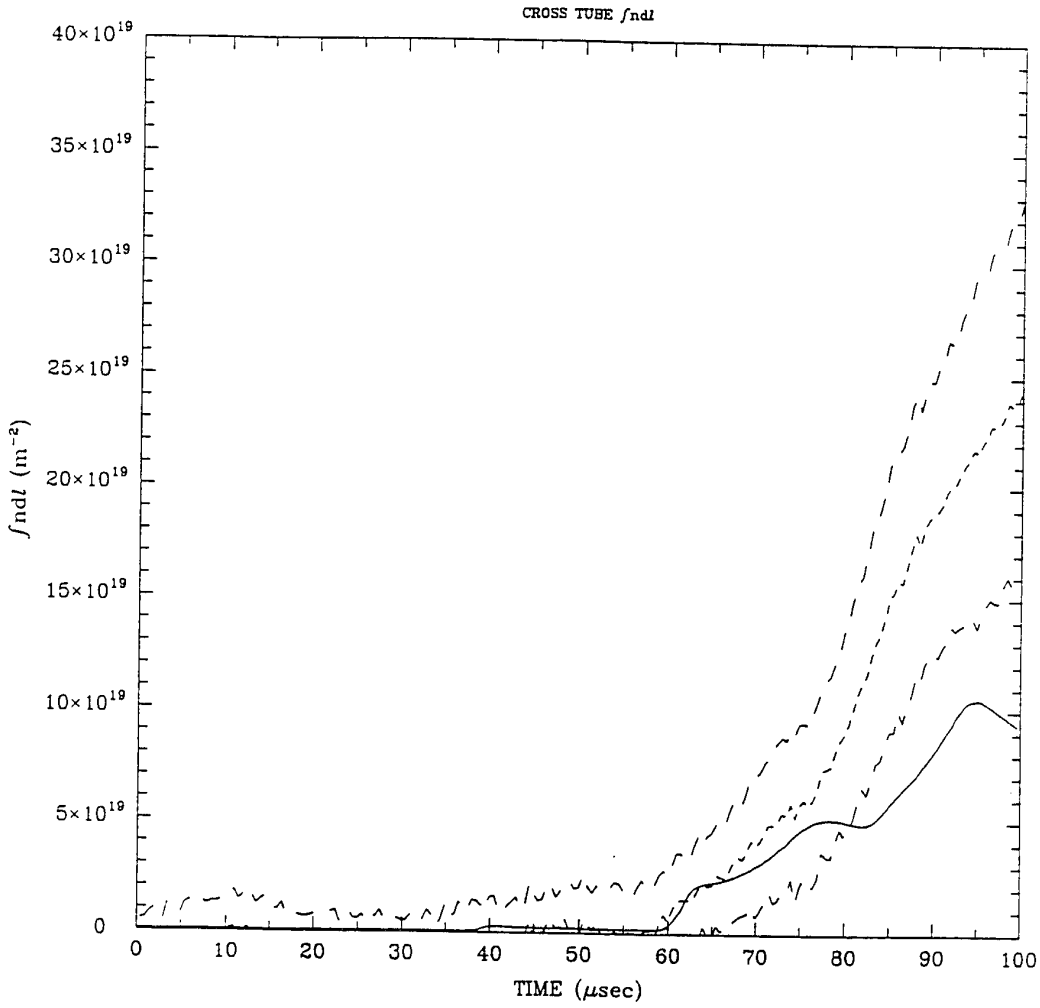

Figure 4.20b: Interferometer data from simulation of run #404 and experiment.

to 60 μsec causes bunching of the magnetic field lines near the inner coil because the magnetic null is not centered at the half-area radius ($r = 15.5$ cm). This results in a large transient magnetic field at the inner coil, and a very large unbalanced magnetic pressure, as seen in the figure.

By 65 μsec the dynamics have pushed the plasma radially outward, ionization and heating have increased the plasma pressure, and the pressure is imbalanced on the outer coil due to overshoot. The radial dynamics damp by 70 μsec, and approximate pressure balance including neutrals is achieved thereafter. The standard factor (`faccx = 1`) for friction due to charge exchange between ions and neutrals is used here. This friction is essential for this multifluid pressure balance, since the ions can be pushed against the neutral fluid at the outer wall without penetrating that fluid.

The question arises: why is there a significant neutral pressure causing magnetic pressure imbalance in programmed formation, but not in tearing formation? In tearing formation runs, there is also a neutral density increase at the outer wall, but only a small neutral pressure there. The difference for the programmed formation seems to be that the plasma is cooler, and does not ionize very quickly. The neutrals do not become fully ionized in the plasma region as they do in the tearing formation (see figure 4.22 of density profiles from programmed formation run #404 and compare to the profiles from tearing formation figure 4.9). The neutral gas stays in contact with the Ohmically heated plasma, and conducts much of this heat away into the high density neutral region near the outer wall. Thus these neutrals are both dense and relatively warm, producing a pressure on the same order as that of the plasma.

Accounting for the energy can be done in the same way as for the tearing formation results. The Poynting flux is again found to be mostly entering through the coils, with less than 1% coming from the ends of the annular control volume. The same is true of the heat conduction losses. The E_{ub} estimate for $E_{\mathrm{mag}} + \frac{2}{3}(E_{\mathrm{plasma}} + E_{\mathrm{neut}})$ holds in approximation.

The energy itemization for programmed formation simulations shows less of the input energy transformed into magnetic or thermal energy than the tearing cases. Figure 4.23 shows the energy input via Poynting flux, the magnetic and plasma thermal energies, the energy lost to radiation by impurities (L_α is trapped), energy

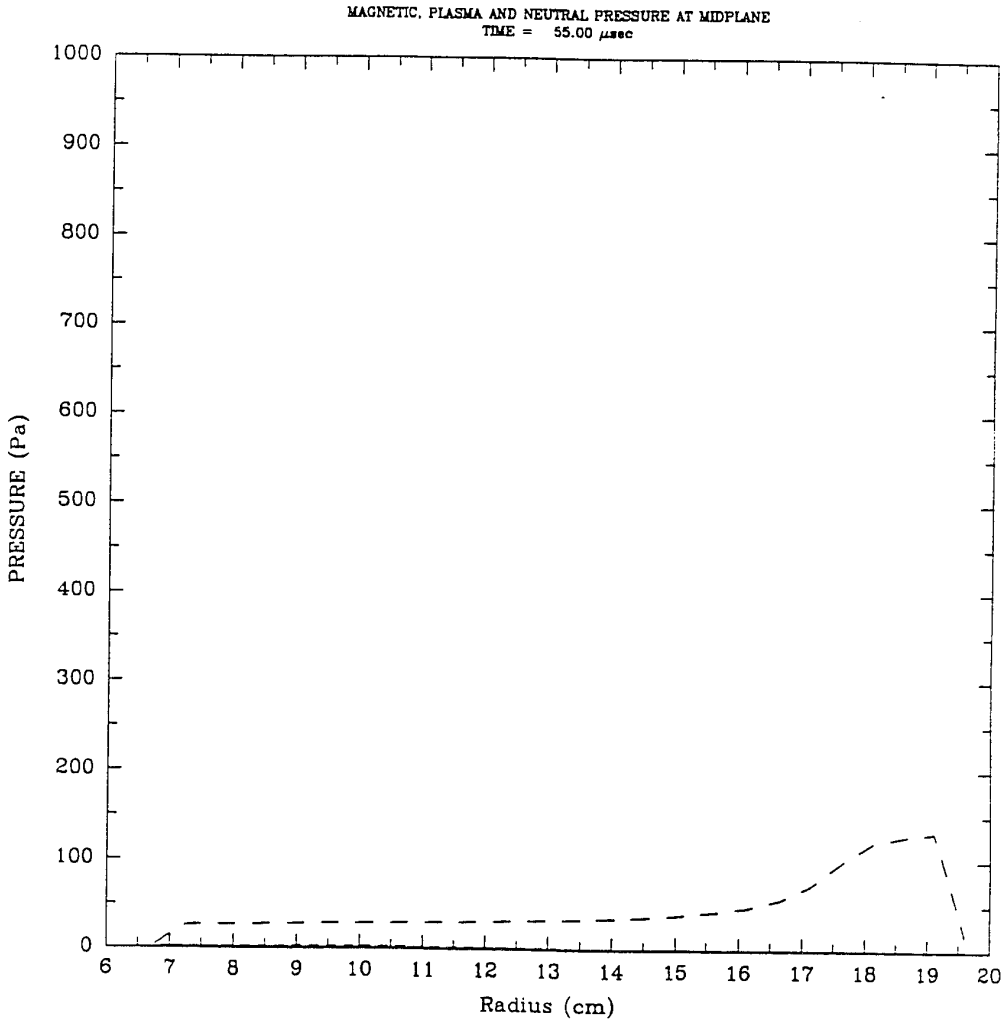

Figure 4.21a: Time sequence of pressure profiles for run #404. $t = 55$ μsec. Solid lines represent p_{mag}, short dashed lines represent $p_{\mathrm{mag}} + p_{\mathrm{plas}}$, and the long dashed lines represent $p_{\mathrm{mag}} + p_{\mathrm{plas}} + p_{\mathrm{neut}}$.

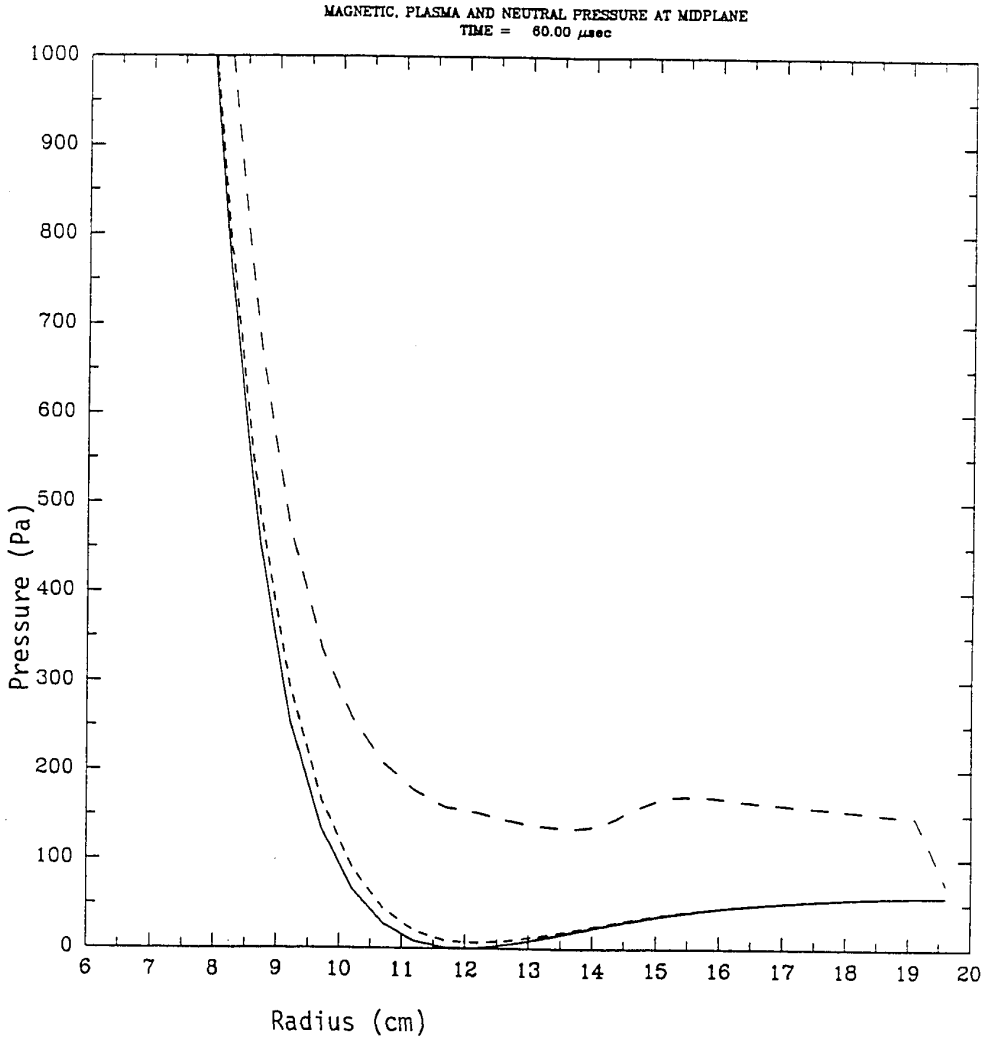

Figure 4.21b: Pressure profile at $t = 60$ μsec.

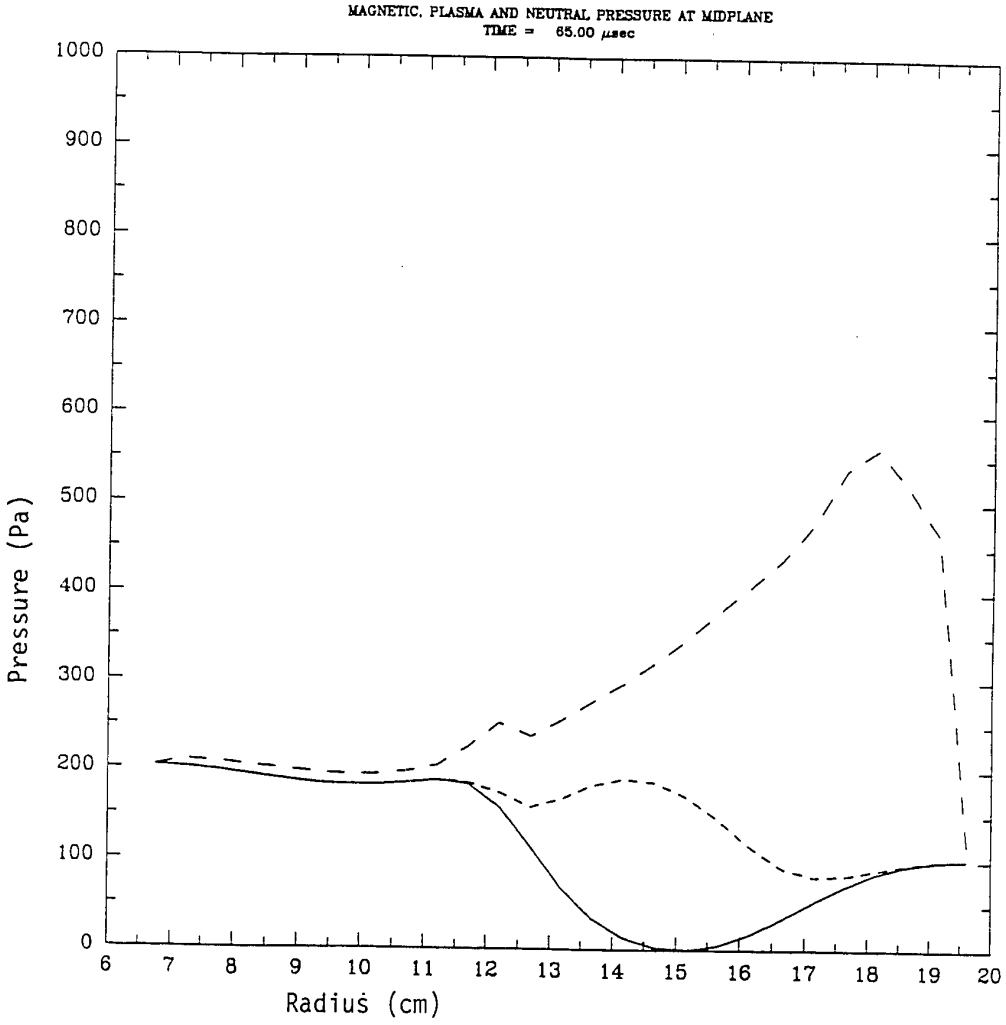

Figure 4.21c: Pressure profile at $t = 65$ μsec.

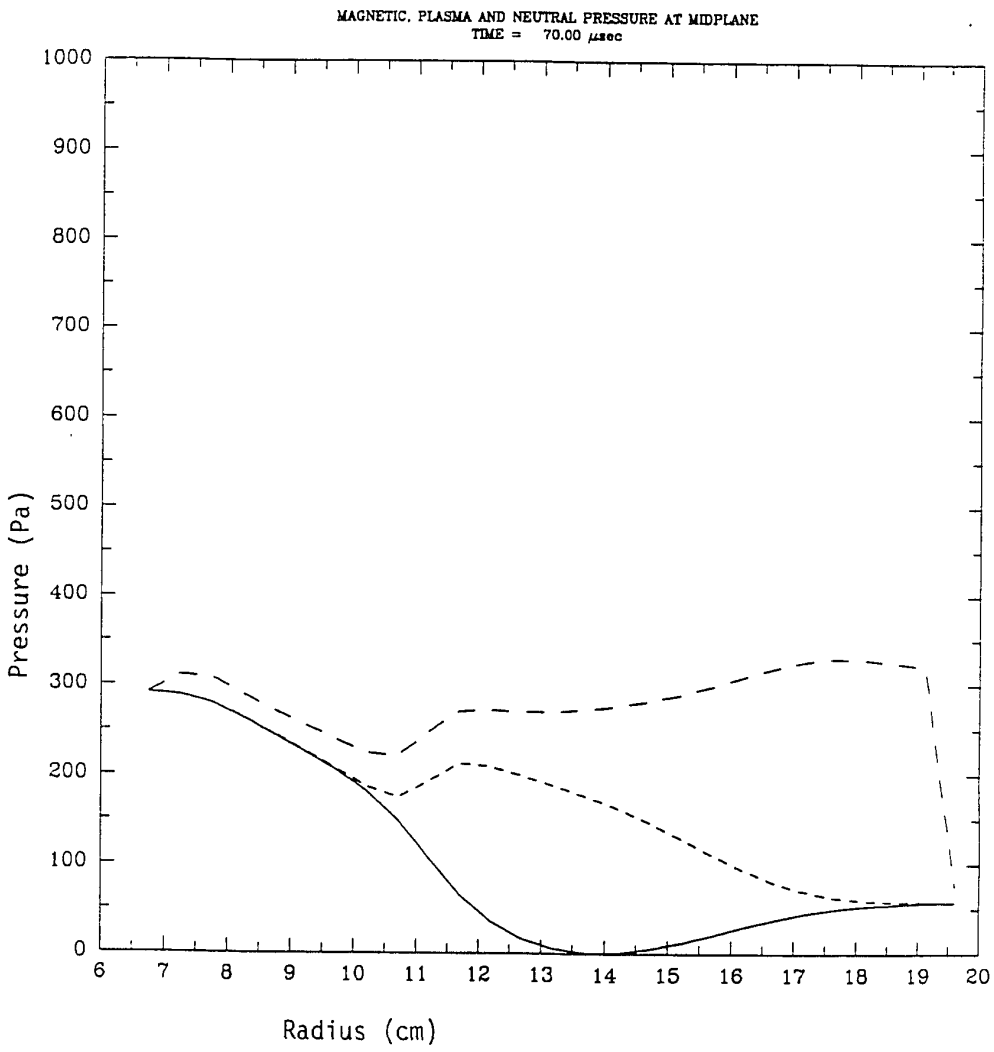

Figure 4.21d: Pressure profile at $t = 70$ μsec.

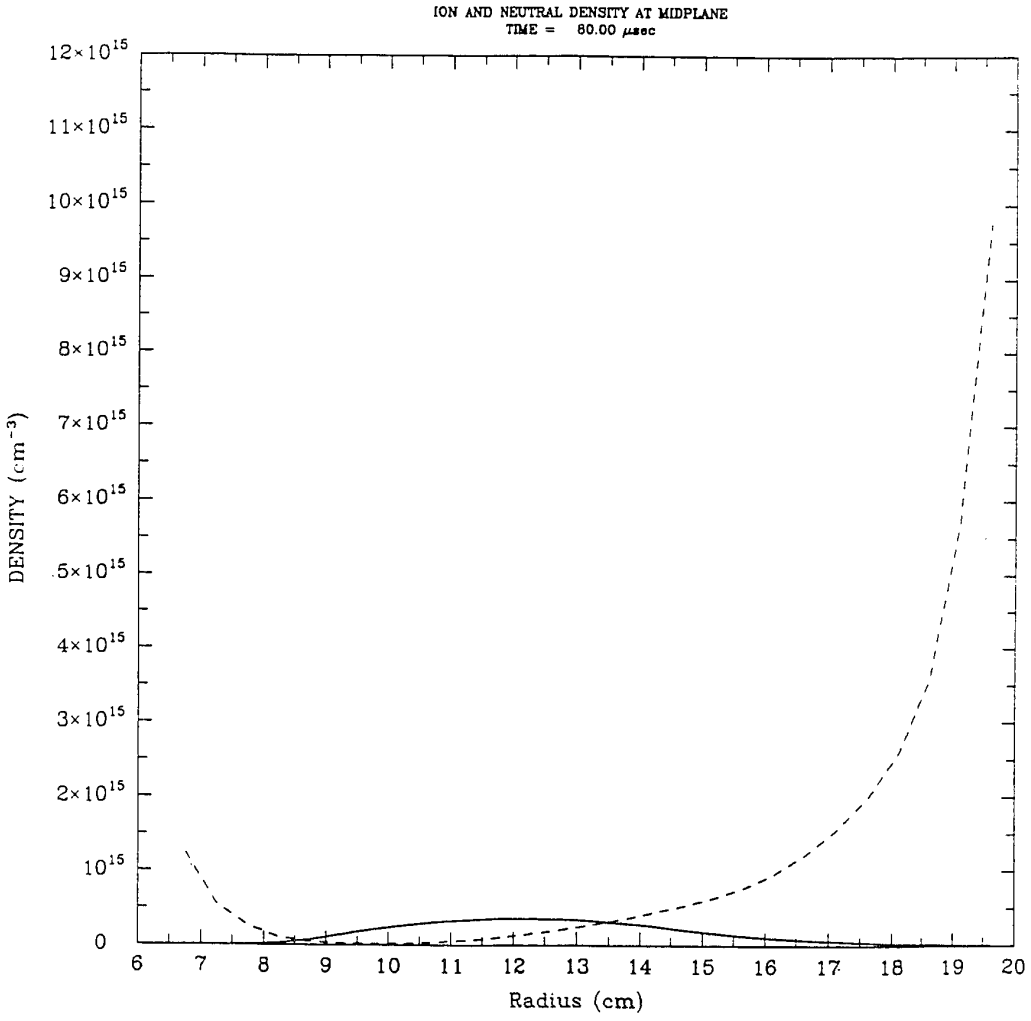

Figure 4.22: Ion and neutral density profiles across the midplane for run #404.

lost by ionization, and the energy hidden from the experimental diagnostics: neutral thermal, kinetic, convection losses, and thermal conduction. Magnetic and plasma thermal energy make up only about 10% and 5% respectively of the input energy. About 36% goes toward ionizing the plasma, while almost half is in the hidden energy.

The energy lost due to ionization and heating neutrals is again about 25 eV per ion produced. There are 1.4 $\times 10^{20}$ neutral particles in the control volume initially, so it would take approximately 0.56 kJ to ionize all of them. There is about 1 kJ of energy stored in magnetic field inside the core before the notch, but the coupling efficiency to the annular region reaches only 18% by $t = 100$ μsec. Thus only about 1.8 $\times 10^{19}$ ions are produced, requiring 0.05 kJ, or 36% of the input energy. The thermal energy in the remaining neutrals is about 0.011 kJ at the end of the simulation, but has a peak of 0.025 kJ at $t = 65$ μsec. The neutrals have more thermal energy than the plasma until 88 μsec, as can be seen in figure 4.24. This thermal energy is the source of the neutral pressure that causes the magnetic pressure imbalance.[4]

Figure 4.24 shows that the greatest energy loss is via heat conduction, followed closely by ionization loss. The magnetic energy and thermal plasma energy is much smaller by comparison. The heat flux vectors at the time of maximum heat conduction loss are shown in figure 4.25. The region midway between the coils has the highest temperature (about 3 eV), and the heat is conducted through the neutrals to the walls. This conduction of heat from the warm ion region to the neutrals is what puts the thermal energy into the neutrals. Warm neutrals conduct heat better than cold neutrals (lower density and higher temperature increase mean free path length and average particle velocity).

4.2.3.2.2 Run #405 For the second programmed formation run, the experimental operating conditions of 5 kV, 14 mTorr are used. These conditions are at higher voltage and lower fill pressure than those for run #404. These operating conditions are in the middle of the typical experimental range, and shots in this

[4] Recall that to avoid conditions for the tilt to occur experimentally, low voltage and high fill density must be used. In such a situation, it is difficult to generate a highly ionized plasma, and so much input energy goes into heating neutrals.

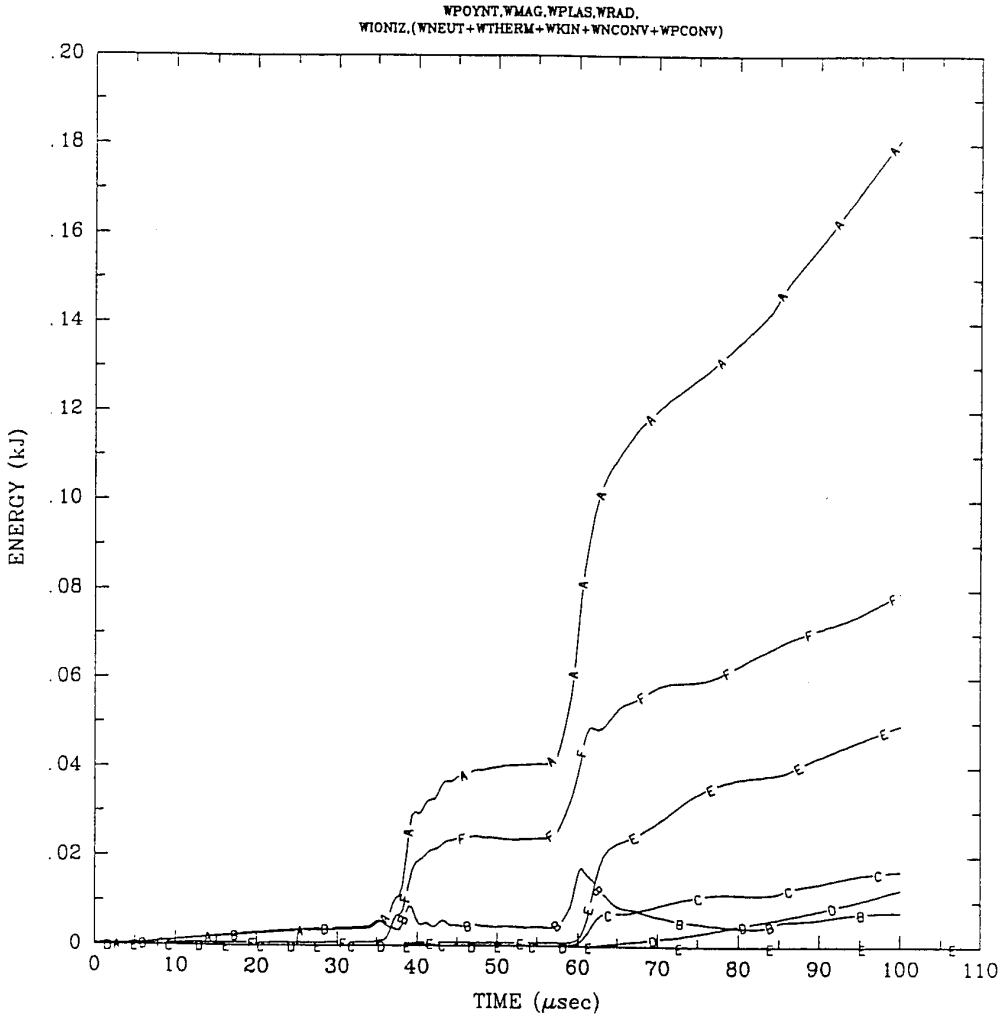

Figure 4.23: (A) E_{in}, (B) E_{mag}, (C) E_{plas}, (D) E_{rad}, (E) E_{ioniz}, (F) $E_{\text{other}} = E_{\text{neut}} + E_{\text{kin}} + E_{\text{conv}} + E_{\text{cond}}$.

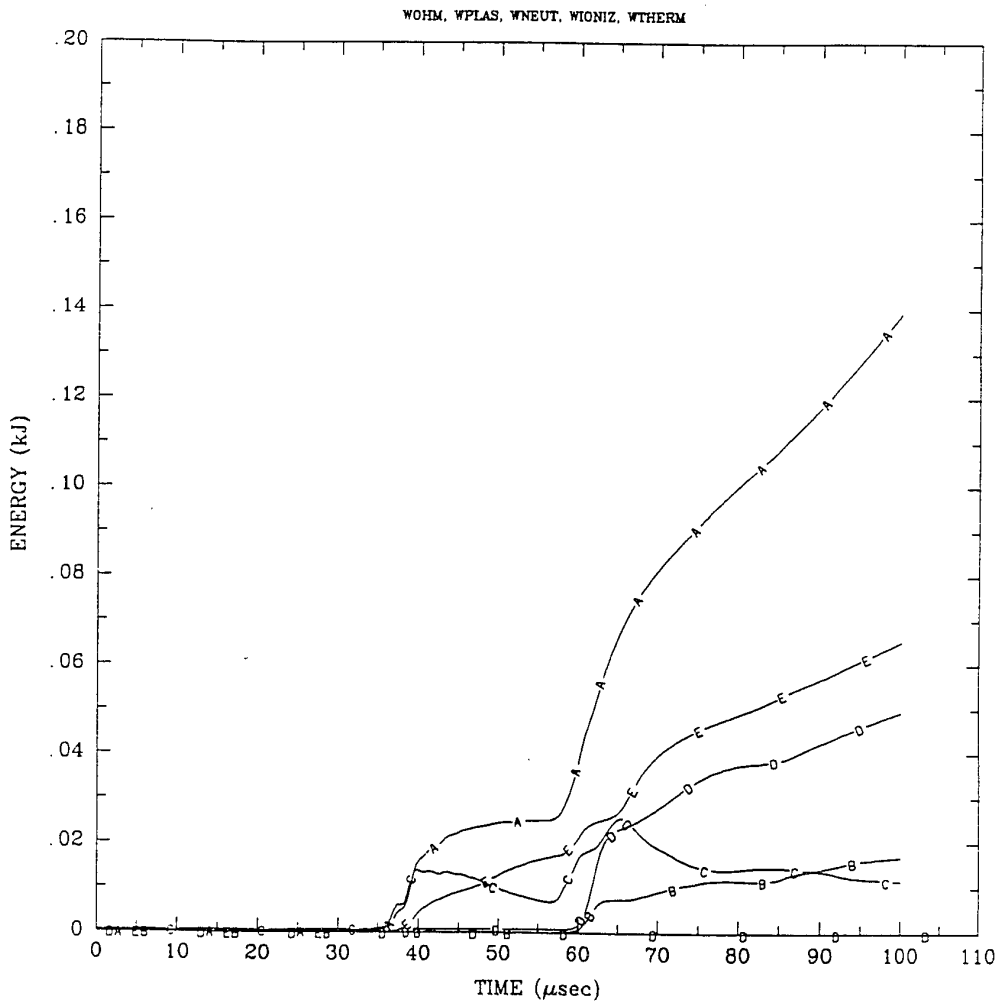

Figure 4.24: (A) E_{Ohm}, (B) E_{plas}, (C) E_{neut}, (D) E_{ioniz}, (E) E_{cond}.

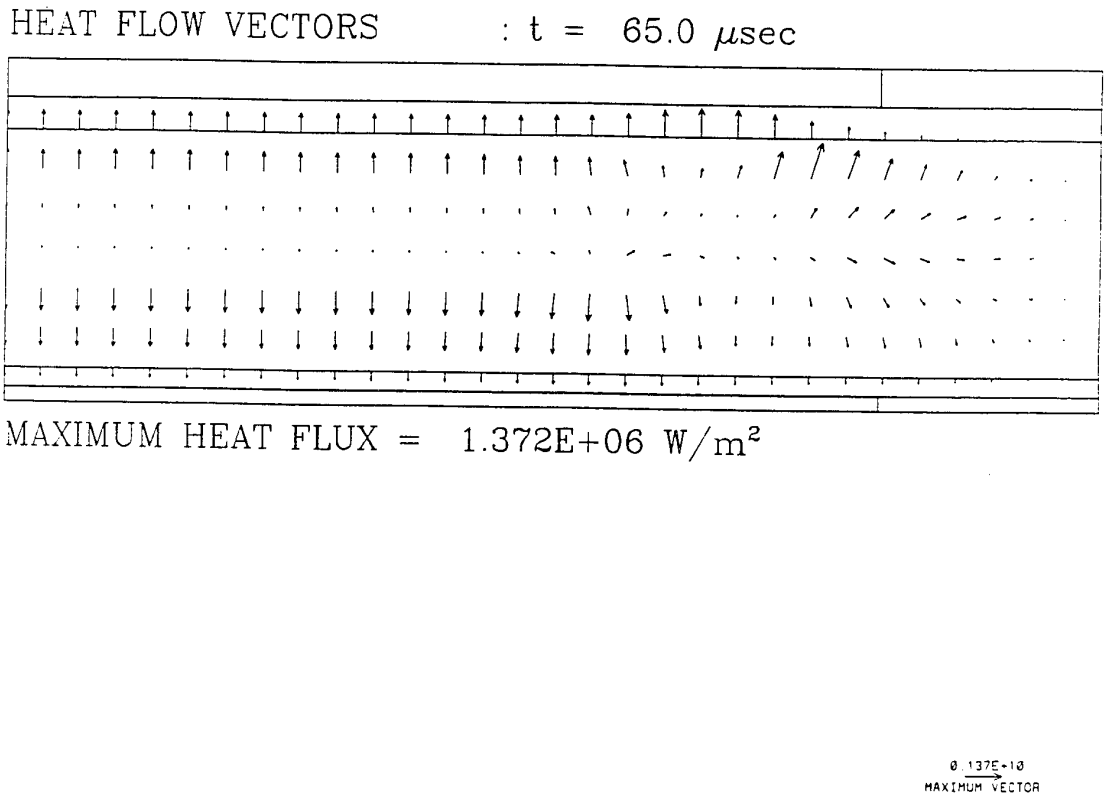

Figure 4.25: Heat flux vectors at 65 μsec in run #404.

range showed signs of the tilting instability [12].

The experimental data for magnetic field and interferometer data can be compared with simulation results for run #405, and are plotted in figure 4.26. In contrast to the results of this comparison for the last run (#404), the magnetic field calculated in this simulation diverges from that of the experiment soon after the notch voltage is applied at $t = 57$ μsec. The transient peak field at the inner coil is again present as in previous runs. The explanation is the same: a compression of flux between the inner coil and an inertial plasma which shifts radially to redistribute the flux after some radial dynamics damp this motion.

The configuration contracts axially from the start of the notch voltage until the end of the run. Figure 4.27 shows the effective length ($L_{\text{eff}} = \int B_z^2(z)\,dz/B_z^2(0)$) as a function of time.[5] The experimental data also shows axial contractions of a similar nature.

Since experimental shots with the operating conditions of this run show tilt instabilities, there could be mechanisms at play to anomalously dissipate flux, and reduce the magnetic fields observed experimentally. The tilt instability requires a three dimensional code to simulate it, and even then, the anomalous processes required to dissipate flux might involve microinstabilities or resistive MHD turbulence. Since COAX does not do this, and this run used only classical resistivity, there are no anomalous dissipative mechanisms to reduce the magnetic fields to the levels observed in experiment.

4.2.3.2.3 Efficiency of Flux Transfer In subsection 2.1, equations are solved to calculate the efficiency of transferring flux from the electrical system or inner coil to the annular region (trapped flux). The efficiency is defined as the ratio of the configuration trapped flux to that supplied by the coils. It is found that the higher the normalized flux decay time $\eta = \omega\tau_\phi$, the better this transfer efficiency. For infinite flux decay time (infinite conductivity), this efficiency goes to 100%.

Figure 4.28 shows the magnetic field at the coils for run #405 (programmed formation, 5 kV, 14 mTorr) with the equivalent field (B_{eq}) produced by 100% flux linkage. For a thin plasma with no resistance, these curves should be equal, neglecting radial dynamics or axial contractions. The result from this run should be

[5] The spikes in effective length at times before the notch are due to the ringing fields.

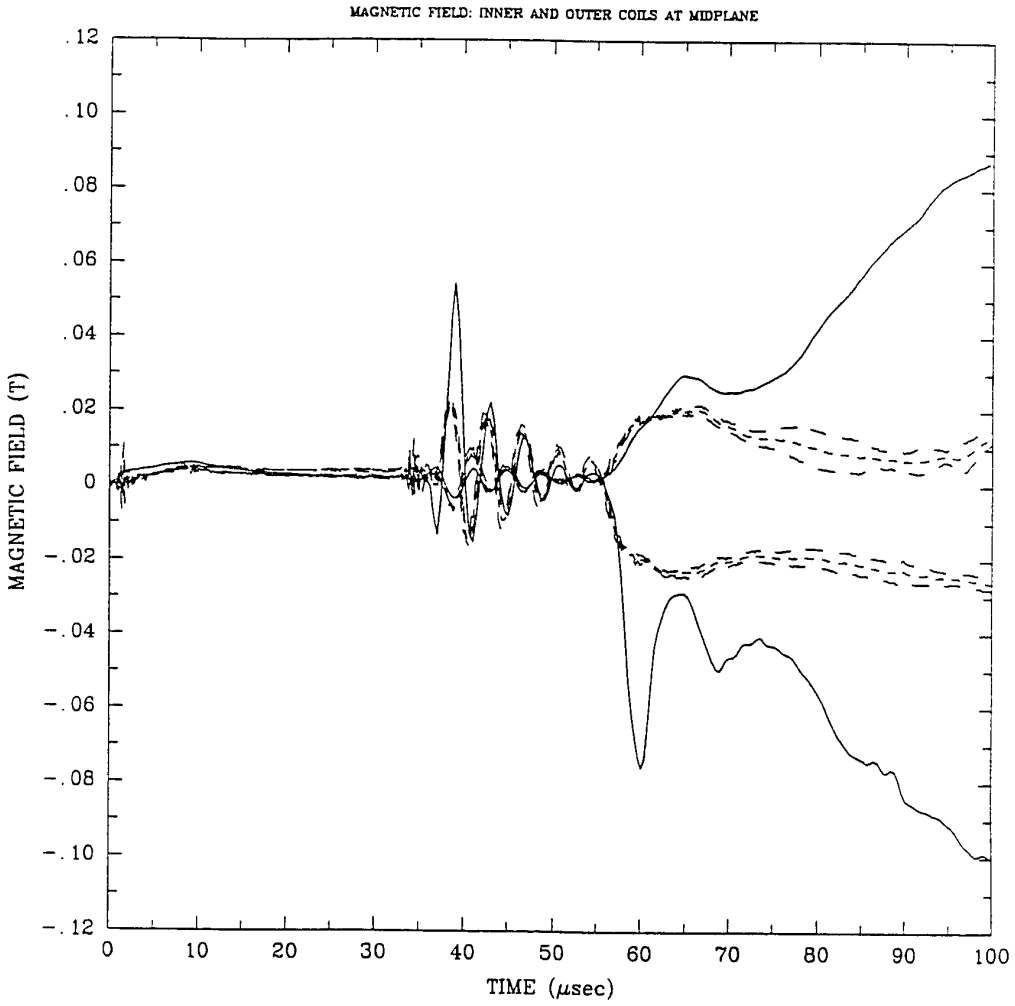

Figure 4.26a: Magnetic field for run #405 compared to experimental data.

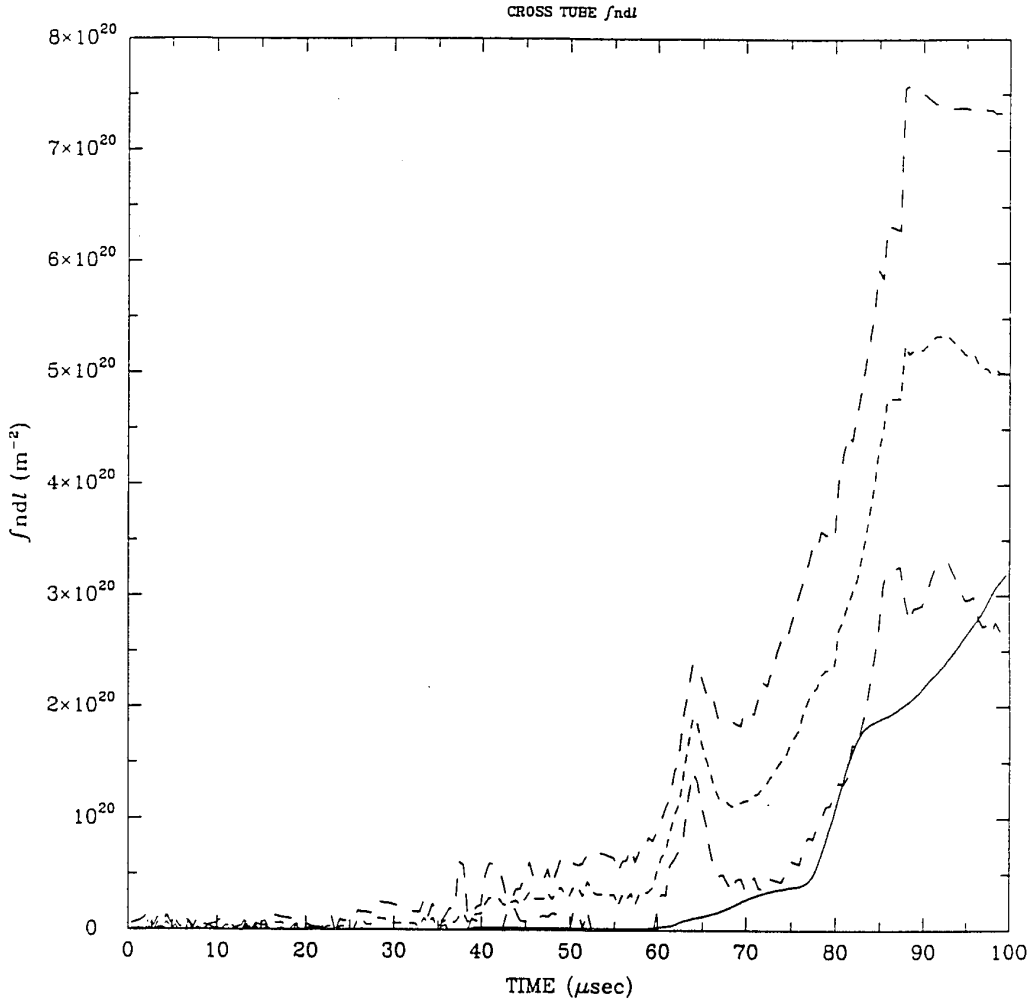

Figure 4.26b: Interferometer data for run #405 compared to experimental data.

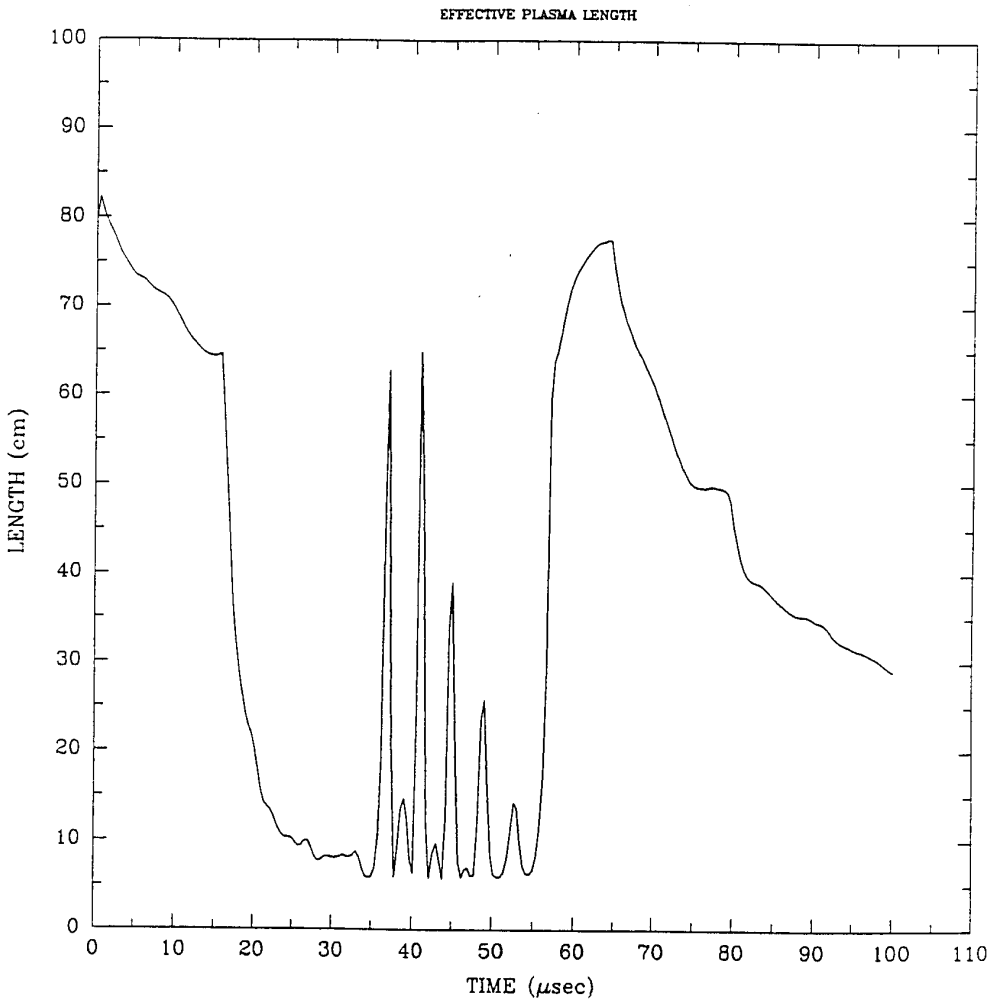

Figure 4.27: Effective length of configuration for run #405.

compared to that of run #394 (tearing formation, 3 kV, 22 mTorr) in figure 4.15. Why does the programmed formation run have lower flux transfer efficiency than the tearing formation run, even though the programmed formation run operates at a higher voltage and lower fill pressure?

Part of the answer is that the 5 kV operating voltage in programmed formation is the voltage at the capacitor banks, and is not the voltage that appears at the coils. There is an external inductor in the electrical circuit to isolate the main capacitor bank from the notch bank (refer to figure 1.1). The actual voltage at the coils at the time of the notch turn-on is 2.3 kV, and after the notch voltage has damped, the voltage is down to about 0.8 kV. In comparison, the tearing formation circuit had smaller external inductance, and so the voltage at the inner coil is 2.4 kV. Thus there is actually a much higher flux addition rate for the tearing formation run compared to the programmed formation run.

Due to the smaller voltage in the programmed formation run, the input energy is also less. Even though there is lower fill pressure, the energy lost by ionization and heat conduction is very substantial, and the temperature is only about 6 eV. The temperature in the tearing formation run rises steadily to about 15 eV before axial contraction raises it even further via compressional heating. Thus the flux decay times should reflect the differences in temperature, with the hotter plasma tending to have a longer flux decay time. Figure 4.29 shows the flux decay time for the programmed run #405. This should be compared to figure 4.14 for tearing run #394. The normalized flux decay time $\eta = \omega\tau_\phi$ is 0.5–2 for run #405 and about 10 for run #394.

4.2.3.3 Summary of Simulations with Validated Model

- Reasonably accurate simulations of CSS plasmas can be obtained with the two fluid model using:
  - Neutrals and ions, with collisions.
  - One-step ionization.
  - Classical resistivity.
- Magnetic activity in tearing formation coincides with axial contraction.

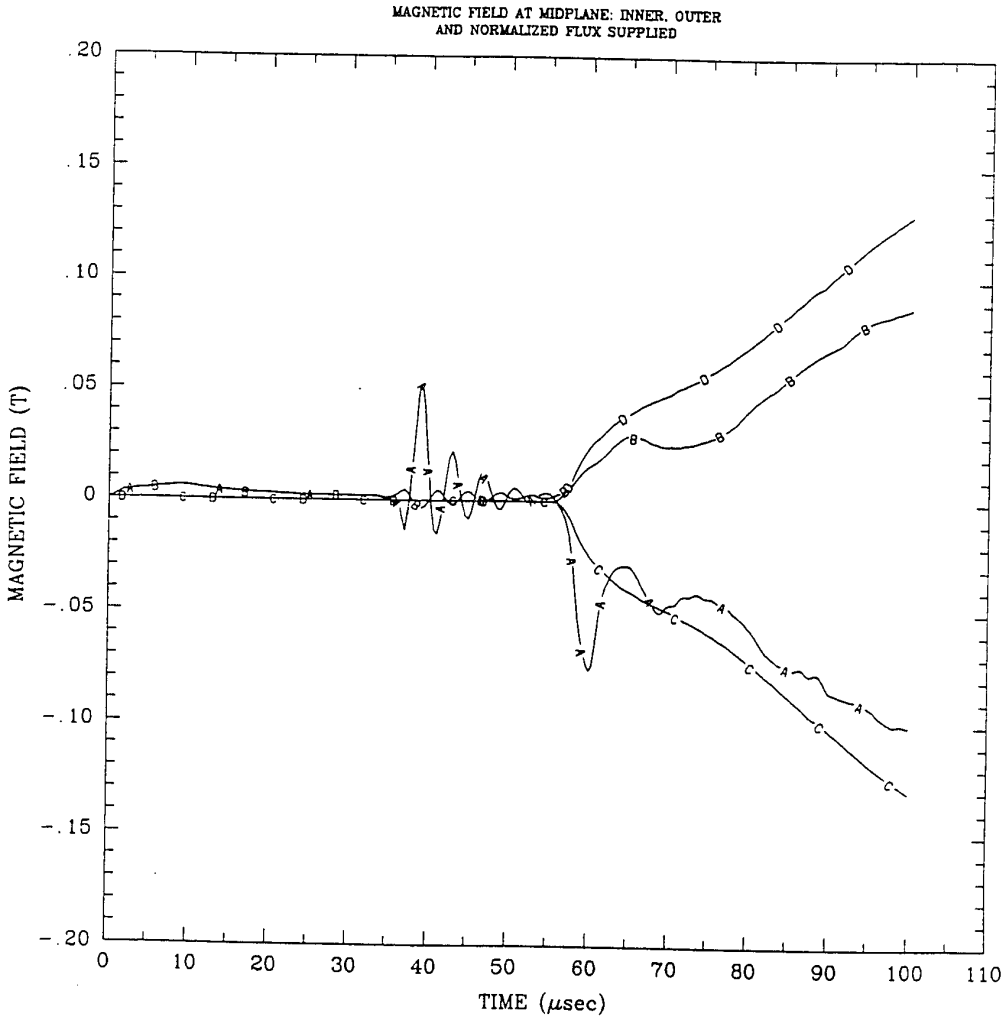

Figure 4.28: Magnetic field (A,B) from simulation #405, and the equivalent field (B_{eq}) produced by 100% flux linkage (C,D). A and C label the inner coil, B and D label the outer coil.

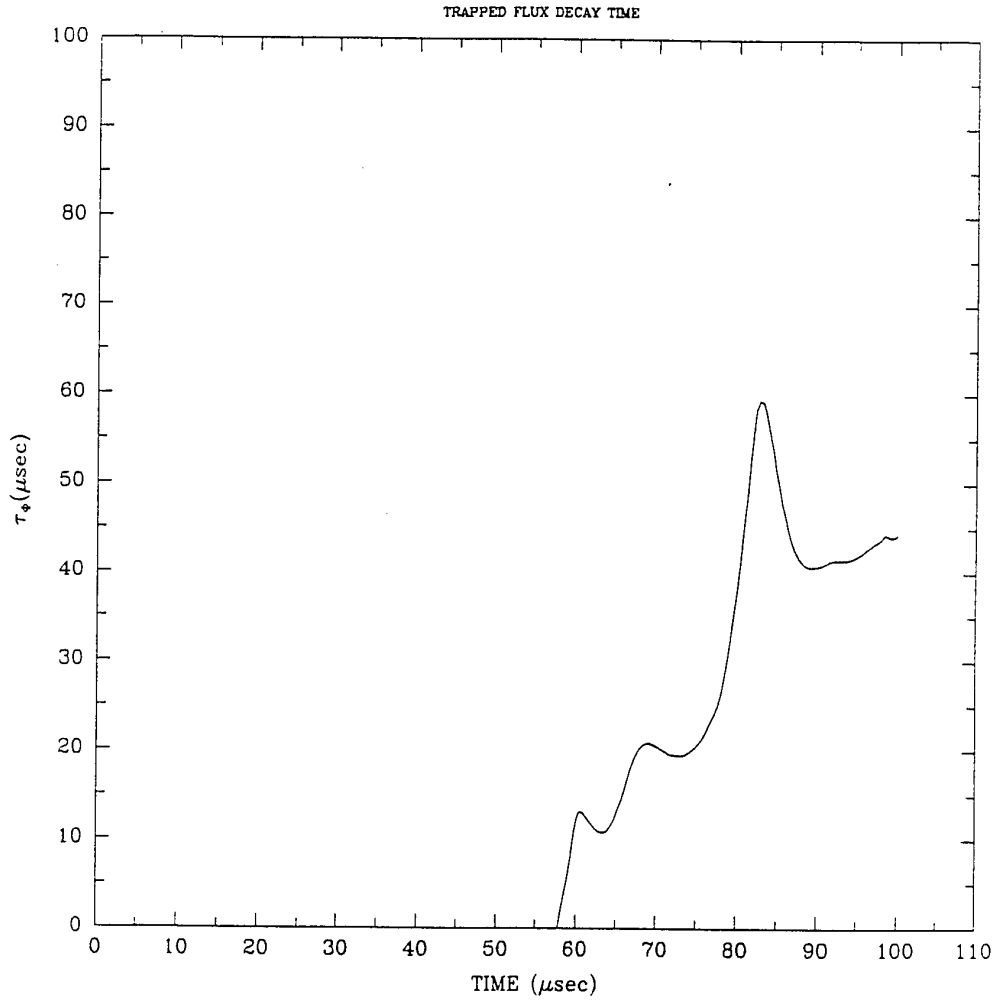

Figure 4.29: Flux decay time for runs #405.

- Low fields in programmed formation (compared to tearing formation) are due to:
  - Less voltage at coils.
  - Greater fraction of energy lost to ionization and heat conduction.
  - Lower resulting temperature.
  - Larger resistance of plasma, lower transfer of flux and energy.
- Tilting plasmas have lower measured magnetic field than the simulations produce because:
  - Tilting plasmas develop anomalous flux dissipation mechanisms.
  - Only classical resistivity was used in simulations (with no tilting).

Chapter 5

SUMMARY

The Coaxial Slow Source experiment was designed to demonstrate annular FRC production with lower voltages and longer formation time scales compared to the field reversed theta pinch method. The initial expectations were that instabilities and anomalous transport would be the important issues to investigate. These are the typical concerns of the FRC community. The result of this dissertation is that interactions of the plasma with neutral gas distinguishes plasmas produced in the CSS as compared to other FRCs.

In fast formation techniques such as the field reversed theta pinch method, partially preionized plasma is rapidly and almost completely ionized. The imploding current sheath sweeps the plasma away from vacuum chamber walls. Atomic physics processes are considered unimportant after this brief formation phase, except for the possibility of radiation from impurities. In the slow formation used in the CSS, neutral and ionized particles can exist simultaneously. Atomic physics processes occur on the same time scales as the configuration lifetime. Instead of a narrow current sheath, the current profile is broad, with a slower Ohmic heating rate. The only heating mechanisms are Ohmic and compressive heating, both of which must compete with comparable energy losses from ionization and heat conduction.

Analysis of the formation technique demonstrated in the Coaxial Slow Source shows the importance of atomic physics processes. Energy is dissipated through processes such as ionization, heat conduction enhanced by neutrals, and impurity radiation. There is no evidence that anomalous transport mechanisms occur until certain magnetic fluctuations are observed experimentally.

Specifically, the results of this dissertation show that:

- The electrical circuit model gives some insight into the coupling between the resistive plasma and the external voltage source.

- The radiation models indicate that radiative collapse and instabilities are pos-

sible when there is a high impurity inventory.

- The COAX code can now accurately simulate the experimental plasma under axisymmetric operating conditions. The addition of the neutral fluid interactions to the code was necessary to achieve accurate simulations.

- Atomics physics processes involving ionization and neutral-ion collisions are very important in slowly forming plasmas such as the CSS:

  - The energy lost in ionization can be a substantial fraction of the energy input into the plasma/magnetic field system.
  - Heat conduction is another energy loss which is enhanced by the charge exchange collisions between ions and neutrals.
  - When the experimental plasma exhibits no azimuthal field fluctuations or asymmetries, the classical resistivity and losses described above allow accurate simulation of the plasma, but when there is magnetic activity, there must be other dissipation mechanisms at work that are not included in the COAX code.
  - Neutral particle pressure can explain the observed magnetic pressure imbalance.

LIST OF REFERENCES

[1] K. D. Hahn, *A transport modeling study of the Coaxial Slow Source plasma*, PhD thesis, University of Washington, Seattle WA, February 1987.

[2] M. Tuszewski, Nucl. Fusion **28**, 2033 (1988).

[3] Z. A. Pietrzyk, G. C. Vlases, R. D. Brooks, K. D. Hahn, and R. Raman, Nucl. Fusion **27**, 1478 (1987).

[4] W. Pierce, R. Maqueda, R. Brooks, and R. Farengo, Nucl. Fusion **33**, 117 (1993).

[5] H. Momota, M. Okamoto, and Y. Nomura, Fusion Tech. **11**, 436 (1987).

[6] F. Hofmann, Nucl. Fusion **15**, 335 (1975).

[7] Y. Kondoh and S. Nagao, Nucl. Fusion **18**, 769 (1978).

[8] R. Raman, *Physics Results from the Initial Operation of a Slow FRC Source*, PhD thesis, University of Washington, Seattle WA, July 1990.

[9] R. J. Smith, *Magnetic Equilibria of the Coaxial Slow Source*, PhD thesis, University of Washington, Seattle WA, 1989.

[10] R. Farengo, Phys. Fluids B **4**, 280 (1992).

[11] W. Pierce, R. Maqueda, R. Farengo, and R. Brooks, Experimental studies of tilting modes in an annular field reversed configuration, November 1991, Poster, American Physical Society—Division of Plasma Physics Conference.

[12] W. Pierce, *Hydromagnetic Stability of a Driven, Dissipative, Annular Field Reversed Configuration*, PhD thesis, University of Washington, Seattle WA, 1993.

[13] S. I. Braginskii, in *Reviews of Plasma Physics*, edited by M. A. Leontovich, Vol. 1, p. 205 (Consultants Bureau, New York, 1965).

[14] I. Lindemuth et al., Plasma Phys. **22**, 207 (1980).

[15] D. J. Rose and Melville Clark, Jr., *Plasmas and Controlled Fusion* (The M.I.T. Press, Cambridge, Massachusetts, 1961).

[16] H. Dreicer, Phys. Rev. **117**, 343 (1960).

[17] M. Harrison, in *Physics of Plasma-Wall Interactions in Controlled Fusion*, edited by D. Post and R. Behrisch, p. 281 (Plenum Press, New York, 1986).

[18] R. Janev, M. Harrison, and H. Drawin, Nucl. Fusion **29**, 109 (1989).

[19] G. Jackson, T. Taylor, and P. Taylor, Nucl. Fusion **30**, 2305 (1990).

[20] I. Hutchinson, *Principles of Plasma Diagnostics* (Cambridge University Press, Cambridge, 1987).

[21] H. L. Anderson, editor, *A Physicist's Desk Reference: The Second Edition of Physics Vade Mecum* (American Institiute of Physics, 1989).

[22] P. Carolan and V. Piotrowicz, Plasma Physics **25**, 1065 (1983).

[23] E. C. Morse and R. W. Ziolkowski, Fusion Tech. **14**, 1325 (1988).

[24] R. McWhirter, in *Plasma Diagnostic Techniques*, edited by R. H. Huddlestone and S. L. Leonard, chapter 5 (Academic Press, New York, 1965).

[25] D. E. Post, R. V. Jensen, C. B. Tarter, W. H. Grassberger, and W. A. Lokke, At. Data Nucl. Data Tables **20**, 397 (1977).

[26] H. R. Griem, *Plasma Spectroscopy* (McGraw Hill, New York, 1964).

[27] R. W. P. McWhirter, in *Plasma Diagnostic Techniques*, edited by R. H. Huddlestone and S. L. Leonard (Academic Press, 1965).

[28] R. Janev et al., Journal of Nuclear Materials **121**, 10 (1984).

[29] D. Duchs and H. R. Griem, Phys. Fluids **9**, 1099 (1966).

[30] D. R. Bates, A. E. Kingston, and R. W. P. McWhirter, Proc. Roy. Soc. **A 270**, 155 (1962).

[31] M. Murakami, J. D. Callen, and L. A. Berry, Nucl. Fusion **16**, 546 (1976).

[32] S. Ortolani and G. Rotagni, Nucl. Instrum. Methods **207**, 35 (1983).

[33] F. W. Perkins and R. A. Hulse, Phys. Fluids **28**, 1837 (1985).

[34] R. Farengo and R. D. Brooks, Phys. Fluids B **3**, 130 (1991).

[35] W. H. Bennett, Phys. Rev. **45**, 890 (1934).

[36] D. Barnes and D. Schnack, Bulletin of the Americal Physical Society **30**, 1455 (1985).

[37] R. Chodura, Nucl. Fusion **15**, 55 (1975).

[38] D. L. Book, Technical Report, Naval Research Laboratory (Naval Research Laboratory, Washington DC 20375, 1990) [NRL Publication 177-4405].

[39] D. Barnes, R. Bishop, R. Milroy, and D. Schnack, Flexible, semi-implicit algorithms for bounded, multi-dimensional MHD calculations, 1990, submitted to Journal of Computational Physics.

[40] D. Harned and W. Kerner, J. Comput. Phys. **60**, 62 (1985).

[41] D. Harned and D. Schnack, J. Comput. Phys. **65**, 57 (1986).

[42] D. Schnack, D. Barnes, Z. Mikic, D. Harned, and E. Caramana, J. Comput. Phys. **70**, 330 (1987).

[43] I. Lindemuth, J. of Computational Phys. **25**, 104 (1977).

[44] E. Freeman and E. Jones, Technical Report, Culham Laboratory, Abingdon, England (Abingdon, England, 1974) [UKAEA Report No. CLM–R137].

[45] R. Janev, W. Langer, K. Evans, Jr., and D.E. Post, Jr., *Elementary Processes in Hydrogen-Helium Plasmas* (Springer-Verlag, 1987).

[46] T.R. Jarboe and R.D. Brooks, CSS: 1990 proposal, 1990, Proposal to Department of Energy.

Appendix A

MAGNETOHYDRODYNAMIC FLUID DESCRIPTION OF THE CSS PLASMA

To properly model a plasma using the MHD fluid equations, care should be taken in deriving the equations from first principles, after which terms which are obviously negligible can be dropped. In the following sections, the Boltzmann equation is used to first find the single fluid equations for each species: electrons, ions, and neutrals, taking account of the interactions between species such as ionization, momentum and energy exchange. Then these equations can be combined to give a single fluid equation for the electron/ion plasma, with another for the neutrals, so that the fluid code COAX can incorporate the effects of ionization and interspecies friction properly.

A.1 Moments of the Boltzmann Equation

The fundamental equation from which to start is the Boltzmann Equation

$$\left[\frac{\partial}{\partial t} + \mathbf{v}\cdot\nabla_x + \frac{e_\alpha}{m_\alpha}\left(\mathbf{E} + \frac{1}{c}\mathbf{v}\times\mathbf{B}\right)\cdot\nabla_{\mathbf{v}}\right] f_\alpha(\mathbf{x},\mathbf{v},t) = \left.\frac{\partial f_\alpha}{\partial t}\right|_{coll} \equiv C_\alpha \tag{A.1}$$

describing the evolution of the distribution function $f_\alpha(\mathbf{x},\mathbf{v},t)$ which is the ensemble-averaged phase-space particle density of species α, where e_α and m_α are the charge and mass, respectively. C_α represents the effects of microfields on the particle dynamics, while the third term on the left hand side give the effects of smoothed fields. Thus C_α can be thought of as a local collision operator describing the time evolution of the species α from binary collisions with the other species present. Braginskii [13] gives a form for the operator C_α in the case of elastic collisions which was be shown to be responsible for effects such as electrical resistivity, heat conduction, and interspecies drag in chapter 1.2. Inelastic collisions cause effects such as ionization, atomic or ionic excitation, and radiative emission. The functional forms for

these collisions is given in the straightforward phenomenological fashion, involving approximations or fits to data for collision cross sections.

To reduce the six dimensions (plus time) of the Boltzmann equation to just three spatial dimensions (plus time), velocity moments of equation (A.1) are taken. This produces macroscopic fluid quantities such as number density, momentum density, and energy density or pressure. Denoting the velocity-space average of any quantity Q as $\langle Q \rangle = \int Q f_\alpha \, d\mathbf{v}/n_\alpha$, with $\int f_\alpha \, d\mathbf{v} = n_\alpha$, we can define the fluid quantities (suppressing the subscript α for now, recognizing that these quantities are defined for each individual species)

$$\begin{aligned} \mathbf{u} &= \langle \mathbf{v} \rangle \\ \mathsf{P} &= mn\langle (\mathbf{v}-\mathbf{u})(\mathbf{v}-\mathbf{u}) \rangle \\ &= p\mathsf{I} + \mathsf{\Pi} \end{aligned} \tag{A.2}$$

where n is the number density, $\mathbf{u}$ is the fluid velocity, and P is the generalized pressure tensor. We separate the pressure tensor into its traceless part $\mathsf{\Pi}$ (which under certain assumptions will be seen to be negligible) and the remaining scalar pressure $p = \frac{1}{3}\mathrm{Tr}(\mathsf{P})$ which is related to the species temperature by the equation of state $p = nT$ (T in units of energy).

The traceless part of the pressure tensor $\mathsf{\Pi}$ is equal to linear combinations of the tensor components of the rate of strain tensor $W_{ij} = \dfrac{\partial v_i}{\partial x_j} + \dfrac{\partial v_j}{\partial x_i} - \dfrac{2}{3}\delta_{ij}\nabla \cdot \mathbf{v}$. The coefficients of these terms are the viscosities, which have the functional dependence on density, temperature, collision time, and cyclotron frequency is $\eta \propto nT\tau/(\omega_c\tau)^m$, where m =0, 1, or 2 depending on magnetic field direction to the tensor component. Thus the ratio of the traceless tensor to the scalar pressure is approximately $\mathsf{\Pi}/p \approx \eta V/nTL \approx \tau V/L(\omega_c\tau)^m$, where V and L are the characteristic velocity and length scale, respectively.

Using typical numbers from CSS simulations, V =1 cm/μsec, L = 2 cm, $\tau_i \approx$ 0.2 μsec, $\omega_i = 5$ μsec^{-1}, assuming $n = 10^{15}$ cm^{-3}, $T = 10$ eV, $B = 1$ kG. The ratio $\mathsf{\Pi}/p < 0.1$ using these numbers (with $m = 0$, and so the ion viscosity is low enough to reduce the nonscalar components of the pressure tensor. The collisionality is high, as $\omega_i\tau_i \approx 1$, that is, the ion cyclotron period is about the same as a collision time. For viscosities dependent on higher powers of $(\omega_i\tau_i)^{-}1$, the results are about the same. The stress tensor $\mathsf{\Pi}$ can be neglected from consideration if desired.

From the moments of equation (A.1), we can construct a set of partial differential equations describing the time evolution of each of the fluid quantities in terms of the others, their spatial derivatives, and the transport terms that depend on the collision operator C. Formally, the equation for the moment $\langle \mathbf{v}^n \rangle$ depends on the moment of $\langle \mathbf{v}^{n+1} \rangle$, and thus an infinite set of coupled equations is required. In practice, only the first three moments are used. Closure is obtained by using the equation of state, neglecting certain terms that are found to be typically small, and determining the transport quantities in terms of the collision operator and the fluid quantities.

The v^0 moment gives the density equation

$$\begin{aligned} \frac{\partial n}{\partial t} + \nabla \cdot n\mathbf{u} &= \int C d\mathbf{v} \\ &= S \end{aligned} \tag{A.3}$$

where S is the particle creation rate. The $m\mathbf{v}$ moment gives the momentum equation

$$\begin{aligned} \frac{\partial (mn\mathbf{u})}{\partial t} + \nabla \cdot (nm\mathbf{u}\mathbf{u}) &= -\nabla \cdot \mathbf{P} \\ &\quad + en\left(\mathbf{E} + \frac{1}{c}\mathbf{u} \times \mathbf{B}\right) + \mathbf{R} + mS\mathbf{u} \\ \mathbf{R} &= \int m(\mathbf{v} - \mathbf{u}) C \, d\mathbf{v} \end{aligned} \tag{A.4}$$

where $\mathbf{R}$ is the interspecies drag from collisions. Using the density equation (A.3), the momentum equation can be written as a velocity equation

$$\begin{aligned} mn\left(\frac{\partial}{\partial t} + \mathbf{u} \cdot \nabla\right)\mathbf{u} &= -\nabla p - \nabla \cdot \mathbf{\Pi} \\ &\quad + en\left(\mathbf{E} + \frac{1}{c}\mathbf{u} \times \mathbf{B}\right) + \mathbf{R} \end{aligned} \tag{A.5}$$

Finally, for closure, an equation for p or T is needed, so the $\frac{1}{2}mv^2$ moment is

taken, which yields

$$\begin{aligned}
\frac{\partial}{\partial t}\left(\frac{1}{2}mnu^2+\frac{p}{\gamma-1}\right) &+ \nabla\cdot\left(\frac{\gamma}{\gamma-1}p\mathbf{u}+\frac{1}{2}mnu^2\mathbf{u}\right) \\
&= en\mathbf{u}\cdot\mathbf{E}+Q-\nabla\cdot\mathbf{q}-\nabla\cdot(\mathbf{u}\cdot\mathbf{\Pi}) \\
&\quad +\mathbf{R}\cdot\mathbf{u}+\tfrac{1}{2}mu^2S \qquad (A.6)\\
Q &= \int\tfrac{1}{2}m(\mathbf{v}-\mathbf{u})^2C d\mathbf{v} \\
\mathbf{q} &= \tfrac{1}{2}mn\langle(\mathbf{v}-\mathbf{u})^2(\mathbf{v}-\mathbf{u})\rangle.
\end{aligned}$$

where $\gamma = 5/3$ for a species of particles with three degrees of freedom, but can be generalized to d degrees of freedom with $\gamma = (d+2)/d$. This can be written as a temperature equation after using the density (A.3), momentum (A.4), and energy (A.6) fluid equations as

$$\begin{aligned}
\frac{n}{\gamma-1}\left(\frac{\partial}{\partial t}+\mathbf{u}\cdot\nabla\right)T &= -nT\nabla\cdot\mathbf{u}-\frac{ST}{\gamma-1} \\
&\quad -\mathbf{\Pi}:\nabla\mathbf{u}+Q-\nabla\cdot\mathbf{q} \qquad (A.7)
\end{aligned}$$

We can also write an equation for the quantity $\varepsilon = n^{2-\gamma}T$,

$$\frac{\partial\varepsilon}{\partial t}+\nabla\cdot\varepsilon\mathbf{u} = (\gamma-1)n^{1-\gamma}(-\mathbf{\Pi}:\nabla\mathbf{u}-ST+Q-\nabla\cdot\mathbf{q}) \qquad (A.8)$$

This form of the energy equation is better suited to numerical solution as it is in the form of a conservation equation for ε with the right hand side as a source.

The quantities $\mathbf{\Pi}$ and $\mathbf{q}$ would seem to prevent closure since they introduce the new fluid quantities of the stress tensor (non-isotropic second order moment) and heat flux (third order moment) into the system. Instead of finding the evolution equations for these moments too, which would introduce yet more new fluid quantities, Braginskii [13] has shown how $\mathbf{\Pi}$ and $\mathbf{q}$ can be determined by the fluid quantities n, $\mathbf{u}$, and T, and the collision operator C by kinetic methods. The friction R and heating rate Q can be calculated similarly, but phenomenological methods are usually used.

The quantity Q is the energy source (or sink) due to collisions, and is very important since besides compressional heating this term alone is responsible for

providing energy to the plasma via Ohmic or fusion heating. Also, the radiation from ion-electron recombination as well as impurity radiation are important energy losses from a transparent plasma. Q also contains terms for energy transfer from species to species.

A.2 Multiple Fluid Model

Various approximations and assumptions are usually taken to get a set of equations for a combined plasma fluid so that calculations can be made. The simplest set of equations is that of ideal magnetohydrodynamics (ideal MHD), with one fluid, and where there are no dissipative mechanisms, energy sources or sinks, nor ionization processes. This description is useful for dynamical stability calculations, where dynamics over time scales shorter than dissipative times can be reasonably approximated. Since the CSS or any slow formation device requires the dynamics calculated on the same timescale as dissipative effects, a resistive version of the ideal MHD equations needs to be used. Also, other collisional effects such as ionization, interspecies friction, radiation losses, etc. need to be included.

To this end, the simplest set of equations (that includes the essential physics) has density equations for both ions and neutrals, momentum equations for both a charged and a neutral fluid, and a single temperature or entropy equation. The electrons are assumed to have the same density as the ions, and are massless, so a separate momentum equations for them is superfluous. If complicated ionization chemistry is desired to be modeled, or impurities with various ionization states are present, rate-diffusion equations for the concentration or densities of these other species could be included also.

The differential equations for the evolution of multiple charged and neutral species, with the majority species being hydrogen or deuterium would then be

$$\begin{aligned} &\partial_t n_\alpha + \nabla \cdot n_\alpha \mathbf{u}_\alpha = S_\alpha, \ \alpha = \text{any species} \\ &\text{and } \mathbf{u}_\alpha = \begin{cases} \mathbf{u}_i & \text{if charged} \\ \mathbf{u}_n & \text{if neutral} \end{cases} \end{aligned} \tag{A.9}$$

$$\partial_t \left(\sum_{charged} \rho_\alpha \right) \mathbf{u}_i + \nabla \cdot \left(\sum_{charged} \rho_\alpha \right) \mathbf{u}_i \mathbf{u}_i = -\nabla \left(\sum_{charged} p_\alpha \right) - \nu_{in} \left(\sum_{charged} \rho_\alpha \right) (\mathbf{u}_i - \mathbf{u}_n) + \left(\sum_{charged} m_\alpha S_\alpha \right) \mathbf{u}_i + \frac{1}{c} \mathbf{J} \times \mathbf{B} \tag{A.10}$$

$$\partial_t \left(\sum_{neutral} \rho_\alpha \right) \mathbf{u}_n + \nabla \cdot \left(\sum_{neutral} \rho_\alpha \right) \mathbf{u}_n \mathbf{u}_n = -\nabla \left(\sum_{neutral} p_\alpha \right) - \nu_{ni} \left(\sum_{neutral} \rho_\alpha \right) (\mathbf{u}_n - \mathbf{u}_i) + \left(\sum_{neutral} m_\alpha S_\alpha \right) \mathbf{u}_n \tag{A.11}$$

$$\partial_t \varepsilon + \nabla \cdot \varepsilon \mathbf{u} = (\gamma - 1) \left(\sum_{all} n_\alpha \right)^{1-\gamma} \sum_{all} [Q_\alpha - \nabla \cdot \mathbf{q}_\alpha - S_\alpha T_\alpha + T(\mathbf{u}_\alpha - \mathbf{u}) \cdot \nabla n_\alpha] \tag{A.12}$$

$$\varepsilon = T \left(\sum_{all} n_\alpha \right)^{2-\gamma} \quad \mathbf{u} = \left(\sum_{all} n_\alpha \mathbf{u}_\alpha \right) / \left(\sum_{all} n_\alpha \right) \tag{A.13}$$

$$(\partial_t + \mathbf{u}_i \cdot \nabla) \psi = \frac{\eta c^2}{4\pi} \Delta^* \psi \tag{A.14}$$

where: $\mathbf{B} = \nabla\psi \times \nabla\theta$, $\mathbf{J} = -(c/4\pi r)\Delta^*\psi\, \hat{\mathbf{e}}_\theta$, $p_\alpha = n_\alpha T$.

Δ^* is called the Grad-Shafranov operator, and in cylindrical coordinates is given by $\Delta^* = \nabla^2 - (2/r)\partial/\partial r$. The ionization source (or sink) terms are given by the S_α terms. Friction between species is represented by the $-\nu_{\alpha\beta}\rho_\alpha(\mathbf{u}_\alpha - \mathbf{u}_\beta)$ terms.

These equations can be simplified by considering only two species (ions and neutrals) with one local velocity. This case thus assumes infinite friction between ions and neutrals. The momentum equations can then be added, resulting in the total mass density and total pressure being the sum of the individual ion and neutral quantities. The resulting set of equations is

$$\partial_t n_i + \nabla \cdot n_i \mathbf{u} = S = -(\partial_t n_n + \nabla \cdot n_n \mathbf{u}) \tag{A.15}$$

$$\partial_t (\rho \mathbf{u}_i) + \nabla \cdot \rho \mathbf{u}_i \mathbf{u}_i = -\nabla p + \frac{1}{c} \mathbf{J} \times \mathbf{B} \tag{A.16}$$

$$\partial_t \varepsilon + \nabla \cdot \varepsilon \mathbf{u} = (\gamma - 1)\left(n_e + n_i + n_n\right)^{1-\gamma}\left(Q - \nabla \cdot \mathbf{q} - ST\right) \tag{A.17}$$

$$\varepsilon = T\left(n_e + n_i + n_n\right)^{2-\gamma} \tag{A.18}$$

$$\left(\partial_t + \mathbf{u}_i \cdot \nabla\right)\psi = \frac{\eta c^2}{4\pi}\Delta^* \psi \tag{A.19}$$

where $p = (n_e + n_i + n_n)T$, and $\rho = m_i(n_i + n_n)$. This is the set of equations used for the infinite friction version of COAX described in chapter 3.2.

VITA

Russell George Berger, Jr. was born in Janesville, Wisconsin in 1954, where he graduated from J.A. Craig High School in 1972. After studying engineering at General Motors Institute from 1972–1974, he continued studies at the University of Wisconsin–Madison leading to the B.S. degree in Applied Mathematics, Engineering, and Physics in 1977. From 1978 to 1985 he studied Physics at the University of Washington, receiving the M.S. degree in 1980, and Candidacy for the Doctorate in 1983. He was employed as a Staff Scientist at Spectra Technology, Inc. from 1985 to 1988. In 1988 he returned to the University of Washington to finish the requirements for the Doctorate in Physics, first with the guidance of Professor George Vlases, and then with Professor Tom Jarboe.